Title
Microfabricated Devices for the Detection of Neurotransmitters

Author
Huang, I-Wen

Publication Date
2020

Peer reviewed|Thesis/dissertation

UNIVERSITY OF CALIFORNIA

Los Angeles

Microfabricated Devices for the Detection of Neurotransmitters

A dissertation submitted in partial satisfaction of the requirements for the degree of Doctor of Philosophy in Chemical Engineering

by

I-Wen Huang

2020

ABSTRACT OF THE DISSERTATION

Microfabricated Devices for the Detection of

Neurotransmitters

by

I-Wen (Brenda) Huang

Doctor of Philosophy in Chemical Engineering

University of California, Los Angeles, 2020

Professor Harold G. Monbouquette, Chair

The ability to monitor simultaneously the electrical activity of neurons and inter-neuronal chemical signaling is expected to lead to an effective means to investigate the complex circuitry underlying brain function. Great advancements have been made in recording electrical activity from large numbers of interconnected neurons concurrently through few-millisecond-timescale measurements. However, corresponding tools to monitor chemical neurotransmission with such high spatiotemporal resolution have yet to emerge. The development of such tools has been particularly challenging because neurotransmitter concentrations are typically low, in the nanomolar to few micromolar ranges. In addition, the neurotransmitter of interest must be detected selectively against the complex background of brain extracellular fluid. The spatiotemporal shortcomings of neurochemical sensors has made problematic the faithful recording of neurotransmitter dynamics, and certainly has made it challenging, if not impossible, to correlate chemical signaling with neuronal activity. In this dissertation, work is presented on the

fabrication and characterization of higher performance microsensors for neurotransmitter detection that better address this need.

A key breakthrough described in this thesis was the several-fold improvement in response time and sensitivity of selective electroenzymatic sensors for glutamate and choline (as surrogate for acetylcholine). Previous devices based on microelectrode arrays (MEAs) of electroenzymatic sensing sites on silicon or ceramic microprobes demonstrated the potential utility of such tools for the monitoring of glutamate and other neurotransmitters *in vivo* during behavioral studies. However, less than optimal sensitivity and response time limited the neuroscience applications of these promising research tools. In this work, the optimization of sensor construction was guided by a detailed mathematical model that prescribed optimal coatings of both permselective films and immobilized enzyme layers so as to maximize performance while maintaining selectivity against interfering species. These design modifications led to glutamate sensors with a ~6-fold sensitivity enhancement, ~10-fold reduction in response time, as well as high-performance choline sensors with remarkable sensitivity and response times in the millisecond range that are near the theoretical performance limits predicted by the model. Importantly, these results were attained without compromising detection limit or selectivity. The much faster response times are expected to allow more faithful recording of neurotransmitter signaling dynamics *in vivo*. Further, great improvements in sensitivity will enable neurochemical recording electrodes to be reduced to cellular dimension and will permit the application of higher density, multiplexed MEAs for simultaneous monitoring of multiple analytes and for facile integration of electrical recording sites. The improved capabilities of these optimized glutamate and choline sensors has been validated by neuroscience collaborators studying the reward-seeking behavior of laboratory rats. By using our microsensors, they were able to rapidly, clearly and continuously monitor cholinergic and

glutamatergic transmissions in the area of the brain associated with cognition and uncover the roles that the neurotransmitters acetylcholine and glutamate play.

Multianalyte sensing microprobes also were created to provide neuroscientists with a new tool to unravel the interplay of multiple neurochemicals *in vivo*. Redox enzymes used in electroenzymatic sensors are most commonly immobilized on microelectrodes by manually spreading a mixture of enzyme and bovine serum albumin (BSA) on an electrode surface coated with permselective films followed by crosslinking with glutaraldehyde. This manual approach clearly becomes problematic when the MEA feature size is less than or equal to ~100 μm. A polydimethylsiloxane (PDMS) microstamping method was developed to enable precise transfer of enzyme onto targeted microelectrodes. Two model enzymes, glucose oxidase and choline oxidase, were successfully stamped onto different sites on the same microprobe to create a dual sensor. The resulting dual sensor showed the expected response to glucose and choline on the appropriate microsensor sites without cross-talk. The performance of the stamped sensor was further improved through the use of a polycation-functionalized zwitterionic polymer, poly(2-methacryloyloxyethyl phosphorylcholine)-g-poly(allylamine hydrochloride), as an alternative enzyme immobilization matrix to BSA. This specially designed polymer addressed the problem of pattern spreading found when using BSA by contributing a stronger intermolecular force, thereby allowing deposition of a much thicker yet more finely defined enzyme pattern. The increase in enzyme loading led to a choline sensor with two-fold improvement in both sensitivity and detection limit. This successful enzyme stamping approach is expected to contribute to neuroscience by enabling the simultaneous recording of multiple neurochemicals in close proximity *in vivo*.

A highly flexible PDMS-based microprobe also was developed to address the long-standing challenge of relative shear motion at the probe-tissue interface that is attributed to the mechanical mismatch between the typically very stiff probe and the surrounding soft neural tissue.

The PDMS microprobe was designed with internal channels filled with gallium (Ga) metal. Ga is solid at room temperature but melts at body temperature. Thus, using Ga in probe construction made possible the deep insertion of probes into rat brains under cooled conditions but these implanted devices later become highly flexible upon Ga melting. This sensor design serves as an attractive platform for chronic *in vivo* studies with freely moving animals where probe micromotion must be minimized to avoid gliosis and permit long term neurochemical recordings.

Finally, the dependency on the existence of appropriate redox enzymes has always been the major limitation on applicability of electroenzymatic sensor technology. A second class of sensing devices were developed using aptamers as the biological recognition elements. Si microprobes with an array of aptamer-based field-effect transistors (FETs) were created. Since aptamers carry a great deal of charge, a change in conformation of its negatively charged phosphodiester backbone upon binding with target in close proximity to semiconductor channel enables signal transduction and amplification by the underlying FET. These aptamer-based FET microprobes exhibit an unprecedented detection limit of ~10 fM (10^{-14} M) to serotonin that is substantially lower than all other analytical methods (typically in the range of 10^{-9} – 10^{-6} M), thereby providing a potential alternative route to detection of neurotransmitters, especially those for which no redox enzymes exist and that are present in the brain at very low concentration. Our main contribution to this project was to help Dr. Anne Andrews group miniaturizing their well-developed aptamer-based FETs in micro-range for *in vivo* application.

The dissertation of I-Wen Huang is approved.

Nigel Maidment

Yi Tang

Yvonne Chen

Harold G. Monbouquette, Committee Chair

University of California, Los Angeles

2020

TABLE OF CONTENTS

CHAPTER 1: INTRODUCTION 1

1.1 ELECTROCHEMICAL SENSING OF NEUROTRANSMITTERS 1

1.1.1 Motivation 1

1.1.2. Current technologies for neurotransmitter detection 2

1.1.3 Microprobes with an array of electroenzymatic sensing sites for detection of neurotransmitters 3

1.1.4 Microprobes capable of multiple neurotransmitters sensing 5

1.1.5 Microprobes with multi-functionalities 6

1.1.6 Microprobes with an array of aptamer-field effect transistors for detection of neurotransmitters 7

1.2 REFERENCES 8

CHAPTER 2: ELECTROENZYMATIC GLUTAMATE SENSING AT NEAR THE THEORETICAL PERFORMANCE LIMIT 13

2.1 INTRODUCTION 14

2.2 EXPERIMENTAL 17

2.2.1 Reagents 17

2.2.2 Instrumentation 18

2.2.3 Sensor preparation 18

2.2.4 Electrochemical measurement 19

2.2.5 Diffusion coefficient measurement 20

2.2.6 Mathematical Model and Simulations 20

2.3 RESULTS AND DISCUSSION 20

2.3.1 Optimization of permselective films 20

2.3.2 Hydrogen peroxide diffusion coefficient in permselective films and the crosslinked GlutOx layer 22

2.3.3 Effect of Enzyme loading and Activity 27

2.3.4 Optimal enzyme layer thickness 30

2.3.5 Comparison in performance between our optimized and previously reported sensors 30

2.3.6 Response time 31

2.3.7. Simulation Results 33

2.4 CONCLUSION 35
2.5 REFERENCES 36
CHAPTER 3: CHOLINE DETECTION AT NEAR THE THEORETICAL PERFORMANCE LIMIT OF ELECTROENZYMATIC SENSORS 40
3.1 INTRODUCTION 41
3.2 EXPERIMENT 43
3.2.1 Reagents 43
3.2.2 Instrumentation 44
3.2.3 Sensor preparation 44
3.2.4 Electrochemical measurement 46
3.2.5 Mathematical Model and Simulations 46
3.3 RESULTS AND DISCUSSION 47
3.3.1 Effect of Enzyme loading and Activity 47
3.3.2 Optimal enzyme layer thickness 50
3.3.3 Optimized sensor performance 51
3.3.4 Response time 52
3.3.5 Stability 53
3.3.6 Simulations to determine theoretical performance limits 54
3.4 CONCLUSION 57
3.5 REFERENCES 58
CHAPTER 4: NUCLEUS ACCUMBENS CHOLINERGIC INTERNEURONS OPPOSE CUE-MOTIVATED BEHAVIOR 62
4.1 INTRODUCTION 63
4.2 METHODS AND MATERIALS 64
4.2.1 Subjects 64
4.2.2 Surgery 65
4.2.3 Behavioral Procedures 65
4.2.4 Data Analysis 69
4.2.5 Approach Validation 69
4.3 RESULTS 70
4.3.1 Chemogenetic Inhibition of NAc Cholinergic Interneurons Augments Cue-Motivated Behavior 70
4.3.2 Optical Stimulation of NAc Cholinergic Interneurons Concurrent With Reward Cue Presentation Blunts Cue-Motivated Behavior 73

4.3.3 Acetylcholine Release From NAc Cholinergic Interneurons Works via b2-Containing Nicotinic Receptors to Blunt Cue-Motivated Behavior 75
4.4 DISCUSSION 78
4.5 REFERENCES 81
CHAPTER 5: MICROBIOSENSOR FABRICATION BY POLYDIMETHYLSILOXANE STAMPING FOR COMBINED SENSING OF GLUCOSE AND CHOLINE 92
5.1 INTRODUCTION 93
5.2 EXPERIMENTAL 95
5.2.1 Reagents 95
5.2.2 Instrumentation 95
5.2.3 Fabrication of mold and PDMS stamps 96
5.2.4 Sensor preparation 97
5.2.5 PDMS μCP with alignment 97
5.2.6 Electrochemical measurements 98
5.3 RESULTS AND DISCUSSION 99
5.3.1 PDMS stamping of enzymes 99
5.3.2 Glucose microbiosensor performance 100
5.3.3 Choline microbiosensor performance 102
5.3.4 Dual sensor and effect of interferents 104
5.4 CONCLUSIONS 105
5.5 REFERENCES 105
CHAPTER 6: IMPROVED MICROCONTACT PRINTING OF CHOLINE OXIDASE USING A POLYCATION-FUNCTIONALIZED ZWITTERIONIC POLYMER AS ENZYME IMMOBILIZATION MATRIX 108
6.1 INTRODUCTION 109
6.2 METHOD 111
6.2.1 Reagents 111
6.2.2 Instrumentation 112
6.2.3 Synthesis of PMPC conjugated PAH via RAFT polymerization (PMPC-g-PAH) 112
6.2.4 Sensor preparation 114
6.2.5 Sensors calibration 115
6.3. RESULT AND DISCUSSION 116
6.3.1 Problems in BSA-ChOx ink 116
6.3.2 PMPC-g-PAH-ChOx ink 118

6.3.3 Stamped choline microsensor performance 120
6.3.4 Enzyme Affinity 122
6.4 CONCLUSION 123
6.5 REFERENCES 124
CHAPTER 7: FLEXIBLE, MULTIFUNCTIONAL NEURAL PROBE WITH LIQUID METAL ENABLED, ULTRA-LARGE TUNABLE STIFFNESS FOR DEEP-BRAIN CHEMICAL SENSING AND AGENT DELIVERY 127
7.1 INTRODUCTION 128
7.2 EXPERIMENTAL SECTION 130
7.2.1. ULTS probe design and working principle 130
7.2.2 Fabrication of ULTS probes 131
7.2.3 Biosensor preparation 134
7.2.4 In vitro biosensor characterization and testing 135
7.2.5 Acute in vivo studies 136
7.3 RESULTS AND DISCUSSION 137
7.3.1 Characterization of probe tunable stiffness and implantation in brain phantoms 137
7.3.2 Demonstration of probe flexibility in brain phantoms 140
7.3.3 In vitro probe characterization 140
7.3.4 Probe implantation in rats 142
7.3.5 In vivo probe testing 144
7.4 CONCLUSION 146
7.5 REFERENCES 147
CHAPTER 8: IMPLANTABLE, APTAMER-BASED FIELD-EFFECT TRANSISTOR MICROPROBES: TOWARD MONITORING OF SEROTONIN IN MICE 151
8.1 INTRODUCTION 152
8.2 MATERIALS AND METHODS 154
8.2.1 Materials 154
8.2.2 Fabrication Process 154
8.2.3 Surface Modification of Microprobes 155
8.2.4 Ex vivo sensing in brain tissue homogenates 155
8.2.5 Electrochemical measurements 156
8.3 RESULTS AND DISCUSSIONS 156
8.3.1 Fabrication and characteristics of In_2O_3-based FET microprobes 156
8.3.2 Characteristics of aptamer FET transfer curves: I_{DS} versus V_{GS} sweeps 159

8.3.3 Microsensor performance in brain tissue homogenates 162
8.3.4 Real-time detection of serotonin- I_{DS} versus time 163
8.3.5 Selectivity of serotonin aptamer based microsensor 164
8.4 CONCLUSION 164
8.5 REFERENCES 165
CHAPTER 9: RECOMMENDATIONS FOR FUTURE WORK 167
9.1 ELECTROENZYMATIC NEUROTRANSMITTER SENSING 167
9.2 PDMS MICROCONTACT PRINTING (MCP) TO FABRICATE MICRONEUROPROBES FOR MULTI-SENSING OF NEUROTRANSMITTERS 168
9.3 IMPLANTABLE APTAMER FIELD-EFFECT TRANSISTOR NEUROPROBES TOWARDS IN VIVO NEUROTRANSMISSIONS MONITORING OF SEROTONIN IN MICE 170
9.5 REFERENCES 173
APPENDIX A: MICROPROBE FABRICATION FOR ELECTROENZYMATIC SENSORS 173
A.1 MATERIALS 173
A.2 PROCESS TRAVELER 174
APPENDIX B: PREPARATION OF GLUTAMATE AND CHOLINE SENSORS 178
B.1 MATERIALS 178
B.2 PROCEDURE 179
B.2.1 Probe Assembly 179
B.2.2. Acid clean 180
B.2.3 Bare sensor test 180
B.2.4 PPD deposition and Nafion coating 180
B.2.5 Enzyme Immobilization 180
APPENDIX C: MEASUREMENT OF RESPONSE TIME 181
APPENDIX D: MICROPROBE FABRICATION FOR IN_2O_3-BASED FETS ARRAY 186
APPENDIX E: TROUBLESHOOTING AND COMMON ISSUES 188
E.1 MICROPROBE FABRICATION 188

LIST OF FIGURES

Figure 2.1. Schematic of an electroenzymatic glutamate (Glut) sensor with permselective films and a glutamate oxidase (GlutOx) enzyme layer. 15

Figure 2.2. Scanning electron microscopy (SEM) image of the microelectrode array probe..... 19

Figure 2.3. Testing set-up for microsensor response time. Rapid switching of solution flow onto the microprobe was controlled by alternating between pumped streams of PBS buffer and analyte solution. 20

Figure 2.4. (a) Comparison of H2O2 sensitivity among sensors prepared with PPy/180 °C-Nafion, PPD/180 °C-Nafion, and PPD/115 °C-Nafion. (b) The Nafion thicknesses corresponding to the three different sensor preparations. Inset: SEM image of a Nafion film on Pt. (c) Representative current responses of PPD/115 °C-Nafion coated sensors to 250 μM AA, 5 μM DA, and H2O2 administered in 20 μM concentration increments. (Error bars shown are 95% confidence intervals.) 22

Figure 2.5. Representative current vs. potential curves showing the charge transfer, mass transport controlled and water dissociation regions at a bare Pt RDE using a potential sweep rate of 20 mV/s with rotation rates of 100, 200, 400, 800, 1600 rpm in PBS and 0.2 mM H_2O_2 solution. 25

Figure 2.6. (a) Oxidation of 0.2 mM H_2O_2 in PBS (pH 7.4) at Nafion-coated Pt RDEs annealed at 180°C and 115°C using a potential sweep rate of 20 mV/s with rotation rates of 100, 200, 400, 800, 1600, 2400 rpm. (b) Koutecky-Levich plot of data for a bare Pt RDE (gray trace) and for 180°C-Nafion/Pt (blue trace) and 115°C-Nafion/Pt (red trace) RDEs. Current data were obtained at 0.7 V vs. Ag/AgCl. 25

Figure 2.7. (a) Representative current response of Glut sensors crosslinked *via* BS3 (red trace) and GAH (blue trace) to interferents (250 μM AA and 5 μM DA), followed by three 20 μM step increases in H_2O_2 concentration. (b) Glut sensitivity comparison between BS3 and GAH crosslinked GlutOx sensors with error bars giving 95% confidence intervals. In all cases, the mass ratio of GlutOx to BSA was 1 : 4 and the enzyme layer was less than 5 μm thick. 29

Figure 2.8. Effect of GlutOx concentration on the Glut sensitivity, where f_{glutox} is varied from 0.02 to 0.95. In all cases, sensors were crosslinked with BS3 and the layer thickness was less than 5 μm. Error bars represent 95% confidence intervals. 29

Figure 2.9. Sensor sensitivity based on the linear range of calibration curves (0–60 μM Glut) versus immobilized GlutOx layer thickness. In all cases, $f$glutox = 0.2, and sensors were crosslinked with BS3. 31

Figure 2.10. (a) Sensor sensitivity and (b) detection limit based on the linear range of the calibration curves (0–60 μM Glut) for the improved (current) and previously published (old) (ref. 11) Glut sensors. Error bars represent 95% confidence intervals. 31

Figure 2.11. Representative sensor response to a 0–40 μM step-change in Glut concentration for base-case Glut sensor (blue trace), the improved Glut sensor (orange trace) and a step-change in H2O2 for bare Pt sensor (grey trace) as reference. Dimensionless response is the current divided by the steady-state current. 32

Figure 2.12. Simulations of sensor sensitivity to Glut as a function of GlutOx mass fraction in the enzyme layer (f_{glutox}) and enzyme layer thickness. 34

Figure 3.1. (a) SEM and (b) optical microscope image of the bare microelectrode array probe. (c) Optical microscope image of the microelectrode array probe after polymer and enzyme deposition. 45

Figure 3.2. (a) Ch sensitivity comparison between GAH, BS3 and EGS crosslinked Ch sensors with error bar giving 95% confidence intervals. (b) Effect of EGS concentration on the Ch sensitivity. In all cases, the mass ratio of ChOx to BSA was 2 : 3 and the enzyme layer was ~3-4 μm to ensure equivalent enzyme loading. 48

Figure 3.3. Effect of immobilized ChOx concentration on the Ch sensitivity of sensors crosslinked via BS3 (grey trace) and sensors crosslinked via EDC (orange trace). In all cases, the enzyme layer thickness was ~3-4 μm. Error bars represent 95% confidence intervals. 50

Figure 3.4. (a) Simulation result and (b) experimental result of sensor sensitivity versus immobilized ChOx layer thickness. In all cases, f_{ChOx} = 0.4, and sensors were crosslinked via BS3. Simulations assume a void fraction in the enzyme layer of 0.6. 51

Figure 3.5. Representative current responses of optimized Ch sensors tested in batch with key interferents AA (250 μM), DA (5 μM), target Ch (final 20, 40, 60 μM in solution), interferent DA (final 15 μM in solution), H_2O_2 (20 μM) and Ch (final 100 μM in solution) in series. 52

Figure 3.6. Representative sensor response to a step-change in Ch concentration from 0 to 60 μM for the optimized Ch sensor (blue trace) and a step-change in H_2O_2 for bare Pt sensor (orange trace) as a benchmark. 53

Figure 3.7. Stability of GAH-crosslinked (blue trace) and BS3-croslinked (orange trace) Ch sensors stored in PBS at 4 °C. Data shown with 95% confident intervals (n = 4 for both cases). 54

Figure 3.8. Simulated sensitivity as a function of enzyme layer thickness for fchox=0.4 and experimental values for reference. 57

Figure 4.1. Chemogenetic inhibition of nucleus accumbens (NAc) cholinergic interneurons augments cue-motivated behavior. (A) Schematic representation of human M4 muscarinic receptor [hM4D(Gi)]–mCherry expression in the NAc for all subjects. Slides represent 0.7–1.7 mm anterior to bregma. (B) Representative immunofluorescent images of hM4D(Gi)- mCherry expressing cholinergic interneurons in the NAc. (C) Colocalization of choline acetyltransferase

(ChAT) staining and hM4D(Gi)-mCherry expression in the NAc. (D) CNO:hM4D(Gi) attenuation of optically evoked (473 nm, 20 Hz, 5–30 mW, 10-ms pulse width, 5-second duration) acetylcholine release in the NAc in vivo [see Supplemental Figure S1 for histology demonstrating hM4D(Gi) and channelrhodopsin-2 expression in cholinergic interneurons; *n* = 4]. Mean 61 SEM. (E) Procedure schematic. (F, G) Lever press rate during each 2-minute period of the Pavlovian-to-instrumental transfer test, averaged across trials compared between the conditional stimulus (CS)–free (baseline) (BL), neutral control stimulus ($CS^{Ø}$), and reward-predictive cue (CS^{+}) periods for the vehicle-treated and CNO-treated conditions in hM4D(Gi) (*n* = 19) (F) or mCherry control (*n* = 16) (G) subjects. Mean ± 1 SEM. *p < .05, **p < .01, ***p < .001. ac, anterior commissure; CNO, clozapine N-oxide; LP, lever press; Ø, no reward; Pel, pellet reward; Veh, vehicle. [Images in panel (A) reproduced with permission from Paxinos and Watson (100).] 72

Figure 4.2. Optical stimulation of nucleus accumbens (NAc) cholinergic interneurons concurrent with reward-predictive cue blunts cue-motivated behavior. (A) Schematic representation of channelrhodopsin-2 (ChR2)– enhanced yellow fluorescent protein (eYFP) expression and fiber tips in the NAc for all subjects. Slides represent 0.7–1.7 mm anterior to bregma. (B) Representative immunofluorescent images of ChR2-eYFP–expressing cholinergic interneurons in the NAc. (C) Colocalization of choline acetyltransferase (ChAT) staining and ChR2-eYFP expression in the NAc. (D) Optically evoked acetylcholine release in *vivo* by blue light delivery (473 nm, 10 Hz, 10 mW, 5-ms pulse width, 120-second duration) to ChR2-expressing cholinergic interneurons in the NAc (see Supplemental Figure S3 for histology; *n* = 5/group). Mean ± 1 SEM. (E) Procedure schematic. The blue triangle indicates light delivery. (F, G) Lever press rate during each 2-minute period of the Pavlovian-to-instrumental transfer test, averaged across trials compared between the conditional stimulus (CS)–free (baseline) (BL), neutral control stimulus (CSØ), and reward-predictive cue (CS1) periods for tests in which optical stimulation occurred during the baseline stimulation, CSØ, and CS1 periods in ChR2 (*n* = 9) (F) or eYFP control (*n* = 8) (G) subjects. Mean ± 1 SEM. ***p < .001. ac, anterior commissure; LP, lever press; Ø, no reward; Pel, pellet reward. 75

Figure 4.3. Acetylcholine release from nucleus accumbens (NAc) cholinergic interneurons works via β_2-containing nicotinic receptors to blunt cuemotivated behavior. (A) Schematic representation of channelrhodopsin-2 (ChR2)–enhanced yellow fluorescent protein expression and fiber/injector tips in the NAc for all subjects. Slides represent 0.7–1.7 mm anterior to bregma. (B) Representative immunofluorescent images of ChR2–enhanced yellow fluorescent protein–expressing cholinergic interneurons in the NAc. (C) Colocalization of choline acetyltransferase (ChAT) staining and ChR2– enhanced yellow fluorescent protein expression in the NAc. (D) Procedure schematic. The blue triangle indicates light delivery. (E) Lever press rate during each 2-minute period of the Pavlovian-to-instrumental transfer test, averaged across trials compared between the conditional stimulus (CS)–free (baseline) (BL), neutral control stimulus ($CS^{Ø}$), and reward-predictive cue (CS^{+}) periods for the tests with either intra-NAc vehicle or DhβE with or without optical stimulation during CS^{+} (*n* = 11). Mean ± 1 SEM. **p < .01, ***p < .001. ac, anterior commissure; DhβE, dihydro-b-erythroidine; LP, lever press; Ø, no reward; Pel, pellet reward. . 77

Figure 5.1. (a) Fabrication process for a SU-8 mold and a PDMS microstamp. (b) Scanning electron microscope (SEM) image of a PDMS microstamp. 97

Figure 5.2. Alignment setup for a PDMS microstamp and a microelectrode array on a silicon-based microprobe. 99

Figure 5.3. 100Å~ optical microscope image of a microelectrode array on a microprobe (a) before and (b) after PDMS stamping of ChOx and GOx with alignment. 100

Figure 5.4. Calibration plot for the glucose biosensor. The biosensor response in stirred solution was recorded for sequential injections of glucose to give concentrations of 0, 40, 80, 160, 240, 440, 640, 840, 1040, 1240 and 1440 µM, at a constant potential of 0.7 V (vs. Ag/AgCl) in stirred PBS buffer (pH 7.4). Error bars: Standard error of the mean (*n* = 5). 101

Figure 5.5. Representative calibration plot for the choline biosensor. The biosensor response in stirred solution was recorded for sequential injections of choline chloride to give concentrations of 0, 10, 20, 40, 60, 80, 100, 120, and 140 µM, at a constant potential of 0.7 V (vs. Ag/AgCl) in stirred PBS buffer (pH 7.4). The inset plot shows the lower analyte concentration range (0–60 µM). Error bars: Standard error of the mean (*n* = 4). 103

Figure 5.6. Combined sensing of glucose and choline at a constant potential of 0.7 V (vs. Ag/AgCl). The microprobe was tested in stirred PBS solution with sequential injections to give 20 µM, 40 µM and 60 µM of choline chloride, 0.6 mM of glucose, 250 µM and 500 µM of ascorbic acid (AA), 5 µM of dopamine (DA) and 1.2 mM of glucose. The control site was coated with the same permselective PPD film as the sensing sites. 104

Figure 6.1. Synthesis route of PAH-*g*-PMPC polymer 113

Figure 6.2. Proton NMR of PAH-CTA and PAH-*g*-PMPC 113

Figure 6.3. Scanning electron microscopy (SEM) image of the microelectrode array probe.... 115

Figure 6.4. Schematic diagram for the preparation of choline sensors by modifying the electrode surface with different permselective layers (PPD and Nafion), chitosan, and choline oxidase. 115

Figure 6.5. Diagram illustrating the enzyme transferring process of µCP. The PDMS stamp is inked with enzyme solution (a), carefully aligned to the target electrode surface under the microscope (b), and gently contacted for few seconds (c). This transfer formed a patterned enzyme layer on the microprobe (d). 116

Figure 6.6. Distinct ChOx pattern on chitosan-coated substrate with various wettabilities after PDMS stamping of BSA-ChOx ink. 117

Figure 6.7. Optical microscope image of BSA-ChOx pattern on microsensors after exposure to GAH vapor and its corresponding cross-section SEM image. 118

Figure 6.8. Contact angle measurements for (a) PMPC-g-PAH and (b) DI water as reference on PDMS stamps. 119

Figure 6.9. Optical microscope image of PMPC-g-PAH-ChOx pattern on microsensors after exposure to GAH vapor and its corresponding cross-section SEM image. 120

Figure 6.10. (a) Representative current response of stamped BSA-ChOx (blue trace) and stamped PMPC-g-PAH-ChOx (red trace) Ch sensors to interferents, 250 μM AA and 5 μM DA, following by three 20 μM step increase in ChCl and a 20 μM increase in H2O2. (b) Choline sensitivity and (c) limit of detection calibration over a range of 0-60 μM. (error showing 95% confident interval) 121

Figure 6.11. Comparison between K_M and V_{max} observed from choline stamped microsensors with PMPC-g-PAH-ChOx (blue curve; K_M^{app} = 110±18 μM; V_{max} = 7.9±0.6 nA with n = 4) and BSA-ChOx (orange curve; ; K_M^{app} = 101±27 μM; V_{max} = 5.8±1.7 nA with n = 5) with error bar shown 95% confident interval. 123

Figure 7.1. Design and working principle of ULTS probes. (a) An exploded-view drawing of a ULTS probe with 3 layers of PDMS thin-films integrated with Pt electrodes for electrochemical sensing. The first PDMS layer serves as the bottom substrate of the probe. Three through-layer holes (vias) are patterned, one serving as liquid outlet, and two for electrical connection to the sensing electrodes. The second PDMS layer is composed of three microfluidic channels, one for drug delivery and two filled with liquid metal (Ga) for electrical connections. The third PDMS layer has one liquid channel filled with liquid Ga, which is then frozen to stiffen the probe. (b) Schematics illustrating the swelling of the ULTS probe shank under different Ga filling pressures: i) no pressure, flat state; ii) positive pressure, inflated state; iii) negative pressure (suction), deflated state. (c) Picture of a fabricated ULTS probe in the stiff state for brain implantation. (d) A ULTS probe in the soft state with integrated drug delivery function. Inset, a SEM image of the probe tip showing the outlet of the drug delivery channel and Pt electrodes. (e–g) Schematic of the implantation procedure. Tissue is cooled down from the surface by the application of chilled saline. The white dashed line represents the temperature of the Ga melting point, 30 °C, above which the probe becomes flexible. After implantation, Ga melts and is removed from the stiffening channel by suction to reduce probe thickness and stiffness. Temperature is represented in color scale. 133

Figure 7.2. Characterization of probe tunable stiffness and implantation capability in brain phantoms. (a) Schematic cross-sectional view of an inflated probe. (b,c) Characterization of the probe shank swelling with respect to different Ga filling pressure. Dashed lines represent the boundaries of the probe (144 μm-wide). The slightly longer distance under 60 psi is a measurement artifact due to steep edge of the largely deformed probe and the cone shape of the profilometer's stylus. (d) Demonstration of a 2 cm-long ULTS probe implanted in a brain phantom (0.6% agarose gel) at room temperature, with a Ga injection pressure of 60 psi to achieve maximum stiffness. (e) Top, picture of a 4 × 2 probe array by stacking two 4-shank probes. Bottom, insertion of a 1 cm-long, 4-shank probe in a brain phantom. (f) ULTS probe in the “inflated” state with 15 psi injection pressure. Top, SEM ‘bird's-eye’ view. Inset, front view showing a shank swelling height of 40 μm, scale bar, 40 μm. Bottom, side-view of an inflated probe implanted in a brain phantom. (g) ULTS probe in the “deflated” state. Top, SEM ‘bird's eye’ view. Bottom, side-view of a probe in a brain phantom deflated by active suction of Ga. 139

Figure 7.3. Demonstration of probe flexibility in brain phantoms. (a) Pictures of a “soft” ULTS probe in a brain phantom. Probe base was moved in all directions to simulate the relative motion between skull and brain with no resulting deformation of the brain phantom. (b,c) Comparison of silicon (Si), SU-8 and ULTS probes with a 500 μm horizontal movement of the brain phantom. Each dotted line is extended from the probe tip vertically. Arrows indicate the reference points in the brain phantom. (d,e) Comparison of Si, SU-8 and ULTS probes with a vertical movement of the probe base. The dotted line indicates the original level of probe tips. Solid lines in (e) indicate the probe tips’ positions after probe movement. 141

Figure 7.4. In vitro characterization of biosensor and chemical delivery functions. (a) Schematic diagram of the coatings on a single electrode on the ULTS probe. (b) Calibration curve for Glut sensing showing a linear correlation in the physiological range, up to 160 μM. Mean ± SEM of 4 sensors. (c) Current response of a Glut biosensor to Glut, the physiological interferents – dopamine (DA) and ascorbic acid (AA), and H_2O_2 in stirred PBS solution (pH 7.4). Arrows indicate the sequential injections to give total concentrations of 20 μM Glut, 40 μM Glut, 5 μM DA, 250 μM AA, 60 μM Glut and 20 μM H_2O_2. (d) Optical image showing delivery of liquid (aqueous solution of Allura Red AC) into a brain phantom (0.6% agarose gel). (e, f) In vitro testing of chemical delivery in brain phantoms (0.6% agarose gel in aCSF). H_2O_2 (40 μM) (e) and Glut (150 μM) (f) were injected at 60 psi with injection duration of 4.8 s, 2.4 s, 1.2 s, 0.6 s and 0.3 s indicated by the arrows (injection volumes in the range ~1–20 nL). 143

Figure 7.5. Probe Implantation in Rats. (a) Schematic of a coronal brain slice illustrating the targeted implantation location in the rat striatum. (b) Schematic of the implantation procedure. Bilateral craniotomies were performed above the striata and chilled sterile saline was perfused across the skull surface. A miniaturized temperature probe was inserted remote from the recording site at the targeted implantation depth. (c) Optical image of a ULTS probe (arrow) implanted in a rat brain. (d) A representative brain temperature curve showing the brain cooling and temperature recovery process. Arrows indicate the start and end of the application of chilled saline solution. 145

Figure 7.6. *In vivo* characterization of biosensor and chemical delivery functions. (a) Detection of repeated injections of Glut (500 μM) via the fluid channel into the rat striatum. Glut solutions were injected at 2 min intervals at 60 psi with injection durations of 2.4 s, 1.2 s, 0.6 s and 0.3 s, respectively, indicated by the brackets. (b) Repeated injection (arrows) of potassium-enriched artificial cerebrospinal fluid (100mM K^+ aCSF) in rat striatum to induce Glut release. Solutions were injected at 60 psi with an injection duration of 4.8 s at 2 min intervals. Signal amplitude was considerably reduced following the initial stimulation, recovering only partially after a prolonged period (25 min) free from stimulation. 146

Figure 8.1. Schematics of the microprobe fabrication process (left) and a single device FET at the shank of microprobe (right). The schematic shows the layers on the microprobes, where from top to bottom are parylene, Au electrode, In_2O_3, and the Si substrate. 158

Figure 8.2. (a) Photograph of a 4” Si wafer with 150 microprobe devices before the deep reactive-ion etching (DRIE) process. (b) Photograph showing two released microprobes after DRIE next to a quarter dollar. (c) Scanning electron microscope (SEM) image of the shank of a microprobe

with false colors. (d) Photograph of a solid-state measurement setup. (e, f) Representative transfer and output characteristics, respectively. 158

Figure 8.3. (a) Schematic illustration of the electrical measurement setup used for serotonin sensing experiments. 1x PBS (pH 7.4) was used as a gate liquid, and gate bias (V_{GS}) was applied through a Ag/AgCl reference electrode. (b)(c) Serotonin-aptamer-field-effect transistor (FET) microprobe responses to serotonin led to increases in source-drain current. 161

Figure 8.4. (a) Serotonin aptamer field-effect transistor (FET) microprobe responses to serotonin in 1x PBS. Error bars: standard error mean for 4 devices. (b) Hypothesized mechanism of stem-loop aptamer serotonin-induced reorientation away from semiconductor channels at distances within or near the Debye length. 161

Figure 8.5. (a) Schematic illustration of brain tissue homogenate preparations. Brains from *Tph2* knockout mice were removed and mixed with 1x artificial cerebrospinal fluid. Tissues were sonicated on ice to generate the brain tissue homogenates. (b) Schematic illustration of the *in vitro* measurement setup. (c) Serotonin response curve in brain tissue homogenates. Error bars are ± standard error of the mean with n = 3. 162

Figure 8.6. (a) Representative real-time measurements of serotonin aptamer FET microprobes in 1x PBS and (b) its calibration plot. Concentrations ranging from 10 fM to 10 uM were spiked into stirred beakers. 163

Figure 9.1. Schematic of (a) “roof-collapse” issue from current stamp design, (b) potential solutions of designing stamp with deeper grooves and (c) using “stamp-pad” 169

Figure 9.2. Schematic of (a) the In_2O_3 patterning process and (b) single device FET at the shank of neuroprobe with In_2O_3 pattern. 172

Figure C.1. (a) First generation of flow cell set-up. The flow injection system for the measurement of response time for a microprobe consists of a pump, a Rheodyne valve and a flow cell. (b) Schematic working mechanism of an automated six-port Rheodyne valve switching between analyte loading mode (shown in blue arrows) and analyte injecting mode (shown in red arrows). 182

Figure C.2. The second generation of flow cell set-up with shorter and straighter traveling path from Rheodyne valve to the electrode surface. 182

Figure C.3. (a)(b) Testing set-up for microsensor response time. Rapid switching of solution flow onto the microprobe was controlled by alternating between pumped streams of PBS buffer and analyte solution. (c) Representative Glut sensor response time versus flow rate with response to H_2O_2 shown in grey trace and to Glut shown in blue trace. (d) Representative experimental result of current versus time. 184

Figure C.4. Representative current versus time result for (a) Glut and (b) Ch sensors using peristaltic pump to introduce analyte to the flow cell. 185

LIST OF TABLES

Table 3.1. Comparison of the performance characteristics of Ch sensor of this work with other recently reported electroenzymatic Ch sensors. 53

Table 5.1. Comparison of the performance characteristics of the glucose microbiosensor of this work with other recently reported electroenzymatic glucose biosensors. 101

Table 5.2. Comparison of the performance characteristics of the choline microbiosensor of this work with other recently reported electroenzymatic choline biosensors. 103

ACKNOWLEDGEMENT

I would like to first express sincere thanks to my PhD advisor, Professor Harold G. Monbouquette, for the amazing guidance and support throughout my entire graduate school career. He always provides critical advice to our work, teaches us how to efficiently plan our experiments and how to see the whole picture of our research. He encourages us to speak out our own opinions and try on new things. Besides, I am impressed by his kindness and geniality. He cares about not only research progresses but also our well-beings and life beyond the lab. We all are motivated by his optimism and enthusiasm. These knowledge and wisdom learned from him are something I will always cherish and carry for the rest of my life.

I would also like to thank my dissertation committee, Professor Nigel Maidment, Yvonne Chen and Yi Tang for their time and input. In addition, I would like to acknowledge funding support from NIH. I would also like to thank my collaborators on my projects, including Professor Kate Wassum, Professor Nigel Maidment, Professor Eric Chiou, Dr. Annie Collins, Dr. Zhan Zhu, Dr. Will Wen, Dr. Bo Wang and Lauren MacIntyre on the electroenzymatic sensors projects and Professor Anne Andrews, Professor Paul Weiss and Chuanzhen Zhao on the aptamer-based sensors projects. They give me the opportunity to learn and work on creating sensor under different sensing mechanism. Professor. Anne Andrews's passion about science is very motivated. I also appreciate Dr. Ming Zhao for cooperating with me on the stamping project. I would also like to thank all the staff especially Dr. Wilson Lin, Dr. Max Ho, Noah Bodzin, Huynh Do, Hoc Ngo, Brian Matthews and Tom Lee at UCLA nanolab for their endless help and patience.

In addition, I also like to thank my lab members, both past and present, with their help and support during my time at UCLA. Dr. Allison Yorita and Dr. Lili Feng taught me the basic in microprobe fabrication and creation electroenzymatic sensor. Dr. Bonhye Koo passed me skills in DNA chip fabrication and many skills in nanolab. I also appreciate these three past members

for encourage me to go for PhD program. Present students Mac Clay, Zhenrong Zheng, Yan Cao and Dima Ruckodanov were all important to make this lab a warm and friendly place. I also appreciate my undergrad students Yuwan Guo and Jingjing Nie for helping on conducted experiments and collecting data. They were able to do the assigned work independently without showing tiredness. Their contribution was very essential to the completion on my first paper.

I am also grateful for have met Jenny Monbouquette. She has given me so much love, joy and enthusiasm. I would also like to thank my classmates Dr. Carly Bond, Dr. Anthony Denicola, Dr. Eugenia Zah, Dr. Alec Jaeger, Dr. Meng-Yin Lin, Dr. Patrick Ho, Dr. Jeff Chang and Ximin Chen in the chemical engineering department. I am incredibly grateful to have met them during my time here. I am also like to thank my relative Teresa Chen for being one of my biggest supporters in the USA, and always being by my side when I need her.

Finally, I would like to express my deepest appreciation for my family mom, dad and my brother for supporting me unconditionally. Their endless love has helped me overcome any difficulties and challenges in my life. I would never be able to come this far without them.

VITA

2012	*B.S., Chemistry* National Taiwan Normal University Taipei, Taiwan
2013 – 2020	*Graduate Student Researcher, Department of Chemical Engineering* University of California, Los Angeles Los Angeles, CA
2015 – 2018	*Teaching Assistant, Department of Chemical Engineering* University of California, Los Angeles Los Angeles, CA

PUBLICATIONS AND PRESENTATIONS

I-Wen Huang, Mackenzie Clay, Siqi Wang, Yuwan Guo, Jingjing Nie and Harold G. Monbouquette, "Electroenzymatic glutamate sensing at near the theoretical performance limit," Analyst, 2020, 145, 2602-2611

I-Wen Huang, Mackenzie Clay, and Harold G. Monbouquette, "Choline detection at near the theoretical performance limit of electroenzymatic sensors," In preparation

I-Wen Huang, Ming Zhao, and Harold G. Monbouquette, "Improved microcontact printing of choline oxidase using a polycation-functionalized zwitterionic polymer as enzyme immobilization matrix," In preparation

Anne L. Collins, Tara J. Aitken, **I-Wen Huang**, Christine Shieh, Venuz Y. Greenfield, Harold G. Monbouquette, Sean B. Ostlund, and Kate M. Wassum, "Nucleus Accumbens Cholinergic Interneurons Oppose Cue-Motivated Behavior," Biological Psychiatry, 2019, 86 (5), 388-396

Bo Wang, Bonhye Koo, **Li-wen Huang** and Harold G. Monbouquette, "Microbiosensor fabrication by polydimethylsiloxane stamping for combined sensing of glucose and choline," Analyst, 2018, 143, 5008-5013

Ximiao Wen, Bo Wang, Shan Huang, Tingyi "Leo" Liu, Meng-Shiue Lee, Pei-Shan Chung, Yu Ting Chow, **I-Wen Huang**, Harold G. Monbouquette, Nigel T. Maidment, Pei-Yu Chiou, "Flexible, multifunctional neural probe with liquid metal enabled, ultra-large tunable stiffness for deep-brain chemical sensing and agent delivery," Biosensors and Bioelectronics, 2019, 131, 37–45

Chuanzhen Zhao, **I-Wen Huang**, Kevin M. Cheung, Nako Nakatsuka, Hongyan Yang, Paul S. Weiss, Harold G. Monbouquette, and Anne M. Andrews. “Implantable aptamer field-effect transistor neuroprobes towards *in vivo* neurotransmissions monitoring of serotonin in mice,” In preparation

I-Wen (Brenda) Huang, Mackenzie Clay, and Harold Monbouquette, “Simulation-Guided Optimizations of Electroenzymatic Biosensors to Monitor Glutamate in Vivo,” SfN Annual Meeting, San Diego, CA, November 2018.

I-Wen (Brenda) Huang, Mackenzie Clay, and Harold Monbouquette, “Simulation-Guided Optimizations of Electroenzymatic Biosensors to Monitor Glutamate in Vivo,” Annual BRI Neuroscience Poster Session, Los Angeles, CA, November 2017.

Chapter 1: Introduction

1.1 Electrochemical sensing of neurotransmitters

1.1.1 Motivation

Understanding the information transfer and processing within the mammalian nervous system is one of the most urgent challenges faced by the biomedical community. Although basic neuroscience research of the past century has greatly advanced our outstanding of neuronal function, the ability to record and manipulate the dynamics of the nervous system remains insufficient to restore function following nerve injury or to treat many neurological disorders, such as Parkinson's disease and depressive disorder. In the central nervous system, action potentials propagate along the axon, aided by voltage-sensitive ion channels, and provoke the release of various neurotransmitters into the chemical junction between neurons called the synapse. Neurons and cells with corresponding chemical receivers on their surface are then programmed to response when exposed to neurotransmitters. The ability to concurrently record neurochemical signaling and the electrical activity of nearby neurons, both on fast timescales of milliseconds, is therefore expected to be an effective way for investigating complex problems associated with understanding brain functions. This concurrent recording with exquisite spatial precision as well has been made possible recently by combining electrodes for both electrochemical and electrical recording onto a single probe.[1–3] However, unlike electrical signals that can be easily recorded with small electrodes (~ 10 × 10 μm^2) on millisecond timescales, much larger recording sites typically are needed for chemical sensing in order to get sufficient signal at neurochemical concentrations under 100 μM. Up until recently, electrochemical sensors for neurotransmitters typically have had sizes of >1000 μm^2 and slow response times of ~1 s or more.[4–9] The spatiotemporal mismatch has made problematic the faithful recording of the dynamic of neurotransmitters and the desired correlation of chemical neurotransmission with neuronal

activity. The problem is particularly challenging because of the broad array of chemical species involved that must be detected selectively against the complex background of brain extracellular fluid. In this dissertation, we focus on the fabrication and characterization of neurochemical sensors aimed at cellular scale dimensions (~10 μm) with faster response time, higher multiplexity and better long-term stability while maintaining high selectivity and low detection limit.

1.1.2. Current technologies for neurotransmitter detection

Historically, *in vivo* measurement of neurotransmission has been best studied by using the technique of microdialysis.[10–13] In microdialysis, a semi-permeable probe is inserted into the brain region or tissue of interest and the probe inlet connects to a syringe pump which continuously perfuses through the probe. Molecules below the molecular weight cutoff of the membrane diffuse across the membrane according to their concentration gradient and are collected in the dialysate stream for analysis via methods such as high-performance liquid chromatography (HPLC) and mass spectroscopy (MS). While microdialysis has advantages including low detection limit and high multiplexity, the typical minute-to-minute time resolution limits the detection of rapid neurotransmission events. This is attributed to the combination of slow sampling time by dialysis from the brain combined with the intrinsic response time of the analytical method to which it is coupled.

Electrochemical sensing offers significant improvements over microdialysis in temporal resolution. Since the sensing electrode is in direct contact with the extracellular fluid in the brain, it potentially provides near-real-time feedback on chemical release. There are various electrochemical methods used for detection, such as cyclic voltammetry (CV) and constant potential amperometry (CPA). CV relies on continuous, cyclical ramping up and down of the potential at the electrode surface while monitoring current flow as electroactive compounds are

reduced or oxidized. Compounds can then be distinguished by features in their resulting current waveform. With very high scan rate and waveform application frequency, it allows rapid acquisition of a voltammogram within several milliseconds, thereby enabling nearly continuous recording. This fast scan cyclic voltammetry (FSCV) in combination with carbon-fiber microelectrodes has become a very popular method for *in vivo* monitoring of electroactive neurochemicals such as dopamine, norepinephrine and serotonin.[14–16] However, data analysis of FSCV is complicated for *in vivo* experiments as many interferents that have similar voltammetric features are simultaneously released in the brain during a recording session, which can introduce inconsistencies and reduce confidence in conclusions drawn. On the other hand, CPA is a method by which the electrode is held at a constant potential at which compounds are oxidized or reduced upon contact with the electrode. This method theoretically provides the fastest data sampling rate and a most straightforward real-time view of rapid chemical signaling events. Unlike FSCV, the CPA approach inherently lacks an integral means for chemical identification of the monitored species, therefore the electrodes are usually prepared with the modification of polymers or biological elements to provide a degree of selectivity for the analyte to be measured. This sensor design philosophy has also expanded the scope of neurochemical studies by enabling monitoring of non-electroactive neurotransmitters such as glutamate and acetylcholine.

1.1.3 Microprobes with an array of electroenzymatic sensing sites for detection of neurotransmitters

The concept of enzyme-based electrode was introduced by Clark and Lyons in 1962.[17] The first device relied on the use of a sensing electrode that was pressed tightly against the enzyme-entrapped membrane to monitor the electroactive products generated by the enzyme-catalyzed reaction. To date, the vast majority of research including that of our group uses highly

sensitive hydrogen peroxide (H_2O_2) electrodes coupled with H_2O_2-producing, enzyme-catalyzed oxidization reactions to construct sensors for non-electroactive neurotransmitters. These enzyme-based amperometric biosensors consist of an electrode upon which permselective films are deposited as well as an immobilized enzyme layer. Typically, oxidase enzymes are chosen to selectively catalyze the oxidation of a targeted substrate with oxygen serving as electron acceptor to generate H_2O_2. The generated H_2O_2 is transduced into electrical current signal through the oxidation of H_2O_2 by an underlying metal electrode poised at oxidizing potential. Therefore, the measured current magnitude can be used to correlate to the target concentration external to the sensor. Because oxidation of H_2O_2 requires a relatively high potential that simultaneously oxidizes other interferents in brain extracellular fluid, such as ascorbic acid (AA) and dopamine (DA), to give false signal, the electrode surface generally must be coated with permselective films to allow H_2O_2 to pass while blocking electroactive interfering species. A variety of polymeric materials, including overoxidized polypyrrole (OPPy), polyphenylenediamine (PPD) and Nafion, have been well studied and demonstrated as effective permselective films for application in our field.[18–20] By using semiconductor fabrication methods, these biosensors can be manufactured reproducibly and with much smaller dimensions, allowing for more accurate measurements in the brain with less tissue damage. Our silicon-based microprobe with microelectrode arrays (MEAs) are currently 150 μm thick, 140 μm wide and 9 mm long, with four 6000 μm^2 (40 μm x 150 μm) Pt recording sites arranged in pairs at the tip.

Previously our group and others have demonstrated the feasibility of electroenzymatic microsensors with response time in the ~1 s range for monitoring glutamate and acetylcholine *in vivo*.[7–9,21–26] However, less than optimal response time and sensitivity has limited the spatiotemporal resolution of this promising research technique. Our detailed mathematical model points out the thick coating of permselective films and enzyme layers on the electrode surface

has been the major factor that limits the performance of sensors.[27] Therefore, systematic improvements of electroenzymatic glutamate and choline microsensors with nearer to optimal coatings were conducted and characterized based on the guidance of the model.

1.1.4 Microprobes capable of multiple neurotransmitters sensing

Information processes in brains are known to be very complex and are controlled by neuronal networks influenced by interactions among multiple neurotransmitters and metabolites. A multiplexed sensor that allows simultaneous monitoring of multiple compounds is expected to be useful to unravel the interplay of multiple neurochemicals and greatly facilitate our understanding of the connection between neurochemistry and behaviors. Existing techniques including microdialysis and FSCV also allow multiple analyte measurements, however, their application is commonly limited by insufficient temporal resolution and restricted application to electroactive species, respectively. On the other hand, our current sensor design that combines microelectrode arrays (MEAs) microprobe to electroenzymatic sensing approaches potentially offers a means for multianalyte sensing with high spatiotemporal resolution. However, this necessitated the development of methods to precisely transfer multiple enzymes onto selected microelectrodes on the same microprobe. Enzymes are most commonly immobilized on the electrode by manually spreading a mixture enzyme and bovine serum albumin (BSA) on the coated electrode surface following by crosslinking with glutaraldehyde, which becomes problematic when the array feature size is less than or equal to ~100 μm. Methods such as adsorbing or entrapping oxidization within an electropolymerized film have demonstrated the capability of selective enzyme immobilization on targeted microelectrodes. However, the published experimental reports show that the very thin enzyme layers realized result in low sensitivity.[28–30] On the other hand, microcontact printing (μCP) based on polydimethylsiloxane

(PDMS) stamping is an emerging method for transferring proteins and other chemicals to surfaces in high-resolution patterns with feature sizes down to the μm – nm range.[31–33] The process of μCP consists of several important steps including replication of the microelectrode pattern in the PDMS stamp, "inking" the stamp with a solution of desired molecules to be deposited and briefly forming a conformational contact with the substrate to leave behind the desired pattern of "ink" molecules. Here, we demonstrated the feasibility of the μCP method for transferring two enzymes, glucose oxidase and choline oxidase, separately onto selected individual sites of an MEA to create a dual sensing microprobe for glucose and choline.[5] Subsequently, the chemistry of the enzyme "ink" was modified through the use of a special synthetic polymer to replace BSA as enzyme immobilization matrix. This allowed printing thicker and more finely detailed enzyme patterns that resulted in much higher sensor sensitivity.

1.1.5 Microprobes with multi-functionalities

The main concern with using an implantable microprobe has been the invasiveness of the recording electrodes. Although effective for many purposes, Si-based devices establish a poor mechanical match between such rigid material and soft brain tissue. Consequences include adverse immune response and the encapsulation of devices by scars leading to significant loss of electrode performance during chronic operation. This issue is important when creating neuroprobes capable of delivering stimulus while continuously recording the state of the neuronal environment, which is essential not only to fundamental research in neuroscience, but also to the development of procedures for treating many neurological and physiological diseases.[5,34,35] Such multifunctional neuroprobes are most commonly achieved by implanting assemblies of probes with differing functions using injection cannulae that can cause significant damage to the targeted

brain region due to the large footprint.[36] In this work, we developed flexible, PDMS-based, neuroprobe-incorporated, microfluidic channels for local delivery of chemical agents. Using gallium (Ga) in the probe construction to provide sufficient stiffness during implantation at relatively low temperature while softening after implantation, we also overcame the common challenge of insertion of flexible probes deep into the brain without using external shuttle carriers that may cause other tissue damage.[37] Such a neuroprobe platform that minimizes the footprint of implants and mechanical mismatch to soft neural tissue potentially offers a useful means to achieve multifunctional chronic operation.

1.1.6 Microprobes with an array of aptamer-field effect transistors for detection of neurotransmitters

The electroenzymatic approach is not generalizable to the detection of many molecules because of its dependence on the existence of specific redox enzymes to detect specific analytes. In addition, some neurotransmitters can present in very low concentrations in all brain regions and do not generate sufficient oxidative or reductive signals. To address those issues, Nakatsuka and Andrews *et al*. developed a new technology for sensitive and selective detection of neurotransmitters. Inspired by the ability to select aptamers to reversibly bind to specific targets and to undergo significant conformational change upon binding with target, they used aptamers as target-recognition elements and field-effect transistors (FETs) to transduce the target-aptamer binding reaction into an electrical signal.[38] FET sensing relies on the binding of a charged species on a semiconductor gate surface, resulting in depletion or accumulation of carriers within the transistor structure and a change in the induced conductance of the transistor channel.[34] When coupling aptamers with FETs, Nakatsuka overcame the issue commonly existing in traditional

FET sensing that small target molecules with few or no charges have minimal impact on the FET conductance. For example, dopamine and serotonin are monoamine neurotransmitters that only carry single positive charges at physiological pH and exist in the brain at low concentration. As aptamers carry a great amount of charge and are covalently bound to the gate surface, a change in conformation of its negatively charged phosphodiester backbone upon binding with target enables signal transduction and amplification by the FET. These aptamer-based FETs exhibited concentration-dependent responses to physiologically relevant serotonin and dopamine concentrations (10 pM to 100 nM) with a detection limit of 10 fM. Such an LOD is substantially lower than the nM to μM range demonstrated recently by other analytical methods. In order to make such high-performance technology practical for use *in vivo*, we cooperated with Andrews' group and miniaturized the aptamer-based FETs to make them implantable. The smaller size of these aptamer-based FETs microprobes (with shank of *ca.* 150 μm wide, thick and 9 mm long and FETs pairing on the tip) will allow minimal invasiveness for *in vivo* measurements and point-of-care diagnosis. The fabricated microprobes maintained high performance and exhibited linear response over a wide range of target concentration (10^{-15} – 10^{-3} M) with response time on the order of seconds. This novel microprobe relying on the combination of ultrathin indium oxide (In_2O_3) layer as oxide gate and aptamer as target-recognition element can serve as a generalizable platform to construct highly sensitive, selective and label-free FET-based biosensors.

1.2 References

1. Disney, A. A., McKinney, C., Grissom, L., Lu, X. & Reynolds, J. H. A multi-site array for

combined local electrochemistry and electrophysiology in the non-human primate brain. *J. Neurosci. Methods* **255**, 29–37 (2015).

2. Fuchsberger, K. *et al.* Multiwalled carbon-nanotube-functionalized microelectrode arrays fabricated by microcontact printing: Platform for studying chemical and electrical neuronal signaling. *Small* **7**, 524–530 (2011).
3. Johnson, M. D., Franklin, R. K., Gibson, M. D., Brown, R. B. & Kipke, D. R. Implantable microelectrode arrays for simultaneous electrophysiological and neurochemical recordings. *J. Neurosci. Methods* **174**, 62–70 (2008).
4. Burmeister, J. J. *et al.* Improved ceramic-based multisite microelectrode for rapid measurements of L-glutamate in the CNS. *J. Neurosci. Methods* **119**, 163–171 (2002).
5. Wang, B., Koo, B., Huang, L. W. & Monbouquette, H. G. Microbiosensor fabrication by polydimethylsiloxane stamping for combined sensing of glucose and choline. *Analyst* **143**, 5008–5013 (2018).
6. Keihan, A. H., Sajjadi, S., Sheibani, N. & Moosavi-Movahedi, A. A. A highly sensitive choline biosensor based on bamboo-like multiwall carbon nanotubes/ionic liquid/Prussian blue nanocomposite. *Sensors Actuators B Chem.* **204**, 694–703 (2014).
7. Burmeister, J. J. *et al.* Ceramic-based multisite microelectrode arrays for simultaneous measures of choline and acetylcholine in CNS. **23**, 1382–1389 (2008).
8. Tseng, T. T. C., Yao, J. & Chan, W. C. Selective enzyme immobilization on arrayed microelectrodes for the application of sensing neurotransmitters. *Biochem. Eng. J.* **78**, 146–153 (2013).
9. Tseng, T. T. C. & Monbouquette, H. G. Implantable microprobe with arrayed microsensors for combined amperometric monitoring of the neurotransmitters, glutamate and dopamine. *J. Electroanal. Chem.* **682**, 141–146 (2012).

10. Yang, H., Sampson, M. M., Senturk, D. & Andrews, A. M. Sex-and SERT-Mediated Differences in Stimulated Serotonin Revealed by Fast Microdialysis. *ACS Chem. Neurosci.* **6**, 1487–1501 (2015).

11. Rogers, M. L. *et al.* Continuous online microdialysis using microfluidic sensors: Dynamic neurometabolic changes during spreading depolarization. *ACS Chem. Neurosci.* **4**, 799–807 (2013).

12. Westerink, B. H. C. Brain microdialysis and its application for the study of animal behaviour. *Behav. Brain Res.* **70**, 103–124 (1995).

13. Sandlin, Z. D., Shou, M., Shackman, J. G. & Kennedy, R. T. Microfluidic Electrophoresis Chip Coupled to Microdialysis for in Vivo Monitoring of Amino Acid Neurotransmitters. *Anal. Chem.* **77**, 7702–7708 (2005).

14. Michael, D. J., Joseph, J. D., Kilpatrick, M. R., Travis, E. R. & Wightman, R. M. Improving Data Acquisition for Fast-Scan Cyclic Voltammetry. (1999). doi:10.1021/ac990491

15. Kile, B. M. *et al.* Optimizing the temporal resolution of fast-scan cyclic voltammetry. *ACS Chem. Neurosci.* **3**, 285–292 (2012).

16. Hashemi, P., Dankoski, E. C., Petrovic, J., Keithley, R. B. & Wightman, R. M. Voltammetric detection of 5-hydroxytryptamine release in the rat brain. *Anal. Chem.* **81**, 9462–9471 (2009).

17. L. Clark Jr., C. L. ELECTRODE SYSTEMS FOR CONTINUOUS MONITORING IN CARDIOVASCULAR SURGERY. *Ann. N. Y. Acad. Sci.* **102**, 29 (1962).

18. Wahono, N. *et al.* Evaluation of permselective membranes for optimization of intracerebral amperometric glutamate biosensors. *Biosens. Bioelectron.* **33**, 260–266 (2012).

19. Hamdi, N., Wang, J. J. & Monbouquette, H. G. Polymer films as permselective coatings for H2O2-sensing electrodes. *J. Electroanal. Chem.* **581**, 258–264 (2005).

20. Debiemme-Chouvy, C. A very thin overoxidized polypyrrole membrane as coating for fast time response and selective H2O2 amperometric sensor. *Biosens. Bioelectron.* **25**, 2454–2457 (2010).

21. Huang, I. *et al.* Electroenzymatic glutamate sensing at near the theoretical performance limit. *Analyst* (2020). doi:10.1039/c9an01969c

22. Gouda, M. D., Kumar, M. a., Thakur, M. S. & Karanth, N. G. Enhancement of operational stability of an enzyme biosensor for glucose and sucrose using protein based stabilizing agents. *Biosens. Bioelectron.* **17**, 503–507 (2002).

23. Burmeister, J. J. & Gerhardt, G. A. Self-referencing ceramic-based multisite microelectrodes for the detection and elimination of interferences from the measurement of L-glutamate and other analytes. *Anal. Chem.* **73**, 1037–1042 (2001).

24. Burmeister, J. J. *et al.* Biochemical Approaches for Glutamatergic Neurotransmission. **130**, 327–351 (2018).

25. Malvaez, M. *et al.* Basolateral amygdala rapid glutamate release encodes an outcome-specific representation vital for reward-predictive cues to selectively invigorate reward-seeking actions. *Sci. Rep.* **5**, (2015).

26. Wassum, K. M. *et al.* Silicon wafer-based platinum microelectrode array biosensor for near real-time measurement of glutamate in vivo. *Sensors* **8**, 5023–5036 (2008).

27. Clay, M. & Monbouquette, H. G. A Detailed Model of Electroenzymatic Glutamate Biosensors to Aid in Sensor Optimization and in Applications in Vivo. *ACS Chem. Neurosci.* **9**, 241–251 (2018).

28. Wang, J., Myung, N. V., Yun, M. & Monbouquette, H. G. Glucose oxidase entrapped in polypyrrole on high-surface-area Pt electrodes: a model platform for sensitive electroenzymatic biosensors. *J. Electroanal. Chem.* **575**, 139–146 (2005).

29. Ramanathan, K., Mehrotra, R., Jayaram, B., Murthy, A. S. N. & Malhotra, B. D. Simulation of Electrochemical Process for Glucose Oxidase Immobilized Conducting Polymer Electrodes. *Anal. Lett.* **29**, 1477–1484 (1996).

30. Tseng, T. T.-C., Yao, J. & Chan, W.-C. Selective enzyme immobilization on arrayed microelectrodes for the application of sensing neurotransmitters. *Biochem. Eng. J.* **78**, 146–153 (2013).

31. Quist, A. P., Elisabeth, A. E., Ae, P. & Oscarsson, S. Recent advances in microcontact printing. *Anal Bioanal Chem* **381**, 591–600 (2005).

32. Li, H., Kang, D. J., Blamire, M. G. & Huck, W. T. S. High-Resolution Contact Printing with Dendrimers. *Nano Lett.* **2**, 347–349 (2002).

33. Yoo, P. J. *et al.* Unconventional patterning with A modulus-tunable mold: From imprinting to microcontact printing. *Chem. Mater.* **16**, 5000–5005 (2004).

34. Bernard, A., Renault, J. P., Michel, B., Bosshard, H. R. & Delamarche, E. Microcontact Printing of Proteins. *Adv. Mater.* **12**, 1067–1070 (2000).

35. Perl, A., Reinhoudt, D. N. & Huskens, J. Microcontact Printing: Limitations and Achievements. *Adv. Mater.* **21**, 2257–2268 (2009).

36. Krook-Magnuson, E., Armstrong, C., Oijala, M. & Soltesz, I. On-demand optogenetic control of spontaneous seizures in temporal lobe epilepsy. *Nat. Commun.* **4**, 1–8 (2013).

37. Wen, X. *et al.* Flexible, multifunctional neural probe with liquid metal enabled, ultra-large tunable stiffness for deep-brain chemical sensing and agent delivery. *Biosens. Bioelectron.* **131**, 37–45 (2019).

38. Nakatsuka, N. *et al.* Aptamer – field-effect transistors overcome Debye length limitations for small-molecule sensing. **324**, 319–324 (2018).

Chapter 2: Electroenzymatic Glutamate Sensing at Near the Theoretical Performance Limit

Chapter 2 is a manuscript published with the following citation:

I-Wen Huang, Mackenzie Clay, Siqi Wang, Yuwan Guo, Jingjing Nie and Harold G. Monbouquette, "Electroenzymatic glutamate sensing at near the theoretical performance limit," Analyst, 2020, 145, 2602-2611

I-Wen Huang contributed the majority of experimental work in this paper. This involved designing experiments, create sensors, collecting data, as well as analyzing experimental results.

Abstract

The sensitivity and response time of glutamate sensors based on glutamate oxidase immobilized on planar platinum microelectrodes have been improved to near the theoretical performance limits predicted by a detailed mathematical model. Microprobes with an array of electroenzymatic sensing sites have emerged as useful tools for the monitoring of glutamate and other neurotransmitters *in vivo*; and implemented as such, they can be used to study many complex neurological diseases and disorders including Parkinson's disease and drug addiction. However, less than optimal sensitivity and response time has limited the spatiotemporal resolution of these promising research tools. A mathematical model has guided systematic improvement of an electroenzymatic glutamate microsensor constructed with a 1–2 μm-thick crosslinked glutamate oxidase layer and underlying permselective coating of polyphenylenediamine and Nafion reduced to less than 200 nm thick. These design modifications led to a nearly 6-fold

improvement in sensitivity to 320 ± 20 nA $\mu M^{-1} cm^{-2}$ at 37 °C and a ~10-fold reduction in response time to 80 ± 10 ms. Importantly, the sensitivity and response times were attained while maintaining a low detection limit and excellent selectivity. Direct measurement of the transport properties of the enzyme and polymer layers used to create the biosensors enabled improvement of the mathematical model as well. Subsequent model simulations indicated that the performance characteristics achieved with the optimized biosensors approach the theoretical limits predicted for devices of this construction. Such high-performance glutamate biosensors will be more effective *in vivo* at a size closer to cellular dimension and will enable better correlation of glutamate signaling events with electrical recordings.

2.1 Introduction

As was articulated clearly several years ago,[1] an understanding of information processing in the brain can be had only by unraveling of the interrelated roles of chemical neurotransmission and neuronal electrical activity. Great strides have been made in recording activity simultaneously from large numbers of interconnected neurons through millisecond timescale measurements of action potentials or intracellular Ca^{2+} changes.[2–7] However, corresponding tools to monitor chemical neurotransmission with the cellular-scale spatial resolution and the single-digit millisecond timescale of synaptic signaling events have yet to emerge.[8–11] This spatiotemporal mismatch has made problematic the desired correlation of chemical neurotransmission with neuronal activity. The problem is made particularly challenging by the broad array of chemical species involved that must be detected selectively against the complex background of brain extracellular fluid. Microdialysis and related techniques have been valuable tools for neurotransmitter measurements, although the typical minute-to-minute time resolution limits the detection of rapid neurotransmission events which are known to be much faster.[12,13]

Electrochemical devices based on microelectrode arrays (MEAs) with electroenzymatic sensing sites on silicon or ceramic microprobes have emerged as useful tools for the monitoring of glutamate and choline (as surrogate for acetylcholine) *in vivo*. Our group and others have successfully demonstrated the feasibility of MEAs with response times in the ~1 s range for use in the study of complex neurological diseases and disorders including Parkinson's disease and drug addiction.[14–16] Yet historically, these sensors have lacked the temporal resolution to associate unambiguously release events with local field potentials, and certainly not action potentials. Further, sensitivity limitations have required sensing sites on probes to be much larger than cellular dimension, thereby limiting spatial resolution. This report addresses these challenges through several-fold improvement in the design of a selective electroenzymatic sensor for the important excitatory neurotransmitter, glutamate (Glut).

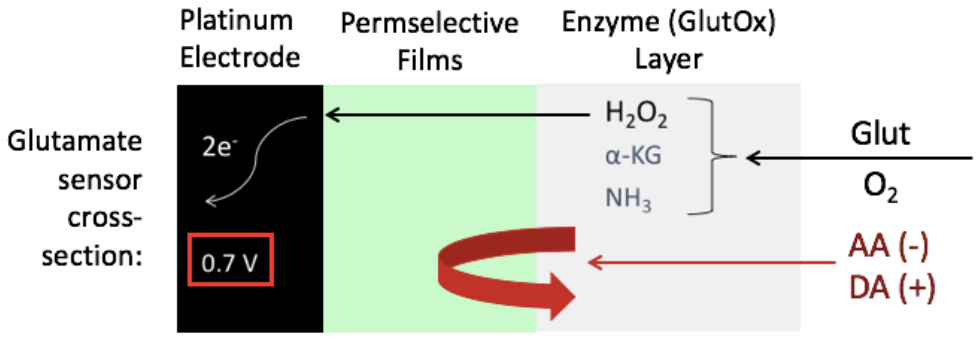

Figure 2.1. Schematic of an electroenzymatic glutamate (Glut) sensor with permselective films and a glutamate oxidase (GlutOx) enzyme layer.

An electroenzymatic Glut sensor consists of an electrode upon which one or more permselective films are deposited as well as an immobilized enzyme (Fig. 1). Typically, glutamate

oxidase (GlutOx) serves as the enzyme and selective molecular recognition element that catalyzes Glut oxidation to α-ketoglutarate with production of hydrogen peroxide (H_2O_2). This recognition event is transduced into an electrical current signal most often through the electrooxidation of H_2O_2 by an underlying Pt electrode poised at oxidizing potential. In this way, Glut concentration may be correlated with measured current magnitude. However, the Pt electrode generally must be coated with permselective films to allow H_2O_2 to pass but to reject electrooxidizable interfering species common to brain extracellular fluid such as ascorbic acid (AA) that could give rise to false signals. Due to the restricted diffusion of Glut through the immobilized GlutOx layer and H_2O_2 through both the enzyme layer and the underlying permselective films, biosensor performance is impacted significantly by sensor construction. A variety of polymeric materials have been used as permselective films including polypyrrole (PPy), polyphenylenediamine (PPD) and Nafion.[17–19] GlutOx is most commonly immobilized on the electrode by spreading a mixture of enzyme and bovine serum albumin (BSA) on the coated electrode surface followed by crosslinking with glutaraldehyde (GAH).[9,11,15,16,19–22]

Our previous simulations of then currently representative Glut sensors of the type illustrated in Fig. 1 suggested that the majority of the Glut diffusing into the enzyme layer is consumed near its outer edge, and that the H_2O_2 concentration in the layer peaks closer to the bulk solution than to the Pt electrode surface.[23] The steeper H_2O_2 concentration gradient in the direction of the bulk solution and the larger corresponding flux indicated that the vast majority of H_2O_2 generated by the GlutOx-catalyzed Glut oxidation reaction escapes from the sensor site and is not available at the Pt electrode surface to give rise to a current signal. These simulations strongly suggest that reducing the enzyme layer thickness while maximizing active enzyme concentration to improve H_2O_2 capture would be an effective strategy to reduce response time and to improve sensitivity.

This report describes sensors fabricated with thinner permselective films and enzyme layers based on the guidance of our simulations. In order to characterize these new sensors, the mass transport properties of H_2O_2 within these permselective and immobilized enzyme films were evaluated experimentally using rotating disk electrodes (RDEs). These values provided improved parameter estimates for our mathematical model, and enabled demonstration that the new Glut biosensors had been improved to near the theoretical performance limit.

2.2 Experimental

2.2.1 Reagents

Nafion (5 wt% in lower aliphatic alcohols and 15–20% water), m-phenylenediamine (PD), pyrrole (Py), bovine serum albumin (BSA) lyophilized powder, glutaraldehyde solution (GAH), L-glutamic acid (Glut), L-ascorbic acid (AA), 3-hydroxytyramine (dopamine, DA), sodium phosphate dibasic, sodium chloride, HCl (36.5–38%), and hydrogen peroxide solution (30%) were purchased from Sigma-Aldrich (St Louis, MO). L-Glutamate oxidase (EC 1.4.3.11) was obtained from US Biological. Bis(sulfosuccinimidyl) suberate (BS3) was purchased from Thermo Fisher Scientific (Pittsburgh, PA). Ag/AgCl glass-bodied reference electrodes with NaCl electrolyte (3 M) and a 0.5 mm-diameter Pt wire auxiliary electrode were obtained from BASi (West Lafayette, IN). Sodium phosphate buffer (PBS, pH 7.4) was composed of 50 mM sodium phosphate dibasic and 100 mM sodium chloride. Four-inch silicon wafers (p-type boron doped; orientation h100i; thickness 150 μm) were purchased from Silicon Valley Microelectronics (Santa Clara, CA). The platinum rotating disk electrodes (RDEs) (5.0 mm disk, 12.0 mm OD PEEK shroud) were purchased from Pine Research (Durham, NC). Microcloth (PSA, 2-7/8″) for electrode polishing was purchased from Buehler (Lake Bluff, Illinois).

2.2.2 Instrumentation

The RDE system (model AFMSRX) was purchased from Pine Research (Durham, NC). Microsensors were calibrated using a Versatile Multichannel Potentiostat (model VMP3) equipped with the 'p' low current option and N'Stat box driven by EC-LAB software (Bio-Logic USA, LLC, Knoxville, TN) in a three-electrode configuration consisting of the sensing electrode, a Pt wire auxiliary electrode, and a Ag/AgCl reference electrode. The film thicknesses on microelectrodes and RDEs were measured using a SEM (Nova 600 SEM/FIB System), a Dektak 8 stylus profilometer, and/or a Wyko NT300 optical profiling system.

2.2.3 Sensor preparation

The silicon-based microelectrode arrays used in this work were manufactured in house using microelectromechanical system (MEMS) techniques. The fabrication and array details are described in our previous work.[11] The microelectrode array probes were 150 μm thick, 140 μm wide and 9 mm long, with four, 6000 μm^2 (40 μm $\times$ 150 μm) Pt recording sites arranged in pairs at the tip (Fig. 2). A PPD film first was electrodeposited on Pt microelectrodes from a 5 mM PD solution in phosphate buffered saline (0.1 M PBS) by holding the voltage constant at 0.85 V vs. Ag/AgCl until the desired total charge was transferred (7.6×10^{-7} coulombs). Alternatively, a PPy film was electrodeposited from 200 mM pyrrole in PBS at 0.85 V vs. Ag/AgCl for 5 min. A Nafion layer then was applied by dip-coating a 2% Nafion solution (diluted from stock with 4 : 1 IPA : water) 3$\times$ for PPy/Nafion and only 1$\times$ for PPD/Nafion, followed by annealing at 115 °C for 20 min (115 °C-Nafion) or 180 °C for 4 min (180 °C-Nafion). Next, an immobilized GlutOx coating was deposited manually by loading a GlutOx and BSA mixture (dissolved in PBS) on the microelectrodes and crosslinking with 174 mM BS3 or 5% GAH vapor for 1 min. After the final crosslinking step, sensors were stored dry at 4 °C for 48 h prior to testing.

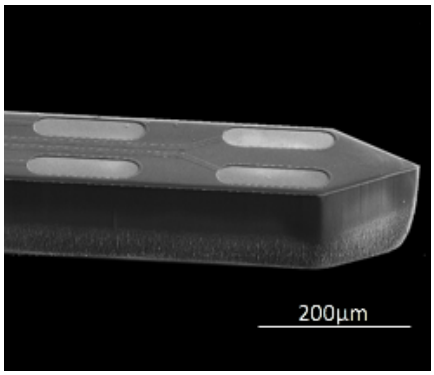

Figure 2.2. Scanning electron microscopy (SEM) image of the microelectrode array probe.

2.2.4 Electrochemical measurement

To determine sensor selectivity and sensitivity, a constant potential of 0.7 V vs. Ag/AgCl was applied to the sensors in stirred PBS buffer solution. After current stabilization, AA, DA, Glut or H_2O_2 were added to give final concentrations of 250 µM AA, 10 µM DA, 20–60 µM Glut and 20 µM H_2O_2. The selected concentrations of AA and DA were chosen to be reflective of those found *in vivo*.[24–26] To test the response time of the Glut microsensors, two peristaltic pump-driven streams of solution (PBS buffer and analyte) flowing from separate pipette tips were positioned close to the microprobe tip (Fig. 3). Rapid step changes in analyte concentration at the microsensors were achieved by alternating between PBS buffer and analyte streams by turning pumps on and off.[22]

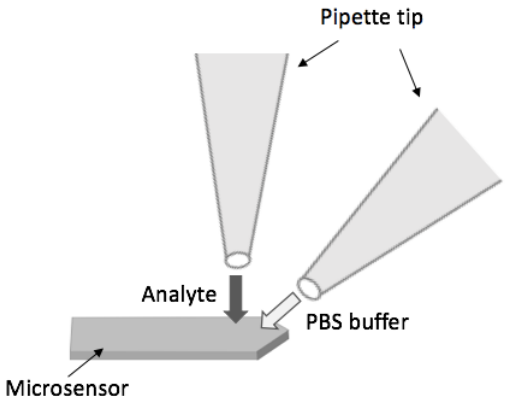

Figure 2.3. Testing set-up for microsensor response time. Rapid switching of solution flow onto the microprobe was controlled by alternating between pumped streams of PBS buffer and analyte solution.

2.2.5 Diffusion coefficient measurement

Diffusion of H_2O_2 within the PPD, Nafion or immobilized enzyme coatings was determined using a Pt RDE. The Pt RDE was polished using a microcloth and a 0.05 μm particle suspension, followed by rinsing with DI water and sonication in isopropyl alcohol. Next, a PPD, Nafion or enzyme film was deposited onto the electrode surface in the same way described in the sensor preparation section above. Linear sweep voltammetry (LSV) from 0.2 V to 0.9 V *vs.* Ag/AgCl was used as well as constant potential amperometry with varied rotation rate (see Results and discussion). Aftermath software was used for collection of voltammetric data (Pine Research, Durham, NC).

2.2.6 Mathematical Model and Simulations

Simulations of sensor performance were generated using an established model for electroenzymatic sensors with updated values for transport parameters based on this work, adjusted for temperature dependence.[23] In the model, sets of partial differential equations describe the one-dimensional transport and reaction rates of Glut, O_2, and H_2O_2 within separately considered PPD, Nafion, and immobilized enzyme coatings. Boundary conditions simulate a step-change in Glut concentration from 0 to 20 μM on the microsensor surface at t = 0. Numerical solutions of model equations were generated using COMSOL (COMSOL, Inc. Los Angeles).

2.3 Results and Discussion

2.3.1 Optimization of permselective films

Our published Glut sensor modeling study showed that permselective film thicknesses and transport properties are important parameters to address in sensor optimization.[23] Dopamine

(DA) and ascorbic acid (AA) are two common, electroactive interferents found in brain extracellular fluid at relatively high concentration that should be rejected by permselective films coated on the sensing electrode surface (Fig. 1). For what we will refer to as the base-case microsensor in this study, a PPy film and a Nafion overlayer annealed at 180 °C for 4 min (180 °C-Nafion) were used to reject DA and AA, respectively, yet to permit transport of H_2O_2 to the Pt electrode surface.[11] However, this PPy/180 °C-Nafion combination resulted in slow H_2O_2 diffusion to the electrode surface and low Glut sensitivity, mostly due to the overly thick Nafion coating necessary for adequate AA rejection, which was measured by SEM at 304 ± 87 nm (n = 3). Alternatively, when PPD was used as the underlying permselective film, a much thinner 180 °C-Nafion coating (96 ± 10 nm (n = 5)) was adequate, thereby improving H_2O_2 sensitivity ~3-fold from 121 ± 52 nA μM^{-1} cm^{-2} (n = 4) to 372 ± 70 nA μM^{-1} cm^{-2} (n = 15) (Fig. 4).

The Nafion annealing temperature also impacts sensor performance significantly. In order to improve the mechanical stability of Nafion coatings and to reduce water solubility, dip-coated Nafion films normally must be heated above the glass transition temperature (T_g = 109 °C for protonated Nafion) to anneal them.[27,28] However, the choice of annealing temperature and duration of the annealing process also affects Nafion properties. As illustrated in Fig. 4, we found that lowering the annealing temperature from 180 °C to 115 °C while increasing the baking time from 4 min to 20 min resulted in a further improvement of the H_2O_2 sensitivity by ~25% to 536 ± 69 nA μM^{-1} cm^{-2} (n = 15). The improved annealing process resulted in an even thinner final Nafion layer thickness of 71 ± 11 nm (n = 5) while retaining excellent selectivity against AA. This result is in agreement with the recently published work of Leppänen et al. showing that very thin Nafion films can retain effective anion exclusion properties.[29]

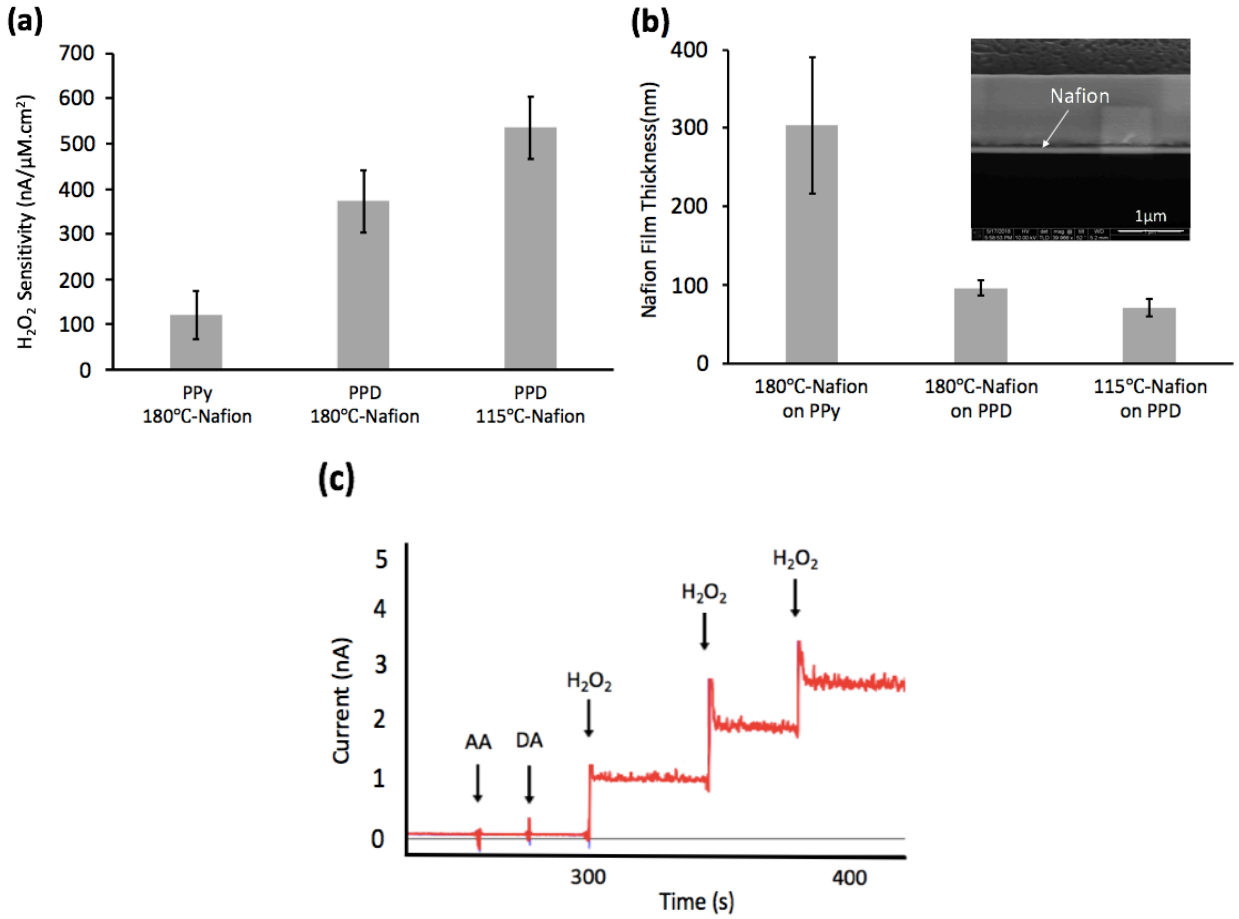

Figure 2.4. (a) Comparison of H2O2 sensitivity among sensors prepared with PPy/180 °C-Nafion, PPD/180 °C-Nafion, and PPD/115 °C-Nafion. (b) The Nafion thicknesses corresponding to the three different sensor preparations. Inset: SEM image of a Nafion film on Pt. (c) Representative current responses of PPD/115 °C-Nafion coated sensors to 250 μM AA, 5 μM DA, and H2O2 administered in 20 μM concentration increments. (Error bars shown are 95% confidence intervals.)

2.3.2 Hydrogen peroxide diffusion coefficient in permselective films and the crosslinked GlutOx layer

In addition to electrode coating thicknesses, measurements of H_2O_2 diffusivities in the permselective films and crosslinked enzyme layers are needed to improve the accuracy of sensor

simulations and to better guide sensor optimization. There are three “resistances” that can limit the rate of H_2O_2 oxidation at the coated Pt electrode: (1) the transport of H_2O_2 in the external diffusion boundary layer just above the coated electrode surface, (2) the diffusion of H_2O_2 within the deposited films and (3) the H_2O_2 electrooxidation kinetics at the Pt surface. The overall current density can be described in terms of these serial resistances by a form of the Koutecky–Levich equation,[17,30–35]

$$\frac{1}{I} = \frac{1}{I_k} + \frac{1}{I_f} + \frac{1}{I_l} \tag{1}$$

where I is the measured current, I_k is the current in the absence of any mass transfer limitations, I_f is the current when limited totally by diffusion in a film deposited on the electrode and I_l is the current when limited totally by mass transfer through the liquid boundary layer on the coated or uncoated electrode surface. Further, I_l can be modeled using the Levich equation, and eqn (1) then becomes[35]

$$\frac{1}{I} = \frac{1}{I_k} + \frac{1}{I_f} + \frac{1}{B_L \omega^{1/2} C} \tag{2}$$

where B_L is the Levich constant, ω is the electrode rotation rate (radians per s), and C is the bulk concentration of H_2O_2. The Levich constant is a function of H_2O_2 diffusivity in the bulk liquid, D_l, and the kinematic viscosity of the liquid medium, ν, such that[35]

$$B_L = 0.62nFAD_l^{2/3}\nu^{-1/6} \tag{3}$$

where n is the stoichiometric number of electrons transferred in the electrode reaction, F is Faraday’s constant, and A is the electrode surface area.

Representative current–potential (I–E) curves corresponding to bare Pt and Nafion-coated Pt RDEs in 0.2 mM H_2O_2 are shown in Fig. 5 and 6, respectively. The anodic current increases

initially as the voltage and the electrode rotation rate are increased as expected, while water dissociation occurs in the potential region above 0.85–1.0 V *vs*. Ag/AgCl. The limiting current condition (plateau current) on bare Pt (Fig. 5) is achieved when the current is limited by the rate at which H_2O_2 is transported to the Pt electrode surface. When Nafion films are deposited on the Pt surface, these films ultimately limit the current achievable; and the electrode rotation rate, which influences external transport, has little to no impact (Fig. 6a). These results also show that diffusion of H_2O_2 was more hindered in 180 °C-Nafion than 115 °C-Nafion.

In order to obtain estimates for the diffusivities in Nafion, the current was set at 0.7 V *vs*. Ag/AgCl while the electrode rotation rate was varied. The plot of the inverse of the recorded current versus the inverse square root of the electrode rotation rate shows a linear relationship as expected from eqn (2). Since the bathing solution (0.2 mM H_2O_2 in PBS) is unchanged during the whole experiment, the slopes of the lines are about the same (Fig. 6b). For the bare Pt RDE, extrapolation to infinite rotation rate yields an inverse current intercept close to zero, which indicates that the system was limited by mass transfer through the liquid boundary layer. Thus, to a good approximation, I_f may be obtained directly from the plot intercept for the coated electrodes assuming that external mass transport to the coated electrodes is approximately the same as that for bare Pt. Since I_f can be defined as a function of Nafion film thickness, δ, and the H_2O_2 effective diffusivity in the Nafion film, D_f, according to,[35]

$$I_f = nFAD_f C/\delta \tag{4}$$

an estimate for D_f may be calculated from the intercept of the Koutecky–Levich plot.

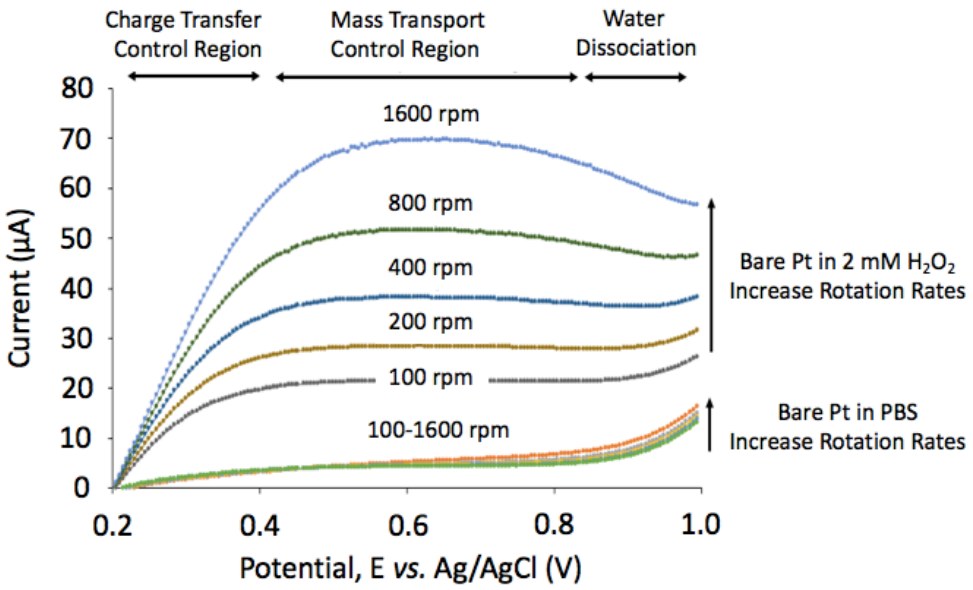

Figure 2.5. Representative current vs. potential curves showing the charge transfer, mass transport controlled and water dissociation regions at a bare Pt RDE using a potential sweep rate of 20 mV/s with rotation rates of 100, 200, 400, 800, 1600 rpm in PBS and 0.2 mM H_2O_2 solution.

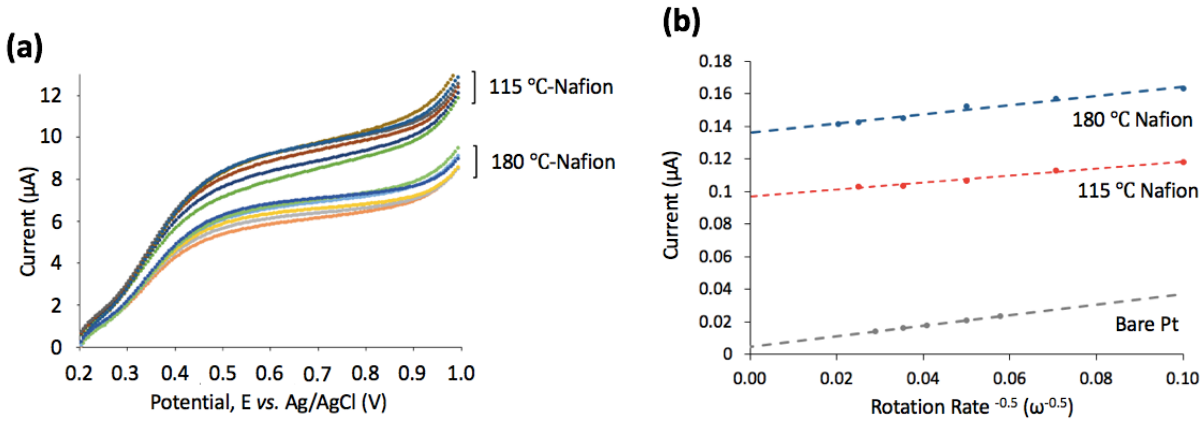

Figure 2.6. (a) Oxidation of 0.2 mM H_2O_2 in PBS (pH 7.4) at Nafion-coated Pt RDEs annealed at 180°C and 115°C using a potential sweep rate of 20 mV/s with rotation rates of 100, 200, 400, 800, 1600, 2400 rpm. (b) Koutecky-Levich plot of data for a bare Pt RDE (gray trace) and for 180°C-Nafion/Pt (blue trace) and 115°C-Nafion/Pt (red trace) RDEs. Current data were obtained at 0.7 V vs. Ag/AgCl.

For the larger RDE electrodes, the thickness difference between the dip-coated 180 °C-Nafion and 115 °C-Nafion films were more obvious at ~2 μm and ~1 μm, respectively, than what was observed for our micromachined microelectrode array probes, probably due to the substantial differences in geometry. The average values of D_f were found to be (1.7 ± 0.2) × 10^{-7} cm^2 s^{-1} (n = 3) for 180 °C-Nafion and (1.3 ± 0.2) × 10^{-7} cm^2 s^{-1} (n = 3) for 115 °C-Nafion. Since these effective diffusivities are approximately the same, these results highlight the importance of the thinner 115 °C-Nafion films that still show excellent selectivity against interferents. Also, these results are in rough agreement with literature values for effective diffusivity of the slightly smaller O_2 molecule in Nafion in the range of ~2 × 10^{-7} - 2 × 10^{-6} cm^2 s^{-1}.[31,36,37] The broad range of values is due primarily to the different preparation conditions for the films and membranes studied.

The data and estimated diffusivities were further examined by comparing the values of I_k and the slope ($1/B_L$) to expected values. Specifically, I_k is the current limited by the kinetics of the electrooxidation of H_2O_2 on Pt, assuming no mass transfer limitations, so the value of I_k should match the value calculated using published reaction kinetics.[38] RDE data gave I_k = 0.208 mA, in general agreement with that derived from published data of 0.273 mA. The measured slope was validated by checking consistency with the known value of H_2O_2 diffusivity at room temperature in water, 1.43 × 10^{-5} cm^2 s^{-1}.[39] Based on the measured slope and eqn (3), a comparable diffusivity of 0.94 × 10^{-5} cm^2 s^{-1} was obtained. Thus, this RDE analysis appears to be giving at least semiquantitative results that are well within an order of magnitude of those expected.

A similar experimental procedure was followed to obtain estimates for H_2O_2 effective diffusivities in the PPD film and in the crosslinked GlutOx deposit. For the PPD film, the mean value of the H_2O_2 diffusion coefficient was found to be (1.7 ± 0.3) × 10^{-8} cm^2 s^{-1} (n = 3), based on the measured film thickness of ~20 nm. This result is in agreement with literature data for H_2O_2 diffusivity in overoxidized polypyrrole (OPPy) (10^{-8} cm^2 s^{-1}), which is a similar polymer.[17] The

average estimated value for the effective H_2O_2 diffusion coefficient in the GAH-crosslinked GlutOx layer on the Pt RDE was found to be $\sim 1.6 \times 10^{-6}$ cm^2 s^{-1}, which is about an order of magnitude less than that in free solution due to a deposit porosity less than unity as well as its substantial tortuosity. The effective diffusivities of Glut and O_2 in permselective films and the GlutOx layer were obtained from the H_2O_2 effective diffusivities scaled by the ratio of the molecular diffusivities with that of H_2O_2. These measured values for deposit thicknesses and effective diffusivities provide improved parameters for our simulation studies described below.

2.3.3 Effect of Enzyme loading and Activity

Most commonly, GlutOx is immobilized on electrodes by spreading a mixture of GlutOx and BSA on the electrode surface and crosslinking with GAH. However, the many variations of methods used produces layers of different compositions and thicknesses that directly affect the sensor performance. Typical reported immobilized enzyme layer thicknesses have been in the 10-20 μm range. However, our simulation results suggest immobilized GlutOx layers 1-3 μm thick may be optimal to ensure high sensitivity while achieving rapid response time (if GlutOx activity is well preserved during the immobilization process).[23] Therefore, our experimental strategy was first to improve enzyme activity retention during the immobilization process, and then to optimize systematically the layer thickness.

Homobifunctional crosslinker, BS3, which like GAH also reacts with amine groups, appeared to be a good alternative due to its longer spacer arm, 11.4 Å *vs*. 5 Å. We hypothesized that this longer spacer arm would result in less enzyme crowding and better access to enzyme active sites. Also, the BS3-crosslinked enzyme layer might be more permeable overall. Crosslinking conditions for both BS3 and GAH were investigated individually before making comparisons. GAH concentrations and vapor exposure times were varied as were BS3

concentrations to find the best conditions for use of each crosslinker. After this simple optimization procedure, sensors made with enzyme crosslinked via BS3 showed ~1.5-fold improvement in sensitivity compared to those crosslinked via GAH, which showed sensitivity of 259 ± 25 nA μM^{-1} cm^{-2} (n = 11) and 196 ± 24 nA μM^{-1} cm^{-2} (n = 11), respectively. Further, the importance of permselective film and enzyme layer thicknesses on sensor performance should be evident here again. Compared to our base-case sensors, a ~4-fold improvement in Glut sensitivity was achieved merely by applying a thinner permselective film and halving the enzyme layer thickness to ~5 μm even while using the inferior crosslinker, GAH (Fig. 7).

For our existing sensor designs, a direct investigation of the effect of deposited enzyme concentration on sensor performance can be performed easily by changing the relative proportion of GlutOx and BSA without changing enzyme layer thickness. The protein mass fraction of GlutOx (f_{glutox}) was varied from 0.02 to 0.95 for the sensors coated optimally with PPD and 115 °C-Nafion and crosslinked with BS3. Based on the experimental results shown in Fig. 8, Glut sensitivity goes through a peak at f_{glutox} = ~0.4. Theoretically, as GlutOx mass fraction decreases for thicker enzyme layers, more Glut diffuses deeper into the layer before being oxidized resulting in more penetration of H_2O_2 to the electrode surface, less loss back to the bulk medium, and a greater current signal.[23,40] However, for the very thin enzyme layers explored here, an optimum f_{glutox} is expected. At low enzyme mass fraction, decreased Glut sensitivity was observed due to insufficient active enzyme available to consume Glut at a high rate. On the other hand, high enzyme concentration corresponding to f_{glutox} ≥ 0.5 was found not to be preferable either due to the fact that GlutOx does not have an abundance of surface lysines available for crosslinking, unlike BSA. The relatively low BSA concentration at high f_{glutox} led to poor crosslinking, an unstable enzyme layer, and great difficulty in gathering data for Fig. 8 at high enzyme concentration. As a

result, f_{glutox} = 0.2 was chosen as the target level for future work since there is little compromise in sensitivity in exchange for excellent stability.

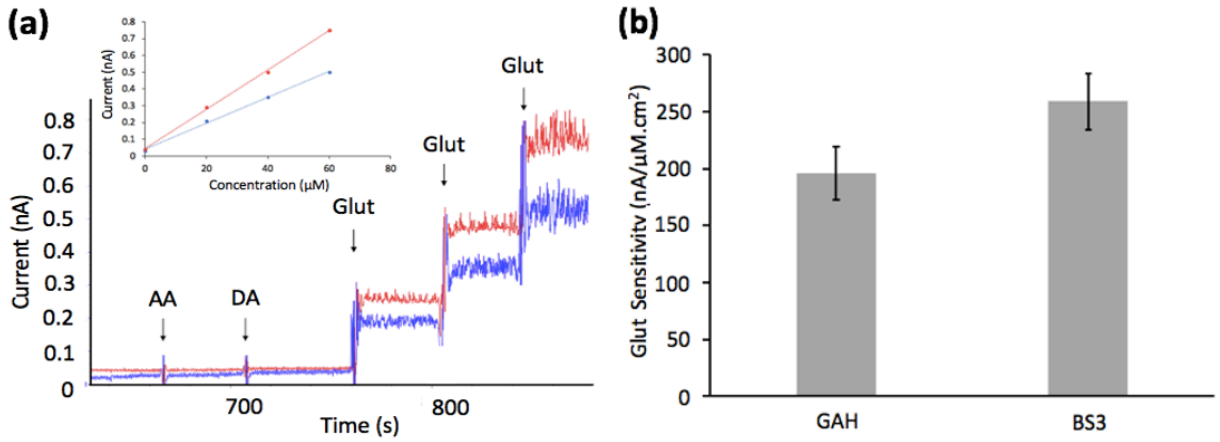

Figure 2.7. (a) Representative current response of Glut sensors crosslinked *via* BS3 (red trace) and GAH (blue trace) to interferents (250 μM AA and 5 μM DA), followed by three 20 μM step increases in H_2O_2 concentration. (b) Glut sensitivity comparison between BS3 and GAH crosslinked GlutOx sensors with error bars giving 95% confidence intervals. In all cases, the mass ratio of GlutOx to BSA was 1 : 4 and the enzyme layer was less than 5 μm thick.

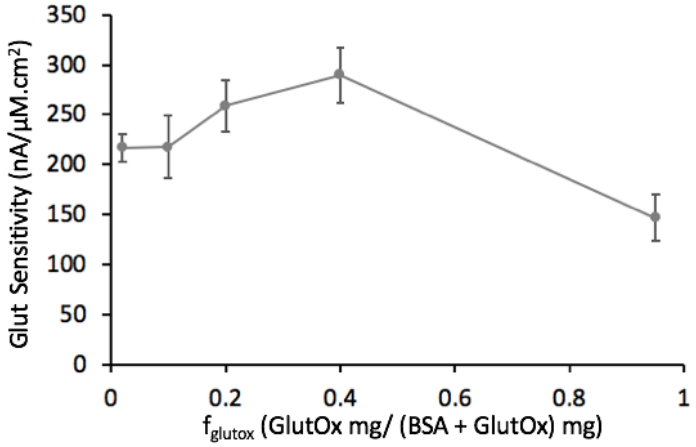

Figure 2.8. Effect of GlutOx concentration on the Glut sensitivity, where f_{glutox} is varied from 0.02 to 0.95. In all cases, sensors were crosslinked with BS3 and the layer thickness was less than 5 μm. Error bars represent 95% confidence intervals.

2.3.4 Optimal enzyme layer thickness

Our experimental results of Fig. 9 show the expected result that Glut sensitivity goes through an optimum with regard to enzyme layer thickness. The Glut sensitivity drops sharply for GlutOx layer thickness less than a micron and remains a roughly constant value over the 1–2 μm thickness range. These results match stimulations well (see below) and are consistent with other published experimental reports showing that very thin enzyme layers realized by electropolymerization result in low sensitivity.[40,41] As discussed earlier, the decrease in Glut sensitivity with thickness for thicker GlutOx layers is due to the greater diffusional mass-transfer limitation and the loss of the majority of H_2O_2 generated in the enzyme layer back to the bulk solution. Also, the added mass-transfer resistance of a thick enzyme layer leads to a slower response time.

2.3.5 Comparison in performance between our optimized and previously reported sensors

Sensors with the optimal permselective film (PPD/115 °C-Nafion) topped with an enzyme layer of optimal thickness of 1–2 μm with mass fraction of GlutOx (f_{glutox}) = 0.2 and crosslinked with BS3 led to excellent sensitivity of 320 ± 19.6 nA $\mu M^{-1}\,cm^{-2}$ (n = 18), which is a ~6-fold improvement compared with our previously reported design (51 ± 1.96 nA $\mu M^{-1}\,cm^{-2}$) without sacrificing selectivity and detection limit (signal-to-noise ratio equal to 3).[11] The detection limit for the improved sensors and those previously reported are 0.70 ± 0.08 μM (n = 18) and 0.79 ± 0.31, respectively (Fig. 10). Noise limited improvement in detection limit despite the large increase in sensitivity achieved with the optimized sensors.

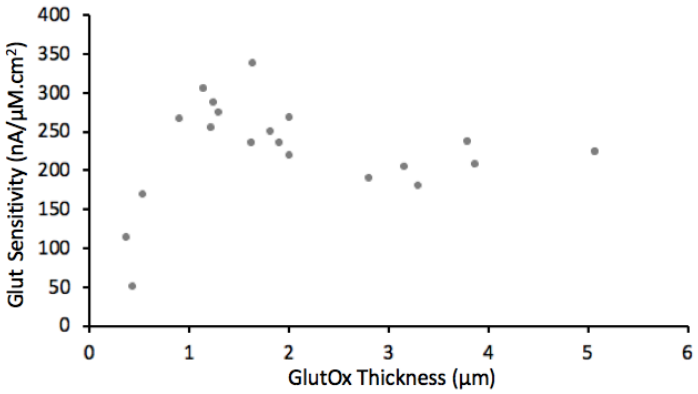

Figure 2.9. Sensor sensitivity based on the linear range of calibration curves (0–60 μM Glut) versus immobilized GlutOx layer thickness. In all cases, f_{glutox} = 0.2, and sensors were crosslinked with BS3.

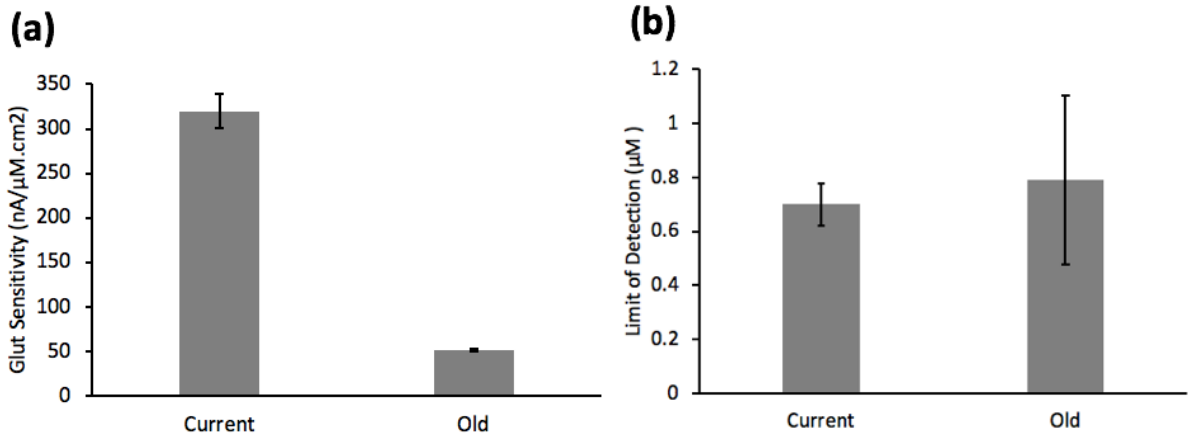

Figure 2.10. (a) Sensor sensitivity and (b) detection limit based on the linear range of the calibration curves (0–60 μM Glut) for the improved (current) and previously published (old) (ref. 11) Glut sensors. Error bars represent 95% confidence intervals.

2.3.6 Response time

Response time is defined here as the time for the current signal to reach 90% of its steady-state value in response to a step change in Glut from zero to 40 μM under conditions where external mass transfer is essentially eliminated. Our previous results and other published response times are in the ~1 s range,[11,42] mostly due to the overly thick enzyme and permselective

layers thought to be needed for high sensitivity and selectivity. Our improved sensors having thin enzyme and polymer layers enabled a faster response time of 0.080 ± 0.012 s (n = 5), which is a ~10-fold improvement over prior work (Fig. 11).[11] The fact that the bare Pt response to H_2O_2 appears as a near step change as expected given very rapid electrooxidation kinetics suggests that this method for measuring response time essentially eliminates the external mass transfer resistance. In contrast, the intrinsic response of our optimized Glut biosensor is obscured by the rate of external mass transfer when the measurement is attempted in a stirred beaker or a simple flow cell. However, the response time measurement method, whether using a stirred beaker or pump-driven buffer streams (Fig. 3), was not seen to affect sensor calibration and therefore the determination of sensitivity. In fact, essentially the same response time was measured for our early Glut sensor design using the pump-driven buffer streams (Fig. 11). The higher temporal resolution exhibited by the optimized Glut sensor will enable better correlation of Glut signaling *in vivo* with local field potentials, which occur at <100 Hz.[4] Straightforward correlation with single-unit action potentials will require improvement of response time to the single-digit millisecond range, which may be attainable without sacrificing sensitivity by further optimization of these biosensors (see below).

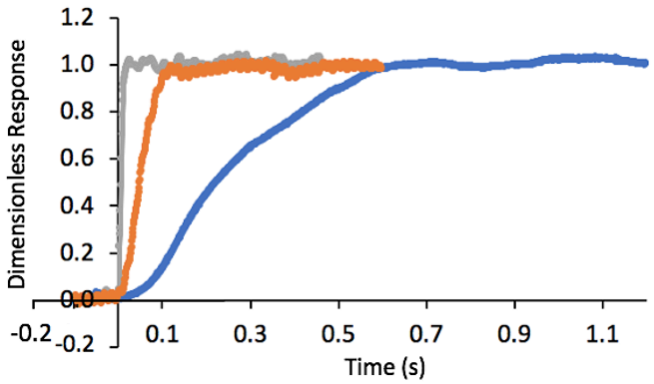

Figure 2.11. Representative sensor response to a 0–40 μM step-change in Glut concentration for base-case Glut sensor (blue trace), the improved Glut sensor (orange trace) and a step-change in H2O2 for bare Pt sensor (grey trace) as reference. Dimensionless response is the current divided by the steady-state current.

2.3.7. Simulation Results

Using the newly measured values of coating thicknesses and transport parameters, a mathematical model for Glut sensor performance *in vitro* was updated to estimate the theoretical limits of sensitivity and response time for these improved sensors.[23] For the simulations, an external mass transfer coefficient of 0.05 cm s^{-1} and the currently optimized permselective film thicknesses were used. Note that at this mass transfer coefficient value and above, there is little or no impact on predicted sensor response time. Also, an appropriate range of f_{glutox} and enzyme layer thicknesses were chosen for comparison with experimental work (Fig. 12). As expected, simulations predict that increasing f_{glutox} increases sensitivity and reduces the optimal enzyme layer thickness. The comparison with representative experimental data suggest that improvements to sensor design described here have brought performance near the theoretical sensitivity limit of ~375 nA μM^{-1} cm^{-2} for this sensor construction at f_{glutox} = 0.2. As suggested by the simulations shown in Fig. 12, even higher sensitivities of ~450 nA μM^{-1} cm^{-2} at f_{glutox} = 0.4 and ~550 nA μM^{-1} cm^{-2} at f_{glutox} = 1.0 (data not shown) are possible if stable enzyme layers can be created at these concentrations and all activity is retained upon immobilization. Theoretically, sensitivities well above 1000 nA μM^{-1} cm^{-2} are possible, although such results would require additional hypothetical improvements including better transport properties of the immobilized enzyme layer, essentially no mass transfer resistance of the permselective films, and improved H_2O_2 electrooxidation kinetics.

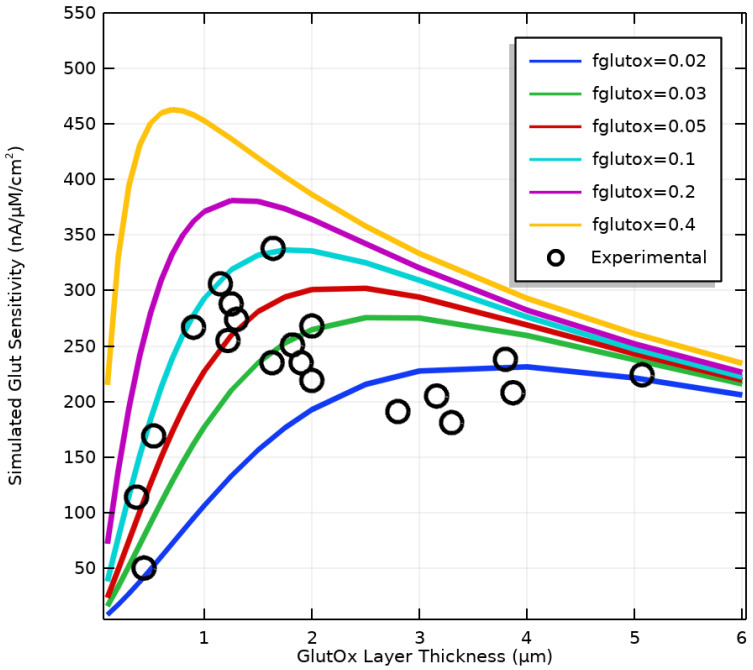

Figure 2.12. Simulations of sensor sensitivity to Glut as a function of GlutOx mass fraction in the enzyme layer (f_{glutox}) and enzyme layer thickness.

Experimental results are consistent with simulated results in terms of optimal enzyme layer thickness and sensitivity for simulated values of f_{glutox} in the range of ~0.02 to <0.2, given measured thicknesses and transport properties of microelectrode coatings. The observation that most experimental results correspond to simulations at lower f_{glutox} values than the experimental preparation of 0.2 suggests that enzyme activity was reduced substantially upon immobilization. It is suspected that amine crosslinking negatively impacts immobilized enzyme activity both through direct inactivation of the active site and steric hindrance effects, so that actual active f_{glutox} after crosslinking is less than the f_{glutox} used to prepare the sensor.

Response time predictions showed little dependence on f_{glutox}, and fell within the range of ~8–10 ms for sensors with optimal enzyme layer thicknesses (1–2 μm). The discrepancy between experimental and simulated response time may be due to key differences in the experimental and

model sensors. In particular, the model assumes a perfectly planar, rigid sensor surface, whereas SEM images show that the surface is rough and probably soft. Thus, external mass transport from the bulk liquid *in vitro* to the sensor surface likely is impacted. Also, the model does not account for the likely possibility that Glut adsorbs to sites in the immobilized enzyme layer and that there likely are dead-end pores as well. Both of these possibilities could contribute to the longer response times observed experimentally but would not necessarily affect sensitivity. In any case, the value of these response times measured *in vitro* where an effort is made to reduce the impact of external mass transfer on the measurement is clear in comparing sensors, but the relevance to utility in practice is not so straightforward since the surrounding medium is essentially quiescent in the brain. The true value of these improved sensors may best be assessed from performance *in vivo*. Recently, data was reported showing excellent recording of ms-scale Glut signals *in vivo* using an innovative Glut biosensor with a thin GlutOx layer.[43] Although the response time and sensitivity were not measured *in vitro*, these results offer promising evidence of the utility of high-performance Glut biosensors as neuroscience research tools going forward.

2.4 Conclusion

Guided by a detailed mathematical model of electroenzymatic Glut sensors based on crosslinked GlutOx immobilized on planar Pt microelectrodes coated with permselective polymer films, a ~6-fold improvement in sensitivity from ~50 to ~320 nA μM^{-1} cm^{-2} and a ~10-fold improvement in response time from ~0.8 s to ~80 ms was achieved while maintaining a low detection limit of ~0.70 μM and excellent selectivity against AA and DA. The transport properties of the enzyme layer and polymer films used to construct the biosensors were measured directly so as to improve the predictive capability of the mathematical model. Subsequent model simulations showed that the experimentally attained biosensor performance approaches the

theoretical limits of sensitivity (~550 nA μM^{-1} cm^{-2}) and response time (~8–10 ms) achievable with electroenzymatic Glut sensors of this construction using this enzyme. Such high-performance biosensors will enable monitoring of Glut signaling with near cellular-scale spatial resolution and at a temporal resolution closer to that of electrical recordings, particularly local field potentials.[4]

2.5 References

1. A. M. Andrews, *Acs Chemical Neuroscience*, 2013, **4**, 645-645.
2. C. Sekirnjak, P. Hottowy, A. Sher, W. Dabrowski, A. M. Litke and E. J. Chichilnisky, *J Neurosci*, 2008, **28**, 4446-4456.
3. B. Eversmann, M. Jenkner, F. Hofmann, C. Paulus, R. Brederlow, B. Holzapfl, P. Fromherz, M. Merz, M. Brenner, M. Schreiter, R. Gabl, K. Plehnert, M. Steinhauser, G. Eckstein, D. Schmitt-Landsiedel and R. Thewes, *Ieee J Solid-St Circ*, 2003, **38**, 2306-2317.
4. G. S. Hong and C. M. Lieber, *Nat Rev Neurosci*, 2019, **20**, 330-345.
5. I. L. Jones, P. Livi, M. K. Lewandowska, M. Fiscella, B. Roscic and A. Hierlemann, *Anal Bioanal Chem*, 2011, **399**, 2313-2329.
6. Q. J. Liu, W. W. Ye, L. D. Xiao, L. P. Du, N. Hu and P. Wang, *Biosensors & Bioelectronics*, 2010, **25**, 2212-2217.
7. E. H. Kim, G. Chin, G. Rong, K. E. Poskanzer and H. A. Clark, *Accounts of Chemical Research*, 2018, **51**, 1023-1032.
8. J. J. Burmeister, F. Pomerleau, P. Huettl, C. R. Gash, C. E. Wemer, J. P. Bruno and G. A. Gerhardt, *Biosensors & Bioelectronics*, 2008, **23**, 1382-1389.
9. L. N. Q. Hoa, H.-R. Chen and T. T. C. Tseng, *Electroanal*, 2018, **30**, 561-570.

10. E. Walker, J. Wang, N. Hamdi, H. G. Monbouquette and N. T. Maidment, *Analyst*, 2007, **132**, 1107-1111.

11. K. M. Wassum, V. M. Tolosa, J. Wang, E. Walker, H. G. Monbouquette and N. T. Maidment, *Sensors-Basel*, 2008, **8**, 5023-5036.

12. M. Parkin, S. Hopwood, D. A. Jones, P. Hashemi, H. Landolt, M. Fabricius, M. Lauritzen, M. G. Boutelle and A. J. Strong, *J Cereb Blood Flow Metab*, 2005, **25**, 402-413.

13. M. L. Rogers, D. Feuerstein, C. L. Leong, M. Takagaki, X. Niu, R. Graf and M. G. Boutelle, *ACS Chem Neurosci*, 2013, **4**, 799-807.

14. A. L. Collins, T. J. Aitken, I. W. Huang, C. Shieh, V. Y. Greenfield, H. G. Monbouquette, S. B. Ostlund and K. M. Wassum, *Biol. Psychiatry*, 2019, DOI: 10.1016/j.biopsych.2019.02.014, Ahead of Print.

15. M. Malvaez, V. Y. Greenfield, A. S. Wang, A. M. Yorita, L. L. Feng, K. E. Linker, H. G. Monbouquette and K. M. Wassum, *Sci Rep-Uk*, 2015, **5**.

16. E. C. Rutherford, F. Pomerleau, P. Huettl, I. Stromberg and G. A. Gerhardt, *J Neurochem*, 2007, **102**, 712-722.

17. C. Debiemme-Chouvy, *Biosens Bioelectron*, 2010, **25**, 2454-2457.

18. N. Hamdi, J. J. Wang and H. G. Monbouquette, *Journal of Electroanalytical Chemistry*, 2005, **581**, 258-264.

19. N. Wahono, S. Qin, P. Oomen, T. I. Cremers, M. G. de Vries and B. H. Westerink, *Biosens Bioelectron*, 2012, **33**, 260-266.

20. J. J. Burmeister, F. Pomerleau, M. Palmer, B. K. Day, P. Huettl and G. A. Gerhardt, *J Neurosci Meth*, 2002, **119**, 163-171.

21. J. J. Burmeister, F. Pomerleau, J. E. Quintero, P. Huettl, Y. Ai, J. Jakobsson, M. Lundblad, A. Heuer, J. T. Slevin and G. A. Gerhardt, *Neuromethods*, 2018, **130**, 327-351.

22. T. T. C. Tseng and H. G. Monbouquette, *Journal of Electroanalytical Chemistry*, 2012, **682**, 141-146.

23. M. Clay and H. G. Monbouquette, *Acs Chemical Neuroscience*, 2018, **9**, 241-251.

24. K. T. Kawagoe, P. A. Garris, D. J. Wiedemann and R. M. Wightman, *Neuroscience*, 1992, **51**, 55-64.

25. J. A. Stamford, Z. L. Kruk and J. Millar, *Brain Res*, 1984, **299**, 289-295.

26. B. Ghasemzedah, J. Cammack and R. N. Adams, *Brain Res*, 1991, **547**, 162-166.

27. B. Ilic, P. Neuzil, T. Stanczyk, D. Czaplewski and G. J. Maclay, *Electrochem. Solid-State Lett.*, 1999, **2**, 86-87.

28. S. Vengatesan, E. Cho, H.-J. Kim and T.-H. Lim, *Korean J. Chem. Eng.*, 2009, **26**, 679-684.

29. E. Leppanen, A. Peltonen, J. Seitsonen, J. Koskinen and T. Laurila, *Journal of Electroanalytical Chemistry*, 2019, **843**, 12-21.

30. D. A. Gough and J. K. Leypoldt, *Anal. Chem.*, 1979, **51**, 439-444.

31. D. R. Lawson, L. D. Whiteley, C. R. Martin, M. N. Szentirmay and J. I. Song, *J. Electrochem. Soc.*, 1988, **135**, 2247-2253.

32. J. A. Leddy, A. J. Bard, J. T. Maloy and J. M. Saveant, *J. Electroanal. Chem. Interfacial Electrochem.*, 1985, **187**, 205-227.

33. C. Malitesta, F. Palmisano, L. Torsi and P. G. Zambonin, *Anal. Chem.*, 1990, **62**, 2735-2740.

34. L. D. Spurlock, A. Jaramillo, A. Praserthdam, J. Lewis and A. Brajter-Toth, *Anal. Chim. Acta*, 1996, **336**, 37-46.

35. A. J. Bard and L. R. Faulkner, *Electrochemical methods : fundamentals and applications*, Wiley, New York, 2nd edn., 2001.

36. A. T. Haug and R. E. White, *J. Electrochem. Soc.*, 2000, **147**, 980-983.

37. Z. Ogumi, Z. Takehara and S. Yoshizawa, *Journal of the Electrochemical Society*, 1984, **131**, 769-773.

38. S. B. Hall, E. A. Khudaish and A. L. Hart, *Electrochim. Acta*, 1997, **43**, 579-588.

39. S. A. M. Vanstroebiezen, F. M. Everaerts, L. J. J. Janssen and R. A. Tacken, *Anal Chim Acta*, 1993, **273**, 553-560.

40. M. R. Ryan, J. P. Lowry and R. D. O'Neill, *Analyst (Cambridge, U. K.)*, 1997, **122**, 1419-1424.

41. K. McAteer and R. D. O'Neill, *Analyst (Cambridge, U. K.)*, 1996, **121**, 773-777.

42. K. N. Hascup, E. C. Rutherford, J. E. Quintero, B. K. Day, J. R. Nickell, F. Pomerleau, P. Huettl, J. J. Burmeister and G. A. Gerhardt, 2007.

43. Y. Wang, D. Mishra, J. Bergman, J. D. Keighron, K. P. Skibicka and A.-S. Cans, *ACS Chemical Neuroscience*, 2019, **10**, 1744-1752.

Chapter 3: Choline detection at near the theoretical performance limit of electroenzymatic sensors

Abstract

High performance microsensors for choline sensing based on choline oxidase and polymer deposited on planar platinum-based electrodes have been created following the guidance from a detailed mathematical model. Implantable microsensors with an array of electroenzymatic sensing sites have been demonstrated to be an effective means for the recording of choline and other neurochemicals *in vivo* to study many neurological disorders including addiction. However, most electroenzymatic sensors perform less than optimal sensitivity and response time. This becomes problematic when the sensing site is reduced in size to that approaching cellular dimension (~10 μm) and neurochemical signaling events are correlated with electrical recordings responding in millisecond range. Model simulations well describing the observed sensor performance indicated the importance of creating thinner layers of highly active enzyme, guiding systematic improvement of an electroenzymatic choline sensors constructed with a ~5 μm-thick crosslinked choline oxidase (ChOx) layer topped on only 200 nm-thick permselective films (poly(*m*-phenylenediamine) and Nafion). These sensors performed high sensitivity of 658 ± 40 nA μM^{-1} cm^{-2} (n = 20) at 37°C and fast response time of 0.36 ± 0.05 s (n = 8) while maintaining excellent selectivity, which is approaching the theoretical performance limits predicted by the mathematical model for device of this type and demonstrating sensitivities over five times what has been previously reported. Such outstanding sensitivity will provide greater flexibility in the design of microsensors by enabling the fabrication of smaller and more densely arrayed sensing sites. And the fast response time will enable better resolution of transient choline signals. This high performance microsensors have been successfully employed for the monitoring

of choline signaling *in vivo* and offered insight on regulatory of choline release on freely moving rats over cue-motivated behavior.

3.1 Introduction

Understanding information processing in the brain is key to developing treatments for complex neurological disorders including drug addiction. Such processes are controlled by neuronal networks influenced by chemical neurotransmission and neuronal electrical activity. Therefore, there is a great impetus to develop advanced technologies that can simultaneously monitor and correlate neuronal activity both electrophysiologically and chemically *in vivo*. Current implantable devices enable recording of activity simultaneously from large numbers of interconnected neurons through millisecond timescale measurements of action potentials with cellular-scale spatial resolution.[1–5] However, techniques for neurochemical recording have yet to achieve such high spatiotemporal resolution due to slow sensor kinetics exacerbated by the need for selectivity against the complex background of brain extracellular fluid.[6–14] Historically, broadly applicable neurotransmitter detection *in vivo* has been accomplished using microdialysis probes coupled to high performance liquid chromatography (HPLC). However, the typically minute-to-minute temporal resolution and relatively large size of the probes has limited utility of this technique. Micromachined microprobes supporting an array of microelectrode sensing sites have emerged as alternative tools to monitor concentration changes for a limited number of neurochemicals. These microsensors, once implanted in the brain, are in direct contact with extracellular fluid potentially providing a means for near-real time neurochemical sensing.[15–19] Microelectrode sites on these microprobes may be modified with permselective polymer films and immobilized redox enzymes to create selective electroenzymatic sensors. For example, the electroenzymatic choline (Ch) sensor developed in this work consists of a platinum (Pt)

microelectrode coated first with permselective polyphenylenediamine (PPD) and Nafion films and then a layer of cross-linked choline oxidase (ChOx). ChOx catalyzes the 4-electron oxidation of Ch to betaine in the presence of oxygen to give 2 equivalents of hydrogen peroxide (H_2O_2), which diffuses through the underlying polymer layers to the electrode surface held at oxidizing potential where it is electrooxidized thereby generating a current signal indicating the presence of Ch. Electrooxidizable interfering species existing in brain extracellular fluid such as dopamine (DA) and ascorbic acid (AA), which are larger than H_2O_2 and charged, are blocked from the electrode surface by the PPD and Nafion films.

$$\mathrm{Ch} + \mathrm{O_2} \xrightarrow{\mathrm{ChOx}} \text{betaine aldehyde} + \mathrm{H_2O_2} \quad (1)$$

$$\text{betaine aldehyde} + \mathrm{O_2} + \mathrm{H_2O} \xrightarrow{\mathrm{ChOx}} \text{betaine} + \mathrm{H_2O_2} \quad (2)$$

Ch is a useful surrogate for the important neurotransmitter, acetylcholine (ACh), which is turned over very rapidly to choline in the brain. Our group and others have demonstrated successfully the feasibility of such electroenzymatic Ch sensors with response times in the ~1 range for the detection of Ch both *in vitro* and *in vivo*.[14,17,19,20] However, such a temporal response still is not fast enough to detect rapid neurotransmitter signaling events that are thought to occur on the millisecond time scale. Furthermore, the previously published sensitivities are too low to create small microsensors with cellular scale spatial resolution. To address these challenges of spatiotemporal resolution, a mathematical model has been developed for devices of this type. Our previous glutamate (Glut) sensor modeling and experimental studies showed that different compositions and layer thicknesses of the enzyme layer can greatly affect the performance of the resulting sensors.[21,22] To construct an electroenzymatic sensor, the protein catalyst most commonly is immobilized by loading a mixture of enzyme and BSA on the microelectrode surface and crosslinking with GAH.[9,11,14,18,23–25] The resulting enzyme layer thicknesses typically have

been in the 10 μm range to ensure larger signal. Our simulation results suggested that such thick coatings cause elevated mass-transfer resistances leading to long response times.[22] If enzyme activity and accessibility could be preserved well during the immobilization process, the density of active enzyme in the layer could be increased so that layer thicknesses could be reduced without a compromise in sensitivity. The systematic optimization of Glut sensors based on the guidance of our simulations has led to great success in the improvement of Glut sensor performance.[22]

In this work, a model has been developed for electroenzymatic Ch sensors. Model simulations here also illustrated the importance of reducing immobilized enzyme layer thickness while maximizing active enzyme concentration in order to maximize H_2O_2 generation near the electrode surface thereby shortening diffusion times and improving current signals. Therefore, a similar experimental strategy whereby enzyme activity retention is first enhanced followed by an optimization of immobilized enzyme layer thickness was followed again for the optimization of Ch sensor. The optimized, thinner enzyme layer results in a higher sensitivity and faster response time that approaches theoretical limits while maintaining low detection limit and excellent selectivity.

3.2 Experiment

3.2.1 Reagents

Nafion (5 wt% in lower aliphatic alcohols and water, contains 15-20% water), *m*-phenylenediamine (PD), bovine serum albumin (BSA) lyophilized powder, choline oxidase (ChOx, from Alcaligenes sp.), choline chloride (Ch), glutaraldehyde solution (25% in water, GAH), L-ascorbic acid (AA), 3-hydroxytyramine (dopamine, DA), sodium phosphate dibasic, sodium chloride, and hydrogen peroxide solution (30%) were purchased from Sigma-Aldrich (St. Louis, MO). Sulfuric acid (30% in water), hydrogen chloride (36.5-38%), bis(sulfosuccinimidyl)suberate

(BS3), sulfo-(ethylene glycol bis(sulfosuccinimidyl succinate)) (EGS), and (1-ethyl-3-(3-dimethylaminopropyl)carbodiimide hydrochloride) (EDC) were purchased from Thermo Fisher Scientific (Pittsburgh, PA). Ag/AgCl glass-bodied reference electrodes with NaCl electrolyte (3M) and a 0.5-mm-diameter Pt wire auxiliary electrode were obtained from BASi (West Lafayette, IN). Sodium phosphate buffer (PBS, pH 7.4) was composed of 50 mM sodium phosphate dibasic and 100 mM sodium chloride. Four-inch, 150 μm silicon wafers were purchased from Silicon Valley Microelectronics (Santa Clara, CA).

3.2.2 Instrumentation

Electrochemical preparation and calibration of the microsensors were performed using a Versatile Multichannel Potentiostat (model VMP3) equipped with the 'p' low current option and N'Stat box driven by EC-LAB software (Bio-Logic USA, LLC, Knoxville, TN) in a three-electrode configuration consisting of the sensing electrode, a Pt wire auxiliary electrode, and a Ag/AgCl reference electrode. The film thicknesses on microelectrodes were measured using a scanning electron microscope, SEM (Nova 600 SEM/FIB System).

3.2.3 Sensor preparation

Fig. 1 shows a scanning electron micrograph (SEM) and optical microscope image of the microelectrode array (MEA) tip of a single probe used in this work. The probe shafts were 150 μm thick, 140 μm wide and 9 mm long with four 6000 μm^2 (40 μm x 150 μm) Pt recording sites arranged in pairs at the tip. Microelectrode array probes were manufactured using microelectromechanical system (MEMS) fabrication techniques as described in our previous work.[11] Each microsensor was cleaned with 0.1 M H_2SO_4 solution by cycling the potential between -0.2 V and 1.5 V at scan rate of 50 mV/s *vs*. Ag/AgCl, repeated at least 4 times. Afterward, a poly-phenylenediamine (PPD) film was electrodeposited from a 5 mM PD solution in phosphate-

buffered saline (0.1 M PBS) by holding the voltage constant at 0.85 V vs. Ag/AgCl until the total transferred charge reached 7.6×10^{-7} coulombs. A Nafion layer then was applied by dip-coating a 2% Nafion solution (diluted from stock with 4:1 IPA:water) once, followed by annealing at 115 °C for 20 min. Next, enzyme immobilization was accomplished by manually loading a ChOx and BSA mixture in different ratio onto the microelectrode sites and exposing the deposit to different crosslinkers as described below.

In this work, four different crosslinkers including three amine-to-amine crosslinkers with different spacer arm lengths (GAH, BS3, EGS) and one carboxyl-to-amine crosslinker (EDC) were used and compared. Each crosslinking condition was individually optimized before making comparisons. The previously loaded ChOx/BSA mixture was exposed to (1) 5% GAH vapor for 1 min at room temperature (2) BS3 by manually topping a layer of BS3 solution (100 mg/ml in PBS) (3) EGS by manually topping a layer of EGS solution (100 mg/ml in PBS). When crosslinked with EDC, the ChOx and BSA were mixed directly with EDC solution to give a final EDC concentration of ~6.3 mg/ml in PBS before deposition on a microelectrode. After the crosslinking step, sensors were stored dry in 4 °C for 48 h prior to testing.

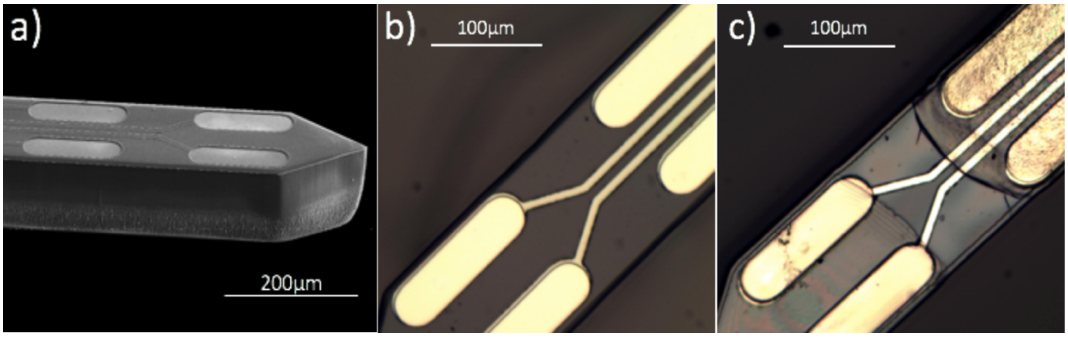

Figure 3.1. (a) SEM and (b) optical microscope image of the bare microelectrode array probe. (c) Optical microscope image of the microelectrode array probe after polymer and enzyme deposition.

3.2.4 Electrochemical measurement

To determine the selectivity and sensitivity, a constant potential of 0.7 V *vs*. Ag/AgCl was applied to the microsensors in stirred PBS buffer solution at pH 7.4 and ~37 °C. Selectivity was assessed relative to AA and DA, which are electroactive interferents commonly found in brain extracellular fluid (ECF). Their typical concentrations in ECF are in the range of a few hundred μM for AA and from nM to a few μM for DA.[26,27] In selectivity tests, the current signal from a probe immersed in stirred buffer was allowed to stabilize. Subsequently AA and DA were added separately to the beaker to reach final concentrations of 250 μM AA and 10 μM DA. Next, serial injections were made to give final concentrations of 20-100 μM Ch and 20 μM H_2O_2 to determine sensitivities to both species. The response time ($T_{0\text{-}90\%}$) of Ch sensors were evaluated from the rapid step changes in current after analyte injection in stirred PBS buffer.

3.2.5 Mathematical Model and Simulations

Simulations of sensor performance were generated using an adaptation of our established model for electroenzymatic glutamate (Glut) sensors that includes the incorporation of ChOx rather than glutamate oxidase into the enzyme coating on Pt microelectrode sensing sites.[22,28] In the model, sets of partial differential equations describe the one-dimensional transport and reaction rates of Ch, betaine aldehyde, O_2, and H_2O_2 within and between separately modelled PPD, Nafion, and immobilized enzyme domains. Each of these species is able to diffuse freely within the void spaces of the coatings in which they are soluble, with modified diffusivities based on experimentally measured values. Numerical solutions were obtained using COMSOL (COMSOL, Inc. Los Angeles), using boundary conditions that simulate a step-change in Ch concentration from 0 to 20 μM at the microsensor surface at time (t) = 0.

3.3 Results and discussion

3.3.1 Effect of Enzyme loading and Activity

To improve enzyme activity retention, alternative homobifunctional crosslinkers BS3 and EGS that like GAH also react with amine groups at neutral pH were studied. We demonstrated that Glut sensors made with enzyme crosslinked with BS3 showed great improvement in sensitivity compared to those crosslinked with GAH, probably due to the longer spacer arm of BS3, 11.4 Å *vs* 5 Å.[22] In this work, besides BS3 and GAH, the crosslinker EGS with the longest spacer arm 16.1 Å was used in order to explore further the effect of the length of crosslinker spacer arm on resulting sensor performance. Before making a comparison among these three crosslinkers, crosslinking conditions were investigated individually by varying crosslinker concentrations and vapor exposure times to find the best conditions for use of the crosslinker for Ch sensor fabrication. A representative EGS optimization procedure is illustrated in Fig. 2(b).

After this optimization process, Ch sensors made with enzyme crosslinked with BS3 showed the greatest sensitivity compared to those crosslinked with GAH or EGS, which showed sensitivity of 557 $\pm$ 99 nA μM^{-1} cm^{-2} (n = 11), 409 $\pm$ 59 nA μM^{-1} cm^{-2} (n = 12) and 351 $\pm$ 101 nA μM^{-1} cm^{-2} (n = 4), respectively. This ~1.5-fold improvement in sensitivity of Ch sensors crosslinked with BS3 compared to those crosslinked via GAH agrees with our previous work as discussed eariler.[22] However, it is interesting to see the decrease in Ch sensitivity when longer crosslinker was used. We hypothesize that the length of spacer arm not only determines the accessibility of substrate to the enzyme active site, but also the void fraction within the enzyme layer and the concentration of active enzyme entrapped in the BSA/ChOx network. The medium length of the BS3 spacer arm may be preferable, because such a length (11.4 Å) is long enough to reduce enzyme crowding and improve active site accessibility, but also short enough to maintain a stable, high enzyme concentration in the crosslinked BSA/ChOx network.

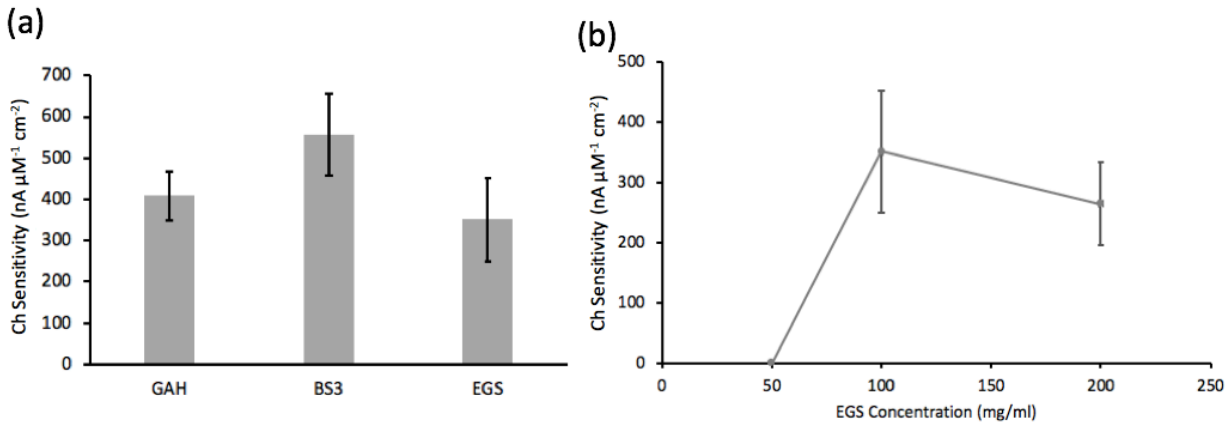

Figure 3.2. (a) Ch sensitivity comparison between GAH, BS3 and EGS crosslinked Ch sensors with error bar giving 95% confidence intervals. (b) Effect of EGS concentration on the Ch sensitivity. In all cases, the mass ratio of ChOx to BSA was 2 : 3 and the enzyme layer was ~3-4 µm to ensure equivalent enzyme loading.

The effort to improve Ch sensor performance was carried further by conducting a study of the effect of deposited enzyme concentration on sensor performance, which can be performed straightforwardly by changing the relative proportion of ChOx and BSA without changing enzyme layer thickness of ~ 3-4 µm. To test independently the effect of varied active enzyme concentration in the catalytic layer, the mass fraction of ChOx (f_{chox}) was varied from 0.2 to 0.8 for the sensors coated with PPD and Nafion and crosslinked with BS3. The experimental Ch sensitivity versus f_{chox} plot showed that Ch sensitivity goes through a peak at f_{chox} = 0.4 and drops to zero at high enzyme concentration corresponding to f_{chox} = 0.8. (Fig. 3) It is noteworthy that this trend also was observed for GAH and EGS crosslinked Ch sensors. For the thin enzyme layer explored here, a decrease in Ch sensitivity was expected due to insufficient active enzyme available to turnover Ch at the high rate needed for a strong current signal. However, high enzyme concentration also was found not to be preferable. This result again matched our previously published data on Glut sensor optimization showing that there are insufficient lysine groups available for crosslinking of

the protein layer at low concentrations of lysine-rich BSA. The relatively low BSA concentration at high f_{chox} led to poor crosslinking of the enzyme layer and low sensitivity as illustrated in Fig. 3.

This result prompted us to consider a side experiment to try crosslinkers reacting with carboxyl groups of which ChOx has an abundance on its surface. The heterobifunctional crosslinker, EDC, which crosslinks with carboxyl and amine groups, was chosen due to its ready commercial availability. The mass fraction of ChOx was varied from f_{chox} = 0.2 to f_{chox} = 1.0 and the experimental results are shown as the orange trace in Fig. 3. This amine-to-carboxyl crosslinker enabled the stable immobilization of ChOx in the absence of BSA (f_{chox} = 1.0). This result supports our unsurprising contention that the availability of crosslinkable functional groups on the enzyme surface plays an important role in stable enzyme immobilization at higher concentration. However, a decrease in Ch sensitivity at high enzyme concentration was still observed, which may be due to hindered accessibility of the enzyme active site and/or increased enzyme deactivation as more crosslinker reacts directly with ChOx instead of BSA. Overall, sensors crosslinked with EDC showed lower Ch sensitivity of 435 $\pm$ 27 nA μM^{-1} cm^{-2} (n = 6) compared to those crosslinked with BS3 at optimal values of f_{chox}. As a result, the BS3 crosslinked sensor with f_{chox} = 0.4 was chosen for future work due to its best sensitivity.

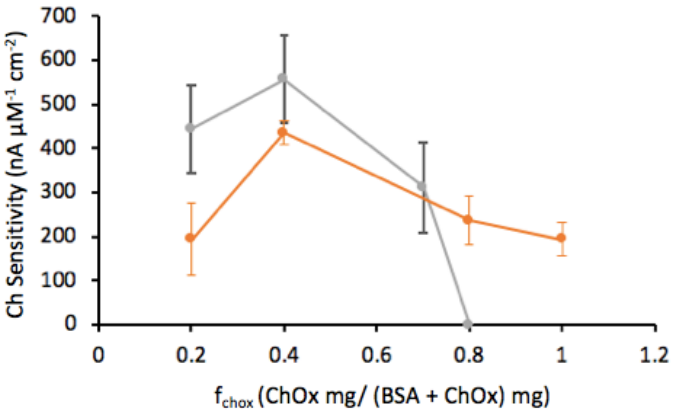

Figure 3.3. Effect of immobilized ChOx concentration on the Ch sensitivity of sensors crosslinked via BS3 (grey trace) and sensors crosslinked via EDC (orange trace). In all cases, the enzyme layer thickness was ~3-4 µm. Error bars represent 95% confidence intervals.

3.3.2 Optimal enzyme layer thickness

Fig. 4 shows Ch sensitivity for varied thicknesses of the enzyme layer, using the optimal f_{chox} of 0.4 and best crosslinker (BS3). Ch sensitivity decreased sharply for enzyme layer thicknesses of less than 3 µm due to an insufficient amount of deposited enzyme as expected. Sensitivity reached a plateau as enzyme layer thickness increases beyond ~4 µm. Since response time is known to increases with layer thickness, a ChOx layer thickness of 4-6 µm was determined to be best to ensure high Ch sensitivity and fast response time. The plateau for enzyme layers more than 3 µm thick may be due to be the result of a counterbalance between the greater availability of active enzyme and greater mass-transfer limitation due to a thicker enzyme layer.

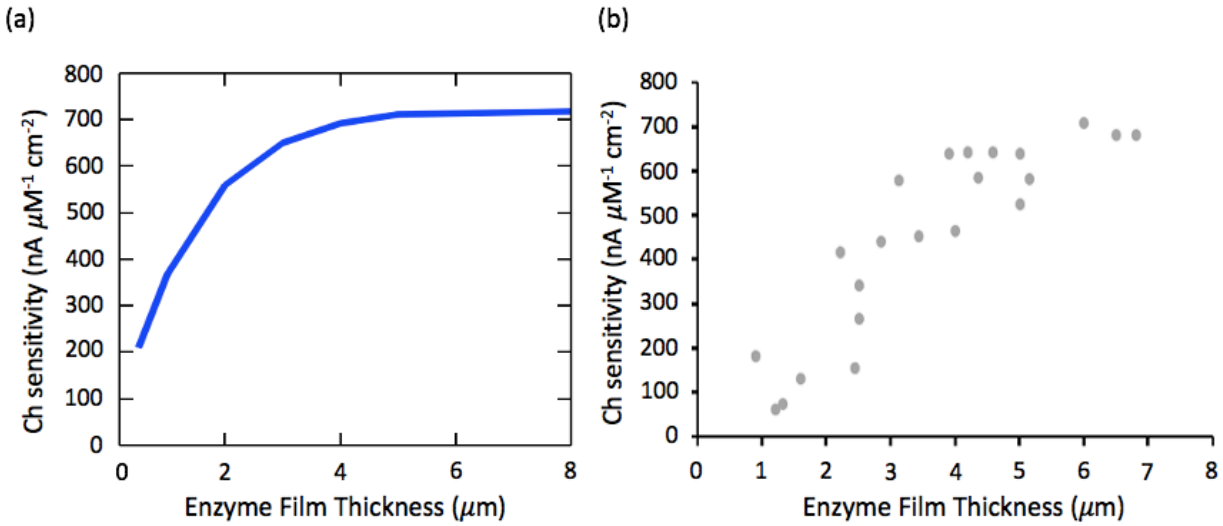

Figure 3.4. (a) Simulation result and (b) experimental result of sensor sensitivity versus immobilized ChOx layer thickness. In all cases, f_{ChOx} = 0.4, and sensors were crosslinked via BS3. Simulations assume a void fraction in the enzyme layer of 0.6.

3.3.3 Optimized sensor performance

The sensitivity of the best constructed Ch sensor was based on the slope of the linear range of calibration curves (0-100 μM Ch), and the detection limit was determined at a signal-to-noise ratio of 3. Ch sensors generated with optimal enzyme layer composition f_{chox} = 0.4, crosslinked with BS3, and with enzyme layer thickness in the 4-6 μm range showed high Ch sensitivity of 658 ± 40 nA μM^{-1} cm^{-2} (n = 20), low detection limit of 0.34 ± 0.06 μM (n = 20), and excellent selectivity against two common interferents, AA and DA, tested at physiologically relevant concentrations (Fig. 5).

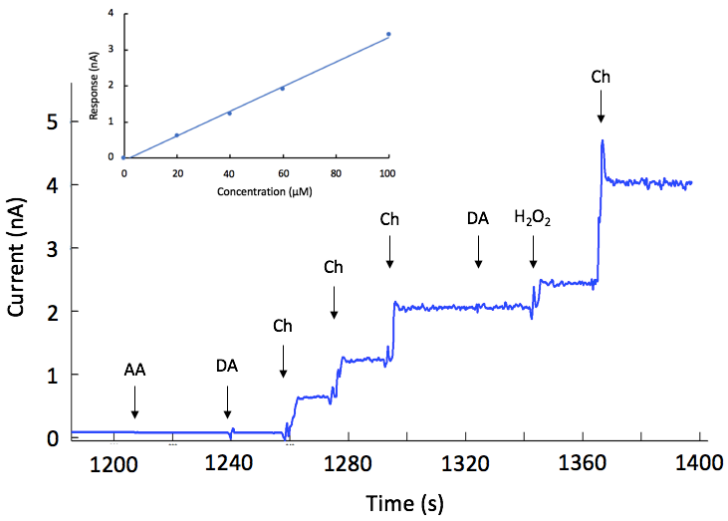

Figure 3.5. Representative current responses of optimized Ch sensors tested in batch with key interferents AA (250 μM), DA (5 μM), target Ch (final 20, 40, 60 μM in solution), interferent DA (final 15 μM in solution), H_2O_2 (20 μM) and Ch (final 100 μM in solution) in series.

3.3.4 Response time

Response time is defined here as the time for the current signal to reach 90% of its steady-state value in response to a step change in Ch from zero to 60 μM in a stirred beaker. Compared to other sensors in the published literature that reported response times of Ch sensors as ~1s[14,17], our improved sensor with thinner enzyme and permselective layers showed fast response time of 0.36 ± 0.05 s (n = 8) without compromising sensitivity and selectivity (Fig. 6). The very rapid response of bare Pt to 10 μM H_2O_2 is also shown in Fig. 6 as a benchmark, which is close to a step as expected. This great improvement in temporal resolution of Ch sensors enables more accurate monitoring of Ch extracellular concentration especially when distinguishing multiphasic and more complex Ch fluctuations. A comparison of the analytical parameters of the best constructed Ch sensor here with other electroenzymatic Ch sensors in the literature is presented in Table. 1, which showing improved Ch sensor of this work has remarkable sensitivity and response time.

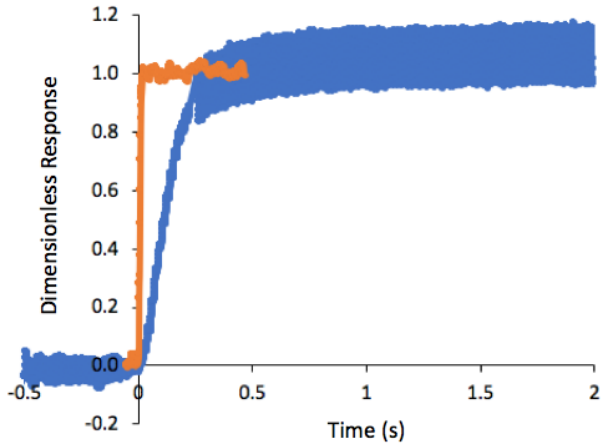

Figure 3.6. Representative sensor response to a step-change in Ch concentration from 0 to 60 μM for the optimized Ch sensor (blue trace) and a step-change in H_2O_2 for bare Pt sensor (orange trace) as a benchmark.

Sensitivity (nA μM^{-1} cm^{-2})	Response time (s)	Limit of detection (μM)	Reference
654	0.35	0.34	This work
354	2	0.45	29
286	1.5	1.00	14
204	4	0.60	30
128	1.16	0.12	17
75	2	15.00	31

Table 3.1. Comparison of the performance characteristics of Ch sensor of this work with other recently reported electroenzymatic Ch sensors.

3.3.5 Stability

The stability of the Ch sensor *in vitro* was expressed as half-slef, the amount of time required for the sensitivity to be reduced to one-half of its original value, for sensors stored in PBS at 4 °C. The decay in sensitivity over time, nondimensionalized to be relative to the initial sensitivity, is shown in Fig. 7. Results showed that Ch sensors crosslinked via BS3 (n = 4) had

longer half time than those crosslinked conventionally with GAH (n = 4), which were ~11 days and ~ 8 days, respectively. After 2 weeks the GAH-crosslinked Ch sensors exhibited less than 10% of initial sensitivity, whereas BS3-crosslinked Ch sensors retained 40% sensitivity over the same time period. The fast decrease in Ch sensitivity after 2 weeks from GAH-crosslinked sensors is likely due to the instability of the enzyme layer in solution, which was readily observed under the microscope. We hypothesize that the shorter spacer arm of GAH has greater chance to form intramolecular bonds that are not contributing to building up a three-dimensional network unlike intermolecular bond.[25]

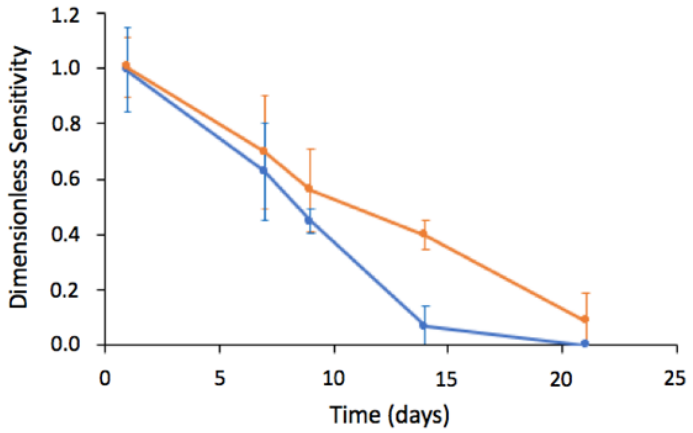

Figure 3.7. Stability of GAH-crosslinked (blue trace) and BS3-croslinked (orange trace) Ch sensors stored in PBS at 4 °C. Data shown with 95% confident intervals (n = 4 for both cases).

3.3.6 Simulations to determine theoretical performance limits

Simulations of optimized Ch sensors (Figure 8) predicted the maximum theoretical sensitivities for sensors with the required permselective films and with the enzyme layer thicknesses and compositions tested experimentally. In comparing these results to experimental data it is clear that these performance limits have nearly been reached. If it were possible to increase f_{chox} to 1 and maintain enzyme function, sensitivity could potentially reach 900 nA μM^{-1}

cm^{-2}, and if the void fraction (ε) were lower, thinner layers (meaning faster response times) would have higher sensitivities. A Noticeable benefit of the conditions modelled and experimentally verified is the range of enzyme layer thicknesses where optimal sensitivity is maintained, which is not seen at other void fractions.

Initial model development revealed many similarities to previous work, showing that coating thicknesses have the largest effect on sensitivity and response time and that when enzyme layers are thin enough the properties of the enzyme layer become very important;[22] it also revealed some important differences in enzyme layer properties between ChOx layers and GlutOx layers. Coating thicknesses, reaction rates, and transport rates were investigated in great detail for Glut sensors, and in the Ch sensor model the properties of the optimized permselective films were assumed to be unaffected by changes to the enzyme layer. Uncertainties in the ChOx layer were related to enzyme immobilization and could not be simply measured, including the void fraction and the fraction of successfully immobilized enzyme. Accordingly, Ch sensor simulations were designed to test variations in these properties over a range of enzyme layer thicknesses so that values could be verified by making the appropriate comparisons to experimental data.

Initial simulations assumed that an enzyme layer with immobilized ChOx would have the same mass transfer properties as one with GlutOx, although this led to a poor description of the experimental sensitivity as enzyme layer thickness is varied. For Ch sensors, higher sensitivities were observed using sensors with thicker enzyme layers than originally predicted and the range of optimal thicknesses was much wider. After considering possible sources of error in the simulation, a much better fit was found if the void fraction in the enzyme layer was 0.66, double what is expected in a Glut sensor, with the diffusivity appropriately modified according to the random pore model (Fig. 9). The other noticeable difference from the Glut sensor is that the fraction of oxidase in the enzyme layer (f_{chox}) does not need to be modified to fit experimental data,

suggesting that much more enzymatic activity is maintained upon immobilization of ChOx as opposed to GlutOx. In simulating lower values of f_{chox}, sensitivity across all thicknesses decreases proportionately, with no change to the shape of the curve.

Ultimately, deviations from original expectations suggest that optimal immobilization of ChOx produces a layer with a higher void fraction in which a greater extent of enzymatic activity is maintained, possibly due to an increase in the accessibility of active sites in a less compact enzyme layer. Still, simulation results show that the predicted sensitivities must be shifted by ~1 μm to match experimental results. This suggests that a sensor with a given ChOx layer thickness is performing as if it had a theoretically thinner layer, or that in the time between measuring the enzyme thickness on a probe and testing its sensitivity ~1 μm of the layer is lost or removed; this may be a consequence of the large void fraction of the enzyme layer and may be related to the loss in sensitivity of a sensor over time.

Similar to Glut sensors, simulations show that response time increases linearly with enzyme layer thickness, is not noticeably affected by changes to the void fraction or the fraction of functional ChOx in the enzyme layer, and simulated response time could be an order of magnitude faster than what has been seen experimentally. This difference could be the result of difficulties in experimentally measuring response time or in transient conditions not included in the model. It is likely that adsorption of Ch onto surfaces within the enzyme layer delays the approach to maximal signal in response to a step change in Ch concentration. This hypothesis is supported by experimental data showing reduced response times for later additions of Ch (Fig. 6), and will be investigated in greater detail to determine if there is an impact on *in vivo* response to transient Ch concentrations in the brain.

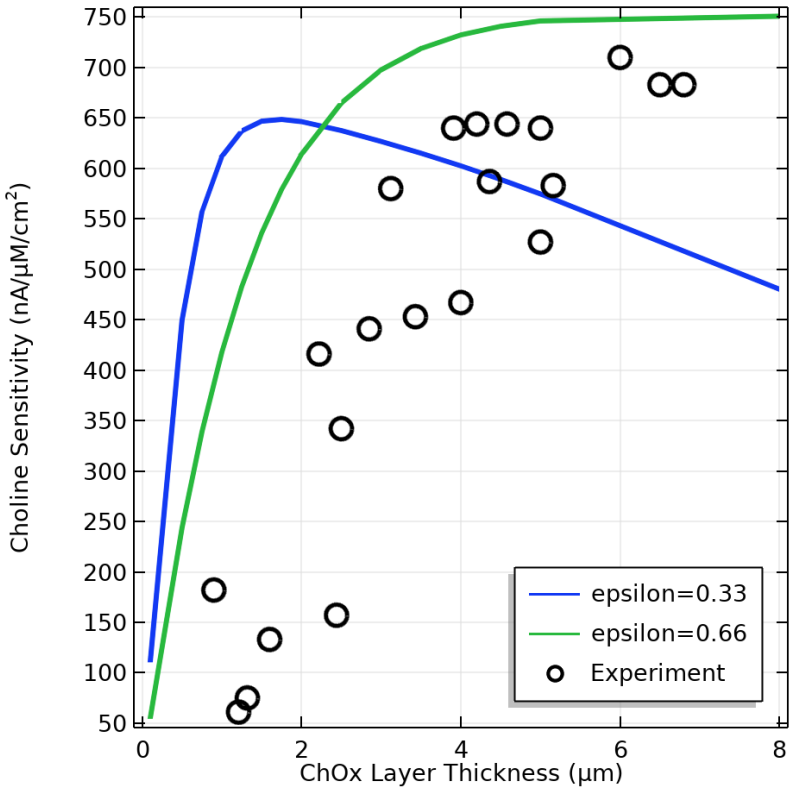

Figure 3.8. Simulated sensitivity as a function of enzyme layer thickness for fchox=0.4 and experimental values for reference.

3.4 Conclusion

The detailed mathematical model has guided the experimental work to improve the composition and thickness of the immobilized ChOx layer attaining Ch electroenzymatic sensors performance approaching the theoretical limits of sensitivity of 654 ± 40 nA μM^{-1} cm^{-2} (n = 20) and fast response time of 0.36 ± 0.05 s (n = 8) without compromising sensitivity and selectivity. The improvement in Ch sensors will provide greater feasibility to fabrication of smaller, more densely arrayed chemical sensing sites in cellular scale and allow better correlation of chemical and electrical signaling in the brain.

3.5 References

1. Du, J., Blanche, T. J., Harrison, R. R., Lester, H. A. & Masmanidis, S. C. Multiplexed, High Density Electrophysiology with Nanofabricated Neural Probes. *PLoS One* **6**, 26204 (2011).
2. Rios, G., Lubenov, E. V, Chi, D., Roukes, M. L. & Siapas, A. G. Nanofabricated Neural Probes for Dense 3-D Recordings of Brain Activity. *Nano Lett.* **16**, 6857–6862 (2016).
3. Jun, J. J. *et al.* Fully integrated silicon probes for high-density recording of neural activity. *Nature* **551**, 232–236 (2017).
4. Hong, G. & Lieber, C. M. Novel electrode technologies for neural recordings. *Nat. Rev. Neurosci.* **20**, 330–345 (2019).
5. Jones, I. L., Livi, P. & Lewandowska, M. K. The potential of microelectrode arrays and microelectronics for biomedical research and diagnostics. *Anal. Bioanal. Chem.* **399**, 2313–2329 (2011).
6. Jaquins-Gerstl, A. & Michael, A. C. A review of the effects of FSCV and microdialysis measurements on dopamine release in the surrounding tissue. *Analyst* **140**, 3696 (2015).
7. Yang, H., Thompson, A. B., Mcintosh, B. J., Altieri, S. C. & Andrews, A. M. Physiologically Relevant Changes in Serotonin Resolved by Fast Microdialysis. *ACS Chem. Neurosci.* **4**, 790–798 (2013).
8. Sandlin, Z. D., Shou, M., Shackman, J. G. & Kennedy, R. T. Microfluidic Electrophoresis Chip Coupled to Microdialysis for in Vivo Monitoring of Amino Acid Neurotransmitters. *Anal. Chem.* **77**, 7702–7708 (2005).
9. Rutherford, E. C., Pomerleau, F., Huettl, P., Strömberg, I. & Gerhardt, G. A. Chronic second-by-second measures of L-glutamate in the central nervous system of freely moving rats. *J. Neurochem.* **102**, 712–722 (2007).
10. Parkin, M. C. *et al.* Dynamic changes in brain glucose and lactate in pericontusional areas

of the human cerebral cortex, monitored with rapid sampling on-line microdialysis: Relationship with depolarisation-like events. *J. Cereb. Blood Flow Metab.* **25**, 402–413 (2005).

11. Wassum, K. M. *et al.* Silicon wafer-based platinum microelectrode array biosensor for near real-time measurement of glutamate in vivo. *Sensors* **8**, 5023–5036 (2008).
12. Rogers, M. L. *et al.* Continuous online microdialysis using microfluidic sensors: Dynamic neurometabolic changes during spreading depolarization. *ACS Chem. Neurosci.* **4**, 799–807 (2013).
13. Bowser, M. T. & Kennedy, R. T. In vivo monitoring of amine neurotransmitters using microdialysis with on-line capillary electrophoresis. *Electrophoresis* **22**, 3668–3676 (2001).
14. Wang, B., Koo, B., Huang, L. W. & Monbouquette, H. G. Microbiosensor fabrication by polydimethylsiloxane stamping for combined sensing of glucose and choline. *Analyst* **143**, 5008–5013 (2018).
15. Malvaez, M. *et al.* Basolateral amygdala rapid glutamate release encodes an outcome-specific representation vital for reward-predictive cues to selectively invigorate reward-seeking actions. *Sci. Rep.* **5**, (2015).
16. Collins, A. L. *et al.* Archival Report Nucleus Accumbens Cholinergic Interneurons Oppose Cue-Motivated Behavior. *Biol. Psychiatry* **86**, 388–396 (2019).
17. Burmeister, J. J. *et al.* Ceramic-based multisite microelectrode arrays for simultaneous measures of choline and acetylcholine in CNS. **23**, 1382–1389 (2008).
18. Khan, A. & Ghani, S. A. Multienzyme microbiosensor based on electropolymerized o-phenylenediamine for simultaneous in vitro determination of acetylcholine and choline. *Biosens. Bioelectron.* **31**, 433–438 (2012).
19. Jerusalinsky, D. *et al.* Acetylcholine and Choline Amperometric Enzyme Sensors

Characterized in Vitro and in Vivo. *Biosens. Bioelectron* **9**, 1098–1106 (1997).

20. Garguilo, M. G., Huynh, N., Proctor, a & Michael, a C. Amperometric sensors for peroxide, choline, and acetylcholine based on electron transfer between horseradish peroxidase and a redox polymer. *Anal. Chem.* **65**, 523–528 (1993).
21. Clay, M. & Monbouquette, H. G. A Detailed Model of Electroenzymatic Glutamate Biosensors to Aid in Sensor Optimization and in Applications in Vivo. *ACS Chem. Neurosci.* **9**, 241–251 (2018).
22. Huang, I. *et al.* Electroenzymatic glutamate sensing at near the theoretical performance limit. *Analyst* (2020). doi:10.1039/c9an01969c
23. Burmeister, J. J. *et al.* Improved ceramic-based multisite microelectrode for rapid measurements of L-glutamate in the CNS. *J. Neurosci. Methods* **119**, 163–171 (2002).
24. Burmeister, J. J. *et al.* Biochemical Approaches for Glutamatergic Neurotransmission. **130**, 327–351 (2018).
25. Migneault, I., Dartiguenave, C., Bertrand, M. J. & Waldron, K. C. Glutaraldehyde: Behavior in aqueous solution, reaction with proteins, and application to enzyme crosslinking. *Biotechniques* **37**, 790–802 (2004).
26. Ghasemzedah, B., Cammack, J. & Adams, R. N. Dynamic changes in extracellular fluid ascorbic acid monitored by in vivo electrochemistry. *Brain Res.* **547**, 150–154 (1991).
27. Kawagoe, K. T., Garris, P. A., Wiedemann, D. J. & Wightman, R. M. Regulation of transient dopamine concentration gradients in the microenvironment surrounding nerve terminals in the rat striatum. *Neuroscience* **51**, 55–64 (1992).
28. Fan, F. & Gadda, G. On the catalytic mechanism of choline oxidase. *J. Am. Chem. Soc.* **127**, 2067–2074 (2005).
29. Keihan, A. H., Sajjadi, S., Sheibani, N. & Moosavi-Movahedi, A. A. A highly sensitive

choline biosensor based on bamboo-like multiwall carbon nanotubes/ionic liquid/Prussian blue nanocomposite. *Sensors Actuators B Chem.* **204**, 694–703 (2014).

30. Magar, H. S., Ghica, M. E., Abbas, M. N. & Brett, C. M. A. A novel sensitive amperometric choline biosensor based on multiwalled carbon nanotubes and gold nanoparticles. *Talanta* **167**, 462–469 (2017).

31. Zhang, H., Yin, Y., Wu, P. & Cai, C. Indirect electrocatalytic determination of choline by monitoring hydrogen peroxide at the choline oxidase-prussian blue modified iron phosphate nanostructures. *Biosens. Bioelectron.* **31**, 244–250 (2012).

Chapter 4: Nucleus Accumbens Cholinergic Interneurons Oppose Cue-Motivated Behavior

Chapter 4 is a manuscript published with the following citation:

Anne L. Collins, Tara J. Aitken, **I-Wen Huang**, Christine Shieh, Venuz Y. Greenfield, Harold G. Monbouquette, Sean B. Ostlund, and Kate M. Wassum, "Nucleus Accumbens Cholinergic Interneurons Oppose Cue-Motivated Behavior," Biological Psychiatry, 2019, 86 (5), 388-396

I-Wen Huang's contribution to this work focused on microsensor fabrication. This involved using microfabrication techniques to pattern and create the microelectrode probes, as well as depositing the polymer and enzmye layers used to make a selective choline sensor. Sensor testing and calibration was also provided.

Abstract

BACKGROUND: Environmental reward–predictive stimuli provide a major source of motivation for adaptive reward pursuit behavior. This cue-motivated behavior is known to be mediated by the nucleus accumbens (NAc) core. The cholinergic interneurons in the NAc are tonically active and densely arborized and thus well suited to modulate NAc function. However, their causal contribution to adaptive behavior remains unknown. Here we investigated the function of NAc cholinergic interneurons in cue-motivated behavior.

METHODS: We used chemogenetics, optogenetics, pharmacology, and a translationally analogous Pavlovian-toinstrumental transfer behavioral task designed to assess the motivating influence of a reward-predictive cue over reward-seeking actions in male and female rats.

RESULTS: The data show that NAc cholinergic interneuron activity critically opposes the motivating influence of appetitive cues. Chemogenetic inhibition of NAc cholinergic interneurons augmented cue-motivated behavior. Optical stimulation of acetylcholine release from NAc cholinergic interneurons prevented cues from invigorating reward-seeking behavior, an effect that was mediated by activation of b2-containing nicotinic acetylcholine receptors.

CONCLUSIONS: NAc cholinergic interneurons provide a critical regulatory influence over adaptive cue-motivated behavior and therefore are a potential therapeutic target for the maladaptive cue-motivated behavior that marks many psychiatric conditions, including addiction and depression.

4.1 Introduction

Environmental reward–predictive stimuli provide a major source of motivation for adaptive reward pursuit behaviors.[1] This incentive motivational value can become dysfunctional in many psychiatric disease states.[2] Indeed, it can become amplified, allowing cues to become potent triggers for maladaptive compulsive overeating,[3] alcohol abuse,[4-7] or drug seeking.[8-12] Stress, anxiety, and depression [13-16] can also disrupt the motivating influence of appetitive cues, resulting in dampened or inappropriate motivation. The nucleus accumbens (NAc) core has been implicated in cue-motivated behavior.[17-19] However, little is known about the function of the major NAc neuromodulator acetylcholine. Such information is crucial given the purported importance of cholinergic signaling in many mental illnesses.[20-21]

Cholinergic interneurons provide the primary, though not exclusive,[22] source of acetylcholine in the NAc.[23] Despite accounting for only 1% to 2% of the population, these largebodied, tonically active neurons are densely arborized,[24-29] making them ideally suited to modulate NAc function and associated behaviors. Cholinergic interneurons have also been shown to locally regulate striatal dopamine release.[30-32] NAc cholinergic signaling is elevated under

conditions that discourage vigorous reward seeking, such as satiety,[33-34] and has been implicated in anxiety-like and depression-like states [35-36] marked by blunted motivation. Cholinergic interneurons are also transiently activated by informative environmental stimuli. Cues that discourage motivated behavior activate the cholinergic interneurons,[37-38] whereas reward-predictive cues that encourage motivated behavior cause a characteristic pause in cholinergic interneuron activity.[29, 37, 39-46] Still, very little is known of the causal contribution of NAc cholinergic interneurons to motivation.

We sought to fill this gap in knowledge by assessing the function of NAc cholinergic interneurons in cue-motivated behavior. Working from the evidence that cholinergic interneurons increase their activity when vigorous motivated behavior is disadvantageous and pause when active reward pursuit is encouraged, we tested the hypothesis that NAc cholinergic interneuron activity functions to oppose the motivating influence of appetitive cues. Chemogenetic and optogenetic methods were used to selectively manipulate NAc cholinergic interneuron activity. We used the Pavlovianto-instrumental transfer (PIT) test to measure cue-motivated behavior. This test is translationally analogous to that used in humans in health and disease [5,11,17.47-55] and assesses the invigorating influence of an environmental reward predictive stimulus over instrumental reward-seeking activity. Because the Pavlovian and instrumental components are trained separately, PIT isolates the incentive motivational value of the cue from other processes through which cues trigger action, such as via discriminative control or a stimulus response relationship.

4.2 Methods and materials

4.2.1 Subjects

Adult (3–5 months) male and female ChAT::Cre^{+} bacterial artificial chromosome transgenic rats (Long-Evans background)[56] were used for all experiments. Although bacterial

artificial chromosome transgenic ChAT::Cre^{+} mice have been shown to overexpress the vesicular acetylcholine transporter, which can lead to behavioral and electrophysiological changes[57], we found normal expression of the behaviors of interest here, similar to our prior reports in wild-type rats[58–60]. Pups were weaned at postnatal day 21 and housed in groups until experiment onset. Handling occurred daily, beginning at postnatal day 60. Training and testing were performed during the dark phase of a 12-hour reverse dark/light cycle. Rats were food restricted to approximately 85% free-feeding body weight, and water was provided ad libitum in the home cage. All procedures were conducted in accordance with the National Research Council Guide for the Care and Use of Laboratory Animals and were approved by the University of California, Los Angeles, Institutional Animal Care and Use Committee.

4.2.2 Surgery

Standard surgical procedures, described previously[58,61,62], were used for infusion of adeno-associated viruses (AAVs) and implantation of optical fiber or microinfusion injector/optical fiber guide cannula into the NAc core. Rats were anesthetized with isoflurane, and a nonsteroidal anti-inflammatory agent was administered preoperatively and postoperatively to minimize pain and discomfort. Surgical details for each experiment are provided in Supplemental Methods. Expression and placement were verified with standard histological procedures (see Supplemental Methods).

4.2.3 Behavioral Procedures

General Training and Testing. Rats received Pavlovian and instrumental training in conditioning chambers (Med Associates, Inc., Fairfax, VT), as described previously[58–60]. Rats first received 8 days of Pavlovian training, in which one of two auditory stimuli (75-dB tone or white noise; counterbalanced across rats) was paired with noncontingent delivery of 45-mg chocolate-flavored,

grain-based pellets (Bio-Serv, Flemington, NJ). During each 2-minute presentation of the conditional stimulus (CS^+), pellets were presented on a random-interval 30-second schedule. The CS^+ was presented 63/session with a random 2- to 4-minute intertrial interval (mean 3 minutes). The lever was never present during these sessions.

All rats then received 8 days of instrumental conditioning in which lever pressing earned delivery of a single chocolate pellet. Each session lasted until 20 outcomes had been earned or 30 minutes had elapsed. Rats received 1 day each of continuous, random-interval 15-second and random-interval 30-second schedules of reinforcement, followed by 5 days on the final random-interval 60-second schedule. The CS^+ was never present during this training.

Rats received one session of habituation to the neutral control stimulus ($CS^{\varnothing}$), which consisted of six 2-minute presentations of the $CS^{\varnothing}$ (opposite stimulus as the CS^+), with a 2- to 4-minute intertrial interval. No rewards were delivered during this session.

On the day before each PIT test, rats were given a single 30-minute instrumental extinction session in which no cues were present and the lever was available, but presses were unrewarded. During each PIT test, the lever was continuously available, but pressing was not reinforced. Responding was extinguished for 5 minutes to establish a low rate of baseline performance, after which each CS was presented 4 times in pseudorandom order, also without accompanying reward. Each CS lasted 2 minutes with a 4-minute fixed intertrial interval. Rats received one Pavlovian and two instrumental retraining sessions identical to the above sessions in between subsequent PIT tests. In all cases, testing began at least 4 weeks after viral infusion to allow construct expression.

Chemogenetic Inactivation of NAc Cholinergic Interneurons. Before training, ChAT::Cre1 rats were bilaterally infused with a Cre-inducible AAV vector to express the inhibitory designer receptor human M4 muscarinic receptor [hM4D(Gi)] or control fluorophore mCherry selectively in

cholinergic interneurons of the NAc. Following training, rats received PIT tests, counterbalanced for order, one following vehicle and one following intraperitoneal injection of the hM4D(Gi) ligand clozapine-N-oxide (CNO) (5 mg/kg) (see Supplemental Methods). These experiments were run in two separate cohorts, and data were collapsed across cohorts following analyses indicating no interaction between cohort and any of the variables of primary interest [hM4D(Gi): highest $F_{1,17}$ = 3.23, p = .09; mCherry: highest $F_{1,14}$ = 3.88, p = .07]. Final hM4D(Gi) cohort was n = 19 (8 female; 2 rats were excluded owing to off-target viral spread) and mCherry cohort was n = 16 (8 female). Following PIT testing, a subset of subjects was tested for the influence of NAc cholinergic interneuron inactivation on food consumption and lever pressing on a progressive-ratio response requirement (see Supplemental Methods).

Optical Stimulation of NAc Cholinergic Interneurons. Before training, ChAT::Cre$^+$ rats were bilaterally infused with a Cre-inducible AAV vector to express the excitatory opsin channelrhodopsin-2 (ChR2) or control fluorophore enhanced yellow fluorescent protein (eYFP) selectively in NAc cholinergic interneurons. Optical fibers were implanted bilaterally in the NAc. From the last 2 days of instrumental training and for a single additional Pavlovian retraining session, rats were tethered to the patch cord, but no light was delivered to allow habituation to the optical tether. Following training, rats received four PIT tests, counterbalanced for order, with intervening retraining. During each test, optical fibers were connected via ceramic sleeves to patch cords attached to a commutator. Blue light (473 nm, 10 Hz, 10 mW, 5-ms pulse width, 120-second duration) (see also Supplemental Methods) was delivered for optical activation of ChR2-expressing NAc cholinergic interneurons. For the main experimental condition, light was delivered concurrent with each of the four CS$^+$ presentations, with light and CS$^+$ onset and offset synced. There were three separate control conditions: light delivered concurrent with each CS$^\varnothing$ presentation, light delivered during the CS-free 2-minute baseline periods immediately before

each CS^+ presentation, or light delivered during the CS-free 2-minute baseline periods immediately before each $CS^{\varnothing}$ presentation. There were no significant differences in performance between the pre-CS^+ and pre-$CS^{\varnothing}$ stimulation tests, and thus data were collapsed across these tests into a single baseline stimulation control condition (see Supplemental Figure S4). Final ChR2 cohort was n = 9 (5 female; 5 subjects excluded for lack of expression and/or optical fiber misplacement), and final eYFP cohort was n = 8 (5 female).

Optical Stimulation of NAc Cholinergic Interneurons and Inactivation of NAc β_2-Containing Nicotinic Acetylcholine Receptors. Before training, ChAT::Cre^+ rats were bilaterally infused with a Cre-inducible AAV vector to express ChR2 selectively in NAc cholinergic interneurons. Microinfusion injector/optical fiber guide cannulas were implanted bilaterally above the NAc. Following training, rats received 4 PIT tests, counterbalanced for order with intervening retraining. Before each test, rats were bilaterally infused with either the selective $\alpha_4\beta_2$-containing nicotinic receptor competitive antagonist dihydro-b-erythroidine (DhβE) (15 mg/0.5 mL/side) (see Supplemental Methods) or artificial cerebrospinal fluid vehicle via an injector inserted through the guide cannula designed to protrude 2.5 mm to just above the NAc (26.5 mm). Following infusion, injectors were removed, and optical fibers, also designed to protrude 2.5 mm and thus target the NAc, were placed through guide cannulas and secured via ceramic sleeves. During two of the tests, one each following vehicle or DhβE, blue light (473 nm, 10 Hz, 10 mW, 5-ms pulse width, 120- second duration) was delivered for optical activation of ChR2- expressing NAc cholinergic interneurons concurrent with each CS^+ presentation. During the other two tests, an optical fiber was attached, but no light was delivered. Thus, each rat received four tests: vehicle/no stimulation, vehicle/stimulation during CS^+, DhβE /no stimulation, DhβE /stimulation during CS^+. Following the PIT tests, optical fibers were removed, and dummies were placed in the guide cannulas. Final cohort was n = 11 (all male, 1 rat was excluded owing to a clogged cannula).

4.2.4 Data Analysis

Behavioral Analysis. Lever pressing and entries into the food-delivery port were the primary behavioral output measures for the PIT test. These measures were counted for each 2-minute CS period, with behavioral output during the 2-minute periods before each CS serving as the baseline. For both the chemogenetic inhibition and the optical stimulation experiments, there was no interaction between trial and any of the other variables on lever pressing during the test (highest $F_{6,108} = 1.84$, $p = .13$). Thus, in all cases, data were collapsed across trials.

Sex Differences. Approximately half the subjects in the chemogenetic and optical manipulation experiments were female. In neither experiment was there a main effect of sex [hM4D(Gi): $F_{1,7} = 2.72$, $p = .12$; ChR2: $F_{1,7} = 0.71$, $p = .43$], and sex did not significantly interact with the effect of CS and/or drug or stimulation period on lever pressing (highest $F_{1,17} = 3.41$, $p = .08$). Thus, all data were collapsed across sexes. Because sex did not influence results of the initial optogenetic experiment, the follow-up experiment assessing the influence of intra-NAc DhβE on the behavioral effect of optical stimulation included only male subjects.

Statistical Analysis. Data were processed with Microsoft Excel (Microsoft Corp., Redmond, WA). Statistical analyses were conducted with GraphPad Prism, version 7 (GraphPad Software, San Diego, CA) and SPSS (IBM Corp., Armonk, NY) software. Data were analyzed with Student's t tests, one-way, two-way, and three-way repeated-measures analysis of variance (Geisser-Greenhouse correction). Corrected post hoc comparisons were used to clarify main effects and interactions. All datasets met equal covariance assumptions, justifying analysis of variance interpretation[63]. α levels were set at $p < .05$.

4.2.5 Approach Validation

Optical stimulation and chemogenetic inhibition of NAc cholinergic interneurons was validated in *vivo* with electroenzymatic choline biosensors and constant-potential amperometry

as detailed in Supplemental Methods. Briefly, to confirm chemogenetic inhibition of NAc cholinergic interneurons, silicon wafer–based platinum microelectrode array choline biosensors packaged with an optical fiber affixed to the back surface of the probe (to reduce the photovoltaic artifact) were lowered into the NAc of anesthetized rats expressing ChR2 and hM4D(Gi) in cholinergic interneurons. The ability of blue light (473 nm, 20 Hz, 5–30 mW, 10-ms pulse width, 5-second duration) to evoke acetylcholine release continuously monitored by the sensor was assessed following injection of vehicle or CNO (5 mg/kg, intraperitoneal). Final recording locations were n = 4 in 2 subjects. To confirm stimulation of NAc cholinergic interneurons with the exact light parameters used in the behavioral experiments, choline biosensors/optical fibers were lowered into the NAc of anesthetized rats expressing ChR2 or eYFP in cholinergic interneurons. Choline fluctuations were monitored, and blue light (473 nm, 10 Hz, 10 mW, 5-ms pulse width, 120-second duration) was delivered to evaluate its ability to evoke acetylcholine release in ChR2-expressing subjects. Final ChR2 recording locations were n = 5 in 4 subjects, and final eYFP recording locations were n = 5 in 3 subjects.

4.3 Results

4.3.1 Chemogenetic Inhibition of NAc Cholinergic Interneurons Augments Cue-Motivated Behavior

To evaluate the contribution of NAc cholinergic interneurons to cue-motivated behavior, we first chemogenetically inactivated these cells during a PIT test. Inactivation was achieved by using ChAT::Cre1 rats and a Cre-inducible AAV vector to express the inhibitory designer receptor hM4D(Gi) selectively in cholinergic interneurons of the NAc (Figure 1A–C). In separate subjects expressing both hM4D(Gi) and ChR2 in cholinergic interneurons, CNO (5 mg/kg, intraperitoneal) activation of hM4D(Gi) in cholinergic interneurons was found to effectively attenuate optically evoked NAc acetylcholine release in vivo (Figure 1D).

Rats received Pavlovian training to pair a 2-minute auditory stimulus (CS^+) with a food pellet reward (Figure 1E). An alternative 2-minute auditory stimulus was presented unpaired with reward and served as a control ($CS^\varnothing$). Rats were then instrumentally conditioned, in the absence of the stimuli, to lever press to earn food rewards (see Supplemental Table S1 for training data). At the PIT test, the lever was available and each CS was presented in pseudorandom order to assess the motivating influence of the CS^+ over lever-pressing activity. No rewards were delivered during this test. Increased lever-press rate during the CS^+ provided the measure of cue-motivated behavior (i.e., expression of PIT). Each rat was tested twice, once following injection of vehicle and once following CNO, counterbalanced for order (Figure 1E).

Inactivation of NAc cholinergic interneurons augmented the expression of PIT (CS period: $F_{2,36} = 8.15$, $p = .001$; drug: $F_{1,18} = 0.78$, $p = .39$; CS x drug: $F_{2,36} = 5.2$, $p = .01$) (Figure 1F). Demonstrating PIT, the CS^+ elevated lever pressing relative to both the baseline and the $CS^\varnothing$ periods under vehicle control conditions ($p < .05$). Inactivation of NAc cholinergic interneurons enhanced the invigorating influence of the CS^+ relative to the vehicle control condition ($p < .01$). NAc cholinergic interneuron inactivation predominantly influenced CS^+- invigorated responding; neither baseline nor $CS^\varnothing$ lever-press rate was significantly altered in the CNO condition ($p > .05$). There was no effect of CNO on the expression of PIT in subjects lacking the hM4D(Gi) transgene (CS period: $F_{2,30} = 4.47$, $p = .02$; drug: $F_{1,15} = 0.31$, $p = .58$; CS x drug: $F_{2,30} = 0.45$, $p = .64$) (Figure 1G). Inactivation of NAc cholinergic interneurons did not alter the expression of Pavlovian conditional food-port approach responses during the PIT test. It also did not alter lever pressing during a progressive ratio test or basic food consumption (Supplemental Figure S2). Thus, inactivation of NAc cholinergic interneurons selectively enhanced the motivating influence of a reward-predictive cue over instrumental behavior.

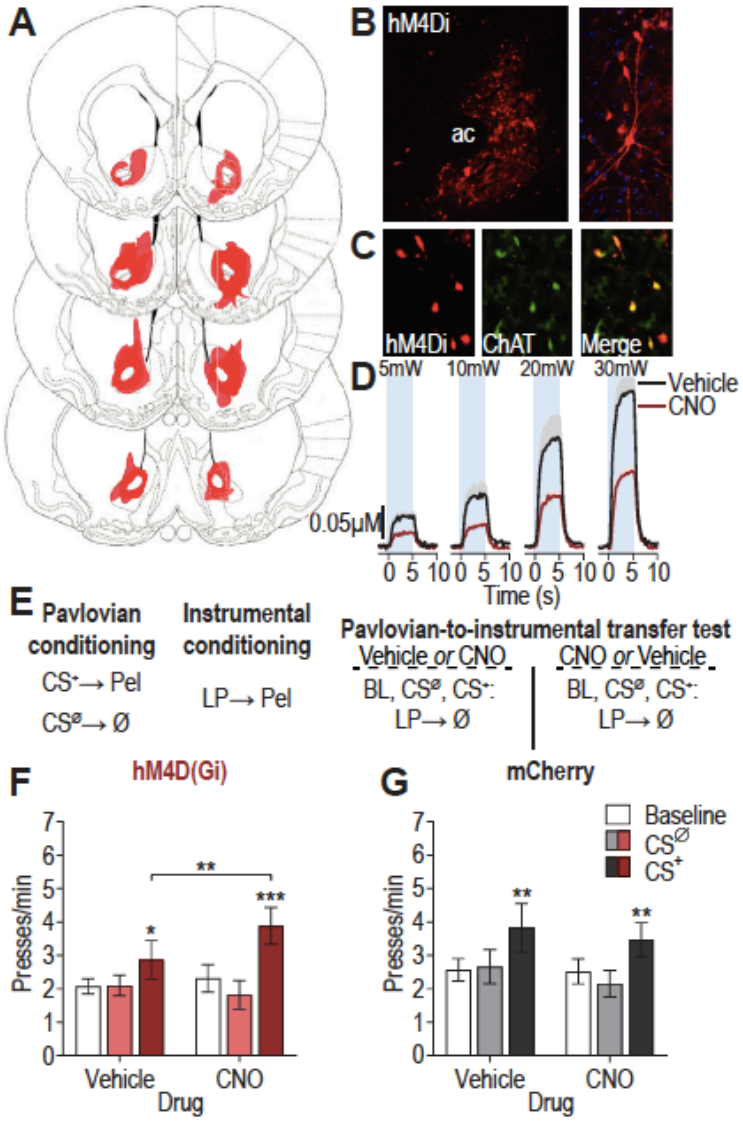

Figure 4.1. Chemogenetic inhibition of nucleus accumbens (NAc) cholinergic interneurons augments cue-motivated behavior. (A) Schematic representation of human M4 muscarinic receptor [hM4D(Gi)]–mCherry expression in the NAc for all subjects. Slides represent 0.7–1.7 mm anterior to bregma. (B) Representative immunofluorescent images of hM4D(Gi)- mCherry expressing cholinergic interneurons in the NAc. (C) Colocalization of choline acetyltransferase (ChAT) staining and hM4D(Gi)-mCherry expression in the NAc. (D) CNO:hM4D(Gi) attenuation of optically evoked (473 nm, 20 Hz, 5–30 mW, 10-ms pulse width, 5-second duration) acetylcholine release in the NAc in vivo [see Supplemental Figure S1 for histology demonstrating hM4D(Gi) and channelrhodopsin-2 expression in cholinergic interneurons; *n* = 4]. Mean 61 SEM. (E) Procedure schematic. (F, G) Lever press rate during each 2-minute period of the Pavlovian-to-instrumental transfer test, averaged across trials compared between the conditional stimulus (CS)–free (baseline) (BL),

neutral control stimulus ($CS^{Ø}$), and reward-predictive cue (CS^{+}) periods for the vehicle-treated and CNO-treated conditions in hM4D(Gi) (*n* = 19) (F) or mCherry control (*n* = 16) (G) subjects. Mean ± 1 SEM. *p < .05, **p < .01, ***p < .001. ac, anterior commissure; CNO, clozapine N-oxide; LP, lever press; Ø, no reward; Pel, pellet reward; Veh, vehicle. [Images in panel (A) reproduced with permission from Paxinos and Watson (100).]

4.3.2 Optical Stimulation of NAc Cholinergic Interneurons Concurrent With Reward Cue Presentation Blunts Cue-Motivated Behavior

The chemogenetic inactivation results suggest that NAc cholinergic interneurons function to oppose cue-motivated behavior. To further test this, we next evaluated the influence of activation of NAc cholinergic interneurons on expression of PIT. We used optical stimulation to provide temporal specificity. The excitatory opsin ChR2 was selectively expressed in NAc cholinergic interneurons (Figure 2A–C) of ChAT::Cre1 rats. Optical stimulation (473 nm, 10 Hz, 10 mW, 2 minutes) of these cells at a frequency in the upper range of their normal firing rate [64,65] was found to increase acetylcholine release in vivo. This increase was restricted to the light-on period ($F_{2,8}$ = 15.15, p = .01) and did not occur in subjects lacking the ChR2 transgene (Figure 2D). Following Pavlovian and instrumental training, during the PIT test, we used a within-subject design to stimulate NAc cholinergic interneurons concurrent with either each 2-minute CS^{+} presentation or, in separate control tests, each $CS^{Ø}$ presentation or an equivalent number and duration of CS-free baseline periods (Figure 2E).

Optical stimulation of NAc cholinergic interneurons during CS^{+} presentation blunted the expression of PIT (CS period: $F_{2,16}$ = 8.07, p = .004; stimulation period: $F_{2,16}$ = 0.71, p = .50; CS X stimulation period: $F_{4,32}$ = 3.79, p = .01) (Figure 2F). Neither baseline nor $CS^{Ø}$ period stimulation altered lever pressing during those periods ($p > .05$) or the significant enhancement in such pressing induced by the CS^{+} ($p < .001$). However, stimulation of NAc cholinergic interneurons concurrent with CS^{+} presentation prevented that cue from increasing lever pressing ($p > .05$).

Light delivery had no effect on the expression of PIT in subjects lacking the ChR2 transgene (CS period: $F_{2,14} = 8.66$, $p = .004$; stimulation period: $F_{2,14} = 0.27$, $p = .77$; CS X stimulation period: $F_{4,28} = 1.04$, $p = .41$) (Figure 2G). Optical stimulation of NAc cholinergic interneurons did not prevent the CS^+ from eliciting Pavlovian conditional food-port approach responses (Supplemental Figure S5), suggesting no deficit in CS^+ recognition. Thus, optical stimulation of NAc cholinergic interneurons blunted the expression of cue-motivated behavior.

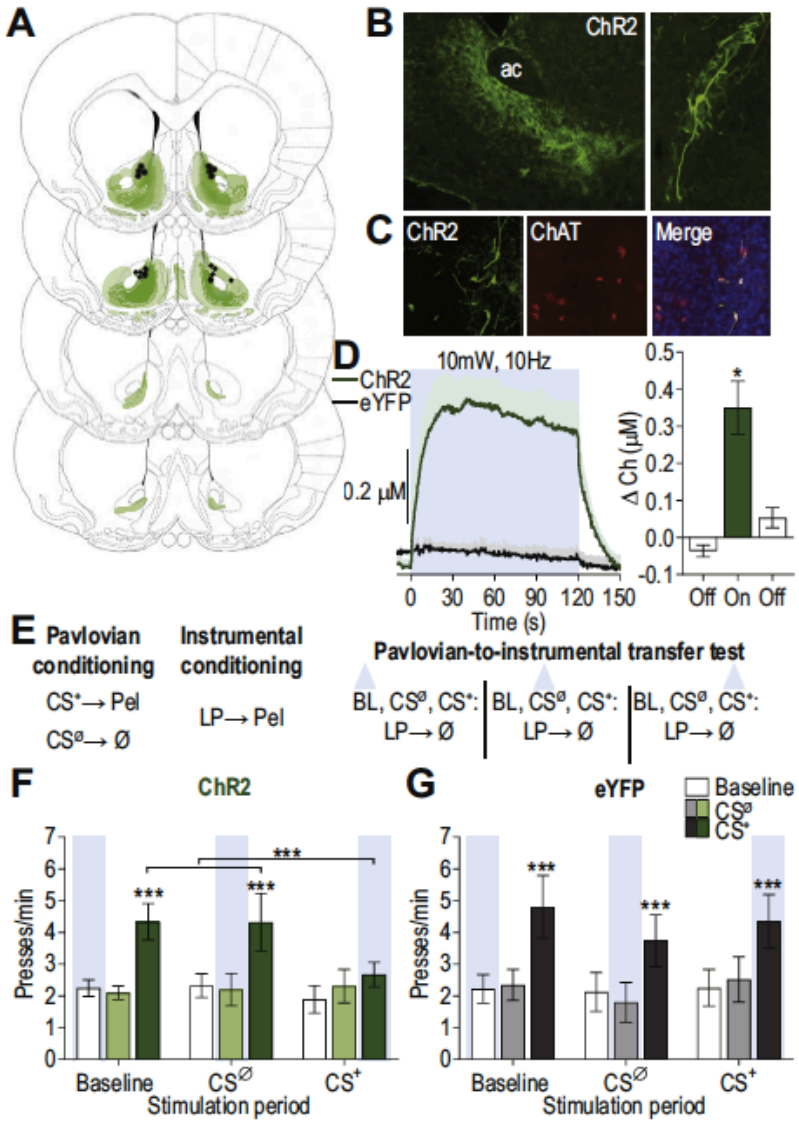

Figure 4.2. Optical stimulation of nucleus accumbens (NAc) cholinergic interneurons concurrent with reward-predictive cue blunts cue-motivated behavior. (A) Schematic representation of channelrhodopsin-2 (ChR2)– enhanced yellow fluorescent protein (eYFP) expression and fiber tips in the NAc for all subjects. Slides represent 0.7–1.7 mm anterior to bregma. (B) Representative immunofluorescent images of ChR2-eYFP–expressing cholinergic interneurons in the NAc. (C) Colocalization of choline acetyltransferase (ChAT) staining and ChR2-eYFP expression in the NAc. (D) Optically evoked acetylcholine release in *vivo* by blue light delivery (473 nm, 10 Hz, 10 mW, 5-ms pulse width, 120-second duration) to ChR2-expressing cholinergic interneurons in the NAc (see Supplemental Figure S3 for histology; *n* = 5/group). Mean ± 1 SEM. (E) Procedure schematic. The blue triangle indicates light delivery. (F, G) Lever press rate during each 2-minute period of the Pavlovian-to-instrumental transfer test, averaged across trials compared between the conditional stimulus (CS)–free (baseline) (BL), neutral control stimulus (CSØ), and reward-predictive cue (CS1) periods for tests in which optical stimulation occurred during the baseline stimulation, CSØ, and CS1 periods in ChR2 (*n* = 9) (F) or eYFP control (*n* = 8) (G) subjects. Mean ± 1 SEM. ***$p < .001$. ac, anterior commissure; LP, lever press; Ø, no reward; Pel, pellet reward.

4.3.3 Acetylcholine Release From NAc Cholinergic Interneurons Works via b2-Containing Nicotinic Receptors to Blunt Cue-Motivated Behavior

These data suggest that cholinergic interneuron activity tempers the motivating influence of reward-predictive cues over reward-seeking actions. Acetylcholine receptors are broadly distributed in the NAc and consist of two major subtypes: metabotropic muscarinic acetylcholine receptors and ionotropic nicotinic acetylcholine receptors (nAChRs). We previously found that activity of the NAc nAChRs, in particular, works to restrain the expression of cue-motivated behavior[58]. Moreover, nAChRs containing the β_2 subunit have been shown to be located exclusively on dopamine axons and terminals[66], where they regulate phasic dopamine release[67–72], which has itself, in the NAc, been shown to track and mediate cue-motivated behavior[9,59,60,73–76]. Thus, we next asked whether the attenuating effect of optical stimulation of NAc cholinergic interneurons over cue-motivated behavior is mediated via these β_2-containing nAChRs. To achieve this, we again selectively expressed ChR2 in NAc cholinergic interneurons (Figure 3A–

C) and evaluated the influence of intra-NAc infusion of DhβE (15 mg/side), a selective $\alpha_4\beta_2$-containing nAChR antagonist, on the suppressive influence of NAc cholinergic interneuron stimulation over PIT expression (Figure 3D).

Blockade of β_2-containing nAChRs recovered the impairment of PIT induced by optical stimulation of NAc cholinergic interneurons during the CS^+ (CS period: $F_{2,22} = 22.69$, $p < .0001$; optical stimulation: $F_{1,11} = 0.08$, $p = .78$; drug: $F_{1,11} = 0.003$, $p = .96$; CS X stimulation: $F_{2,22} = 5.19$, $p = .02$; CS X drug X stimulation: $F_{2,22} = 5.10$, $p = .02$) (Figure 3E). We replicated the suppressive effect of optical stimulation of NAc cholinergic interneurons during CS^+ presentation on the expression of PIT relative to a nonstimulated control condition ($p > .001$). Whereas intra-NAc infusion of DhβE alone at this dose did not influence PIT expression relative to the vehicle infused control condition ($p > .05$), it did alleviate the suppressive effect of cholinergic interneuron stimulation ($p < .01$), allowing subjects to show a significant PIT effect ($p < .001$). These data demonstrate that acetylcholine release from NAc cholinergic interneurons acts via β_2-containing nAChRs to blunt the motivating influence of cues. Secondarily, the data indicate that the effect of optical stimulation of cholinergic interneurons was not due to nAChR desensitization.

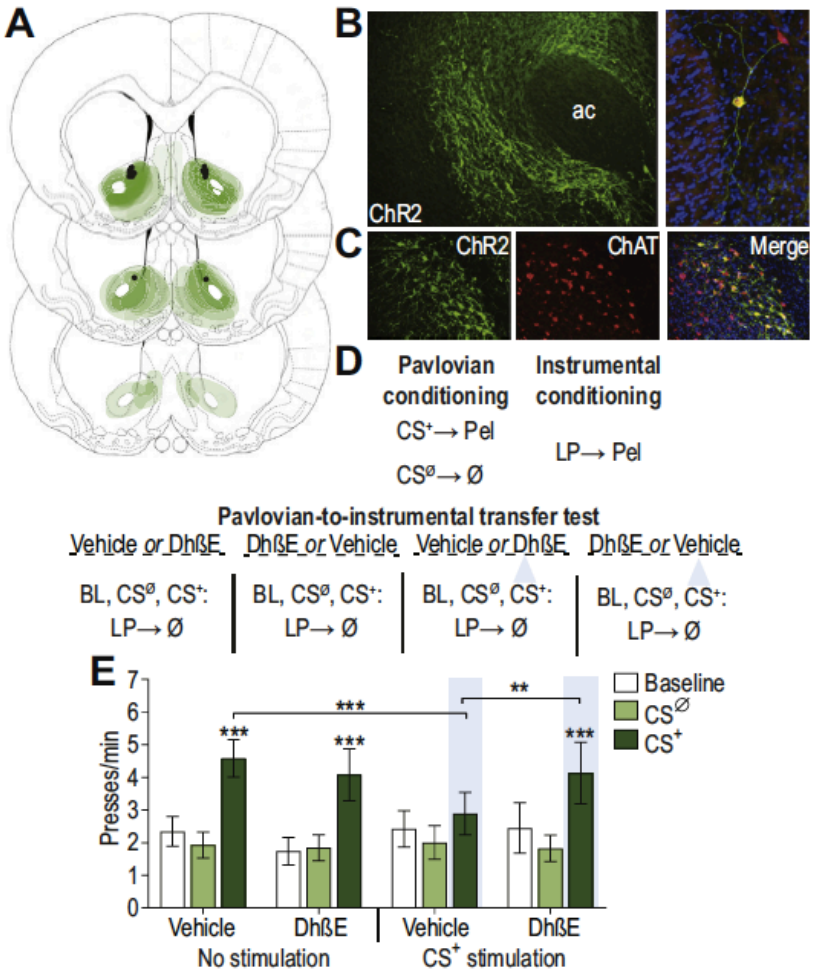

Figure 4.3. Acetylcholine release from nucleus accumbens (NAc) cholinergic interneurons works via β_2-containing nicotinic receptors to blunt cuemotivated behavior. (A) Schematic representation of channelrhodopsin-2 (ChR2)–enhanced yellow fluorescent protein expression and fiber/injector tips in the NAc for all subjects. Slides represent 0.7–1.7 mm anterior to bregma. (B) Representative immunofluorescent images of ChR2–enhanced yellow fluorescent protein–expressing cholinergic interneurons in the NAc. (C) Colocalization of choline acetyltransferase (ChAT) staining and ChR2– enhanced yellow fluorescent protein expression in the NAc. (D) Procedure schematic. The blue triangle indicates light delivery. (E) Lever press rate during each 2-minute period of the Pavlovian-to-instrumental transfer test, averaged across trials compared between the conditional stimulus (CS)–free (baseline) (BL), neutral control stimulus ($CS^{Ø}$), and reward-predictive cue (CS^{+}) periods for the tests with either intra-NAc vehicle or DhβE with or without optical stimulation during CS^{+} (n = 11). Mean ± 1 SEM. **p < .01, ***p < .001. ac, anterior commissure; DhβE, dihydro-b-erythroidine; LP, lever press; Ø, no reward; Pel, pellet reward.

4.4 Discussion

Using a combination of chemogenetic, optogenetic, and pharmacological approaches, we investigated the function of NAc cholinergic interneurons in cue-motivated behavior. The data revealed that cholinergic interneuron activity in the NAc functions to limit the motivational influence of reward-predictive cues over reward-seeking actions. Chemogenetic inactivation of NAc cholinergic interneurons augmented cue-motivated behavior, whereas optical stimulation of these cells temporally restricted to cue presentation prevented cues from motivating action. This mitigating function is achieved via acetylcholine activation of β_2-containing nAChRs.

These data accord well with evidence of the activity patterns of striatal cholinergic interneurons collected in nonhuman primates and rodents. Striatal cholinergic interneurons both tonically and phasically increase their activity when vigorous motivated behavior is discouraged, for example, in states of satiety[33,34], or when cues signal unfavorable (e.g., high effort, low reward) conditions[37]. Cholinergic interneurons also transiently increase their activity when cues signal that reward is available contingent on a no-go response[38], i.e., when motivated movement must be withheld. Striatal cholinergic interneurons transiently pause their activity in response to cues signaling that vigorous reward seeking is advantageous. For example, cholinergic interneurons will pause in response to reward-predictive cues[29,37,39–46] and when cues signal favorable low-effort/high-reward conditions[37]. The current data provide an important causal addition to this literature and reveal that increases in NAc cholinergic interneuron activity function to oppose cue-motivated behavior and that decreases or pauses in such activity are permissive to cue-motivated action. These results also indicate that the NAc inputs that regulate cholinergic interneuron excitability, activity, or synchrony, such as thalamostriatal projections[69], are well positioned to influence cue-motivated behavior. Indeed, recent evidence from the dorsal striatum indicates that

stimulation of rostral intralaminar thalamic inputs can regulate motivated behavior by triggering a rapid burst and then pause in cholinergic interneuron activity[77].

We found the suppressive effect of optical stimulation over cue-motivated behavior to depend on the activity of β_2-containing nAChRs. Acetylcholine release from NAc cholinergic interneurons acts at β_2-containing nAChRs to curtail the motivating influence of appetitive cues. This is consistent with our previous evidence that general nAChR, but not muscarinic acetylcholine receptor, blockade augments cue-motivated behavior[58]. Moreover, that inactivation of β_2-containing nAChRs completely recovered the suppressive influence of optical stimulation of NAc cholinergic interneurons over cue-motivated behavior suggests that, although other acetylcholine receptor subtypes may contribute, β_2-containing nAChRs are a critical locus of action for cholinergic regulation of cue-motivated behavior.

NAc core dopamine release is a major substrate of cue-motivated behavior. Its activity correlates with[58,60,74,78] and is necessary[59,76,79] and sufficient[75,80,81] for the motivational influence of reward-predictive cues. β_2-containing nAChRs are located exclusively on NAc dopamine axons and terminals[66], where they have been found to modulate dopamine release[67–72]. The present data may be considered surprising in light of evidence that optical stimulation of striatal cholinergic interneurons can evoke dopamine release from terminals via action at β_2-containing nAChRs[69,70]. However, a growing body of literature indicates that cholinergic regulation of dopamine release depends on the activity state of the dopamine cells[82,83]. β_2-containing nAChR activity facilitates low probability[32,67,84] and tonic dopamine release[85] but will actually suppress dopamine release that results from high-frequency stimulation, which mimics dopamine neuron burst firing[32,67,84]. Indeed, inactivation of β_2-containing nAChRs in the NAc will augment dopamine release induced by high-frequency stimulation ex *vivo* [68,71], and general nAChR inactivation in the NAc will potentiate the phasic dopamine release response to reward-predictive cues in awake-behaving

animals[58]. Thus, we speculate that NAc cholinergic interneuron activity may restrain the motivating influence of reward-predictive cues via attenuating their ability to elicit dopamine release, with pausing in their signaling being permissive to such release and associated motivation.

The suppressive function of NAc cholinergic interneurons over cue-motivated behavior is interesting in light of how these cells are regulated. NAc cholinergic interneurons are controlled by several factors that mediate food-related motivation and responsivity to food cues. For example, they express receptors for the adiposity and satiety signal insulin, activation of which increases their activity and modulates NAc dopamine signaling through an nAChR-dependent mechanism[86]. They also express receptors for corticotropin-releasing factor, which mediates the positive and negative effects of stress[87–90]. NAc corticotropin-releasing factor receptor activation increases cholinergic interneuron activity[91] and acetylcholine release[92] and regulates dopamine release[91]. Moreover, serotonin, a neuromodulator long linked to motivation and mood and recently in the NAc linked to adaptive social behavior[93], attenuates the excitability of NAc cholinergic interneurons via presynaptic 5-hydroxytryptamine 1A and postsynaptic 5-hydroxytryptamine 1B receptors[94]. Thus, NAc cholinergic interneurons are well positioned to mitigate cue-motivated behavior when vigorous motivated action would not be beneficial and to promote cue-motivated behavior when it is adaptive. Dysfunction in this mechanism could therefore lead to the dysregulated motivation underlying some mental illnesses. Indeed, cues can become unnaturally strong motivators of drug-seeking behavior in addiction[4,8,95,96], and NAc cholinergic interneurons have been linked to addiction-like behaviors[97,98]. Depression can be characterized by avolitional symptoms[95,99], and NAc cholinergic interneurons have been linked to depression-like behavior[35]. Therefore, these results have implications for the understanding and treatment of these and other diseases marked by maladaptive motivation.

4.5 References

1. Corbit LH, Balleine BW (2016): Learning and motivational processes contributing to Pavlovian-instrumental transfer and their neural bases: Dopamine and beyond. Curr Top Behav Neurosci 27:259–289.
2. Cartoni E, Balleine B, Baldassarre G (2016): Appetitive Pavlovianinstrumental transfer: A review. Neurosci Biobehav Rev 71:829–848.
3. Johnson AW (2013): Eating beyond metabolic need: How environmental cues influence feeding behavior. Trends Neurosci 36:101–109.
4. Garbusow M, Schad DJ, Sebold M, Friedel E, Bernhardt N, Koch SP, et al. (2016): Pavlovian-to-instrumental transfer effects in the nucleus accumbens relate to relapse in alcohol dependence. Addict Biol 21:719–731.
5. Garbusow M, Schad DJ, Sommer C, Jünger E, Sebold M, Friedel E, et al. (2014): Pavlovian-to-instrumental transfer in alcohol dependence: A pilot study. Neuropsychobiology 70:111–121.
6. Corbit LH, Janak PH (2016): Changes in the influence of alcoholpaired stimuli on alcohol seeking across extended training. Front Psychiatry 7:169.
7. Corbit LH, Janak PH (2007): Ethanol-associated cues produce general pavlovian-instrumental transfer. Alcohol Clin Exp Res 31:766–774.
8. Robinson MJ, Robinson TE, Berridge KC (2013): Incentive salience and the transition to addiction. In: Miller PM, editor. Biological Research on Addiction, vol. 2. San Diego: Academic Press, 391–399.
9. Ostlund SB, LeBlanc KH, Kosheleff AR, Wassum KM, Maidment NT (2014): Phasic mesolimbic dopamine signaling encodes the facilitation of incentive motivation produced by repeated cocaine exposure. Neuropsychopharmacology 39:2441–2449.

10. LeBlanc KH, Ostlund SB, Maidment NT (2012): Pavlovian-to-instrumental transfer in cocaine seeking rats. Behav Neurosci 126:681–689.
11. Hogarth L, Maynard OM, Munafò MR (2014): Plain cigarette packs do not exert Pavlovian to instrumental transfer of control over tobaccoseeking. Addiction 110:174–182.
12. Leblanc KH, Maidment NT, Ostlund SB (2013): Repeated cocaine exposure facilitates the expression of incentive motivation and induces habitual control in rats. PLoS One 8:e61355.
13. Quail SL, Morris RW, Balleine BW (2017): Stress associated changes in Pavlovian-instrumental transfer in humans. Q J Exp Psychol (Hove) 70:675–685.
14. Morgado P, Silva M, Sousa N, Cerqueira JJ (2012): Stress transiently affects Pavlovian-to-instrumental transfer. Front Neurosci 6:93.
15. Pielock SM, Sommer S, Hauber W (2013): Post-training glucocorticoid receptor activation during Pavlovian conditioning reduces Pavlovian-instrumental transfer in rats. Pharmacol Biochem Behav 104:125–131.
16. Huys QJ, Gölzer M, Friedel E, Heinz A, Cools R, Dayan P, et al. (2016): The specificity of Pavlovian regulation is associated with recovery from depression. Psychol Med 46:1027–1035.
17. Talmi D, Seymour B, Dayan P, Dolan RJ (2008): Human pavlovianinstrumental transfer. J Neurosci 28:360–368.
18. Corbit LH, Balleine BW (2011): The general and outcome-specific forms of Pavlovian-instrumental transfer are differentially mediated by the nucleus accumbens core and shell. J Neurosci 31:11786–11794.
19. Corbit LH, Muir JL, Balleine BW (2001): The role of the nucleus accumbens in instrumental conditioning: Evidence of a functional dissociation between accumbens core and shell. J Neurosci 21:3251–3260.

20. Scarr E, Gibbons AS, Neo J, Udawela M, Dean B (2013): Cholinergic connectivity: Its implications for psychiatric disorders. Front Cell Neurosci 7:55.
21. Dulawa SC, Janowsky DS (2018): Cholinergic regulation of mood: From basic and clinical studies to emerging therapeutics [published online ahead of print Aug 17]. Mol Psychiatry.
22. Dautan D, Huerta-Ocampo I, Witten IB, Deisseroth K, Bolam JP, Gerdjikov T, et al. (2014): A major external source of cholinergic innervation of the striatum and nucleus accumbens originates in the brainstem. J Neurosci 34:4509–4518.
23. Zhou FM, Wilson CJ, Dani JA (2002): Cholinergic interneuron characteristics and nicotinic properties in the striatum. J Neurobiol 53:590–605.
24. Rymar VV, Sasseville R, Luk KC, Sadikot AF (2004): Neurogenesis and stereological morphometry of calretinin-immunoreactive GABAergic interneurons of the neostriatum. J Comp Neurol 469:325–339.
25. Descarries L, Gisiger V, Steriade M (1997): Diffuse transmission by acetylcholine in the CNS. Prog Neurobiol 53:603–625.
26. Descarries L, Mechawar N (2000): Ultrastructural evidence for diffuse transmission by monoamine and acetylcholine neurons of the central nervous system. Prog Brain Res 125:27–47.
27. Wilson CJ, Chang HT, Kitai ST (1990): Firing patterns and synaptic potentials of identified giant aspiny interneurons in the rat neostriatum. J Neurosci 10:508–519.
28. Inokawa H, Yamada H, Matsumoto N, Muranishi M, Kimura M (2010): Juxtacellular labeling of tonically active neurons and phasically active neurons in the rat striatum. Neuroscience 168:395–404.

29. Aosaki T, Tsubokawa H, Ishida A, Watanabe K, Graybiel AM, Kimura M (1994): Responses of tonically active neurons in the primate's striatum undergo systematic changes during behavioral sensorimotor conditioning. J Neurosci 14:3969–3984.
30. Cachope R, Cheer JF (2014): Local control of striatal dopamine release. Front Behav Neurosci 8:188.
31. Cragg SJ (2006): Meaningful silences: How dopamine listens to the ACh pause. Trends Neurosci 29:125–131.
32. Sulzer D, Cragg SJ, Rice ME (2016): Striatal dopamine neurotransmission: Regulation of release and uptake. Basal Ganglia 6:123–148.
33. Mark GP, Rada P, Pothos E, Hoebel BG (1992): Effects of feeding and drinking on acetylcholine release in the nucleus accumbens, striatum, and hippocampus of freely behaving rats. J Neurochem 58:2269–2274.
34. Helm KA, Rada P, Hoebel BG (2003): Cholecystokinin combined with serotonin in the hypothalamus limits accumbens dopamine release while increasing acetylcholine: A possible satiation mechanism. Brain Res 963:290–297.
35. Warner-Schmidt JL, Schmidt EF, Marshall JJ, Rubin AJ, Arango- Lievano M, Kaplitt MG, et al. (2012): Cholinergic interneurons in the nucleus accumbens regulate depression-like behavior. Proc Natl Acad Sci U S A 109:11360–11365.
36. Hoebel BG, Avena NM, Rada P (2007): Accumbens dopamineacetylcholine balance in approach and avoidance. Curr Opin Pharmacol 7:617–627.
37. Nougaret S, Ravel S (2015): Modulation of tonically active neurons of the monkey striatum by events carrying different force and reward information. J Neurosci 35:15214–15226.
38. Lee IH, Seitz AR, Assad JA (2006): Activity of tonically active neurons in the monkey putamen during initiation and withholding of movement. J Neurophysiol 95:2391–2403.

39. Ravel S, Legallet E, Apicella P (2003): Responses of tonically active neurons in the monkey striatum discriminate between motivationally opposing stimuli. J Neurosci 23:8489–8497.
40. Morris G, Arkadir D, Nevet A, Vaadia E, Bergman H (2004): Coincident but distinct messages of midbrain dopamine and striatal tonically active neurons. Neuron 43:133–143.
41. Joshua M, Adler A, Mitelman R, Vaadia E, Bergman H (2008): Midbrain dopaminergic neurons and striatal cholinergic interneurons encode the difference between reward and aversive events at different epochs of probabilistic classical conditioning trials. J Neurosci 28:11673–11684.
42. Apicella P, Scarnati E, Schultz W (1991): Tonically discharging neurons of monkey striatum respond to preparatory and rewarding stimuli. Exp Brain Res 84:672–675.
43. Shimo Y, Hikosaka O (2001): Role of tonically active neurons in primate caudate in reward-oriented saccadic eye movement. J Neurosci 21:7804–7814.
44. Kimura M, Rajkowski J, Evarts E (1984): Tonically discharging putamen neurons exhibit set-dependent responses. Proc Natl Acad Sci U S A 81:4998–5001.
45. Apicella P (2007): Leading tonically active neurons of the striatum from reward detection to context recognition. Trends Neurosci 30:299–306.
46. Aosaki T, Kimura M, Graybiel AM (1995): Temporal and spatial characteristics of tonically active neurons of the primate's striatum. J Neurophysiol 73:1234–1252.
47. Bray S, Rangel A, Shimojo S, Balleine B, O'Doherty JP (2008): The neural mechanisms underlying the influence of pavlovian cues on human decision making. J Neurosci 28:5861–5866.
48. Prévost C, Liljeholm M, Tyszka JM, O'Doherty JP (2012): Neural correlates of specific and general Pavlovian-to-instrumental transfer within human amygdalar subregions: A high-resolution fMRI study. J Neurosci 32:8383–8390.

49. Allman MJ, DeLeon IG, Cataldo MF, Holland PC, Johnson AW (2010): Learning processes affecting human decision making: An assessment of reinforcer-selective Pavlovian-to-instrumental transfer following reinforcer devaluation. J Exp Psychol Anim Behav Process 36:402–408.
50. Nadler N, Delgado MR, Delamater AR (2011): Pavlovian to instrumental transfer of control in a human learning task. Emotion 11:1112–1123.
51. Trick L, Hogarth L, Duka T (2011): Prediction and uncertainty in human Pavlovian to instrumental transfer. J Exp Psychol Learn Mem Cogn 37:757–765.
52. Martinovic J, Jones A, Christiansen P, Rose AK, Hogarth L, Field M (2014): Electrophysiological responses to alcohol cues are not associated with Pavlovian-to-instrumental transfer in social drinkers. PLoS One 9:e94605.
53. Lovibond PF, Colagiuri B (2013): Facilitation of voluntary goaldirected action by reward cues. Psychol Sci 24:2030–2037.
54. Seabrooke T, Le Pelley ME, Hogarth L, Mitchell CJ (2017): Evidence of a goal-directed process in human Pavlovian-instrumental transfer. J Exp Psychol Anim Learn Cogn 43:377–387.
55. Lehner R, Balsters JH, Herger A, Hare TA, Wenderoth N (2016): Monetary, food, and social rewards induce similar Pavlovian-toinstrumental transfer effects. Front Behav Neurosci 10:247.
56. Witten IB, Steinberg EE, Lee SY, Davidson TJ, Zalocusky KA, Brodsky M, et al. (2011): Recombinase-driver rat lines: Tools, techniques, and optogenetic application to dopamine-mediated reinforcement. Neuron 72:721–733.

57. Chen E, Lallai V, Sherafat Y, Grimes NP, Pushkin AN, Fowler JP, et al. (2018): Altered baseline and nicotine-mediated behavioral and cholinergic profiles in ChAT-Cre mouse lines. J Neurosci 38:2177– 2188.
58. Collins AL, Aitken TJ, Greenfield VY, Ostlund SB, Wassum KM (2016): Nucleus accumbens acetylcholine receptors modulate dopamine and motivation. Neuropsychopharmacology 41:2830–2838.
59. Wassum KM, Ostlund SB, Balleine BW, Maidment NT (2011): Differential dependence of Pavlovian incentive motivation and instrumental incentive learning processes on dopamine signaling. Learn Mem 18:475–483.
60. Wassum KM, Ostlund SB, Loewinger GC, Maidment NT (2013): Phasic mesolimbic dopamine release tracks reward seeking during expression of Pavlovian-to-instrumental transfer. Biol Psychiatry 73:747–755.
61. Lichtenberg NT, Pennington ZT, Holley SM, Greenfield VY, Cepeda C, Levine MS, et al. (2017): Basolateral amygdala to orbitofrontal cortex projections enable cue-triggered reward expectations. J Neurosci 37:8374–8384.
62. Malvaez M, Shieh C, Murphy M, Greenfield V, Wassum K (in press): Distinct cortical-amygdala projections drive reward value encoding and retrieval. Nat Neurosci.
63. Tabachnick BG, Fidell LS, Osterlind SJ (2001): Using Multivariate Statistics. New York: Pearson.
64. Bennett BD, Wilson CJ (1999): Spontaneous activity of neostriatal cholinergic interneurons in vitro. J Neurosci 19:5586–5596.
65. Wilson CJ, Goldberg JA (2006): Origin of the slow afterhyperpolarization and slow rhythmic bursting in striatal cholinergic interneurons. J Neurophysiol 95:196–204.

66. Jones IW, Bolam JP, Wonnacott S (2001): Presynaptic localisation of the nicotinic acetylcholine receptor beta2 subunit immunoreactivity in rat nigrostriatal dopaminergic neurones. J Comp Neurol 439:235–247.
67. Exley R, Cragg SJ (2008): Presynaptic nicotinic receptors: A dynamic and diverse cholinergic filter of striatal dopamine neurotransmission. Br J Pharmacol 153(Suppl 1):S283–S297.
68. Exley R, Clements MA, Hartung H, McIntosh JM, Cragg SJ (2008): Alpha6-containing nicotinic acetylcholine receptors dominate the nicotine control of dopamine neurotransmission in nucleus accumbens. Neuropsychopharmacology 33:2158–2166.
69. Threlfell S, Lalic T, Platt NJ, Jennings KA, Deisseroth K, Cragg SJ (2012): Striatal dopamine release is triggered by synchronized activity in cholinergic interneurons. Neuron 75:58–64.
70. Cachope R, Mateo Y, Mathur BN, Irving J, Wang HL, Morales M, et al. (2012): Selective activation of cholinergic interneurons enhances accumbal phasic dopamine release: Setting the tone for reward processing. Cell Rep 2:33–41.
71. Rice ME, Cragg SJ (2004): Nicotine amplifies reward-related dopamine signals in striatum. Nat Neurosci 7:583–584.
72. Zhou FM, Liang Y, Dani JA (2001): Endogenous nicotinic cholinergic activity regulates dopamine release in the striatum. Nat Neurosci 4:1224–1229.
73. Berridge KC (2007): The debate over dopamine's role in reward: The case for incentive salience. Psychopharmacology (Berl) 191:391–431.
74. Aitken TJ, Greenfield VY, Wassum KM (2016): Nucleus accumbens core dopamine signaling tracks the need-based motivational value of food-paired cues. J Neurochem 136:1026–1036.
75. Saunders BT, Richard JM, Margolis EB, Janak PH (2018): Dopamine neurons create Pavlovian conditioned stimuli with circuit-defined motivational properties. Nat Neurosci 21:1072–1083.

76. Lex A, Hauber W (2008): Dopamine D1 and D2 receptors in the nucleus accumbens core and shell mediate Pavlovian-instrumental transfer. Learn Mem 15:483–491.
77. Cover KK, Gyawali U, Kerkhoff WG, Patton MH, Mu C, White MG, et al. (2019): Activation of the rostral intralaminar thalamus drives reinforcement through striatal dopamine release. Cell Rep 26:1389– 1398.e1383.
78. Collins AL, Greenfield VY, Bye JK, Linker KE, Wang AS, Wassum KM (2016): Dynamic mesolimbic dopamine signaling during action sequence learning and expectation violation. Sci Rep 6:20231.
79. Saunders BT, Robinson TE (2012): The role of dopamine in the accumbens core in the expression of Pavlovian-conditioned responses. Eur J Neurosci 36:2521–2532.
80. Peciña S, Berridge KC (2013): Dopamine or opioid stimulation of nucleus accumbens similarly amplify cue-triggered 'wanting' for reward: Entire core and medial shell mapped as substrates for PIT enhancement. Eur J Neurosci 37:1529–1540.
81. Wyvell CL, Berridge KC (2000): Intra-accumbens amphetamine increases the conditioned incentive salience of sucrose reward: Enhancement of reward "wanting" without enhanced "liking" or response reinforcement. J Neurosci 20:8122–8130.
82. Zhang L, Doyon WM, Clark JJ, Phillips PE, Dani JA (2009): Controls of tonic and phasic dopamine transmission in the dorsal and ventral striatum. Mol Pharmacol 76:396–404.
83. Zhang H, Sulzer D (2004): Frequency-dependent modulation of dopamine release by nicotine. Nat Neurosci 7:581–582.
84. Threlfell S, Cragg SJ (2011): Dopamine signaling in dorsal versus ventral striatum: The dynamic role of cholinergic interneurons. Front Syst Neurosci 5:11.
85. Lim SA, Kang UJ, McGehee DS (2014): Striatal cholinergic interneuron regulation and circuit effects. Front Synaptic Neurosci 6:22.

86. Stouffer MA, Woods CA, Patel JC, Lee CR, Witkovsky P, Bao L, et al. (2015): Insulin enhances striatal dopamine release by activating cholinergic interneurons and thereby signals reward. Nat Commun 6:8543.
87. Koob GF (1999): Corticotropin-releasing factor, norepinephrine, and stress. Biol Psychiatry 46:1167–1180.
88. Koob GF, Bloom FE (1985): Corticotropin-releasing factor and behavior. Fed Proc 44:259–263.
89. Lemos JC, Wanat MJ, Smith JS, Reyes BA, Hollon NG, Van Bockstaele EJ, et al. (2012): Severe stress switches CRF action in the nucleus accumbens from appetitive to aversive. Nature 490:402–406.
90. Koob GF, Heinrichs SC, Pich EM, Menzaghi F, Baldwin H, Miczek K, et al. (1993): The role of corticotropin-releasing factor in behavioural responses to stress. Ciba Found Symp 172:277–289; discussion 290–295.
91. Lemos J, Shin J, Ingebretson A, Dobbs L, Alvarez V (2018): Cholinergic interneurons as a novel target of CRF in the striatum that is spared by repeated stress [published online ahead of print Oct 22]. bioRxiv.
92. Chen YW, Rada PV, Bützler BP, Leibowitz SF, Hoebel BG (2012): Corticotropin-releasing factor in the nucleus accumbens shell induces swim depression, anxiety, and anhedonia along with changes in local dopamine/acetylcholine balance. Neuroscience 206:155–166.
93. Dölen G, Darvishzadeh A, Huang KW, Malenka RC (2013): Social reward requires coordinated activity of nucleus accumbens oxytocin and serotonin. Nature 501:179–184.
94. Virk MS, Sagi Y, Medrihan L, Leung J, Kaplitt MG, Greengard P (2016): Opposing roles for serotonin in cholinergic neurons of the ventral and dorsal striatum. Proc Natl Acad Sci U S A 113:734–739.

95. Olney JJ, Warlow SM, Naffziger EE, Berridge KC (2018): Current perspectives on incentive salience and applications to clinical disorders. Curr Opin Behav Sci 22:59–69.
96. Robinson TE, Berridge KC (1993): The neural basis of drug craving: An incentive-sensitization theory of addiction. Brain Res Brain Res Rev 18:247–291.
97. Hikida T, Kitabatake Y, Pastan I, Nakanishi S (2003): Acetylcholine enhancement in the nucleus accumbens prevents addictive behaviors of cocaine and morphine. Proc Natl Acad Sci U S A 100:6169–6173.
98. Hikida T, Kaneko S, Isobe T, Kitabatake Y, Watanabe D, Pastan I, et al. (2001): Increased sensitivity to cocaine by cholinergic cell ablation in nucleus accumbens. Proc Natl Acad Sci U S A 98:13351–13354.
99. Treadway MT, Zald DH (2013): Parsing anhedonia: Translational models of reward-processing deficits in psychopathology. Curr Dir Psychol Sci 22:244–249.
100. Paxinos G, Watson C (1998): The Rat Brain in Stereotaxic Coordinates, 4th ed. San Diego: Academic Press.

Chapter 5: Microbiosensor fabrication by polydimethylsiloxane stamping for combined sensing of glucose and choline

Chapter 5 is a manuscript published with the following citation:

Bo Wang, Bonhye Koo, **Li-wen Huang** and Harold G. Monbouquette. Analyst, 2018, 143, 5008

I-Wen Huang's contribution to this work focused on microsensor fabrication, development of enzyme crosslinking process and formal data analysis. These involved using microfabrication techniques to pattern and create the microelectrode probes, as well as developing and optimizing crosslinker vapor treatment to immobilize the stamped enzyme.

Abstract

High performance microprobes for combined sensing of glucose and choline were fabricated using microcontact printing (μCP) to transfer choline oxidase (ChOx) and glucose oxidase (GOx) onto targeted sites on microelectrode arrays (MEAs). Most electroenzymatic sensing sites on MEAs for neuroscience applications are created by manual enzyme deposition, which becomes problematic when the array feature size is less than or equal to ~100 μm. The μCP process used here relies on use of soft lithography to create features on a polydimethylsiloxane (PDMS) microstamp that correspond to the dimensions and array locations of targeted, microscale sites on a MEA. Precise alignment of the stamp with the MEA is also required to transfer enzyme only onto the specified microelectrode(s). The dual sensor fabrication process began with polyphenylenediamine (PPD) electrodeposition on all Pt microelectrodes to block common interferents (e.g., ascorbic acid and dopamine) found in brain extracellular fluid. Next, a chitosan film was electrodeposited to serve as an adhesive layer. The two enzymes, ChOx

and GOx, were transferred onto different microelectrodes of 2 × 2 arrays using two different PDMS stamps and a microscope for stamp alignment. Using constant potential amperometry, the combined sensing microprobe was confirmed to have high sensitivity for choline and glucose (286 and 117 μA mM^{-1} cm^{-2}, respectively) accompanied by low detection limits (1 and 3 μM, respectively) and rapid response times (≤2 s). This work demonstrates the use of μCP for facile creation of multianalyte sensing microprobes by targeted deposition of enzymes onto preselected sites of a microelectrode array.

5.1 Introduction

The ability to monitor neurotransmitter release and metabolite levels in the brains of freely moving animals is key to understanding neuronal processes underlying complex behaviors and disorders. Such processes are controlled by neuronal networks influenced by interactions among multiple neurotransmitters and metabolites such as glucose (Glu), dopamine (DA), glutamate (Glut) and acetylcholine (ACh).[1–4] Therefore, our understanding of the connection between neurochemistry and behaviors would be greatly facilitated by the capability to monitor *in vivo* multiple neurochemicals simultaneously and in near-real time. The combination of microelectrode array (MEA) microprobes and electroenzymatic sensing approaches potentially offers a means for combined monitoring of multiple neurochemicals in vivo with high spatiotemporal resolution. The existing microdialysis technique also provides for multiple analyte measurements, yet achievement of sufficient spatiotemporal resolution commonly is challenging.[5] Thus, there is impetus to develop implantable microprobes with an array of microsensors capable of combined monitoring of multiple neurochemicals with desirable sensitivity, selectivity and response time characteristics.

We have reported an implantable probe with arrayed microsensors for combined amperometric monitoring of Glut and DA.[6] However, the glutamate oxidase enzyme used in

constructing the Glut sensing sites was manually applied in the usual manner to selected microelectrodes, which is very challenging to achieve consistently given the less than 100 μm spacing between sites. In contrast, DA is directly electrooxidizable, and DA sensing sites were constructed straightforwardly through selective electrodeposition processes.[6] Clearly, if multiple oxidases are to be deposited on selected microelectrodes on the same microprobe for combined sensing of nonelectroactive analytes such as Glut, ACh, and Glu, higher resolution, non-manual methods for enzyme transfer and immobilization must be developed.

Microcontact printing (μCP) based on polydimethylsiloxane (PDMS) stamping is an emerging method for transferring proteins to surfaces in high-resolution patterns with feature size down to 500 nm.[7,8] After mold and stamp fabrication, the stamping process begins by "inking" a protein solution onto the PDMS stamp. The protein pattern defined by the stamp is then transferred onto a target substrate upon contact of the protein-covered PDMS stamp with the surface for a few moments. The process can be designed to maintain activity of transferred proteins, and the PDMS stamp can be re-used after appropriate cleaning.[7–13]

Previously, we utilized PDMS stamping to transfer glucose oxidase (GOx) onto macroscopic, 1.6 mm-dia. platinum disk electrodes to demonstrate the feasibility of PDMS stamping for fabrication of high performance electroenzymatic biosensors.[14] The glucose biosensors made using PDMS stamping showed excellent properties with a sensitivity of ~29 μA mM^{-1} cm^{-2}, a detection limit of ~4 μM, and a response time of ~2 s. In this report, we demonstrate PDMS stamping with microscopic alignment to transfer choline oxidase (ChOx) and glucose oxidase (GOx) separately onto selected individual sites of an MEA. In so doing, we provide the first example of an oxidase-based dual sensing microprobe for nonelectroactive analytes (i.e., glucose and choline) that is suitable for application *in vivo*.

5.2 Experimental

5.2.1 Reagents

Glucose oxidase (*Aspergillus niger*, 9001-37-0), pyrrole (Py), choline oxidase (*Alcaligenes sp.*, 9028-67-5), m-phenylenediamine (PD), choline chloride, glutaraldehyde solution (25%), bovine serum albumin (BSA) lyophilized powder, hydrogen peroxide solution (30%), chitosan (from crab shells, minimum 85% deacetylated), D-(+)-glucose, L-ascorbic acid, and dopamine hydrochloride were purchased from Sigma-Aldrich (St. Louis, MO). Isopropyl alcohol and 1 M sulfuric acid solutions were obtained from Fisher Scientific (Pittsburgh, PA). Ag/AgCl glass-bodied reference electrodes with 3 M NaCl electrolyte and 0.5 mm-diameter Pt wire auxiliary electrodes were purchased from BASi (West Lafayette, IN). Sodium phosphate buffer (PBS, pH 7.4) was composed of 50 mM sodium phosphate (dibasic) and 100 mM sodium chloride. Ultrapure water was generated using a Millipore Milli-Q Water System and was used for preparation of all solutions. Four-inch Si wafers were purchased from Silicon Valley Microelectronics (Santa Clara, CA). SU-8 2075 and SU-8 developer were obtained from MicroChem (Westborough, MA). The Sylgard® 184 silicone elastomer kit was purchased from Dow Corning (Auburn, MI).

The microelectrodes used in this work were silicon-based multielectrode arrays manufactured in house using microelectro- mechanical-system (MEMS) technologies. The fabrication and array details are described in our previous work.[15] The MEA consists of four 6000 μm^2 (40 μm × 150 μm) Pt sites, situated in pairs at the tip of a 9 mm-long shank. The pair nearest the shank tip is 100 μm from the pair farthest from the shank tip, and the paired sites are 40 μm apart. Each site may be modified to act either as a working or control electrode.

5.2.2 Instrumentation

Electrochemical experiments for sensor development, evaluation and calibration were performed using a Versatile Multichannel Potentiostat (model VMP3) equipped with the ‘p’ low

current option and N'Stat box driven by EC-LAB software (Bio-Logic USA, LLC, Knoxville, TN) in a three electrode configuration consisting of the sensing electrode, a Pt wire auxiliary electrode, and a Ag/AgCl glass-bodied reference electrode. A FEI Nova Nano 230 was used for environmental SEM images.

5.2.3 Fabrication of mold and PDMS stamps

The fabrication process for a mold and a PDMS microstamp is illustrated in Fig. 1a. SU-8 2075 was spin-coated on a four-inch Si wafer at 2000 rpm for 30 s to give a ~100 μm thick layer. The layer was soft-baked at 65 °C for 5 min and then at 95 °C for 40 min followed by 27 s of UV exposure (total 216 mJ cm^{-2}). Post exposure baking was done at 65 °C for 5 min and at 95 °C for 10 min. After the layer was patterned in SU-8 developer for 20 min, the mold was cleaned using isopropanol and then left to dry in air at room temperature. PDMS microstamps were fabricated using the Sylgard® 184 silicone elastomer kit. To cover a 4 inch mold, 6 g of monomer was mixed with 0.6 g of curing agent (10 : 1; monomer : curing agent) and then centrifuged at 15 000 rpm for 5 min to minimize air bubbles. After pouring onto the SU-8 mold, the mixture was subsequently degassed under vacuum to remove air bubbles and then cured at 60 °C for 4 hr. The PDMS microstamps were detached from the mold and cut into 1 cm Å~ 1 cm pieces. A fabricated PDMS microstamp is shown in Fig. 1b. To ensure that the enzyme mixture is transferred to the entire microelectrode surface (40 μm Å~ 150 μm), the size of a microstamp surface was designed to be slightly bigger than the size of the microelectrode (50 μm ×160 μm). The PDMS stamps were cleaned in 7.5% hydrogen peroxide with sonication before re-use.

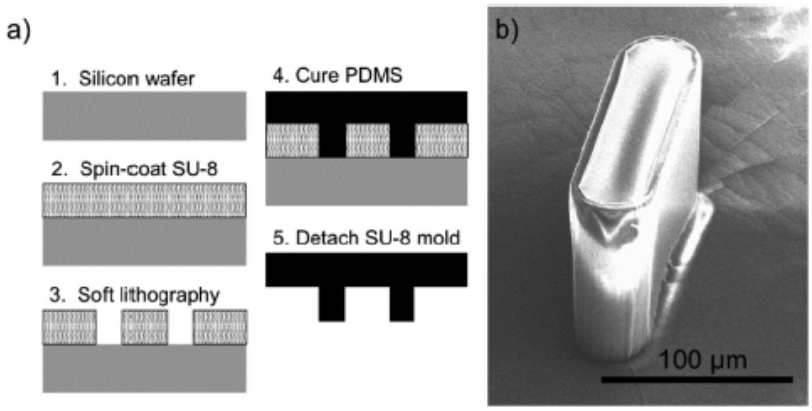

Figure 5.1. (a) Fabrication process for a SU-8 mold and a PDMS microstamp. (b) Scanning electron microscope (SEM) image of a PDMS microstamp.

5.2.4 Sensor preparation

Microelectrodes on microprobes were rinsed with isopropyl alcohol followed by an electrochemical cleaning step with 0.5 M sulfuric acid and sonication in ultrapure water. Next, a polyphenylenediamine (PPD) film was electrodeposited (5 mM PD in stirred PBS, 0.85 V vs. Ag/AgCl, 10 min) onto the microelectrode surfaces.

A solution (0.04% m/v) for chitosan electrodeposition was adjusted to pH 3 using HCl (0.5 M) to dissolve the chitosan flakes. After filtering with a 0.2 µm syringe filter, the pH was adjusted to 5 using NaOH solution (0.5 M). A constant potential of −0.7 V vs. Ag/AgCl was applied at the PPD-coated Pt electrode surface for 2 min while immersed in the chitosan solution to electrodeposit a chitosan film.[16,17]

5.2.5 PDMS µCP with alignment

A droplet (~3 µL) of enzyme mixture was placed on a PDMS microstamp and allowed to rest at room temperature for ~60 min in a closed chamber to prevent evaporation. Enzyme mixtures consisted of ChOx (17.5 mg mL^{-1}) or GOx (10 mg mL^{-1}) mixed with bovine serum

albumin (BSA) in a 1 : 1 mass ratio in phosphate-buffered saline (PBS). After this “inking” step, the excess enzyme solution was wicked away using a Kimwipe, and the microstamp was dried using a nitrogen gun for ~15 s. Since our previous work used a stamp matched with a single, 1.6 mm-dia. disk electrode, microscopic alignment was not required for stamping onto the electrode.[14] However in this work, microscopic alignment was necessary to deposit “inked” enzyme on selected microelectrodes in a 2×2 array on a microprobe where the separation between microelectrodes was 40 μm and 100 μm in the lateral- and axial-directions, respectively. The alignment setup consisted of a microscope with an adjustable stage and a separate custom-built, fixed stage to secure the PDMS stamp, as shown in Fig. 2. The microprobe was attached to the microscope stage and was moved into focus with the surface of the stamp. Alignment of the PDMS microstamp and the target microelectrode was achieved by manipulation of the microscope stage. The microscope stage was then raised further to make contact with the PDMS microstamp. The ChOx mixture and the GOx mixture were stamped onto the upper right and bottom left sites of the microelectrode array. The remaining two microelectrodes, upper left and bottom right, were left as control sites. The contact time was ~1 min to transfer the enzymes from the microstamp to the microelectrode. Subsequently, the microprobe was exposed to vapor from a 5% glutaraldehyde (GAH) solution at room temperature for 1 min to crosslink the chitosan, enzyme and BSA on the microelectrode surfaces. This enzyme stamping and crosslinking process was repeated twice to achieve sufficient enzyme surface concentrations for high-performance sensing of choline and glucose. The fabricated sensors were preserved at 4 °C under dry conditions when not in use.

5.2.6 Electrochemical measurements

Constant potential amperometric measurements were conducted in PBS buffer at 0.7 V vs. Ag/AgCl and at ambient laboratory temperature. More than 30 min of equilibrium time in PBS

buffer was allowed to achieve a stable current before adding analytes. Sensitivity was calculated based on the first few points of sensor calibration curves.

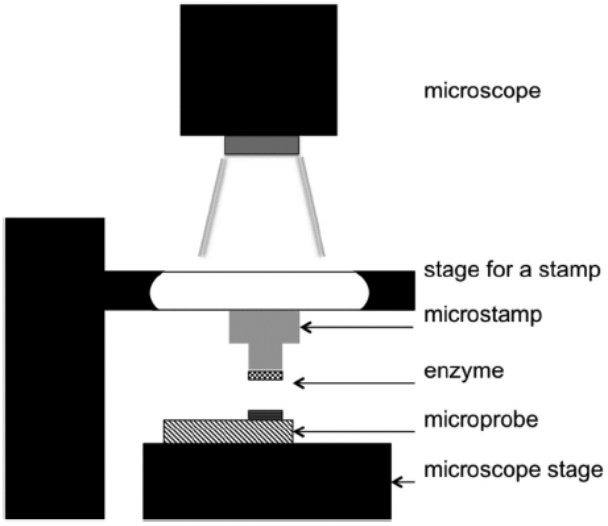

Figure 5.2. Alignment setup for a PDMS microstamp and a microelectrode array on a silicon-based microprobe.

5.3 Results and discussion

5.3.1 PDMS stamping of enzymes

An optical image of the microelectrodes before and after stamping are shown in Fig. 3. A clear deposit of the ChOx and GOx mixtures is evident in the boxed areas of the image (Fig. 3b) that extends slightly beyond the edges of the microelectrode as planned (see Methods). There are no evident surface abnormalities, which implies that alignment and deposition were successful. By increasing the “inking” time (BSA and enzyme mixture on top of stamp) from our previously reported 10 min to 60 min,14 more consistent enzyme layers were formed resulting in more consistent microsensor performance (see below).

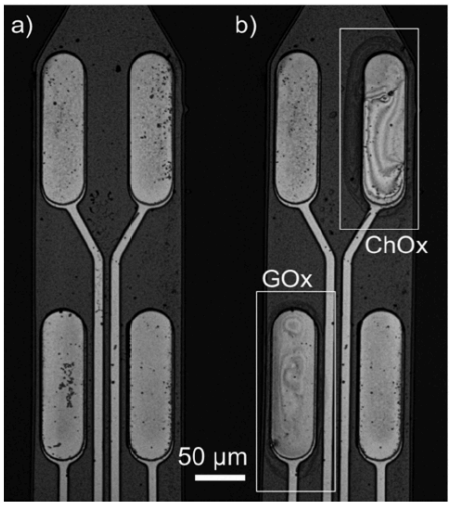

Figure 5.3. 100Å~ optical microscope image of a microelectrode array on a microprobe (a) before and (b) after PDMS stamping of ChOx and GOx with alignment.

5.3.2 Glucose microbiosensor performance

Calibration data for the glucose biosensor is presented as Fig. 4. Glucose biosensors fabricated on the same day exhibited a repeatable, high sensitivity of 117 ± 14 µA mM^{-1} cm^{-2} (n = 9) and detection limit of 3 ± 0.5 µM (n = 9) at a signal-tonoise ratio of 3. The 4-fold improvement in sensitivity as compared to our previously reported work (117 vs. 29 µA mM^{-1} cm^{-2}) is due in large part to reduced exposure to glutaraldehyde vapor (1 min exposure to 5% solution vs. 45 s to 12.5% solution),[14] which suggests that even brief exposure to glutaraldehyde vapor damages enzyme. However, different permselective coatings also were used previously, polypyrrole (PPy) and Nafion, which may have contributed to a difference in performance as well. The sensors described here typically displayed a linear detection range up to ~1.4 mM (R^2 = 0.9997) and a response time (95% of the steady-state current) of <2 s when exposed to a step change in glucose concentration to 40 µM in a stirred beaker.

The performance of our glucose microbiosensor fabricated by µCP compares very well with those described in recently published reports (see Table 1 for examples). In our previous

work,[14] we carefully reviewed the performance characteristics of recently reported glucose biosensors based on immobilized GOx and found our macroscale sensor fabricated by PDMS stamping to exhibit a rare, if not unique, combination of high sensitivity and selectivity, fast response time and low limit of detection. Here, we describe a stamped glucose microbiosensor with substantially improved sensitivity, lower detection limit and still fast response time and impressive selectivity.

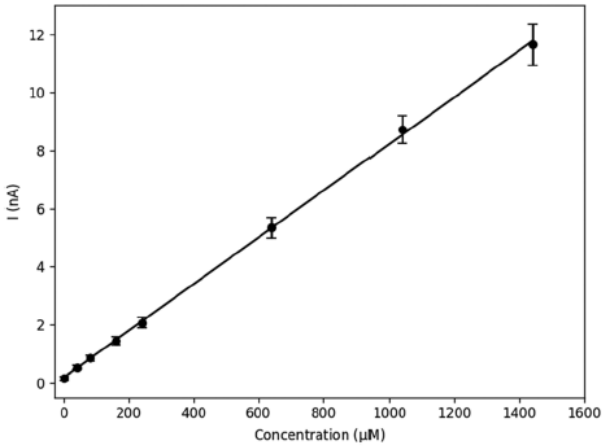

Figure 5.4. Calibration plot for the glucose biosensor. The biosensor response in stirred solution was recorded for sequential injections of glucose to give concentrations of 0, 40, 80, 160, 240, 440, 640, 840, 1040, 1240 and 1440 μM, at a constant potential of 0.7 V (vs. Ag/AgCl) in stirred PBS buffer (pH 7.4). Error bars: Standard error of the mean (*n* = 5).

Enzyme electrodes	Sensitivity (μA mM^{-1} cm^{-2})	LOD (μM)	Resp. time (s)	Ref.
GOx/chitosan/PPD/Pt	117	3	~2	This work
GOx/chitosan/Nafion/PPy/Pt	29.4	4.3	~2	14
GOx/graphene-polyaniline/Pt	22.1	2.77	~5	18
Chitosan/GOx/cysteamine/Au	8.91	49.96	~9	19
GOx/silver-chitosan/Pt	67.17	1	NR[a]	20
Nafion/GOx/carbon-ZnO nanowire/Ti	35.3	1	~5	21

[a] NR: not reported.

Table 5.1. Comparison of the performance characteristics of the glucose microbiosensor of this work with other recently reported electroenzymatic glucose biosensors.

5.3.3 Choline microbiosensor performance

A choline biosensor was fabricated here to provide another example of the utility of PDMS microstamping. A typical calibration curve for the choline biosensor is presented in Fig. 5. Choline biosensors fabricated on the same day exhibited a repeatable, high sensitivity of 286 ± 32 μA mM^{-1} cm^{-2} (n = 4) and detection limit of 1 ± 0.2 μM (n = 4) at a signal-to-noise ratio of 3. The biosensor also displayed a relatively fast response time (~2 s) to a choline step change of 10 μM in a stirred beaker.

Our choline biosensor created by μCP is also competitive with those recently described in the literature (see Table 2). Keihan et al. reported a very high sensitivity (345.4 μA mM^{-1} cm^{-2}) with a low detection limit (0.45 μM), but the biosensors were composed of a complex system consisting of a multiwalled carbon nanotube (MWCNT)/ionic liquid (IL)/Prussian blue (PB) nanocomposite-modified glassy carbon (GC) electrode.[22] Ricci et al. presented results describing a choline biosensor assembled on screen-printed electrodes (SPEs) with a low detection limit (0.5 μM), but with lower sensitivity than our device (Table 2).[23] Rahimi et al. described a choline biosensor based on an amine functionalized multi-walled carbon nanotubes (NH2-MWCNT)/IL system with performance not as good as this report (sensitivity of 125.8 μA mM^{-1} cm^{-2}, detection limit of 3.85 μM), and the response time was not mentioned.[24] Zhang et al. reported a similar response time (2 s) with lower detection limit of 0.4 μM, but the sensitivity was significantly lower (75.2 μA mM^{-1} cm^{-2}). In addition, the biosensors were fabricated using a complex system consisting of poly(diallyldimethylammonium chloride (PDDA) deposited on PB-iron phosphate nanostructures (PB–FePO4).[25] Burmeister et al. reported a ceramic probe-based choline biosensor with low detection limit of 0.4 μM and fast response time of 1.4 s, but a self-referencing

recording mode was needed to remove interfering dopamine signals.[26] Thus, the choline biosensor presented in this work offers an appealing combination of simplicity of design, high performance, and excellent selectivity (see below).

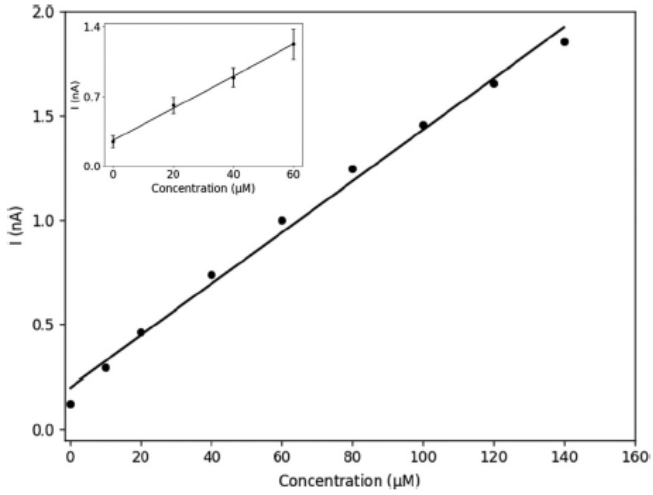

Figure 5.5. Representative calibration plot for the choline biosensor. The biosensor response in stirred solution was recorded for sequential injections of choline chloride to give concentrations of 0, 10, 20, 40, 60, 80, 100, 120, and 140 μM, at a constant potential of 0.7 V (vs. Ag/AgCl) in stirred PBS buffer (pH 7.4). The inset plot shows the lower analyte concentration range (0–60 μM). Error bars: Standard error of the mean (*n* = 4).

Enzyme electrodes	Sensitivity (μA mM^{-1} cm^{-2})	LOD (μM)	Resp. time (s)	Ref.
ChOx/chitosan/PPD/Pt	286	1	~2	This work
ChOx/Nafion/PB/SPE	110	0.5	NR[a]	23
ChOx/IL/NH_2-MWCNT/GC	125.8	3.85	NR[a]	24
ChOx/PB/MWCNT/IL/GC	345.4	0.45	2	22
ChOx/PDDA/PB–$FePO_4$/GC	75.2	0.4	2	25
ChOx/Nafion/Pt	264	0.4	1.4	26

[a] NR: not reported.

Table 5.2. Comparison of the performance characteristics of the choline microbiosensor of this work with other recently reported electroenzymatic choline biosensors.

5.3.4 Dual sensor and effect of interferents

Fig. 6 shows the combined sensing of glucose and choline by our microprobe created by PDMS microstamping. The glucose and choline microbiosensor selectivity was tested against ascorbic acid (AA) and dopamine (DA), common electrooxidizable interferents found in brain extracellular fluid (Fig. 6). Physiologically relevant concentrations of 5 μM dopamine and 250 and 500 μM ascorbic acid were used to test for the false positive signals that might arise in applications *in vivo*. A negligible biosensor response to AA and DA was observed at the constant operating potential of 0.7 V (vs. Ag/AgCl), while the appropriate biosensing sites exhibited the expected responses to hydrogen peroxide and to glucose or choline. These results show that the permselective polyphenylenediamine film effectively blocks access of these key electroactive interferents, which suggests that this microprobe may be a useful implantable tool for neuroscience research.

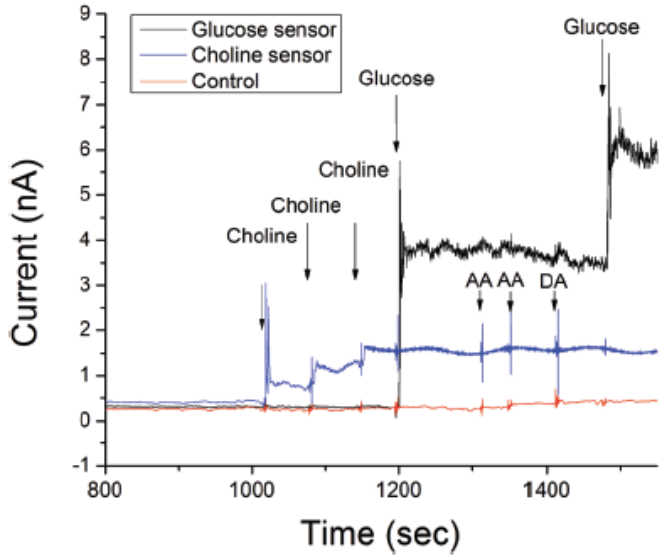

Figure 5.6. Combined sensing of glucose and choline at a constant potential of 0.7 V (vs. Ag/AgCl). The microprobe was tested in stirred PBS solution with sequential injections to give 20 μM, 40 μM and 60 μM of choline chloride, 0.6 mM of glucose, 250 μM and 500 μM of ascorbic acid (AA), 5 μM of dopamine (DA) and 1.2 mM of glucose. The control site was coated with the same permselective PPD film as the sensing sites.

5.4 Conclusions

PDMS stamping has been employed successfully to deposit GOx and ChOx onto selected, distinct sites of a microelectrode array (MEA) to fabricate an implantable microbe for combined sensing of glucose and choline. The microbiosensor sites showed high sensitivity for choline and glucose (286 and 117 μA mM^{-1} cm^{-2}, respectively), fast response times (≤2 s), and low detection limits (1 and 3 μM, respectively). The sensors also were selective against ascorbic acid and dopamine, two electroactive interferents common to brain extracellular fluid. The PDMS microstamping technique is expected to contribute to neuroscience research by making possible the controlled deposition of different enzymes on selected microelectrode sites on a microprobe thereby enabling the combined sensing of multiple neurochemicals in close proximity simultaneously. The high resolution and non-manual nature of this stamping approach for enzyme transfer also should enable a decrease in size of MEAs in order to minimize tissue damage and increase spatial resolution, as well as a higher throughput process to generate microprobes for combined electroenzymatic sensing of multiple analytes.

5.5 References

1. V. M. Andre, C. Cepeda, D. M. Cummings, E. L. Jocoy, Y. E. Fisher, X. W. Yang and M. S. Levine, Eur. J. Neurosci., 2010, 31, 14–28.
2. V. M. Andre, C. Cepeda and M. S. Levine, CNS Neurosci. Ther., 2010, 16, 163–178.
3. C. Cepeda, V. M. Andre, I. Yamazaki, N. P. Wu, M. Kleiman- Weiner and M. S. Levine, Eur. J. Neurosci., 2008, 27, 671– 682.
4. C. C. Lapish, J. K. Seamans and L. J. Chandler, Alcohol.: Clin. Exp. Res., 2006, 30, 1451–1465.

5. I. Chefer Vladimir, C. Thompson Alexis, A. Zapata and S. Shippenberg Toni, Curr. Protoc. Neurosci., 2009, 47, 7.1.1–7.1.28.
6. T. T. C. Tseng and H. G. Monbouquette, J. Electroanal. Chem., 2012, 682, 141–146.
7. A. Bernard, E. Delamarche, H. Schmid, B. Michel, H. R. Bosshard and H. Biebuyck, Langmuir, 1998, 14, 2225– 2229.
8. A. Perl, D. N. Reinhoudt and J. Huskens, Adv. Mater., 2009, 21, 2257–2268.
9. A. Bernard, J. P. Renault, B. Michel, H. R. Bosshard and E. Delamarche, Adv. Mater., 2000, 12, 1067–1070.
10. R. S. Kane, S. Takayama, E. Ostuni, D. E. Ingber and G. M. Whitesides, Biomaterials, 1999, 20, 2363–2376.
11. D. Qin, Y. Xia and G. M. Whitesides, Nat. Protoc., 2010, 5, 491–502.
12. Y. N. Xia and G. M. Whitesides, Annu. Rev. Mater. Sci., 1998, 28, 153–184.
13. L. Yan, X. M. Zhao and G. M. Whitesides, J. Am. Chem. Soc., 1998, 120, 6179–6180.
14. B. Wang, B. Koo and H. G. Monbouquette, Electroanalysis, 2017, 29, 2300–2306.
15. K. M. Wassum, V. M. Tolosa, J. J. Wang, E. Walker, H. G. Monbouquette and N. T. Maidment, Sensors, 2008, 8, 5023–5036.
16. T. T. C. Tseng, J. Yao and W. C. Chan, Biochem. Eng. J., 2013, 78, 146–153.
17. L. Q. Wu, A. P. Gadre, H. M. Yi, M. J. Kastantin, G. W. Rubloff, W. E. Bentley, G. F. Payne and R. Ghodssi, Langmuir, 2002, 18, 8620–8625.
18. X. Feng, H. J. Cheng, Y. W. Pan and H. Zheng, Biosens. Bioelectron., 2015, 70, 411–417.
19. Y. W. Zhang, Y. Q. Li, W. J. Wu, Y. R. Jiang and B. R. Hu, Biosens. Bioelectron., 2014, 60, 271–276.
20. W. T. Shi and Z. F. Ma, Biosens. Bioelectron., 2010, 26, 1098– 1103.

21. J. P. Liu, C. X. Guo, C. M. Li, Y. Y. Li, Q. B. Chi, X. T. Huang, L. Liao and T. Yu, Electrochem. Commun., 2009, 11, 202–205.
22. A. H. Keihan, S. Sajjadi, N. Sheibani and A. A. Moosavi- Movahedi, Sens. Actuators, B, 2014, 204, 694–703.
23. F. Ricci, A. Amine, G. Palleschi and D. Moscone, Biosens. Bioelectron., 2003, 18, 165–174.
24. P. Rahimi, H. Ghourchian and S. Sajjadi, Analyst, 2012, 137, 471–475.
25. H. Zhang, Y. J. Yin, P. Wu and C. X. Cai, Biosens. Bioelectron., 2012, 31, 244–250.
26. J. J. Burmeister, M. Palmer and G. A. Gerhardt, Anal. Chim. Acta, 2003, 481, 65–74.

Chapter 6: Improved microcontact printing of choline oxidase using a polycation-functionalized zwitterionic polymer as enzyme immobilization matrix

ABSTRACT:

Choline oxidase (ChOx) patterning on a microelectrode arrays (MEA) and sensor performance have been greatly improved through the use of microcontact printing (μCP) combined with a polycation-functionalized zwitterionic polymer as enzyme immobilization matrix. μCP has emerged as an effective means to allow surface patterning with feature sizes in millimeter to nanometer range, therefore, it could be useful to create multianalyte sensing microprobe by targeted deposition of multiple enzymes onto selected sites of a MEA. However, less than sufficient enzyme loading in high resolution has limited both the sensitivity and the use of these microsensors. This limitation on creating fine and thick enzyme pattern is due to poor balance between ink-substrate interaction and ink intermolecular interaction. In this report, we used a specially designed polymer, poly(2-methacryloyloxyethyl phosphorylcholine)-*g*-poly(allylamine hydrochloride) (PMPC-*g*-PAH), serving as an alternative matrix to conventional bovine serum albumin (BSA) for enzyme immobilization. During μCP, PMPC-*g*-PAH offers ChOx ink stronger intermolecular force while maintaining high adhesion to microelectrode surface, which allows much thicker ChOx imprinted in high resolution, thereby greatly increasing the choline sensitivity (639 ± 96 nA μM^{-1} cm^{-2} at pH 7.4; n = 4). Furthermore, high affinity of substrate to PMPC-*g*-PAH immobilized ChOx is observed through the investigation on apparent Michaelis Constant (K_M^{app}) of sensors. The use of PMPC-*g*-PAH during μCP for creation of thick enzyme pattern in high resolution provides an attractive route for future work to minimize tissue damage and increase

the number of neurochemicals analyzed by decreasing size of MEAs while maintaining observable response.

6.1 Introduction

The capability to monitor *in vivo* multiple neurochemicals simultaneously in near-real-time has triggered enormous interest from neuroscientist, as behaviors and physiological disorders are controlled by neuronal networks influenced by the complex interplay among various neurotransmitters. While the conventional microdialysis allows multiple analyte measurements and has provided important insight into the regulation of various neurotransmissions, this technique is constrained by its poor temporal resolution which are reported in the range of minutes.[1–4] On the other hand, electrochemical technique relying on the use of microprobe with an array of electroenzymatic sensing sites potentially offers a means for multianalyte sensing in high spatiotemporal resolution, therefore, it has been developed rapidly into a robust analytical technique for neurotransmitters over the past few years.[5–9] Electroenzymatic sensor relies on specific enzyme to catalyze oxidation reaction of targeted substrate to produce product (most commonly hydrogen peroxide (H_2O_2)) that is easily oxidized/reduced at an underlying electrode applied moderate potential to give current signal. Development of microelectrode arrays (MEAs) microprobe for multiple neurotransmitters detection consequently requires method to selectively deposit multiple enzymes onto different sites on the same probe.

Enzyme deposition and immobilization on electrode surface is most commonly achieved by manually loading a mixture of enzyme and bovine serum albumin (BSA) on the electrode surface followed by crosslinking with glutaraldehyde (GAH). However, it becomes problematic when targeted deposition of enzymes is desired to be performed onto the array feature size in micrometer range. In previous work, we have demonstrated the use of microcontact printing (μCP) for creation of multianalyte sensing microprobes by patterning two different enzymes onto

selected, distinct sites on a MEA.[5] Although this accomplishment manifests great potential of MEAs to record *in vivo* neurochemicals in close proximity simultaneously, the use of mixture of BSA and enzyme diluted in water as ink has certain disadvantages. As BSA protein behaves as globular particle that provide poor viscosity of ink, imprinted enzyme patterns are usually either so thin that result in low sensitivity or experiencing sever surface diffusion when higher enzyme loading is attempted. For the application here, spreading of enzyme pattern is highly undesired because it would contaminate the adjacent microelectrode (given less than 100 μm gap in between) that gives false signal. As these problems are inherently related to the ink properties, there has been a need for a new ink that provides high adhesion to substrate, strong intermolecular force within ink and yet similar functionality as BSA to allow enzyme immobilization through covalent crosslinking.

While great strides have been made in modifying ink properties to achieve high resolution patterns, they have been merely focusing on creating very thin layer of chemicals or proteins on substrate via covalent attachement.[10–12] In this report, we designed a novel graft polymer, poly(2-methacryloyloxyethyl phosphorylcholine)-*g*-poly(allylamine hydrochloride) (PMPC-*g*-PAH), serving as an alternative enzyme immobilization matrix to BSA to enhance the capability and efficiency of enzyme transfer to microelectrode surface via μCP. The transfer of enzyme was tested for stamps with 40 μm wide and 150 μm length features corresponding to microelectrode size. In addition to providing free amine-groups for crosslinking with glutaraldehyde, PMPC-*g*-PAH here had advantages over conventional BSA such as minimizing surface diffusion, allowing longer alignment time, enhancing enzyme loading, improving enzyme-substrate affinity, as well as potentially minimizing immune response that allowed long-term stability *in vivo*. This work demonstrated that μCP combined with choline oxidase ink involving PMPC-*g*-PAH allowed fine and thick enzyme pattern selectively imprinted onto targeted sites of a microelectrode array, and

thereby greatly improving microprobe sensitivity to choline. The accomplishment here could potentially make contribution to neuroscientific research by enabling a decrease in size of MEAs in order to minimize tissue damage while providing observable signals for combined electroenzymatic sensing of multiple analytes.

6.2 Method

6.2.1 Reagents

Nafion (5 wt. % in lower aliphatic alcohols and water, contains 15-20% water), *m*-phenylenediamine (PD), bovine serum albumin (BSA) lyophilized powder, choline oxidase (ChOx) from *Alcaligenes* sp., choline chloride, L-ascorbic acid (AA), 3-hydroxytyramine (dopamine, DA), chitosan (from crab shells, minimum 85% deacetylated), glutaraldehyde (GAH) (25% in water), sodium phosphate dibasic, sodium chloride, HCl (36.5-38%), hydrogen peroxide (30 wt% solution in water), polyallylamine hydrochloride (PAH, Mw 17500), 2-methacryloyloxyethyl phosphorylcholine (MPC), Dimethyl sulfoxide (DMSO) and 4-Cyano-4-(phenylcarbonothioylthio)pentanoic acid (CTA) were purchased from Sigma-Aldrich (St. Louis, MO). 1-ethyl-3-(-3-dimethylaminopropyl) carbodiimide hydrochloride (EDC), *N*-hydroxysuccinimide (NHS), and 2,2'-Azobis[2-(2-imidazolin-2-yl)propane] Dihydrochloride (VA-044) were purchased from Thermo Fisher Scientific (Waltham, MA). Solvents were used as received. Ag/AgCl glass-bodied reference electrodes with NaCl electrolyte (3M) and a 0.5-mm-diameter Pt wire auxiliary electrode were obtained from BASi (West Lafayette, IN). Sodium phosphate buffer (PBS, pH 7.4) used for sensors calibration was composed of 50 mM sodium phosphate dibasic and 100 mM sodium chloride. Four-inch silicon wafers (p-type boron doped; thickness 150 μm) were purchased from Silicon Valley Microelectronics (Santa Clara, CA). SU-8 2075 and SU-8 developer were obtained from MicroChem (Westborough, MA). The Sylgard® 184 silicone elastomer kit was purchased from Dow Corning (Auburn, MI).

6.2.2 Instrumentation

Electrochemical preparation and *in vitro* calibration was performed using Versatile Multichannel Potentiostat (VMP3, Bio-Logic) equipped with the 'p' low current option and low current N stat box. A standard three-electrode system consisting of a separate Pt-wire as a counter electrode, a separate Ag/AgCl reference electrode and modified Pt sites on our MEA as the working electrode was used with the VMP3 system in a Faraday cage. The film thicknesses on microelectrodes were measured using a SEM (Nova 600 SEM/FIB system).

6.2.3 Synthesis of PMPC conjugated PAH via RAFT polymerization (PMPC-g-PAH)

The PAH macroCTA was synthesized by conjugating the chain transfer agent to the amino groups of PAH. Briefly, 3 mg 4-cyano-4-(phenylcarbonothioylthio) pentanoic acid was dissolved in 400 µL DMSO. The DMSO solution was mixed with 10.5 mg EDC and 2.5 mg NHS in 50 µL MES buffer (pH 5.0), followed by incubation at 4 °C or 1 h. Then 20 mg PAH in 100 µL MES buffer was added in. The mixture was stirred at room temperature for 24 h. Afterwards, the reaction solution was dialyzed against acetate buffer (pH 5.0) for 4 h to remove EDC, NHS, DMSO and unreacted CTA. The conjugation ratio was determined by UV-vis spectra. The final product was obtained by freeze-drying as a pink solid.

The PMPC-*g*-PAH graft polymer was synthesized via RAFT polymerization. Typically, 10 mg PAH-CTA (CTA, 0.0054 mmol), 80 mg MPC (0.27 mmol), and 8.7 mg VA-044 (0.027 mmol) were dissolved in 500 uL pH 5.0 acetate buffer and added into a schlenk flask. The mixture was deoxygenized through three freeze-pump-thaw processes. Then the flask was placed in water bath at 25 °C and stirred for 6 h. The polymerization was stopped by immersing the flask into liquid nitrogen. Then the reaction solution was dialyzed against DI water to remove the unreacted initiator and monomer. The final product was obtained by freeze drying. The successful synthesis

of PMPC-*g*-PAH was verified by H^1NMR spectrum (Fig 2), which showed PMPC bears about 50 units per polymer chain and the average molecular weight was approximated to be around 16.6k per polymer chain.

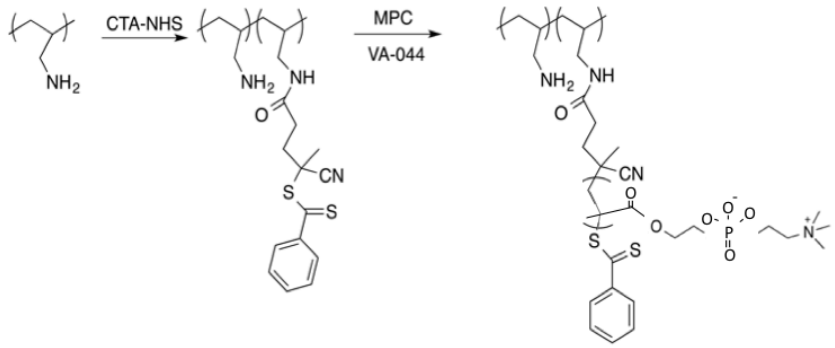

Figure 6.1. Synthesis route of PAH-*g*-PMPC polymer

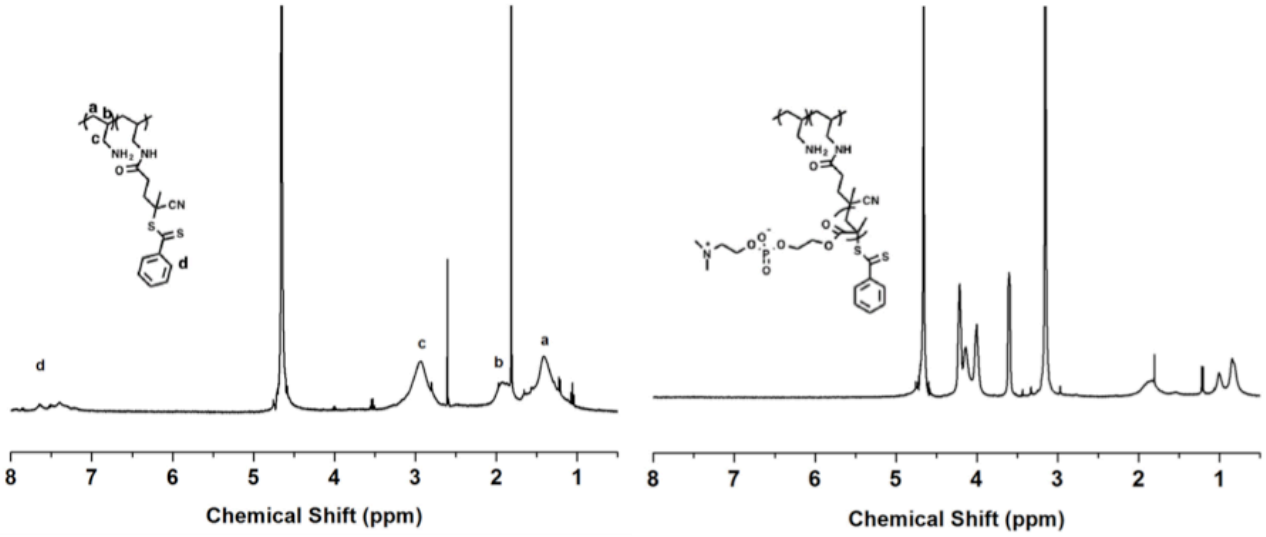

Figure 6.2. Proton NMR of PAH-CTA and PAH-*g*-PMPC

6.2.4 Sensor preparation

The silicon-based microelectrode array probes used in this work were manufactured in house using microelectromechanical system (MEMS) techniques. The processes included the physical vapour deposition of Pt as electrode material, and the chemical vapour deposition of oxide/nitride as insulation. Shaping was done by deep reactive ion etching from the front side. Each probe was 150 µm thick, 140 µm wide and 9 mm long, with four platinum recording sites (40 µm × 150 µm) arranged in pairs at the tip. (Fig. 3)

Our current sensor design is also shown in Fig 4. A PPD film first was electrodeposited on Pt microelectrodes from a 5 mM PD solution in phosphate-buffered saline (0.1 M PBS) by holding the voltage constant at 0.85 V vs. Ag/AgCl for 20 mins. Afterward, a Nafion layer then was coated by dip-evaporating a 2% Nafion solution (diluted from stock with 4:1 IPA:water) and annealed at 115 °C for 20 min. Afterward chitosan was electrodeposited from a solution (0.1% m/v) adjusted to pH = 3 using HCl (0.1M) and stirred over 48 h to ensure the chitosan flakes dissolved completely. After filtering with a 0.2 µm syringe filter, the pH was adjusted to 5 using NaOH solution (0.5 M). A constant potential of −0.7 V *vs*. Ag/AgCl was applied at the Pt electrode surface for 1 min and repeat twice while immersed in the chitosan solution to electrodeposit a chitosan film.[13,14] Finally, enzyme ink, which was prepared by mixing 4 µL ChOx (0.5 U/µL) with either 1 µL PMPC-*g*-PAH polymer (20 mg/ml) or 2 µL BSA solution (60mg/ml) to get PMPC-*g*-PAH-ChOx and BSA-ChOx inks, was printed on the desired microelectrode surface through the µCP method where the process details was described in our previous work and Fig 5.[5] Finally, the printed enzyme layer was exposed to 5% GAH solution (diluted with DI water) for 1 min to get crosslinked.

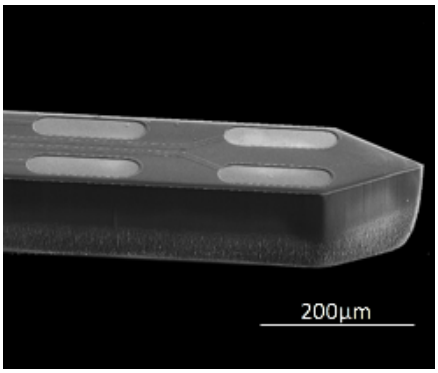

Figure 6.3. Scanning electron microscopy (SEM) image of the microelectrode array probe.

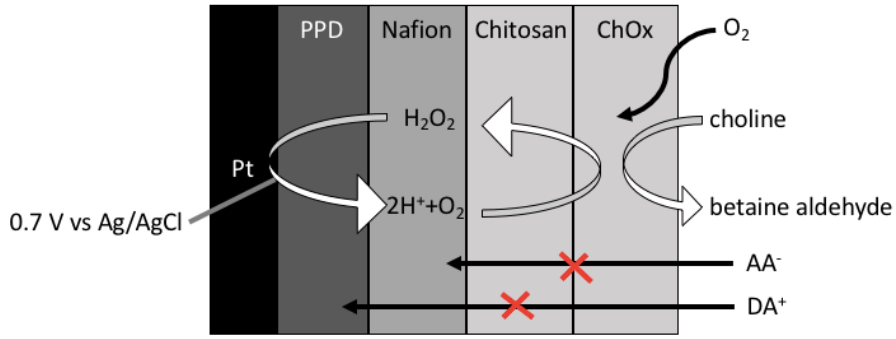

Figure 6.4. Schematic diagram for the preparation of choline sensors by modifying the electrode surface with different permselective layers (PPD and Nafion), chitosan, and choline oxidase.

6.2.5 Sensors calibration

To determine sensor selectivity and sensitivity, a constant potential of 0.7 V vs. Ag/AgCl was applied to the sensors in stirred PBS buffer solution. After few min current stabilization, AA, DA, Ch and H_2O_2 were added to the solution to give final concentration of 250 µM AA, 10 µM DA, 20-60 µM Ch and 20 µM H_2O_2 to assess sensitivity and selectivity.

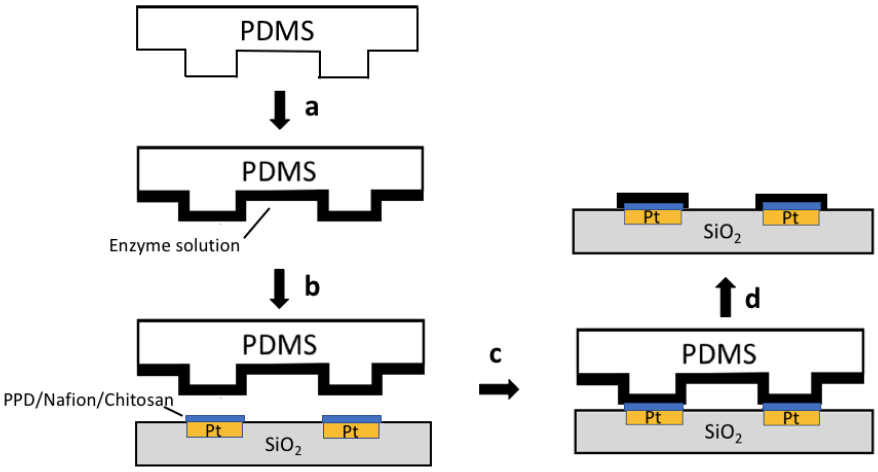

Figure 6.5. Diagram illustrating the enzyme transferring process of μCP. The PDMS stamp is inked with enzyme solution (a), carefully aligned to the target electrode surface under the microscope (b), and gently contacted for few seconds (c). This transfer formed a patterned enzyme layer on the microprobe (d).

6.3. Result and discussion

6.3.1 Problems in BSA-ChOx ink

Unlike conventional μCP that only left a very thin layer of ink on the stamp surface during inking process, printing thick enzyme pattern here skipped the step of removal of excess solution to allow greater amount of ink transferred. However, imprinting fine and thick pattern is very challenging in general as it required a good balance between ink-surface interaction and intermolecular interactions of ink that would allow proper wettability. (Fig. 6) The presence of water molecules in the ink was found helping achieve better adhesive of enzyme because chitosan modified electrode provided a hydrophilic surface. This was validated through experiments based on printing conventional enzyme ink composed of enzyme and BSA diluted in water (BSA-ChOx) in different humidified state. Stamping dry BSA-ChOx ink gave a very thin (in few hundred nm range) enzyme pattern with incomplete coverage. In contrast, presence of excess water in enzyme ink was also found not preferable as it gave molecules high mobility to

spread laterally on imprinted surface. Therefore, it was critical to ensure stamp only made contact to substrate surface within ink transferrable time that ink state had proper water content. Although imprinting thicker ChOx pattern was possible as shown in the last image in Fig. 6, μCP of BSA-ChOx showed limitations on pattern thickness of up to ~ 2 μm along with obvious surface diffusion when ChOx pattern was exposed to vapor of diluted GAH that provided relatively humid environment for crosslinking. (Fig. 7) It was hypothesized that these problems were inherently related to the ink properties as both BSA and ChOx that behave as globular particles that provide relatively weak attractive force within ink. Finally, another undesirable effect of employment of BSA-ChOx ink was its high failure rate, since the ink transferrable time was very short (only last for few seconds) due to fast evaporation of the water that made following alignment of microstamp and the targeted microelectrode a challenging process.

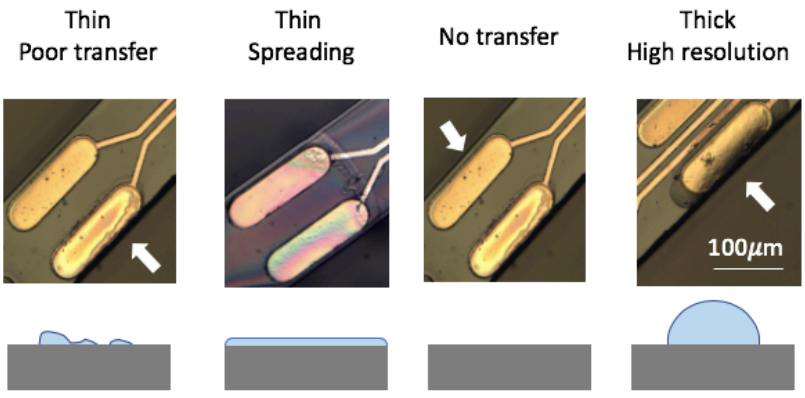

Ink-surface interaction	**Weak**	**Strong**	**Weak**	**Strong**
Ink intermolecular force	**Weak**	**Weak**	**Strong**	**Strong**

Figure 6.6. Distinct ChOx pattern on chitosan-coated substrate with various wettabilities after PDMS stamping of BSA-ChOx ink.

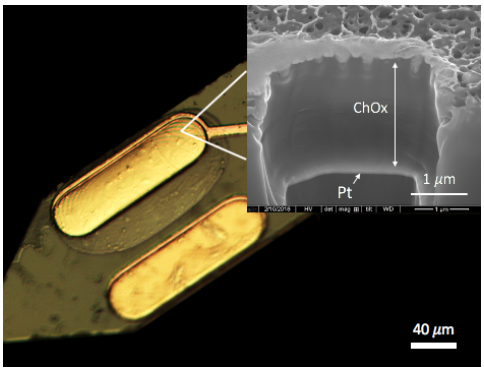

Figure 6.7. Optical microscope image of BSA-ChOx pattern on microsensors after exposure to GAH vapor and its corresponding cross-section SEM image.

6.3.2 PMPC-g-PAH-ChOx ink

It was known that physical properties of the polymer incorporated in enzyme ink are particular important in determining enzyme transfer efficiency during μCP. The key to allow high enzyme loading without pattern spreading on a hydrophilic surface is to use polymer that have hydrophilic chain with sufficiently strong forces between the chains. In Initial experiment that used polymer, poly(N-(3-aminopropyl)methacrylamide) (PAPM), which like PAH and BSA provided free amine-group for GAH crosslinking, were performed due to its ease of tunability on polymer length during free-radical polymerization. (Data is not shown in the report.) Great improvement was achieved through the use of PAPM with sufficiently high molecular weight, presumably because linear PAPM had stronger dispersion force and hydrogen bonding between molecules compared to globular BSA. On the other hand, PAPM with very high molecular weight was also found not favorable, as ink intermolecular interaction would be too strong to be printed. This initial PAPM trial provided valuable insight into the influence of polymer characteristic on μCP. Afterwards commercially available PAH (Mw = 17500 g/mol) was found to be a good alternative to PAPM that also made possible fine and thick ChOx pattern, and thereby was chosen for future work owning to its well-defined structure, conveniency and low price.

To further enhance ink hydrophilicity and provide printed enzyme anti-fouling properties, zwitterionic MPC was conjugated to PAH to get final polymer, PMPC-*g*-PAH. Zwitterionic polymers have been widely used as ultralow fouling materials in the field of biomedical devices due to their nature of superhydrophilicity that could form a shell of water molecules around them to prevent proteins attached on the surface.[15–17] In addition, it is known that enzymes keep their natural conformation on more hydrophilic environment, which the effect of PMPC-*g*-PAH on ChOx activity will be discussed later. The hydrophilicity of PMPC-*g*-PAH was assessed and confirmed by measuring the contact angle on the super hydropholic PDMS stamp that showed a large angle of over 90°. (Fig. 8) Afterwards we tested the PMPC-*g*-PAH performance on μCP of ChOx onto microelectrode. As shown in Fig 9(a)(b), it can be clearly seen that the thickness of the printed PMPC-g-PAH-ChOx was measured to be ~4 μm without observable pattern spreading after exposure to GAH/water vapor, which was ~2-fold thicker than imprinted BSA-ChOx. Moreover, employing PMPC-g-PAH-ChOx has greatly improved μCP success rate by allowing much longer time to make precise alignment and gentle contact between stamp and microprobe. This could be attributed to the stronger hydrogen bonding of water to zwitterionic polymer, which slowers the water evaporation rate.

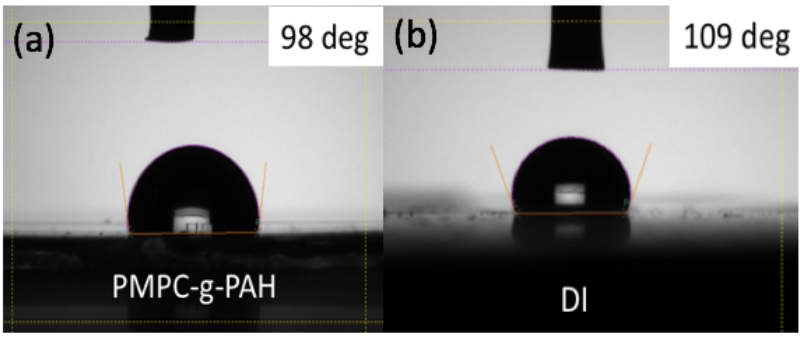

Figure 6.8. Contact angle measurements for (a) PMPC-g-PAH and (b) DI water as reference on PDMS stamps.

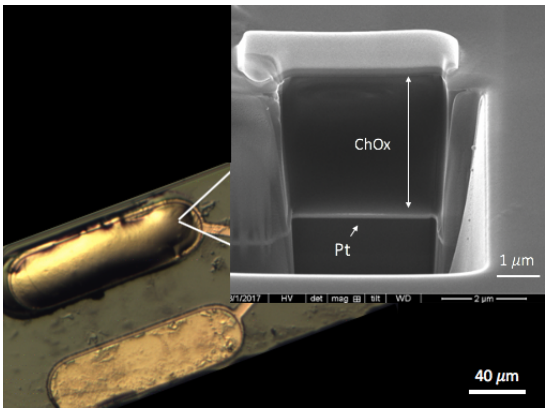

Figure 6.9. Optical microscope image of PMPC-g-PAH-ChOx pattern on microsensors after exposure to GAH vapor and its corresponding cross-section SEM image.

6.3.3 Stamped choline microsensor performance

To demonstrate that enzyme function was retained after μCP and crosslinking, all sensors were tested with choline ranging from 0 – 60 μM in PBS at the constant operating potential of 0.7 V (vs. Ag/AgCl). The choline sensor selectivity was also tested against two common electrooxidizable interferents including ascorbic acid (AA) and dopamine (DA) found in brain extracellular fluid at their physiological concentrations. The results showed that the response current of imprinted electrode increased with increase of thickness of ChOx pattern. Compared to our previously work which also used BSA-ChOx ink to create very thin ChOx pattern (expected to be < 1 μm) that reported sensitivity of 286 ± 63 nA μM^{-1} cm^{-2}, a ~1.5-fold improvement in Ch sensitivity was simply achieved by creating thicker BSA-ChOx pattern here (thickness of ~2 μm; sensitivity of 444 ± 133 nA μM^{-1} cm^{-2} (n = 5)), although there was a little compromise of pattern resolution.[5] (Fig. 10(b)) Further increase in ChOx loading when PMPC-*g*-PAH used as enzyme matrix, led to another 1.5-fold improvement in sensitivity (thickness of ~4 μm; sensitivity of 639 ± 96 nA μM^{-1} cm^{-2} (n = 4)) with high pattern resolution. As these improvements of sensitivity were achieved without sacrificing background noise and selectivity, limit of detections (signal-to-noise

ratio of 3) of imprinted PMPC-*g*-PAH-ChOx and imprinted BSA-ChOx sensors in this work were also greatly improved, which were 0.31 ± 0.06 μM (*n* = 4) and 0.45 ± 0.17 μM (*n* = 5), respectively. (Fig 10(c)) This high sensitivity obtained from PMPC-*g*-PAH-ChOx stamped microsensors has not been surpassed by other choline sensor designed including those with non-selective enzyme immobilization.[5,18–22]

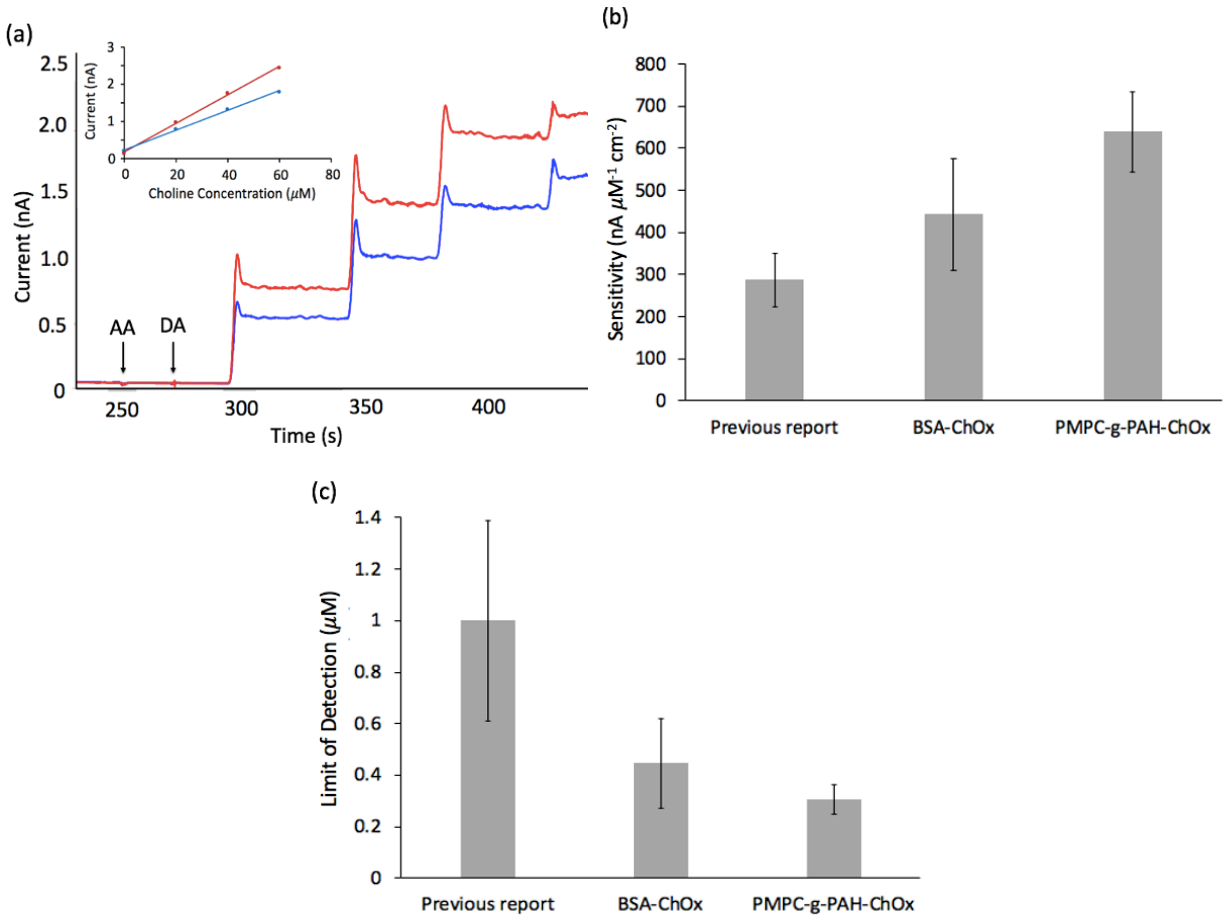

Figure 6.10. (a) Representative current response of stamped BSA-ChOx (blue trace) and stamped PMPC-g-PAH-ChOx (red trace) Ch sensors to interferents, 250 μM AA and 5 μM DA, following by three 20 μM step increase in ChCl and a 20 μM increase in H_2O_2. (b) Choline sensitivity and (c) limit of detection calibration over a range of 0-60 μM. (error showing 95% confident interval)

6.3.4 Enzyme Affinity

The basic Michaelis-Menten enzyme parameters were measured to provide more accessible insights into factors affecting the responsiveness of sensors. When the concentration of co-substrate O_2 is constant, the kinetic of ChOx under conditions of varying concentration of choline could be described in the one-substrate Michaelis-Menten form (Eqn. 3). K_M here is the apparent Michaelis-Menten constant, where the current is measured of the overall rate of enzyme reaction and molecular diffusion and phenomenologically defined the Ch concentration that gives half of the I_{max} response. Here I_{max} across sensor designs could be a good reflection of the amount of active enzyme present.

$$\text{Choline} + O_2 + H_2O \xrightarrow{\text{ChOx}} \text{betaine aldehyde} + H_2O_2 \quad (1)$$

$$H_2O_2 \rightarrow O_2 + 2H^+ + 2e^- \quad (2)$$

$$I_{ch} = \frac{I\max}{1+\frac{KM}{[ch]}} \quad (3)$$

As shown in Fig. 11, ~1.5-fold increase in I_{max} from PMPC-g-PAH-ChOx stamped microsensors compared to those stamped with BSA-ChOx indicated that greater amount of active enzyme was transferred onto the electrode surface after μCP. Furthermore, we typically see $K_M{}^{app}$ value increases with enzyme loading due to the increased diffusion barrier for H_2O_2 traveling through to Pt surface. However, PMPC-*g*-PAH-ChOx stamped microsensors exhibited similar $K_M{}^{app}$ value as those imprinted with BSA-ChOx, which respectively were 110 ± 18 μM (n = 4) and101 ± 27 (n = 5), even though the PMPC-*g*-PAH-ChOx pattern was 2-fold thicker. It was hypothesized that, unlike BSA (pI: 4.7) serveing as a negatively charged matrix, PMPC-g-PAH polymer is globally positively charged, thereby helping counterbalancing polyanionic ChOx to prevent enzymes from aggregation. This result consistent with other published experimental reports showing that pre-coating the Pt with polycation led to a large decrease in the $K_M{}^{app}$.[23] In addition,

presence of zwitterionic MPC might also play an important role on increasing sensitivity and lowering K_M^{app} because its superhydrophilicity would increase penetration of Ch in the enzyme film.

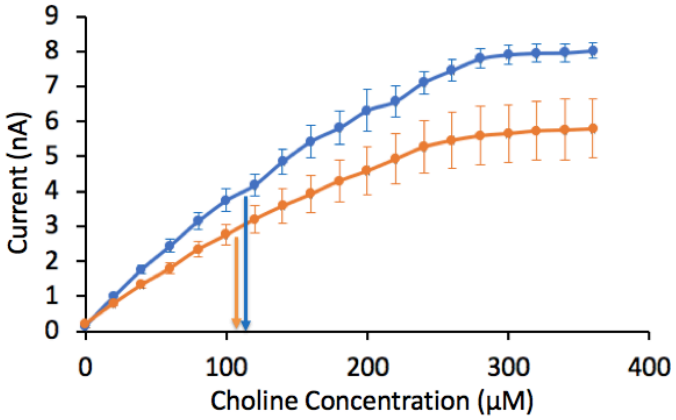

Figure 6.11. Comparison between K_M and V_{max} observed from choline stamped microsensors with PMPC-g-PAH-ChOx (blue curve; K_M^{app} = 110±18 µM; V_{max} = 7.9±0.6 nA with n = 4) and BSA-ChOx (orange curve; ; K_M^{app} = 101±27 µM; V_{max} = 5.8±1.7 nA with n = 5) with error bar shown 95% confident interval.

6.4 Conclusion

Enzyme loading and pattern resolution on the microelectrode surface are two critical factors to allow creation of highly sensitive microprobe for multianalyte sensing. We demonstrated PMPC-*g*-PAH polymer as an effectively alternative enzyme immobilization matrix to BSA for enhancing µCP enzyme. Compared to sensors imprinted with ChOx-BSA, PMPC-*g*-PAH-ChOx printed sensors led to much thicker ChOx pattern in high resolution that showed high sensitivity for Ch (639 ± 96 nA μM^{-1} cm^{-2} (n = 4)), fast response time within a second, and very low limit of detection (0.31 ± 0.06 µM (n = 4)). Furthermore, incorporation of PMPC-*g*-PAH greatly improved µCP success rate by allowing much longer alignment time. Therefore, µCP combined with PMPC-*g*-PAH as enzyme immobilization matrix is expected to contribute to neuroscience research by

making possible the creation of thick enzyme layer in high resolution on selected microelectrode sites on a microprobe thereby enabling highly sensitive detection of multiple analytes in close proximity simultaneously. This high sensitivity will also allow greater flexibility in shrinking electrode surface size in the future to minimize tissue damage. Finally, the use of PMPC-*g*-PAH has potential to provide better stability for long-term experiment *in vivo,* as zwitterionic MPC has been widely reported to minimize immune response, which will require further investigation *in vivo.*[15–17]

6.5 References

1. Yang, H., Thompson, A. B., Mcintosh, B. J., Altieri, S. C. & Andrews, A. M. Physiologically Relevant Changes in Serotonin Resolved by Fast Microdialysis. *ACS Chem. Neurosci.* **4**, 790–798 (2013).
2. Bowser, M. T. & Kennedy, R. T. In vivo monitoring of amine neurotransmitters using microdialysis with on-line capillary electrophoresis. *Electrophoresis* **22**, 3668–3676 (2001).
3. Rutherford, E. C., Pomerleau, F., Huettl, P., Strömberg, I. & Gerhardt, G. A. Chronic second-by-second measures of L-glutamate in the central nervous system of freely moving rats. *J. Neurochem.* **102**, 712–722 (2007).
4. Rogers, M. L. *et al.* Continuous online microdialysis using microfluidic sensors: Dynamic neurometabolic changes during spreading depolarization. *ACS Chem. Neurosci.* **4**, 799–807 (2013).
5. Wang, B., Koo, B., Huang, L. W. & Monbouquette, H. G. Microbiosensor fabrication by polydimethylsiloxane stamping for combined sensing of glucose and choline. *Analyst* **143**, 5008–5013 (2018).
6. Huang, I. *et al.* Electroenzymatic glutamate sensing at near the theoretical performance

limit. *Analyst* (2020). doi:10.1039/c9an01969c

7. Collins, A. L. *et al.* Archival Report Nucleus Accumbens Cholinergic Interneurons Oppose Cue-Motivated Behavior. *Biol. Psychiatry* **86**, 388–396 (2019).
8. Wassum, K. M. *et al.* Silicon wafer-based platinum microelectrode array biosensor for near real-time measurement of glutamate in vivo. *Sensors* **8**, 5023–5036 (2008).
9. Burmeister, J. J. *et al.* Improved ceramic-based multisite microelectrode for rapid measurements of L-glutamate in the CNS. *J. Neurosci. Methods* **119**, 163–171 (2002).
10. Perl, A., Reinhoudt, D. N. & Huskens, J. Microcontact Printing: Limitations and Achievements. *Adv. Mater.* **21**, 2257–2268 (2009).
11. Blinka, E. *et al.* Enhanced microcontact printing of proteins on nanoporous silica surface. *Nanotechnology* **21**, 5302 (2010).
12. Buhl, M., Vonhören, B. & Ravoo, B. J. Immobilization of Enzymes via Microcontact Printing and Thiol-Ene Click Chemistry. *Bioconjug. Chem.* **26**, 1017–1020 (2015).
13. Li-Qun Wu, †,‡ *et al.* Voltage-Dependent Assembly of the Polysaccharide Chitosan onto an Electrode Surface. (2002). doi:10.1021/LA020381P
14. Tseng, T. T.-C., Yao, J. & Chan, W.-C. Selective enzyme immobilization on arrayed microelectrodes for the application of sensing neurotransmitters. *Biochem. Eng. J.* **78**, 146–153 (2013).
15. Xie, X. *et al.* Reduction of measurement noise in a continuous glucose monitor by coating the sensor with a zwitterionic polymer. *Nat. Biomed. Eng.* **2**, 894–906 (2018).
16. Dhanjai, Lu, X., Wu, L., Chen, J. & Lu, Y. Robust Single-Molecule Enzyme Nanocapsules for Biosensing with Significantly Improved Biosensor Stability. *Anal. Chem.* **92**, 5830–5837 (2020).
17. Zhang, E. & Cao, Z. Coated glucose sensors dodge recalibration. *Nat. Biomed. Eng.* **2**,

881–882 (2018).

18. Burmeister, J. J. *et al.* Ceramic-based multisite microelectrode arrays for simultaneous measures of choline and acetylcholine in CNS. **23**, 1382–1389 (2008).

19. Keihan, A. H., Sajjadi, S., Sheibani, N. & Moosavi-Movahedi, A. A. A highly sensitive choline biosensor based on bamboo-like multiwall carbon nanotubes/ionic liquid/Prussian blue nanocomposite. *Sensors Actuators B Chem.* **204**, 694–703 (2014).

20. Zhang, H., Yin, Y., Wu, P. & Cai, C. Indirect electrocatalytic determination of choline by monitoring hydrogen peroxide at the choline oxidase-prussian blue modified iron phosphate nanostructures. *Biosens. Bioelectron.* **31**, 244–250 (2012).

21. Rahimi, P., Ghourchian, H. & Sajjadi, S. Effect of hydrophilicity of room temperature ionic liquids on the electrochemical and electrocatalytic behaviour of choline oxidase. doi:10.1039/c1an15732a

22. Khan, A. & Ghani, S. A. Multienzyme microbiosensor based on electropolymerized o-phenylenediamine for simultaneous in vitro determination of acetylcholine and choline. *Biosens. Bioelectron.* **31**, 433–438 (2012).

23. McMahon, C. P. *et al.* The efficiency of immobilised glutamate oxidase decreases with surface enzyme loading: an electrostatic effect, and reversal by a polycation significantly enhances biosensor sensitivity. *Analyst* **131**, 68–72 (2006).

Chapter 7: Flexible, multifunctional neural probe with liquid metal enabled, ultra-large tunable stiffness for deep-brain chemical sensing and agent delivery

Chapter 7 is a manuscript published with the following citation:

Ximiao Wen, Bo Wang, Shan Huang, Tingyi “Leo” Liu, Meng-Shiue Lee, Pei-Shan Chung, Yu Ting Chow, **I-Wen Huang**, Harold G. Monbouquette, Nigel T. Maidment, Pei-Yu Chiou. Biosensors and Bioelectronics 131 (2019) 37–45

I-Wen Huang’s contribution to this work focused on assisting in sensor preparation and sensor calibration. These involved developing an electrochemical cleaning step to clean the sensing surface and optimizng enzmye immobilization processes to ensure higher sensitivity of sensors.

Abstract

Flexible neural probes have been pursued previously to minimize the mechanical mismatch between soft neural tissues and implants and thereby improve long-term performance. However, difficulties with insertion of such probes deep into the brain severely restricts their utility. We describe a solution to this problem using gallium (Ga) in probe construction, taking advantage of the solid-to-liquid phase change of the metal at body temperature and probe shape deformation to provide temperature-dependent control of stiffness over 5 orders of magnitude. Probes in the stiff state were successfully inserted 2 cm-deep into agarose gel “brain phantoms” and into rat brains under cooled conditions where, upon Ga melting, they became ultra soft, flexible, and stretchable in all directions. The current 30 μm-thick probes incorporated multilayer, deformable microfluidic channels for chemical agent delivery, electrical interconnects through Ga wires, and

high-performance electrochemical glutamate sensing. These PDMS-based microprobes of ultra-large tunable stiffness (ULTS) should serve as an attractive platform for multifunctional chronic neural implants.

7.1 Introduction

Implantable neural probes constitute an important class of technologies used by neuroscientists both to modulate and to detect electrical and chemical neuronal activities in the brain. These tools are also employed clinically for deep brain stimulation (DBS), a treatment for several conditions, including Parkinson's disease, epilepsy, depression and obsessive compulsive disorder (OCD) (Minev et al., 2015; Park et al., 2016; Rivnay et al., 2017). For research purposes, neural probes are often implanted in assemblies with injection cannulae for local microinjection of drugs or viruses thereby providing an additional level of neurological manipulation and control (Jeong et al., 2015a; Rohatgi et al., 2009). However, such assemblies can cause significant damage to the targeted brain region due to their large footprint (Sim et al., 2017). In the past ~30 years, the development of microelectromechanical systems (MEMS) has led to the creation of silicon-based neural probes with integrated microfluidic channels for material delivery (Chen et al., 1997; McAllister et al., 2003; Reed and Lye, 2004). While smaller overall, the large mechanical mismatch and micromotion between such rigid probes (E=200 GPa) and soft brain tissue (E=0.4–15 kPa) is one of several possible triggers of the long-term inflammatory responses that cause neuronal loss and scar formation around the implants, limiting their chronic recording and stimulating capabilities (Jeong et al., 2015b; Jorfi et al., 2015; Rivnay et al., 2017).

In recent years, flexible probes based on plastics such as polyimide and SU-8 have been developed in an attempt to circumvent the mechanical mismatch problem by shrinking the probe dimension aggressively to micron-scale (Liu et al., 2015; Luan et al., 2017; Wu et al., 2015). However, the desirably weak mechanical stiffness presents a major challenge during the deep-

brain implantation process. To mitigate this issue, soft probes were either coated with stiffening polymer that dissolves after implantation (Tien et al., 2013; Xiang et al., 2014), or were made of polymers that soften after implantation (Capadona et al., 2012; Ware et al., 2014). However, deep-brain implantation (> 3 mm) is challenging for such probes due to the low Young's modulus (~2 GPa) of such polymers resulting in the need for large cross-sectional areas to provide sufficient stiffness to prevent buckling during insertion (Tien et al., 2013; Weltman et al., 2016; Wu et al., 2015; Xiang et al., 2014). Soft probes can also be attached to a stiff shuttle, such as a metal syringe or a silicon probe, that can be retracted after insertion (Liu et al., 2015; Luan et al., 2017; Kim et al., 2013). However, the final location of the inserted probes may be disturbed during shuttle retraction and the shuttle may cause undesirable tissue damage (Felix et al., 2013). These latter approaches also require a labor intensive high-precision manual alignment and assembly process, particularly when multi-shank and 3D probe arrays are desired for multi-region recording. Another major concern of some prior flexible probes, such as injectable mesh electrodes or super thin plastic films, is that the materials used in such probes are still “hard” (plastics and nanowires). Thus, the probe structures need to be extremely thin and narrow in order to be flexible, which may compromise the functions that can be integrated on a probe. For example, integration of fluid channels on these probes for drug delivery is difficult since the flow resistance in a channel increases inversely with thickness by ($1/t^3$) (Bruus, 2011). Sensitivity of integrated electrochemical sensing electrodes on these narrow probe structures may also be compromised by their necessarily small surface area. The above-mentioned functions enable the monitoring of chemical transmission and manipulation of brain activities, which are extremely important in understanding brain functions and dissection of neural circuits.

To solve these confounding issues encountered by current flexible probes, here, we present a multifunctional, flexible and stretchable neural probe for chemical sensing and chemical

delivery. The stiffness of this probe can be tuned by 5 orders of magnitude before and after brain insertion, thereby enabling self-implantation into deep brain regions without using external shuttle carriers. Once implanted, the probe becomes soft and flexible within a few minutes. With miniaturized design (30 μm-thick) and soft substrate material (E~1 MPa), this flexible and stretchable probe causes less tissue damage induced by brain movements in all directions (Nguyen et al., 2014; Subbaroyan et al., 2005). Deposition of appropriate enzymes and exclusion polymers onto platinum (Pt) microelectrode sites on the probe permits high-sensitivity electrochemical detection of neurotransmitters in deep-lying brain structures, and the integration of microfluidic channels allows delivery of drugs and other chemicals in the local vicinity of the sensing sites.

7.2 Experimental section

7.2.1. ULTS probe design and working principle

The multifunctional, ultra-large tunable stiffness (ULTS) probe is a compact, multi-layer, free-standing structure that integrates Pt electrodes, microfluidic channels, and electrical interconnects, all on a 30 μm-thick PDMS structure (Fig. 1a). PDMS was used as the structural material due to its low Young's Modulus (E~1 MPa), high stretchability, and biocompatibility (Lee et al., 2016; Minev et al., 2015). Pt microelectrodes for high sensitivity electrochemical sensing were fabricated on small, thin silicon dioxide islands on a separate silicon substrate and transferred onto the ULTS probe. To provide electrical connections to these electrodes on the flexible and stretchable probe without cracking and delamination issues, gallium (Ga), a liquid metal, was used due to its fluidity, high electrical conductivity, and biocompatability (Chow et al., 2018; Dickey, 2017; Hallfors et al., 2013).

Two key physical material properties—the elasticity of PDMS (Fig. 1b) and the near-body-temperature melting point of Ga (~30 °C)—were needed to realize the large tunable stiffness

property of our probes. During fabrication, pressurized liquid Ga was introduced into the stretchable microfluidic “stiffening” channel to deform and enlarge the cross section of the probe and then frozen to solid state (E=10 GPa) to achieve a stiff probe for deep brain implantation (Fig. 1c). At body temperature (~37 °C), Ga melted and was removed from the stiffening channel by suction to reduce probe thickness and stiffness (Fig. 1d). During probe implantation, the brain tissue was transiently cooled to below 30 °C by application of chilled saline to the skull surface, a commonly used local and reversible experimental neuronal inhibition method (Long and Fee, 2008; Peel et al., 2017) and therapeutic process for neuroprotection (Dietrich et al., 2009; Kuluz et al., 1992). After implantation, Ga melted immediately upon brain temperature recovery (Fig. 1e–g).

7.2.2 Fabrication of ULTS probes

The multifunctional ULTS probes were fabricated on silicon wafers using conventional microfabrication processes for electrode patterning, and a customized PDMS thin-film transfer process to form the probe substrate and microchannels with 1 drug delivery port and 2 electrochemical sensing sites. Detailed steps involved in the fabrication of ULTS probes are illustrated in Supplementary Fig. S1, and details of the PDMS thin-film transfer process are described in Supplementary Fig. S2. Key fabrication processes are summarized as follow: (i) Pt electrodes, soldering pads and SiO_2 insulators were patterned on a silicon substrate, which serves as a sacrificial layer. (ii) PDMS thin-film was deposited and patterned by a PDMS lift-off process. This layer of PDMS physically connects the electrodes on the probe tip with the probe base, as well as providing bottom passivation of electrical interconnects and drug delivery channel. (iii) A second PDMS thin-film with microfluidic channels and top passivation was transferred and bonded to the first PDMS layer via O_2 plasma (80 W, 500 mT, 30 s). (iv) A third PDMS stiffening channel was transferred and bonded via O_2 plasma. (v) Liquid Ga was injected into interconnects

and stiffening channels and frozen to solid state to maintain the shape and strength after XeF_2 releasing process. (vi) The probes were released by the silicon undercut using XeF_2. A 2 cm-long single-shank ULTS probe and a 1 cm-long 4-shank probe are designed to demonstrate the mechanical properties of ULTS probes.

Similar to our prior silicon-based probes (Wang et al., 2018), the oval-shaped sensing electrodes (40 ×150 μm, width × length) are located at the tip of the probe shank (0.144 × 9 mm, width × length). Key dimensions of the three PDMS layers and associated channels are as follows: bottom substrate, 5 μm thick, wire & drug delivery channel, 10 μm thick, stiffening channel, 15 μm thick, microchannels for electrical interconnects and drug delivery, 15 × 5 μm (width × height), Ga stiffening channel, 104 × 10 μm (width × height). These conservative design parameters were chosen to achieve a high fabrication yield and may be modified in the future to further reduce the probe dimensions.

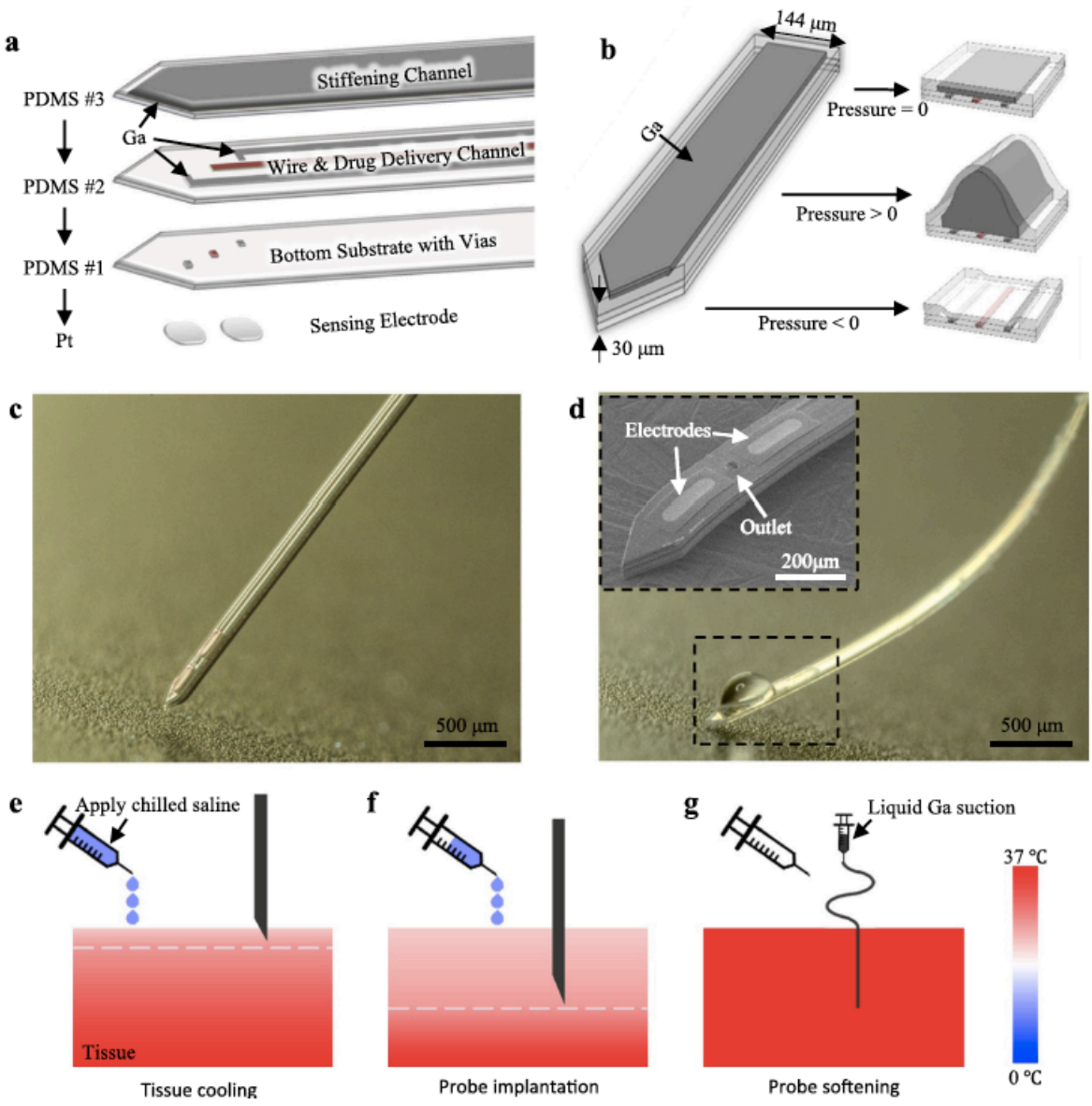

Figure 7.1. Design and working principle of ULTS probes. (a) An exploded-view drawing of a ULTS probe with 3 layers of PDMS thin-films integrated with Pt electrodes for electrochemical sensing. The first PDMS layer serves as the bottom substrate of the probe. Three through-layer holes (vias) are patterned, one serving as liquid outlet, and two for electrical connection to the sensing electrodes. The second PDMS layer is composed of three microfluidic channels, one for drug delivery and two filled with liquid metal (Ga) for electrical connections. The third PDMS layer has one liquid channel filled with liquid Ga, which is then frozen to stiffen the probe. (b) Schematics illustrating the swelling of the ULTS probe shank under different Ga filling pressures: i) no pressure, flat state; ii) positive pressure, inflated state; iii) negative pressure (suction), deflated state. (c) Picture of a fabricated ULTS probe in the stiff state for brain implantation. (d) A

ULTS probe in the soft state with integrated drug delivery function. Inset, a SEM image of the probe tip showing the outlet of the drug delivery channel and Pt electrodes. (e–g) Schematic of the implantation procedure. Tissue is cooled down from the surface by the application of chilled saline. The white dashed line represents the temperature of the Ga melting point, 30 °C, above which the probe becomes flexible. After implantation, Ga melts and is removed from the stiffening channel by suction to reduce probe thickness and stiffness. Temperature is represented in color scale.

7.2.3 Biosensor preparation

Pt microelectrodes on the ULTS probes were modified to serve as enzymatic biosensors for detection of glutamate (Glut), the major excitatory neurotransmitter in the mammalian central nervous system (Danbolt, 2001; Gass and Foster Olive, 2008). Amperometric electroenzymatic methods for the near real-time detection of Glut and other neurochemicals have been described previously using Pt microelectrodes coated with crosslinked, H_2O_2-generating oxidases (e.g. glutamate oxidase (GlutOx)) (Tolosa et al., 2013; Wassum et al., 2008).H_2O_2, generated from the oxidation of substrate (i.e., analyte), which is catalyzed by the oxidase, is electrooxidized by the application of anodic potential to the underlying Pt microelectrodes. The resultant electrical current signals are recorded and correlated to analyte concentration. A layer of poly-*m*-phenylenediamine (PPD) was electrodeposited on the Pt microelectrodes in this study to block the common electroactive interferents in the rat striatum, dopamine (DA) and ascorbic acid (AA) (Wahono et al., 2012; Wang et al., 2018).

All electrochemical experiments were conducted inside Faraday cages, and experimental setups are summarized in Supplementary Fig. S3. Electrochemical preparation and characterization of the microelectrode sensors were performed using a Versatile Multichannel Potentiostat (model VMP3) equipped with the ‘p’ low current option and low current ‘N’ stat box (Bio-Logic USA, LLC, Knoxville, TN, USA) in a three-electrode configuration.

For sensor preparation, microelectrodes on ULTS probes were rinsed with DI water followed by an electrochemical cleaning step with 0.5M sulfuric acid. Electropolymerization of m-phenylenediamine on the electrode surface was conducted using a Pt wire counter electrode, a glass encased Ag/AgCl in 3M NaCl solution reference electrode (Bioanalytical Systems, Inc., West Lafayette, IN, USA) (Supplementary Fig. S3a), and a Pt working electrode on the ULTS probe immersed in a stirred solution of 5mMm-phenylenediamine in phosphate-buffered saline (PBS), with an applied potential of 0.85 V vs. Ag/AgCl for 15 min. After PPD deposition, the GlutOx solution for enzyme immobilization was prepared by mixing 2 µL GlutOx (250 unit/mL) with 3 µL BSA solution (10 mg/mL) containing glutaraldehyde (0.125% v/v). A ~0.1 mL drop of the solution was formed on a syringe tip and gently swiped across the microelectrode sites at the probe tip. This procedure was repeated 11 times for optimal sensitivity (Wassum et al., 2012). The resulting Glut sensor microprobe was left to dry overnight in a desiccator at 4 °C.

7.2.4 In vitro biosensor characterization and testing

A separate microscale iridium oxide (IrOx) reference electrode, described previously (Tolosa et al., 2013) was used for *in vitro* and *in vivo* experiments (Supplementary Fig. S3b). Before IrOx deposition, electrode surfaces were first modified with Pt nanoparticles to increase the surface area (Boehler et al., 2015). To characterize the biosensor, a potential of 0.6 V was applied vs. IrOx in a beaker containing 10 mL of stirred PBS solution, and three 20 µL aliquots of Glut (10 mM) were consecutively added to the same beaker to reach final Glut concentrations of 20, 40 and 60 µM. Additionally, aliquots of the potential interferents, AA and DA, were added to the beaker to attain physiological brain concentrations of 250 µM and 5–10 µM, respectively, to confirm selectivity for Glut over the interferents at physiological concentrations (Spector, 1977; Eriksson et al., 1999). To characterize the linear range of the biosensor, eight 20 µL aliquots of Glut (10 mM) were sequentially added to the beaker containing 10 mL PBS solution to reach final

Glut concentrations of 20, 40, 60, 80, 100, 120, 140 and 160 μM. Before making measurements, 30 min of equilibrium time immersed in PBS was required for the current detected to approach a constant baseline.

Electrochemical sensing experiments in brain phantoms (0.6% agarose gel in artificial cerebrospinal fluid (aCSF)) were conducted with a multichannel FAST-16 potentiostat (Quanteon, LLC, Lexington, KY, USA) using a two-electrode system consisting of a separate microscale IrOx reference electrode and Glut biosensors on the ULTS microprobe (Supplementary Fig. S3d). Amperometric data were collected at 80 kHz, averaged over 0.1 s intervals and further processed using a moving average filter with 11 input points in MATLAB to remove noise at 1 Hz.

7.2.5 Acute in vivo studies

Each Glut biosensor on the ULTS microprobe was calibrated (sensitivity and selectivity) right before and after the in vivo studies (Supplementary Fig. S3c). A calibration factor based on analysis of these data was calculated for each electrode on the ULTS microprobes to be used for *in vivo* experiments. *In vivo* electrochemical sensing experiments were conducted in the same configuration as in brain phantoms (Supplementary Fig. S3d), except for a longer equilibrium time of 60 min.

Male Sprague Dawley rats (260–330 g) were anesthetized with isoflurane and placed in a standard stereotaxic frame for surgery. All experimental procedures and surgeries were conducted in accordance with the Institutional Animal Care and Use Committee of UCLA.

A microscale temperature probe (HYP1-30-1/2-T-G-60-SMP-M, Omega Engineering, Inc.) was lowered through a craniotomy to a depth of 5.0mm at a site remote from the recording area. Chilled sterile saline (~10 °C) was perfused across the skull surface at a flow rate of 1–3 mL/ min to cool the brain tissue to just below 30 °C. The pre-calibrated ULTS probe was then unilaterally implanted into the right striatum (from bregma: A/P+1.0 mm, M/L +2.5 mm and D/V −5.0 mm)

according to the atlas of Paxinos and Watson (4th ed.). After insertion of the probe, the temperature probe was removed and replaced by a microscale IrOx reference electrode at the same location. Animals remained under anesthesia throughout the experiment. High potassium (100 mM) artificial cerebrospinal fluid (aCSF: 27.5mM NaCl, 100mM KCl, 0.9mM NaH_2PO_4, 5mM Na_2HPO_4, 1.2mM $CaCl_2$, 1mM $MgCl_2$, pH 7.4) or Glut (500 μM in normal aCSF–as above except 125mM NaCl and 2.5mM KCl) was injected when the electrode signal reached the equilibrium state.

Changes in signals were recorded following pressure injection of high potassium aCSF or Glut by a pressure source (FemtoJet, Eppendorf) at various time intervals. Responses were recorded across a range of signal amplitudes by increasing the duration of pressure injection (0.3–4.8 s) and thereby increasing the volume injected (~1–20 nL).

7.3 Results and discussion

7.3.1 Characterization of probe tunable stiffness and implantation in brain phantoms

To investigate the tunable stiffness range, we first characterized the probe deformation with respect to different Ga filling pressures using a contact profilometer (Fig. 2a–c). The maximum pressure injected was 60 psi, which resulted in the largest channel deformation of ~67 μm. The range of tunable bending stiffness was determined based on the Young's modulus and the probe shape between the “stiff”, inflated state and the “soft”, deflated state. For estimation, the expanded shape was approximated to be a semi-circle (profile at 30 psi) with a radius of 52 μm. This resulted in a stiffness difference of 5 orders of magnitude between these two states, where the Ga phase change contributes ~4 orders of magnitude and the shape change contributes the remaining 10-fold difference (Supplementary Fig. S4). A larger tunable range can be obtained if using softer elastomers with higher stretchability, which can further increase its

softness in the “soft” state as well as its stiffness in the “stiff” state due to the larger deformation under the same filling pressure.

We implanted the ULTS probes in brain phantoms (0.6% agarose gel), which has similar mechanical properties to neural tissue (Jeong et al., 2015a). A 2 cm-long ULTS probe, filled with Ga at 60 psi, could be implanted successfully into this brain phantom in “stiff” state at room temperature (Fig. 2d), whereas a probe in “soft” state at elevated temperature (T > 30 °C) deformed upon contact with the brain phantom surface. A four-shank ULTS probe was also fabricated and implanted successfully into the brain phantom, demonstrating the capability to scale up to multi-shank probes for large volume neural recordings (Fig. 2e). After implantation, the brain phantom was heated in a water bath to 37 °C to simulate brain temperature recovery. Ga melted and the stiffening channel was deflated by active suction from the inlet of the Ga channel to reduce the bending stiffness in the “soft” state (Fig. 2f, g).

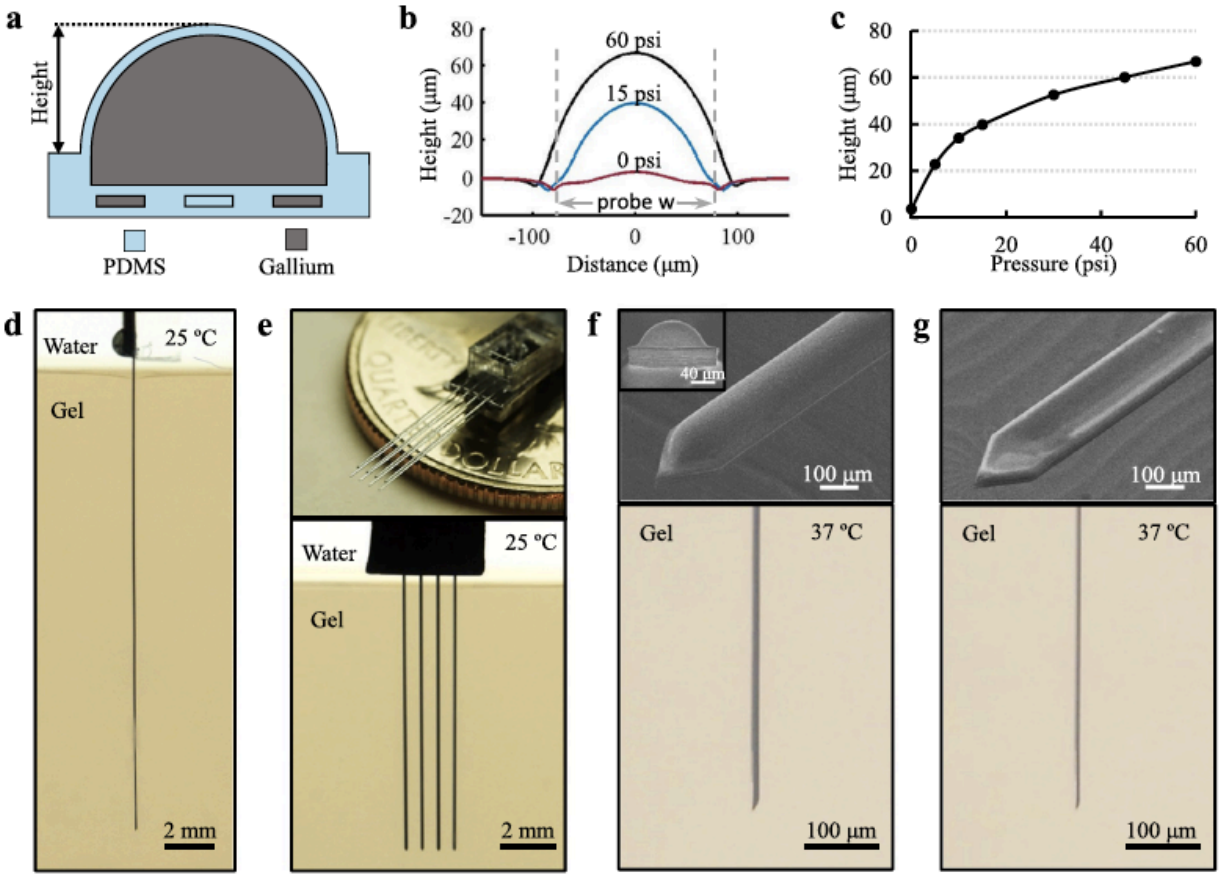

Figure 7.2. Characterization of probe tunable stiffness and implantation capability in brain phantoms. (a) Schematic cross-sectional view of an inflated probe. (b,c) Characterization of the probe shank swelling with respect to different Ga filling pressure. Dashed lines represent the boundaries of the probe (144 μm-wide). The slightly longer distance under 60 psi is a measurement artifact due to steep edge of the largely deformed probe and the cone shape of the profilometer's stylus. (d) Demonstration of a 2 cm-long ULTS probe implanted in a brain phantom (0.6% agarose gel) at room temperature, with a Ga injection pressure of 60 psi to achieve maximum stiffness. (e) Top, picture of a 4 × 2 probe array by stacking two 4-shank probes. Bottom, insertion of a 1 cm-long, 4-shank probe in a brain phantom. (f) ULTS probe in the “inflated” state with 15 psi injection pressure. Top, SEM ‘bird's-eye’ view. Inset, front view showing a shank swelling height of 40 μm, scale bar, 40 μm. Bottom, side-view of an inflated probe implanted in a brain phantom. (g) ULTS probe in the “deflated” state. Top, SEM ‘bird's eye’ view. Bottom, side-view of a probe in a brain phantom deflated by active suction of Ga.

7.3.2 Demonstration of probe flexibility in brain phantoms

To demonstrate the flexibility of ULTS probes, we moved the probe/ brain phantoms to simulate the relative motion between the brain and the skull. As shown in Fig. 3a, the implanted portion of our flexible probe remained steady regardless of the probe movement above the brain phantom. We also compared ULTS probes with silicon and SU-8 based probes of similar dimension, which created large "wounds" (Fig. 3b-e and Supplementary Movie 1). The experiment demonstrated significant reduction of relative motion in all directions compared to probes made of stiffer materials as suggested from previous simulations (Subbaroyan et al., 2005).

7.3.3 In vitro probe characterization

Fig. 4a. illustrates the structure of a biosensor. The sensitivity (8.2 $\pm$ 1.2 pA/μM), detection limit (0.39 $\pm$ 0.07 μM at a signal-tonoise ratio of 3; *n*=4) and response time (~1 s) achieved are comparable to the performance characteristics of our prior silicon-based microprobes with the same sensor design (Tolosa et al., 2013; Wassum et al., 2008). With repetitive addition of Glut, the sensors displayed a linear response up to 160 μM (R^2 = 0.994) (Fig. 4b and Supplementary Fig. S5a), which covers the physiological range (Tolosa et al., 2013; Wassum et al., 2008). For the same sensors, AA and DA were successfully excluded at supra-physiological concentrations by the PPD layer (Fig. 4c).

The drug delivery function of the ULTS probes was initially evaluated by using a pressure source to inject an aqueous solution of Allura Red AC from the probe into brain phantom (Fig. 4d). The flow rate through the PDMS microfluidic channel was linear with pumping pressures in the range of 30–60 psi (R^2=0.995; *n*=3) (Supplementary Fig. S5b). Local injections of H_2O_2 (40 μM) and Glut (150 μM) via the channel into brain phantoms (0.6% agarose gel in aCSF), were rapidly detected by the biosensors, the signal amplitude varying with injection volume (Fig. 4e, f).

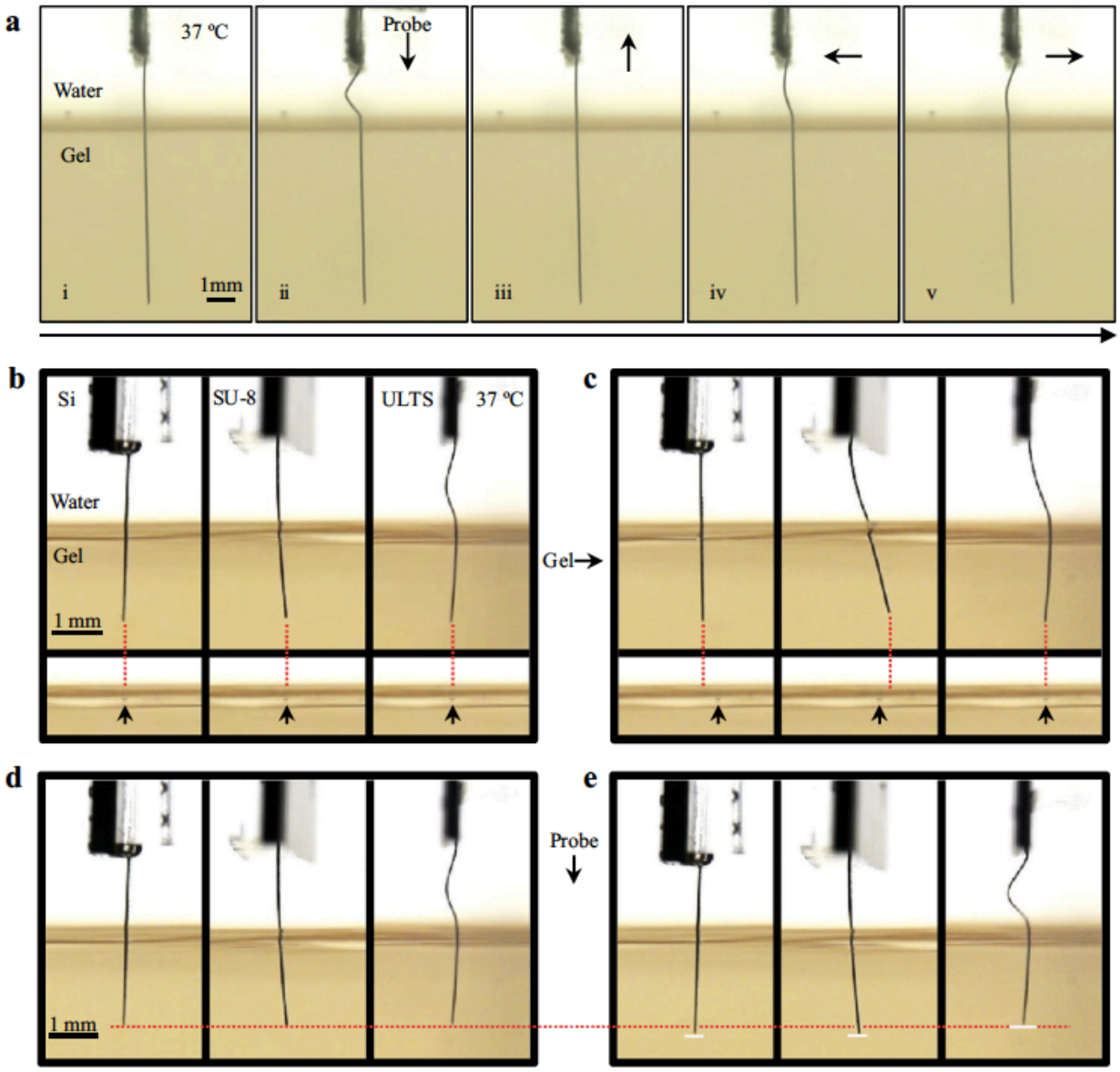

Figure 7.3. Demonstration of probe flexibility in brain phantoms. (a) Pictures of a "soft" ULTS probe in a brain phantom. Probe base was moved in all directions to simulate the relative motion between skull and brain with no resulting deformation of the brain phantom. (b,c) Comparison of silicon (Si), SU-8 and ULTS probes with a 500 μm horizontal movement of the brain phantom. Each dotted line is extended from the probe tip vertically. Arrows indicate the reference points in the brain phantom. (d,e) Comparison of Si, SU-8 and ULTS probes with a vertical movement of the probe base. The dotted line indicates the original level of probe tips. Solid lines in (e) indicate the probe tips' positions after probe movement.

For the current probes, the number of microelectrodes was limited by the large microelectrode size required by electrochemical sensing rather than by the number of electrical interconnects. In contrast, the linewidth of microchannels is defined by lithography, meaning they can be potentially scaled to match the microelectrode count of conventional MEA probes. Although electrophysiological recording and electrical stimulation were not performed in this study, the impedance of the electrodes, 21.4 $\pm$ 1.50 kΩ (*n*=5) at 1 kHz (Supplementary Fig. S6a), is identical to silicon-based probes with Pt electrodes due to the highly conductive liquid metal interconnects. Moreover, a rough Pt surface (Pt grass) (Boehler et al., 2015) can be deposited electrochemically to increase the effective surface area and lower the impedance to 6.74 $\pm$ 0.49 kΩ (*n*=3) at 1 kHz (Supplementary Fig. S6b) resulting in a charge storage capacity of 4.5 mC/cm2 (Supplementary Fig. S6c). Therefore, with modified electrode design, ULTS probes can be readily adapted for electrophysiological recording and electrical stimulation applications.

7.3.4 Probe implantation in rats

We implanted probes in the striatum of rats (Fig. 5a) under continuous isoflurane anesthesia to test their performance *in vivo*. In a typical implantation procedure (Fig. 5b), a 30-gauge mini hypodermic temperature probe was implanted remote from the recording area to monitor the brain temperature at the target implantation depth of the ULTS probe. Chilled sterile saline (~10 °C) was then perfused over the exposed skull surface to reduce the brain temperature to approximately 28 °C at the targeted depth thereby ensuring that the probe would remain straight and stiff throughout the entire implantation procedure. The ULTS probe was then stereotaxically lowered to the targeted region over approximately one minute (Fig. 5c). The body temperature of the rats was kept at 37 °C by a heating pad. The cooling process typically lasted< 10 min, and the brain temperature recovered to baseline in a few minutes (Fig. 5d). We confirmed probe localization within the striatum by bright-field microscopy of brain sections post-mortem

(Supplementary Fig. S7). Implantation of ULTS probes requires selective brain cooling, without altering the core temperature. This practice has been widely used to locally and reversibly inhibit neural activity and alter behavior in research settings, as well as clinically, e.g. for treatment of hypoxic ischemic neonatal encephalopathy, stroke and brain trauma (Wang et al., 2014). As shown repeatedly, brain tissue tolerates well significant temperature reduction for brief periods (1–3 h) (Galuske et al., 2002; Girard and Bullier, 1989; Oku et al., 2009; Percy et al., 2009).

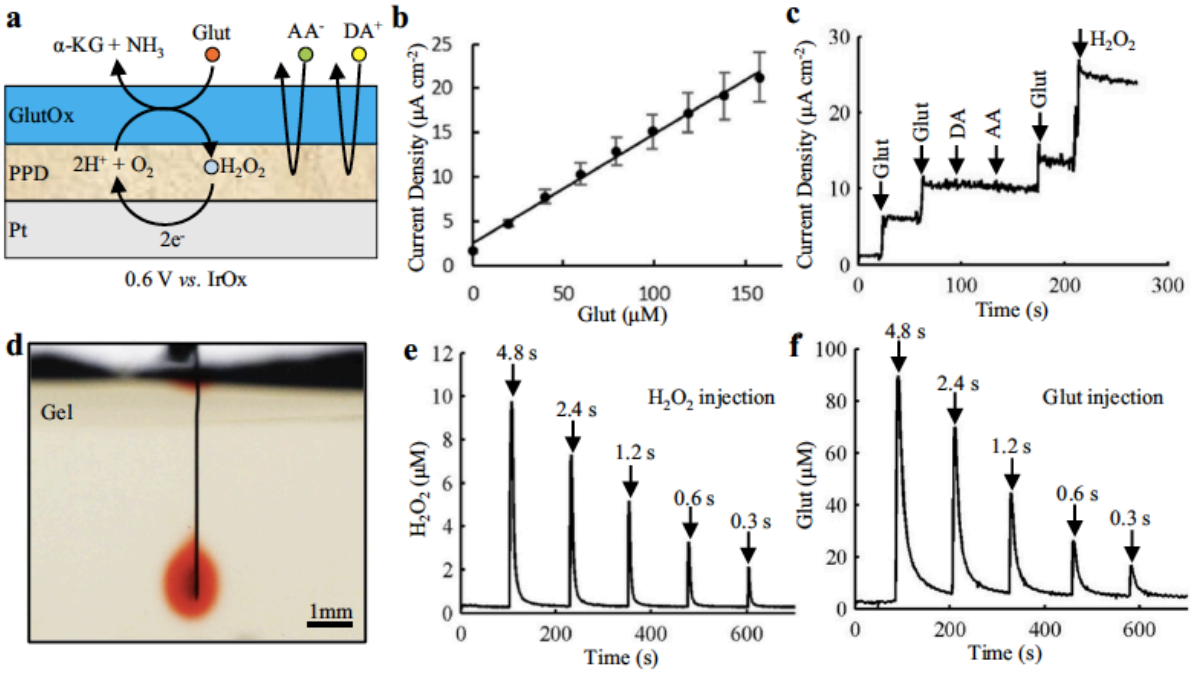

Figure 7.4. In vitro characterization of biosensor and chemical delivery functions. (a) Schematic diagram of the coatings on a single electrode on the ULTS probe. (b) Calibration curve for Glut sensing showing a linear correlation in the physiological range, up to 160 μM. Mean ± SEM of 4 sensors. (c) Current response of a Glut biosensor to Glut, the physiological interferents – dopamine (DA) and ascorbic acid (AA), and H_2O_2 in stirred PBS solution (pH 7.4). Arrows indicate the sequential injections to give total concentrations of 20 μM Glut, 40 μM Glut, 5 μM DA, 250 μM AA, 60 μM Glut and 20 μM H_2O_2. (d) Optical image showing delivery of liquid (aqueous solution of Allura Red AC) into a brain phantom (0.6% agarose gel). (e, f) In vitro testing of chemical delivery in brain phantoms (0.6% agarose gel in aCSF). H_2O_2 (40 μM) (e) and Glut (150 μM) (f) were injected at 60 psi with injection duration of 4.8 s, 2.4 s, 1.2 s, 0.6 s and 0.3 s indicated by the arrows (injection volumes in the range ~1–20 nL).

7.3.5 In vivo probe testing

Electrochemical sensing and drug delivery functions of the ULTS probe were evaluated under continuous anesthesia. Glut (500 μM in aCSF) was pressure-ejected using varying pressure pulse durations to control injection volumes (Fig. 6a). The signal evoked at the sensors by Glut ejection was highly reproducible and typically returned to baseline within 5 s of pressure pulse termination, compared to approximately 100 s in brain phantoms, reflecting differences in diffusion and the presence of active reuptake in brain tissue (Supplementary Fig. S8). Endogenous Glut release was evoked by repeated local ejections of potassium-enriched artificial cerebrospinal fluid (100mM K^+ aCSF) (Fig. 6b). As we reported previously using silicon-based MEA/injection cannula assemblies (Walker et al., 2007), signal amplitude declined abruptly after the first of a series of regularly timed ejections, presumably due to depletion of the readily-releasable neuronal Glut stores, recovering slightly after a 25 min recovery period without any stimulation.

Preliminary tests of the biocompatibility of these flexible neural probes during chronic implantation were performed using GFAP as a marker of astrocytes post-mortem. Rats were implanted bilaterally in the striatum with a flexible probe on one side and a silicon probe with similar dimensions on the contralateral side, and the animals were permitted to recover from anesthesia. In the example shown in Supplementary Fig. S9, 4 weeks after implantation, the soft probe demonstrated reduced astrocytic encapsulation compared to the stiff silicon probe, similar to reports of other flexible probes (Du et al., 2017; Nguyen et al., 2014). An example of data at 9 weeks is presented in Supplementary Fig. S10 showing an overall reduced level of GFAP expression surrounding the probes relative to the example shown at 4 weeks, with a thinner scar formation surrounding the ULTS probes compared to the silicon probes. The ULTS probes exhibits higher GFAP expression at the surface, which is possibly due to the hydrophobic nature

of PDMS. Further improvement in the biocompatibility of ULTS probes for long-term applications may be achieved using anti-fouling coatings, such as poly(ethylene glycol) (PEG)-based materials, poly-Llysine or hyaluronic acid (Zhang and Chiao, 2015; Zhou et al., 2010) or by the delivery of bioactive agents (Lecomte et al., 2017) to counter the hydrophobic nature of PDMS (Zhang and Chiao, 2015; Zhou et al., 2010).

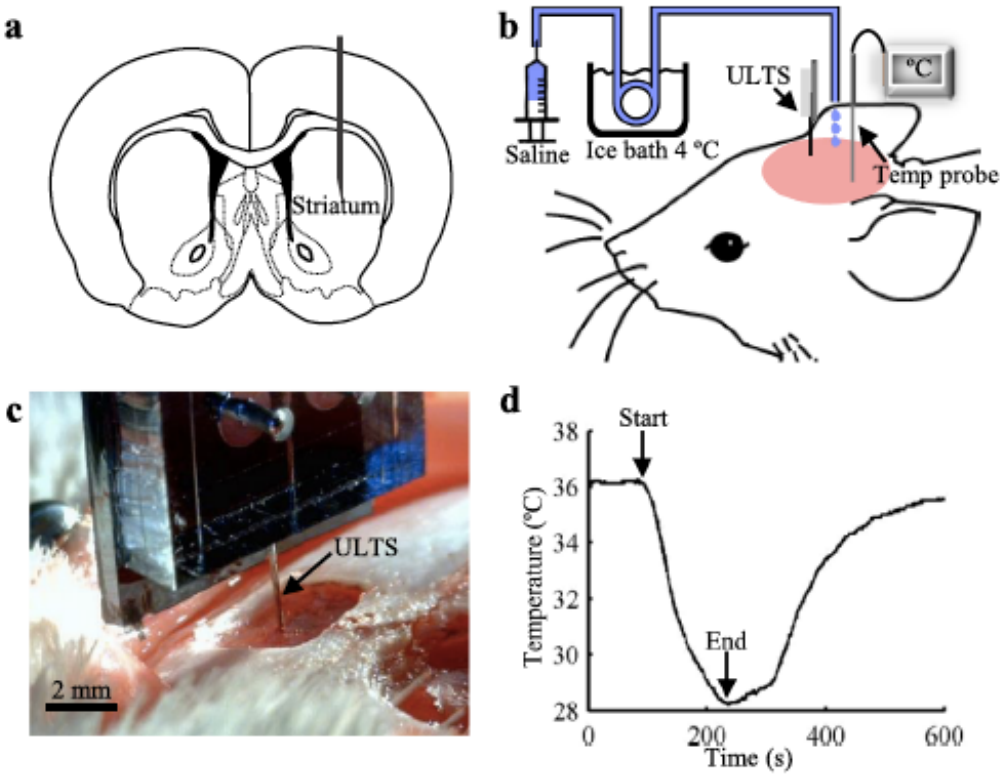

Figure 7.5. Probe Implantation in Rats. (a) Schematic of a coronal brain slice illustrating the targeted implantation location in the rat striatum. (b) Schematic of the implantation procedure. Bilateral craniotomies were performed above the striata and chilled sterile saline was perfused across the skull surface. A miniaturized temperature probe was inserted remote from the recording site at the targeted implantation depth. (c) Optical image of a ULTS probe (arrow) implanted in a rat brain. (d) A representative brain temperature curve showing the brain cooling and temperature recovery process. Arrows indicate the start and end of the application of chilled saline solution.

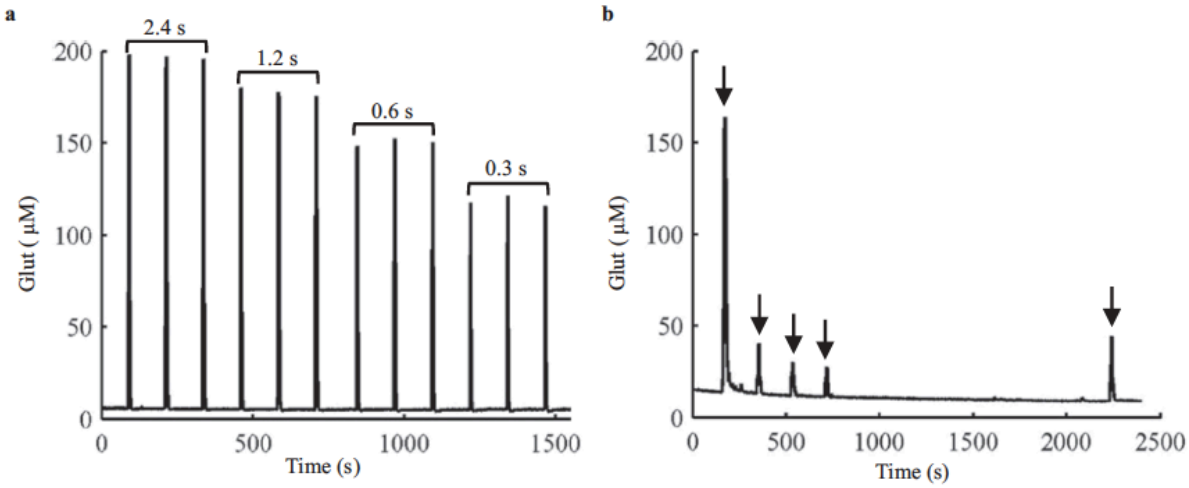

Figure 7.6. *In vivo* characterization of biosensor and chemical delivery functions. (a) Detection of repeated injections of Glut (500 µM) via the fluid channel into the rat striatum. Glut solutions were injected at 2 min intervals at 60 psi with injection durations of 2.4 s, 1.2 s, 0.6 s and 0.3 s, respectively, indicated by the brackets. (b) Repeated injection (arrows) of potassium-enriched artificial cerebrospinal fluid (100mM K^+ aCSF) in rat striatum to induce Glut release. Solutions were injected at 60 psi with an injection duration of 4.8 s at 2 min intervals. Signal amplitude was considerably reduced following the initial stimulation, recovering only partially after a prolonged period (25 min) free from stimulation.

7.4 Conclusion

The development of flexible neural probes is a promising approach to reduce immunoinflammatory response and improve the functionality for long-term applications. However, by reducing the dimensions aggressively, in order to achieve the desired flexibility, such probes often face challenges in the implantation process and the integration of multiple functionalities. In this paper, we designed, fabricated and validated the first ultra-soft, multifunctional neural probe that can be implanted deep into brain tissue without external shuttle carriers or coatings, which was made possible by using a liquid metal, Ga, and soft elastomer substrate in its construction. Taking advantage of the solid to-liquid phase change of the metal at body temperature and the probe shape deformation, a tunable stiffness of 5 orders of magnitude was achieved. Probes were

successively implanted 2 cm-deep into agarose gel “brain phantoms” and rat brain under cooled conditions, while they became ultra soft and flexible upon Ga melting at physiological temperature. With liquid metal wires, Pt electrodes and appropriate coatings, high-performance and stable electrochemical Glut sensing was demonstrated in both stiff and soft states with a sensitivity of 8.2 ± 1.2 pA/μM, detection limit of 0.39 ± 0.07 μM and response time of ~1 s, which are equivalent to the state-of-the-art silicon-based systems. *In vivo* chemical stimulation of Glut was demonstrated by injection of potassium-enriched aCSF through the integrated microfluidic channel. These PDMS-based microprobes of ultra-large tunable stiffness (ULTS), with potential for incorporation of functions such as optogenetics and electrophysiological recording, serve as an attractive platform for multifunctional chronic neural implants.

7.5 References

1. Boehler, C., Stieglitz, T., Asplund, M., 2015. Biomaterials 67, 346–353.
2. Bruus, H., 2011. Lab Chip 11, 3742–3751.
3. Capadona, J.R., Tyler, D.J., Zorman, C.A., Rowan, S.J., Weder, C., 2012. MRS Bull. 37, 581–589.
4. Chen, J., Wise, K.D., Hetke, J.F., Bledsoe, S.C., 1997. IEEE Trans. Biomed. Eng. 44, 760–769.
5. Chow, Y.T., Man, T., Acosta-V.lez, G.F., Zhu, X., Wen, X., Chung, P.-S., Liu, T.“Leo”, Wu, B.M., Chiou, P.-Y., 2018. Adv. Sci. 5, 1700711.
6. Danbolt, N.C., 2001. Progress. Neurobiol. 65, 1–105.
7. Dickey, M.D., 2017. Adv. Mater. 29, 1.
8. Dietrich, W.D., Atkins, C.M., Bramlett, H.M., 2009. J. Neurotrauma 26, 301–312.

9. Du, Z.J., Kolarcik, C.L., Kozai, T.D.Y., Luebben, S.D., Sapp, S.A., Zheng, X.S., Nabity, J.A., Cui, X.T., 2017. Acta Biomater. 53, 46–58.
10. Eriksson, E., Engberg, G., Bing, O., Nissbrandt, H., 1999. Neuropsychopharmacology 20, 287–296.
11. Felix, S.H., Shah, K.G., Tolosa, V.M., Sheth, H.J., Tooker, A.C., Delima, T.L., Jadhav, S.P., Frank, L.M., Pannu, S.S., 2013. J. Vis. Exp. Galuske, R.A.W., Schmidt, K.E., Goebel, R., Lomber, S.G., Payne, B.R., 2002. PNAS 99, 17083–17088.
12. Gass, J.T., Foster Olive, M., 2008. Biochem Pharmacol. 75, 218–265.
13. Girard, P., Bullier, J., 1989. J. Neurophysiol. 62, 1287–1302.
14. Hallfors, N., Khan, A., Dickey, M.D., Taylor, A.M., 2013. Lab Chip 13, 522–526.
15. Jeong, J.-W., McCall, J.G., Shin, G., Zhang, Y., Al-Hasani, R., Kim, M., Li, S., Sim, J.Y.,
16. Jang, K.-I., Shi, Y., Hong, D.Y., Liu, Y., Schmitz, G.P., Xia, L., He, Z., Gamble, P., Ray, W.Z., Huang, Y., Bruchas, M.R., Rogers, J.A., 2015a. Cell 162, 662–674. Jeong, J.-W., Shin, G., Park, S.I., Yu, K.J., Xu, L., Rogers, J.A., 2015b. Neuron 86, 175–186.
17. Jorfi, M., Skousen, J.L., Weder, C., Capadona, J.R., 2015. J. Neural Eng. 12, 011001.
18. Kim, T., McCall, J.G., Jung, Y.H., Huang, X., Siuda, E.R., Li, Y., Song, J., Song, Y.M., Pao, H.A., Kim, R.-H., Lu, C., Lee, S.D., Song, I.-S., Shin, G., Al-Hasani, R., Kim, S., Tan, M.P., Huang, Y., Omenetto, F.G., Rogers, J.A., Bruchas, M.R., 2013. Science 340, 211–216.
19. Kuluz, J.W., Gregory, G.A., Yu, A.C., Chang, Y., 1992. Stroke 23, 1792–1796.
20. Lecomte, A., Descamps, E., Bergaud, C., 2017. J. Neural Eng. Lee, J.H., Kim, H., Kim, J.H., Lee, S.-H., 2016. Lab Chip 16, 959–976.
21. Liu, J., Fu, T.-M., Cheng, Z., Hong, G., Zhou, T., Jin, L., Duvvuri, M., Jiang, Z., Kruskal, P., Xie, C., Suo, Z., Fang, Y., Lieber, C.M., 2015. Nat. Nanotechnol. 10, 629–636.
22. Long, M.A., Fee, M.S., 2008. Nature 456, 189–194.

23. Luan, L., Wei, X., Zhao, Z., Siegel, J.J., Potnis, O., Tuppen, C.A., Lin, S., Kazmi, S., Fowler, R.A., Holloway, S., Dunn, A.K., Chitwood, R.A., Xie, C., 2017. Sci. Adv. 3, e1601966.

24. McAllister, D.V., Wang, P.M., Davis, S.P., Park, J.-H., Canatella, P.J., Allen, M.G., Prausnitz, M.R., 2003. PNAS 100, 13755–13760.

25. Minev, I.R., Musienko, P., Hirsch, A., Barraud, Q., Wenger, N., Moraud, E.M., Gandar, J., Capogrosso, M., Milekovic, T., Asboth, L., Torres, R.F., Vachicouras, N., Liu, Q., Pavlova, N., Duis, S., Larmagnac, A., V.r.s, J., Micera, S., Suo, Z., Courtine, G., Lacour, S.P., 2015. Science 347, 159–163.

26. Nguyen, J.K., Park, D.J., Skousen, J.L., Hess-Dunning, A.E., Tyler, D.J., Rowan, S.J., Weder, C., Capadona, J.R., 2014. J. Neural Eng. 11, 056014.

27. Oku, T., Fujii, M., Tanaka, N., Imoto, H., Uchiyama, J., Oka, F., Kunitsugu, I., Fujioka, H., Nomura, S., Kajiwara, K., Fujisawa, H., Kato, S., Saito, T., Suzuki, M., 2009. J. Neurosurg. 110, 1209–1217.

28. Park, S.I., Shin, G., McCall, J.G., Al-Hasani, R., Norris, A., Xia, L., Brenner, D.S., Noh, K.N., Bang, S.Y., Bhatti, D.L., 2016. Proc. Natl. Acad. Sci. USA 113, E8169–E8177.

29. Peel, T.R., Dash, S., Lomber, S.G., Corneil, B.D., 2017. J. Neurosci. 37, 11715–11730.

30. Percy, A., Widman, S., Rizzo, J.A., Tranquilli, M., Elefteriades, J.A., 2009. Ann. Thorac. Surg. 87, 117–123.

31. Reed, M.L., Lye, W.-K., 2004. Proc. IEEE 92, 56–75.

32. Rivnay, J., Wang, H., Fenno, L., Deisseroth, K., Malliaras, G.G., 2017. Sci. Adv. 3, e1601649.

33. Rohatgi, P., Langhals, N.B., Kipke, D.R., Patil, P.G., 2009. Neurosurg. Focus 27, E8.

34. Sim, J.Y., Haney, M.P., Park, S.I., McCall, J.G., Jeong, J.-W., 2017. Lab Chip 17, 1406–1435.

35. Spector, R., 1977. New Engl. J. Med. 296, 1393–1398.

36. Subbaroyan, J., Martin, D.C., Kipke, D.R., 2005. J. Neural Eng. 2, 103–113.

37. Tien, L.W., Wu, F., Tang-Schomer, M.D., Yoon, E., Omenetto, F.G., Kaplan, D.L., 2013. Adv. Funct. Mater. 23, 3185–3193.

38. Tolosa, V.M., Wassum, K.M., Maidment, N.T., Monbouquette, H.G., 2013. Biosens. Bioelectron. 42, 256–260.

39. Wahono, N., Qin, S., Oomen, P., Cremers, T.I.F., de Vries, M.G., Westerink, B.H.C., 2012. Biosens. Bioelectron. 33, 260–266.

40. Walker, E., Wang, J., Hamdi, N., Monbouquette, H.G., Maidment, N.T., 2007. Analyst 132, 1107.

41. Wang, B., Koo, B., Huang, L., Monbouquette, H.G., 2018. Analyst 143, 5008–5013.

42. Wang, H., Wang, B., Normoyle, K.P., Jackson, K., Spitler, K., Sharrock, M.F., Miller, C.M., Best, C., Llano, D., Du, R., 2014. Front. Neurosci. 8.

43. Ware, T., Simon, D., Liu, C., Musa, T., Vasudevan, S., Sloan, A., Keefer, E.W., Rennaker, R.L., Voit, W., 2014. J. Biomed. Mater. Res. Part B: Appl. Biomater. 102, 1–11.

44. Wassum, K., Tolosa, V., Tseng, T., Balleine, B., Monbouquette, H., Maidment, N., 2012. J. Neurosci. 32, 2734–2746.

45. Wassum, K.M., Tolosa, V.M., Wang, J., Walker, E., Monbouquette, H.G., Maidment, N.T., 2008. Sensors 8, 5023–5036.

46. Weltman, A., Yoo, J., Meng, E., 2016. Micromachines 7, 180.

47. Wu, F., Tien, L.W., Chen, F., Berke, J.D., Kaplan, D.L., Yoon, E., 2015. J. Microelectromech. Syst. 24, 62–69.

48. Xiang, Z., Yen, S.-C., Xue, N., Sun, T., Tsang, W.M., Zhang, S., Liao, L.-D., Thakor, N.V., Lee, C., 2014. J. Micromech. Microeng. 24, 065015.

49. Zhang, H., Chiao, M., 2015. J. Med Biol. Eng. 35, 143–155.

50. Zhou, J., Ellis, A.V., Voelcker, N.H., 2010. Electrophoresis 31, 2–16.

Chapter 8: Implantable, aptamer-based field-effect transistor microprobes: toward monitoring of serotonin in mice

Abstract

The creation of implantable sensors that can monitor the release of a broad range of neurochemicals in the brain would greatly facilitate our understanding of the connection between neurochemistry and behaviors. Field-effect transistors (FETs) can be used to detect analytes without labels and exhibit an exponential response to surface potential changes induced by analyte binding. However, detection of small target molecules with few or no charges is difficult owing to limited impact on semiconductor transconductance and ion shielding in the physiological environment. In this work, silicon-based implantable microprobes with aptamer FETs as sensing sites has been developed for small molecule (*e.g.*, serotonin) detection. This microprobe deploys aptamer as the target-recognition element on its semiconductor channel, analyte binding to which causes significant change in conformation of the negatively charged aptamer phosphodiester backbone in close proximity to the semiconductor surface and modulates the underlying FETs electrical properties. These aptamer-based FET microprobes exhibited concentration-dependent conductance that was linear over a large dynamic range and enabled the detection of serotonin down to femtomolar range in phosphate-buffered saline (1x PBS) and brain tissue homogenates. Lastly, detection of serotonin with a response time on the order of seconds was demonstrated. The capability of FET microsensors for sensitive and fast detection of serotonin could be exploited for monitoring *in vivo* and may provide a generalizable platform for sensing of a wide range of neurochemicals.

8.1 Introduction

While neurons manifest their activity via both electrical action potentials and chemical neurotransmission, monitoring neural activity has traditionally been focus on electrophysiological recording. With recent innovations in micro- and nanofabrication, materials science, and electrical engineering, implantable neural devices for monitoring electrical signaling have become highly sophisticated with high spatiotemporal resolution that enables the recording of large number of interconnected neurons through millisecond timescale measurements of action potentials.[1–3] However, tools that are able to monitor the rapid change in concentration of the neurochemicals of interest *in vivo* has remained a technological challenge.

The most prominent chemical methods consist of microdialysis-based sampling coupled with detection methods such as high-performance liquid chromatography (HPLC), mass spectroscopy (MS)), and electrochemically based signal transduction. However, this sampling method lacks the temporal resolution to effectively monitor neurotransmitter signaling *in vivo* in real time.[4–6] On the other hand, electrochemical measurements including chronoamperometry and fast-scan cyclic voltammetry (FSCV) that rely on charge transfer reactions are usually made with a microelectrode that is in direct contact with the extracellular fluid in the brain, therefore, they offer rapid (sub-second) and direct detection of electroactive analytes. These techniques have been widely employed to monitor neurotransmission *in vivo*, which has greatly improved our understanding of serotonin function in the brain, however, insufficient selectivity was provided.[7–9] Also, it can be challenging to employ FSCV for long-term applications *in vivo,* as some of the side products generated from target redox reactions would adsorb on the sensing surface and lead to electrode fouling.[7] While amperometric detection coupled with enzyme-modified electrodes has been demonstrated to be a useful method to monitor non-electroactive neurotransmitters with high selectivity, these devices can have an unsatisfactory detection limit of ~ 10^{-7} M that is

inadequate to detect certain neurotransmitters in the brain owning to the thick coating on electrode surfaces. For example, serotonin, which is an important neurotransmitter associated with many important behaviors including memory and learning, presents at relatively low extracellular concentration (10^{-12} – 10^{-9} range) in all brain regions where it is found.[10] While its involvement in neurological disorders has been assumed for decades, the progress in our understanding has been limited due to the lack of effective tools to meet physiological requirements.

Inspired by the ability of nucleic acid aptamers to reversibly bind to specific targets with high affinity, Plaxco's group and others have created aptamer-based sensors allowing the monitoring of molecular targets without relying on other specific chemical reactivities.[11–14] Beyond achieving specific molecular detection, Nakatsuka, Andrews *et al*. developed ultrasensitive aptamer-based sensors for serotonin and dopamine by functionalizing aptamers on nanoscale metal oxide semiconducting films.[13,15,16] In this work, we cooperated with the Andrews's group to miniaturize their aptamer-based FETs. To make the probes implantable with constant product quality, we developed a method to microfabricated probes on Si that are 150 μm thick × 140 μm wide. Selected aptamers with a specific type of stem-loop structure for serotonin recognition was used as the demonstration element in this work. The microsensing site was coated with a nanoscale indium oxide (In_2O_3) layer as an ultrasensitive semiconductor surface to which serotonin aptamer was covalently bound. In brief, the working mechanism relied on conformational changes of the charged aptamer backbone that occur upon target capture, introducing significant surface charge redistribution that was easily detected by the underlying FET. The drain current responded proportionally to the target concentration, thereby providing a selective and quantitative determination of the target concentration in the test sample. The device functionality was validated *in vitro* by testing sensor performances in PBS solution and brain tissue homogenates. The selectivity of sensors of this type was attributed to two effects. First, the

nonspecific binding of interferents did not trigger a conformational change in the aptamer. Second, the target binding-induced conformational changed was signaled electrochemically, and other electroactive interferents in this potential condition were rare. These aptamer-based microprobes were highly sensitive and responded to 10^{-15} M serotonin on the order of seconds in physiological environments, making them promising candidates for the real-time monitoring of other monoamine and amino acid neurotransmitters in the brain.

8.2 Materials and Methods

8.2.1 Materials

Prime quality 4" Si wafers (P/B, 0.001-0.005 Ω cm, thickness 150 μm, with 100 nm-thick thermally grown SiO_2 layer) were purchased from Silicon Valley Microelectronics, Inc. (Santa Clara, CA, USA). All chemicals were purchased from Sigma-Aldrich Co. (St. Louis, MO), unless otherwise noted below. Oligonucleotides were obtained from Integrated DNA Technologies (Coralville, IA). Water was deionized before use (18.2 MΩ) via a Milli-Q system (Millipore, Billerica, MA). Ag/AgCl reference electrodes (Super Dri-Ref) were obtained from World Precision Instruments, Inc (Sarasota, FL). Phosphate-buffered saline (1x PBS, Gibco) was purchased from Fisher Scientific (Chino, CA).

8.2.2 Fabrication Process

Aqueous solutions of 0.1 M indium(III) nitrate hydrate (99.999%) were spin-coated onto the 4" heavily doped Si substrates at 3000 rpm for 30 s followed by thermal annealing at 350 °C for 3 hr. Source and drain electrodes (10 nm Ti / 30 nm Au) were patterned by standard photolithography processes and deposited by electron-beam evaporation on top of the In_2O_3 at 10^{-8} Torr with an evaporation rate of 0.1 nm/s. Another photolithographic treatment was performed to define the outline of the probes. Deep reactive ion etching (DRIE) with the Bosch process was

used to etch through the silicon substrate (~150 μm). A thin layer of parylene (~1 μm thick) was coated on the surface using a SCS Parylene C coating system (Indianapolis, IN), and then defined by photolithography and etched by oxygen plasma.

8.2.3 Surface Modification of Microprobes

Covalent attachment of monolayers of aptamers was realized by the following procedure. Released probes were rinsed in ethanol and blow-dried in N_2 to clean the surface. After thorough cleaning, the In_2O_3 surface was pretreated with two different silanes, amine-terminated, (3-aminopropyl)trimethoxysilane (APTMS) and methyl-terminated, trimethoxy(propyl)silane (PTMS) (1:9, v/v), by vapor-phase deposition at 40 ℃ for 1 h and then annealing at 80 ℃ for 10 min to form surface groups. To passivate the Au electrode, the microprobe was incubated in 1 mM ethanolic solution of 1-dodecanethiol for 1 h. Aptamers (as-received) were crosslinked onto the sensing site. The substrate was treated with the linking agent by immersing the probes in 1 mM solution of 3-maleimidobenzoic acid N-hydroxysuccinimide ester (MBS) dissolved in 1:9 (v/v) mixture of dimethyl sulfoxide and 1x PBS for 30 min. Aptamer attachment was then realized by immersing the substrate in a 1 μM solution of aptamer in 1x PBS overnight. Each probe was rinsed with deionized water and blow-dried with N_2 before measurements.

8.2.4 Ex vivo sensing in brain tissue homogenates

Brains lacking serotonin were from Tph2 knockout mice provided by the laboratory of Donald Kuhn (Wayne State University, Detroit, MI). All procedures involving these mice were pre-approved by the Wayne State University Institutional Animal Care and Use Committee. Brains were stored at -70 °C until use. On the day of use, artificial cerebrospinal fluid (1x aCSF) was added to each tube containing sectioned brain (2 μL/mg tissue), following by sonication on ice

using a VirTis Virsonic 600 ultrasonic cell disruptor (Gardiner, NY). Serotonin was added to homogenates in aliquots to give final concentrations of 10^{-14} – 10^{-3} M.

8.2.5 Electrochemical measurements

1x PBS and brain tissue homogenates were used as electrolyte solutions. Commercially available Ag/AgCl reference electrodes were placed next to the FETs in stirred solutions. Characteristics of FET transfer curves [*i.e.*, source-drain current (I_{DS}) versus source-gate voltage sweeps (V_{GS})] were collected using Keithley 4200A (Tektronix, Beaverton, OR) semiconductor analyzer with V_{GS} sweeping from 0 to 400 mV while maintaining the source-drain voltage (V_{DS}) at 10 mV. On the other hand, real-time measurements (*i.e.*, I_{DS} versus time) were performed on a Versatile Multichannel Potentiostat (model VMP3) equipped with the 'p' low current option and N'Stat box driven by EC-LAB software (Bio-Logic USA, LLC, Knoxville, TN) with V_{GS} fixed at 300 mV and V_{DS} maintained at 10 mV. After current stabilization, serotonin was added to give desired final concentrations.

8.3 Results and Discussions

8.3.1 Fabrication and characteristics of In_2O_3-based FET microprobes

A schematic of the fabrication process and the layout of the microprobes is shown in Figure 1. We selected In_2O_3 as the metal oxide semiconductor due to its high relative electron mobility. Thin films of In_2O_3 (~3 nm) were formed onto heavily doped 4-inch Si wafers covered with a 100 nm thick thermal SiO_2 layer to construct the highly sensitive FET (step 1). To obtain larger active sensor areas and uniform current distribution, interdigitated source and drain Au electrodes were patterned on top of the metal oxide layer here (step 2).[17] The Si wafer was etched through using deep reactive-ion etching (DRIE) to define the outlines of individual probes, where width and thickness of the probe shank were both *ca.* 150 μm (step 3). The most challenging was

in the last step to insulate the shaft of the probe, accept for the tip, with a thin layer of parylene (~1 μm thick). Parylene was selected over other conventional insulating materials such as SiO_2 or Si_2N_3 because the etching process of those materials requires an ion beam with high power and high temperature, which can easily remove the underlying, few-nanometer-thick In_2O_3 layer. In contrast, the oxygen plasma etching condition with O_2 pressure of 350 mTorr and power of 300 watts at room temperature allowed etching of the parylene layer while maintaining In_2O_3 and metal functionality on the sensing area. As one can note, the step to shape the Si probe with plasma etching was done prior to the step for parylene deposition and patterning. This is because the parylene melting point (T_m) of 290 °C is relatively low and cannot sustain high process temperature during the Si etching step in by FDRIE. Such steps conducted out of order caused poor coating of the photoresistor on the bumpy substrate surface and resulted in a relatively low success rate of ~70% to fabricate well-insulated In_2O_3-based FETs microprobes. However, since the reduction of circuit size resulted in the capacity to fabricate 150 microprobes on each wafer with two FET recording sites at the tip of each microprobe (Figure 2abc), the spatial resolution was improved and the cost per circuit was still reduced significantly.

To determine the performance of these miniaturized FETs, we first used the highly-doped Si substrate and 100 nm-thick SiO_2 layers as back gate and dielectric layer, respectively, and examined the FET characteristics in a dry state. (Fig 2d) We found that the miniaturization of FETs caused a few orders of magnitude decrease in the drain current, which was expected due to the decrease in carrier amount on a smaller sensing area. Most importantly, these microprobes exhibited high current on/off ratios (I_{on}/I_{off}) of ~10^8, which are comparable to devices with much larger dimension as we reported previously.[13] The high I_{on}/I_{off} shown here made these microprobes promising candidates for sensing neurochemicals at low concentration.

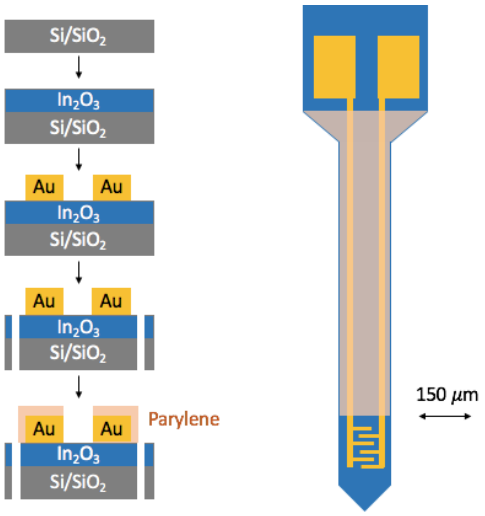

Figure 8.1. Schematics of the microprobe fabrication process (left) and a single device FET at the shank of microprobe (right). The schematic shows the layers on the microprobes, where from top to bottom are parylene, Au electrode, In_2O_3, and the Si substrate.

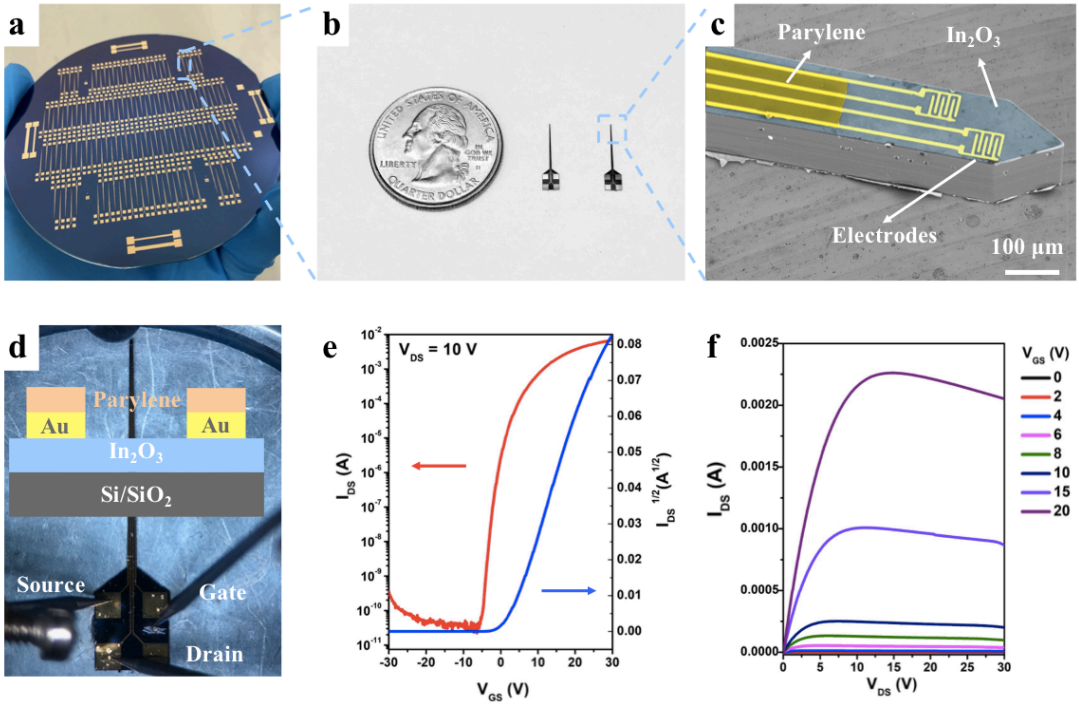

Figure 8.2. (a) Photograph of a 4" Si wafer with 150 microprobe devices before the deep reactive-ion etching (DRIE) process. (b) Photograph showing two released microprobes after DRIE next to a quarter dollar. (c) Scanning electron microscope (SEM) image of the shank of a microprobe with false colors. (d) Photograph of a solid-state measurement setup. (e, f) Representative transfer and output characteristics, respectively.

8.3.2 Characteristics of aptamer FET transfer curves: I_{DS} versus V_{GS} sweeps

Previously recognized serotonin aptamer was immobilized onto In_2O_3 surfaces using amine-terminated silane (APTMS) and amine-thiol crosslinker (MBS).[13] As the size of DNA aptamers was on the order of a few nanometers, steric interactions between neighboring aptamers could inhibit target accessibility and aptamer folding at high aptamer packing densities. Therefore, methyl-terminated silane (PTMS) was codeposted with APTMS on In_2O_3 surface as a spacer prior to MBS coupling chemistry to optimize the surface density of aptamers for effective biosensing. After aptamer functionalization, the performance of each FET microprobe in solution was tested. Figure 3a showed a schematic illustration of the electrical measurement setup used for serotonin sensing experiments. 1x PBS (pH 7.4) was used as a gate liquid, and gate bias (V_{GS}) was applied through an Ag/AgCl reference electrode. A specific amount of serotonin was injected into the gate liquid to modulate serotonin concentration in the liquid environment. Figure 3bc showed the transfer characteristics of liquid-gated aptamer In_2O_3 sensors measured at various serotonin concentrations in solution. All calibrated responses were calculated at the gate-bias voltage of 300 mV since this bias gave maximal current response with minimal sweep-to-sweep variations. Due to variations in active area of sensor and the coverage of aptamer on the microprobe, the current changes can vary significantly from sensor to sensor. To reduced device-to-device variation, the change in drain current was converted to a change in gate voltage, where the absolute sensor response (ΔI_{DS}) that takes into account baseline subtraction was divided by the change in source-drain current with voltage sweep ($\Delta I_{DS}/\Delta V_{GS}$).[18] This method relies on correlations between absolute sensor responses and gate dependence in liquid-gate sensing set-ups.

The increase in transconductance upon addition of serotonin was consistent with our previous findings on devices of larger dimension.[13] This was hypothesized that substantial

portions of negatively charged backbones of serotonin aptamers moved away from n-type semiconductor channels, thereby decreasing electrostatic repulsion of charge carriers and increasing transconductance. (Fig 4b) As serotonin concentration was increased, the transfer characteristics of the device continuously shifted upward. (Fig 4a) The linear working range of the aptamer FETs microprobe was determined to be 10^{-15} – 10^{-3} M, as shown in Figure 4a. Such a sensitivity limit was substantially lower than the nM to μM range demonstrated recently by other analytical methods. However, there were some FETs showing poor baseline that did not stabilize after 10 mins or gave no response to serotonin. This could be due to the limited or even no serotonin aptamer attached on the electrode surface as the sensing area on the microprobe was small. When aptamer packing densities became too low, the number of aptamers on the surface might not produce an observable signal above the background noise. Currently we were using a ratio of 1:9 APTMS:PTMS deposited on substrate, which was the ratio optimized on larger FETs but might not be the best for miniaturized FETs used here. As a result, we expected that the performance of aptamer-based microprobes could be improved by optimizing the surface functionalization process, especially the packing density of aptamers (aptamer/cm^2).

In addition, a control experiment was carried out to confirm that the observed conductance changes were due to the specific binding of serotonin to the aptamer. Addition of a serotonin solution to FETs functionalized with the scrambled serotonin sequence (with same number and types of nucleotides as correct aptamer sequence but with pseudo-random orders) produced negligible changes in conductance. This control showed that there was little nonspecific binding of the target on the surface channel. Since aptamers carried much greater charge than small molecules such as serotonin, their conformational changes were typically expected to dominate surface charge densities and surface charge density changes, as compared to the electrostatic gating effects of analytes.

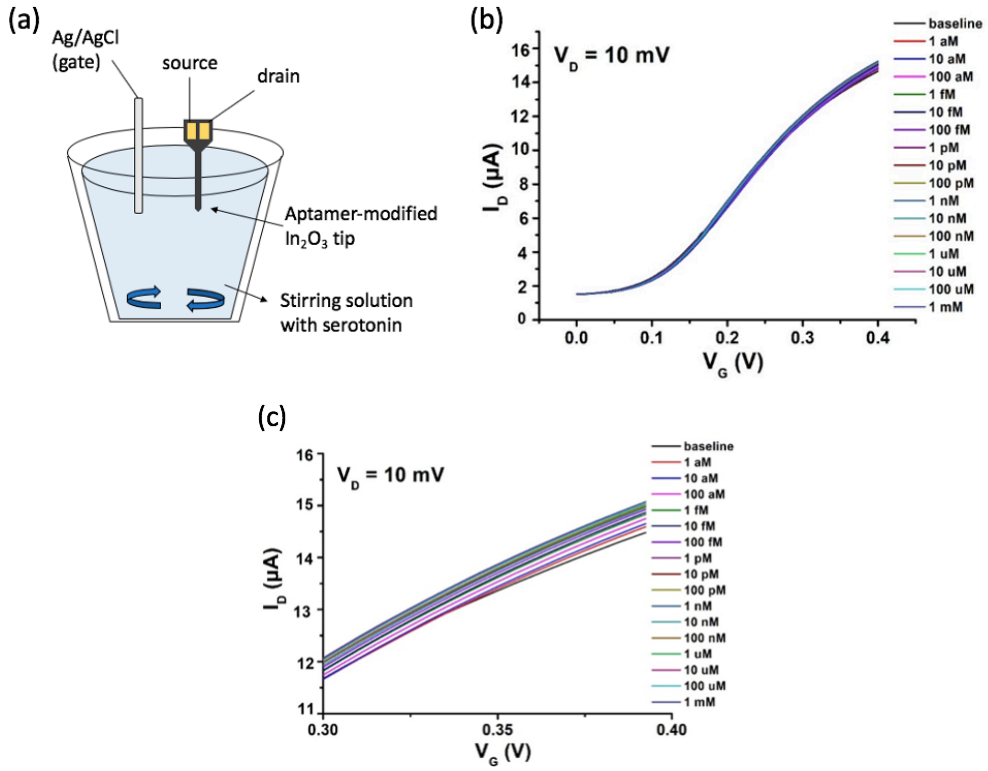

Figure 8.3. (a) Schematic illustration of the electrical measurement setup used for serotonin sensing experiments. 1x PBS (pH 7.4) was used as a gate liquid, and gate bias (V_{GS}) was applied through a Ag/AgCl reference electrode. (b)(c) Serotonin-aptamer-field-effect transistor (FET) microprobe responses to serotonin led to increases in source-drain current.

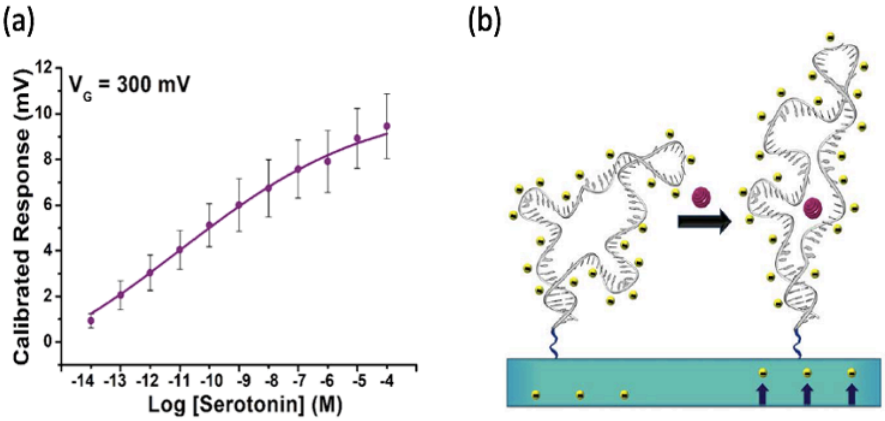

Figure 8.4. (a) Serotonin aptamer field-effect transistor (FET) microprobe responses to serotonin in 1x PBS. Error bars: standard error mean for 4 devices. (b) Hypothesized mechanism of stem-loop aptamer serotonin-induced reorientation away from semiconductor channels at distances within or near the Debye length.

8.3.3 Microsensor performance in brain tissue homogenates

To further evaluate the capability *in vivo* of the microsensors, more experiments mimicking the brain environments were performed. Brain tissue from Tph2 knockout mice lacking serotonin in central nervous system (CNS) were homogenized in aCSF to test microprobe performance. As shown in Figure 5c, these serotonin microprobes showed linear responses over a wide range of target concentrations from 10^{-15} to ~10^{-6} M. At high serotonin concentration corresponding to more than 10^{-6} M, decreased sensitivity was observed possibly due to the nonspecific adsorption of protein and other material to the electrode surface when exposing the sensor to brain tissue homogenates for long periods of time. However, this linear range was adequate to monitor the fluctuation of serotonin concentrations in the brain which is thought to be in the ~10^{-9} M range.

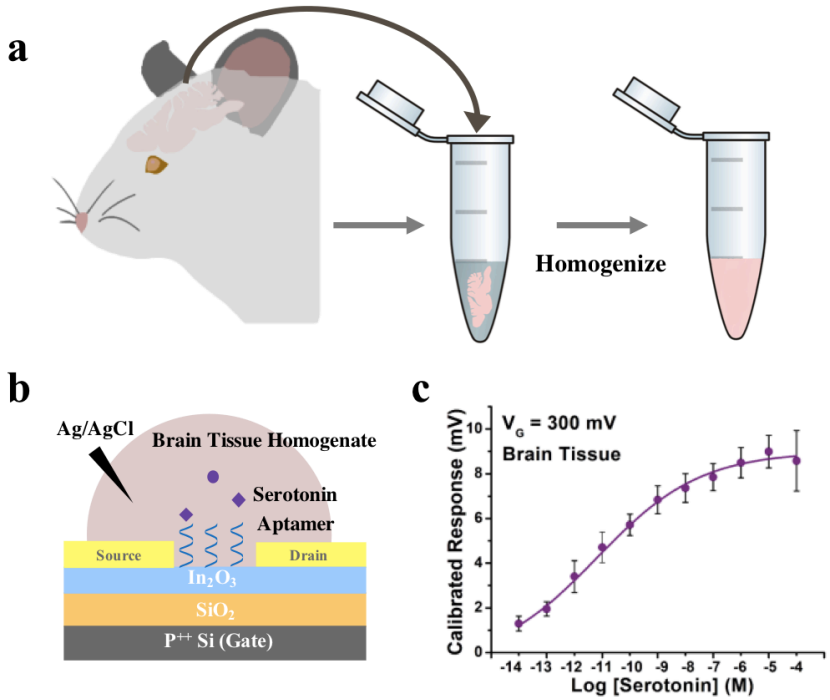

Figure 8.5. (a) Schematic illustration of brain tissue homogenate preparations. Brains from *Tph2* knockout mice were removed and mixed with 1x artificial cerebrospinal fluid. Tissues were sonicated on ice to generate the brain tissue homogenates. (b) Schematic illustration of the *in vitro* measurement setup. (c) Serotonin response curve in brain tissue homogenates. Error bars are ± standard error of the mean with n = 3.

8.3.4 Real-time detection of serotonin- I_{DS} versus time

Finally, we performed real-time detection of serotonin in 1x PBS buffer solution. The drain current of the serotonin aptamer FET device was continuously monitored at V_{GS} = 300 mV and V_{DS} = 10 mV while serotonin was introduced into the buffer solution.(Fig 6) To compensate for device-to-device variations in sensor response, relative sensor response (%) was employed here. This real-time test demonstrated that our aptamer FETs microprobe responded quickly to serotonin concentration changes, however, with relatively poor linearity compared to the result for transfer curve measurement. We hypothesized that the observed current can vary with continual application of the potential, as this treatment could alter the chemistry on the In_2O_3 surface with time. Moreover, the continual application of positive V_{GS} that maintained the In_2O_3 gate surface always in the state of negative charge could prevent the negatively charged aptamer attached on the surface from approaching the surface by charge repulsion, which further restricted the conformation change of aptamer. According to our previous hypothesis, the serotonin aptamer had complementary shape for serotonin only when folded. This charge repulsion from gate surface to aptamer that made aptamer folding unfavorable would hinder serotonin binding to aptamer at the beginning. To further explore this issue, it was decided to put more effort to the investigation on the effect of applied potential condition (*e.g.*, frequency) on sensor response.

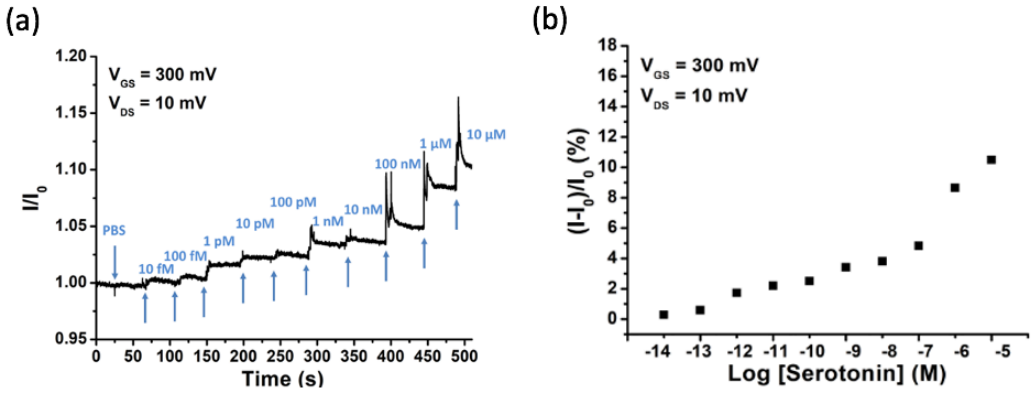

Figure 8.6. (a) Representative real-time measurements of serotonin aptamer FET microprobes in 1x PBS and (b) its calibration plot. Concentrations ranging from 10 fM to 10 uM were spiked into stirred beakers.

8.3.5 Selectivity of serotonin aptamer based microsensor

The selectivity toward serotonin was inherent to the aptamer itself. Experiments to verify selectivity of serotonin-aptamer based FETs sensor against serotonin precursors and its metabolites that have similar chemical structures, along with other monoamine neurotransmitters that may co-exist at the brain, such as L-5-hydroxytryptophan (L-5-HTP), 5-hydroxyindoleacetic acid (5-HIAA), dopamine, and norepinephrine, were performed in the report published by Andrew's group in 2018.[13]

8.4 Conclusion

The above studies demonstrated that the newly developed fabrication process to create implantable serotonin aptamer FETs microprobe resulted in high performance devices. These microprobes were capable of highly sensitive detection that was linear over a large dynamic range with a response time on the order of seconds in physiological environments (*e.g.*, PBS and brain tissue homogenates). This developed microprobe platform is a promising candidate for the detection of other neurotransmitters at low detection limit in order to advance the understanding of neurotransmission in the brain. Advancements in this direction will provide more knowledge for the treatment of neurological diseases and disorders, accelerating the deployment of new medical inventions in the neuroscience field.

I-Wen Huang's contribution to this work focused on FETs microprobe fabrication. This involved designing fabrication process flow and optimizing process condition. Calibration of aptamer-functionalized FETs microprobe was also provided.

8.5 References

1. Jun, J. J. *et al.* Fully integrated silicon probes for high-density recording of neural activity. *Nature* **551**, 232–236 (2017).
2. Du, J., Blanche, T. J., Harrison, R. R., Lester, H. A. & Masmanidis, S. C. Multiplexed, High Density Electrophysiology with Nanofabricated Neural Probes. *PLoS One* **6**, 26204 (2011).
3. Rios, G., Lubenov, E. V, Chi, D., Roukes, M. L. & Siapas, A. G. Nanofabricated Neural Probes for Dense 3-D Recordings of Brain Activity. *Nano Lett.* **16**, 6857–6862 (2016).
4. Yang, H., Sampson, M. M., Senturk, D. & Andrews, A. M. Sex-and SERT-Mediated Differences in Stimulated Serotonin Revealed by Fast Microdialysis. *ACS Chem. Neurosci.* **6**, 1487–1501 (2015).
5. Jaquins-Gerstl, A. & Michael, A. C. A review of the effects of FSCV and microdialysis measurements on dopamine release in the surrounding tissue. *Analyst* **140**, 3696 (2015).
6. Yang, H., Thompson, A. B., Mcintosh, B. J., Altieri, S. C. & Andrews, A. M. Physiologically Relevant Changes in Serotonin Resolved by Fast Microdialysis. *ACS Chem. Neurosci.* **4**, 790–798 (2013).
7. Hashemi, P., Dankoski, E. C., Petrovic, J., Keithley, R. B. & Wightman, R. M. Voltammetric detection of 5-hydroxytryptamine release in the rat brain. *Anal. Chem.* **81**, 9462–9471 (2009).
8. Daws, L. C. *et al.* Transport mechanisms governing serotonin clearance in vivo revealed by high-speed chronoamperometry. *J. Neurosci. Methods* **143**, 49–62 (2005).
9. Montañez, S., Munn, J. L., Owens, W. A., Horton, R. E. & Daws, L. C. 5-HT1B receptor modulation of the serotonin transporter in vivo: Studies using KO mice. *Neurochem. Int.* **73**, 127–131 (2014).
10. Lee, W. H. *et al.* hig. *Anal. Chem.* **88**, 1230–1237 (2016).
11. Arroyo-Currás, N. *et al.* Subsecond-Resolved Molecular Measurements in the Living Body Using Chronoamperometrically Interrogated Aptamer-Based Sensors. *ACS Sensors* **3**, 360–366 (2018).
12. Arroyo-Currás, N., Dauphin-Ducharme, P., Scida, K. & Chavez, J. L. From the Beaker to the Body: Translational Challenges for Electrochemical, Aptamer-Based Sensors. *Anal. Methods* **12**, 1288–1310 (2020).
13. Nakatsuka, N. *et al.* Aptamer – field-effect transistors overcome Debye length limitations

for small-molecule sensing. **324**, 319–324 (2018).

14. Swensen, J. S. *et al.* Continuous, real-time monitoring of cocaine in undiluted blood serum via a microfluidic, electrochemical aptamer-based sensor. *J. Am. Chem. Soc.* **131**, 4262–4266 (2009).
15. Kim, J. *et al.* Fabrication of High-Performance Ultrathin In 2 O 3 Film Field-Effect Transistors and Biosensors Using Chemical Lift-Off Lithography. *ACS Nano* **9**, 4572–4582 (2015).
16. Zhao, C. *et al.* Large-Area, Ultrathin Metal-Oxide Semiconductor Nanoribbon Arrays Fabricated by Chemical Lift-Off Lithography HHS Public Access. *Nano Lett* **18**, 5590–5595 (2018).
17. Rim, Y. S. *et al.* Printable Ultrathin Metal Oxide Semiconductor-Based Conformal Biosensors. *ACS Nano* **9**, 12174–12181 (2015).
18. Ishikawa, F. N. *et al.* A Calibration Method for Nanowire Biosensors to Suppress Device-to-device Variation. *ACS Nano* **3**, 3969–3972 (2009).

Chapter 9: Recommendations for future work

9.1 Electroenzymatic Neurotransmitter Sensing

Since the sensitivities of electroenzymatic sensors for glutamate and choline sensing have been greatly improved while maintaining excellent selectivity as mentioned in chapters 2 and 3, future work with this project will focus on employing the optimized polymer and enzyme conditions to create thinner neuroprobes with higher density of recording sites. This includes the increase in lead density, decrease in recording site area and use of a thinner wafer. Due to the difficulty of directly handling thinner Si wafer corresponding to wafer thickness less than 100 μm, silicon-on-insulator (SOI) substrate is suggested to be used. SOI substrates consists of a thin insulating layer such as SiO_2 sandwiched between a thin layer of Si (device layer) and the thick Si substrate called a carrier wafer. This buried SiO_2 layer is used as an etch-stop layer during the fabrication process, which controls the probe thickness. The carrier wafer is etched through from the back side at the very last step to release the probe shaft. Afterward the polymer and enzyme layers can be deposited on the recording sites to make the probe sensitive and selective. Even though a systematic improvement of sensors has been accomplished as described in chapters 2 and 3, the optimal immobilization condition of polymer and enzyme might be different for a newly designed probe as compared to the old one, which would require further optimization.

In addition, it is always recommended to further push the spatiotemporal resolution of our sensors as far as we can to ensure more accurate correlation between action potentials and neurochemical signals. Methods by which the electroenzymatic sensors could be modified to increase sensitivity and reduce response time include improving enzyme activity retention and maximizing deposited enzyme concentration during the immobilization process by using better crosslinkers. As mentioned in chapters 2 and 3, the most desired crosslinker should have proper spacer arm length and should react with target functional groups that the immobilized enzyme

has an abundance of available on the surface for crosslinking (such as carboxyl group on glutamate oxidase and choline oxidase) so that a highly concentrated and stable enzyme layer can be achieved. However, the crosslinker reacting with carboxyl groups with medium spacer arm currently is not commercially available (see chapter 3). It will be worthwhile to try such a crosslinker if one can obtain or synthesize one. Once concentrated active enzyme can be successfully immobilized, the enzyme layer thickness can be further reducing to get the highest sensitivity and fastest response time.

Finally, more functionalities such as electrical recording, on-probe reference electrode and drug delivery will be integrated to our probe to meet the requirements of future objectives in neuroscience. More reliability studies and chronic experiments *in vivo* need to be performed to validate the functionality of these probes.

9.2 PDMS microcontact printing (μCP) to fabricate microneuroprobes for multi-sensing of neurotransmitters

Current work is being done to demonstrate the feasibility of PDMS μCP to selectively transfer the model enzymes, choline oxidase and glucose oxidase, with pattern size in micro range during the dual-sensing microprobe fabrication. However, our current μCP set-up still presents some problems and here are some improvements that could be made to address these issues.

Unlike conventional application of μCP to modify surface with self-assembled monolayer molecules, applying this method to the fabrication of electroenzymatic microprobe requires high enzyme loading on the electrode surface to ensure sufficient active enzyme available to consume substrate at high rate. In chapter 6, we placed a droplet (~3 μL) of enzyme “ink” on a PDMS microstamp and wicked away the excess after this “inking” step, resulting in a sensor that has only a thin layer (~300 nm thick) of enzyme transferred onto the surface. In order to print more

enzyme onto the microprobe, in our later work in chapter 8 the “wicking away of the excess ink step” was skipped and the resting time before printing was prolonged until the whole ink becomes “printable” gel. This little modification on printing process successfully led to sensors with higher enzyme loading (~4000 nm thick) and thus better sensor sensitivity. But the issue arises from this method is that the excess ink on the stamp base surface (“roof”) could collapse onto the substrate during the printing process. One way this could be addressed could be to design the stamp with deeper grooves to reduce the chance of ink on the stamp base contacting the substrate surface, which can be done by modifying the mask used for stamp fabrication (Fig. 1). Because deeper grooves of the stamp might lead to deformation of the soft stamp such as buckling, the force exerted during printing should be gentler. Another way to address this issue is to use a “stamp pad” method, where the PDMS stamp is placed in contact with a surface wetted with ink solution to localize the inking to the stamp corrugation.[1,2]

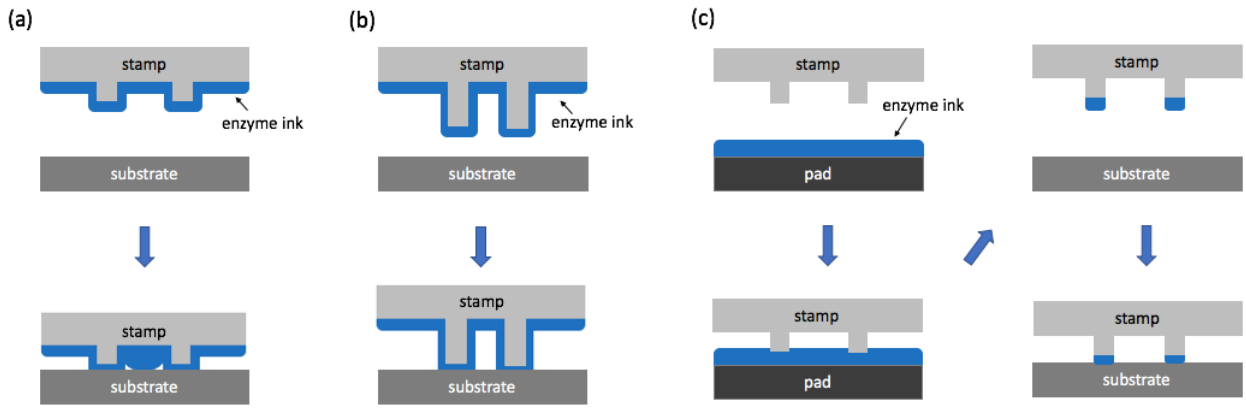

Figure 9.1. Schematic of (a) “roof-collapse” issue from current stamp design, (b) potential solutions of designing stamp with deeper grooves and (c) using “stamp-pad”

Diffusion of the imprinted enzyme ink during and after the printing process is another concern in stamp fabrication in general. Such problem is enhanced in our project when higher enzyme loading, corresponding to stamped layer of a few microns thick, is required per stamp. Bass et al. demonstrated that higher molecular weight alkylthiols such as octadecanethiol diffuses less on a metal surface compared to hexadecanethiol.[3] A similar result was achieved by our group as shown in chapter 8 using a specially designed polymer to replace conventional BSA as ink solution can limit the diffusion problem during printing. However, the polymer used in chapter 8 is not easy to access and requires special techniques to synthesize. It is recommended to use other commercially available polymers and thoroughly investigate the effect of polymer molecular weight on printing results and also sensor performance.

After further modifying the printing process, this project should focus on employing this method to more enzymes and even the permselective polymer layers. New microprobes with denser microelectrode arrays and smaller sensing sites will be fabricated in the future and will require submicron to nanoscale printing to pattern multiple enzymes. This can be done by modifying a mask for the electrode patterning step. In addition, sensors capable of simultaneously recording multiple neurochemicals must be developed to meet the needs in neuroscience studies to understand complex behaviors and neurological disorders. Thus, *in vivo* studies should be followed in both chapter 6 and 8 to prove the sensing ability of the microprobes.

9.3 Implantable Aptamer Field-Effect Transistor Neuroprobes Towards in Vivo Neurotransmissions Monitoring of Serotonin in Mice

Future work for developing aptamer field-effect transistor microprobes will first focus on improving the fabrication process, especially in the creation of patterned In_2O_3 and insulation layers. Current fabrication employs spin-coating an aqueous solution of indium(III) nitrate hydrate over the whole 4-inch Si wafer and annealing at high temperature to form an In_2O_3 film, where

gold electrodes were directly patterned on top. This design is not perfect and will lead to cross-talking between FETs integrated on the same probe when more than one FET are used for the measurement. Thus, In_2O_3 film will be patterned to ensure each individual FET on the microprobe can function properly when multiple sensing is conducted. Using photolithography following by advanced oxide etching (AOE) on In_2O_3 film before gold electrodes patterned is expected to easily solve this problem (Fig. 2). Currently parylene C is used as insulation material, however, its poor thermal resistance has made the parylene C film unable to survive after processing at high temperature, such as Si-etching in FDRIE and oxide-etching in AOE. Thus, unlike the fabrication of microprobe for electroenzymatic sensors, insulation layer deposition and patterning designed for In_2O_3-based microprobe were done in the very final step after Si etching through FDRIE was done. The issue that arises from this processing order is that photoresist cannot be evenly spin-coated on this partially etched-through Si wafer, even though the Si wafer was attached on a blue tape, which inevitably led to an uneven parylene etching result on different part of the wafer. Using other insulation materials, such as parylene N, parylene HT, with higher melting temperature and thermal resistance is expected to withstand the higher processing temperature in FDRIE so that a better insulation quality could be obtained by doing the Si etch through process in the final step.

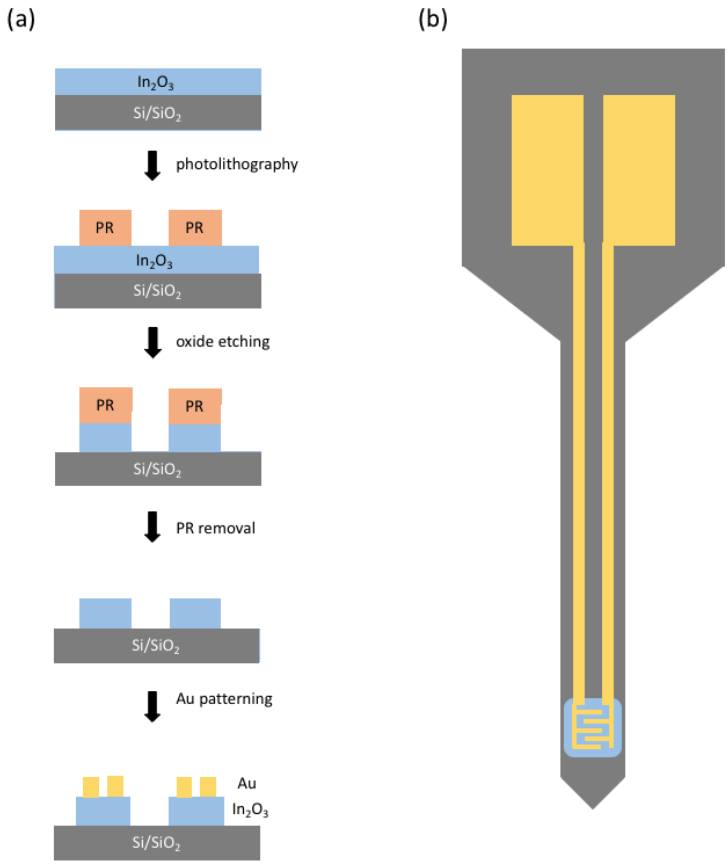

Figure 9.2. Schematic of (a) the In_2O_3 patterning process and (b) single device FET at the shank of neuroprobe with In_2O_3 pattern.

Creating an aptamer FET-based sensor that can simultaneously monitor multiple neurotransmitters is also another area of focus for future work. Currently, serotonin aptamer is immobilized on the In_2O_3 surface through the process of immersing the microprobe in a solution of thiolated DNA overnight, which will be problematic when different aptamers are immobilized on different FETs integrated on the same probe. To address this issue, other methods, such as microcontact printing or ink jet printing, that can selectively place aptamer solution onto different desired areas with high spatial resolution could be applied during the sensor construction. However, the optimization of printing or ink jeting conditions for different aptamers might take

some time. Concentration of aptamer solution might need to be increased due to the smaller volume of solution exposed to the contacting area on microprobe.

Further study on improving spatiotemporal resolution of these aptamer FET-based sensors to sub-second response time and cellular size sensing area is of important for the utilizing of sensors *in vivo*. We typically see a current response within few seconds of target injections into the beaker, which is not sufficient to monitor the rapid transmission of neurochemicals that is reported to be as fast as micro-second. To mitigate this issue, modifying DNA sequence or immobilization methods would be helpful to increase the rate of target binding and unbinding to the aptamer. Finally, *in vivo* study should always be followed to prove the feasibility of sensing of these microprobes in actual practice.

9.5 References

1. Libioulle, L., Bietsch, A., Schmid, H., Michel, B. & Delamarche, E. Contact-Inking Stamps for Microcontact Printing of Alkanethiols on Gold. (1999). doi:10.1021/la980978y
2. Pompe, T. *et al.* Submicron Contact Printing on Silicon Using Stamp Pads. *Colloids Surf., A* **12**, 2398–2401 (1996).
3. Bass, R. B. & Lichtenberger, A. W. Microcontact printing with octadecanethiol. *Appl. Surf. Sci.* **226**, 335–340 (2004).

Appendix A: Microprobe Fabrication for Electroenzymatic Sensors

A.1 Materials

Silicon wafers were ordered from Silicon Valley Microelectronics (Santa Clara, CA) with the following parameters: 100 mm diameter, p-type boron doped, orientation <1 0 0>, 150 μm

thickness. All microfabrication was conducted in the Nanoelectronics Research Facility (NRF) at UCLA.

A.2 Process Traveler

Process	Step	Name	Description	Remarks
I. Field oxide formation process				
	1	Label	Label wafer on the back unpolished side	Use diamond pen
Cleaning Steps	2	Piranha bath	Remove organic contaminants: • H_2SO_4:H_2O_2 = 17:1 • T=70°C; time=10min	• Use wafer carrier • Refresh solution with 250mL H_2O_2 if hasn't been used that day
	3	Rinse	Time = 2min	• Use rinse cycle in PFC hood
	4	HF bath	Remove native oxide: 5s in HF:DI=1:10 or 1s in BOE	• Caution very corrosive.
	5	Rinse	Time = 2min., N_2 blow dry after	• Gentle water stream • Don't use spin dryer (wafers will break)
Furnace	6	Oxide furnace	Thermally grow 1μm SiO_2 • Wet recipe (WET1100.001) • T=1100°C, time=2.5hr	• Keep everything clean (gloves/mask on) • High temperature (use caution) • Use quartz boat. Load wafers ASAP/
	7	Nanospec	Measure SiO_2 thickness (Silicon dioxide on silicon)	Measure center/top/bottom/left/right, average it
Cleaning Steps	8	Piranha bath	Remove organic contaminants: H_2SO_4:H_2O_2 = 17:1 T=70°C; time=10min	• Use wafer carrier • Refresh solution with 250mL H_2O_2 if hasn't been used that day
	9	Rinse	Time = 2min	Use rinse cycle in PFC hood
II. Electrode sites, channels, and bonding pads formation				
Lithography I	10	Dehydration bake	T=150°C Time ≥ 5 min	Drive off moisture, and improve PR adhesion
	11	HDMS coat	Improve PR adhesion Time ≥ 5 min	• HMDS: hexamethyldisilazane • Toxic (operate underneath hood) • Do not place wafer in the middle of metal

				container. Handle dips down and will break wafer when putting cover on.
	12	Photoresist spin coat	PR: AZ5214-EIR Thickness: ~1.6μm 2500 RPM Ramp = 1000 Time = 30sec	• Clean wafer chuck with acetone • Make sure PR covers at least 2/3 of the wafer surface prior to spin
	13	Soft bake	T=100°C Time = 1 min. (critical) Place at the center of hotplate	Make sure wafer is flat on hotplate
	14	Exposure	Karl Suss alignment: Soft contact Expose for 9.5 sec (when power = 8 mW/cm^2)	If power varies, use this formula to correct exposure time: t (sec) = 18*(8/actual power in mW/cm^2)
	15	Development	Remove exposed PR DIW:AZ400K=5:1 Developer ~19 sec.	Swishing back and forth
	16	Microscope	Inspection	• Make sure wafer is fully developed. • DO NOT hardbake after this step (for better lift-off results)
		Remove ~100Å PR	Tegal (~2 mins) Or Technics	Remove 100A PR for the whole wafer to prevent metal from being washed off during Lift-off
Metal Deposition	17	Metal deposition	Old CHA (evaporated metal deposition) Cr/Pt = 200Å/1000Å Deposition rate: 1Å/sec	• Deposit metal within 3 days after Litho I • Total deposition time: ~3hrs
	18	Lift-off	Sonicate in acetone (in 2L beaker)	• Use 3 beakers of acetone in series to clean each wafer • Keep wafers wet by rinsing with acetone • Rinse with DIW and dry with N_2
	19	Microscope	Inspection	Check for broken leads, chipped sites
III. Insulation layer deposition				
Oxide/Nitride Deposition	20	PECVD oxide	STS PECVD: 7500Å Recipe: HFSIOST Time: ~30min	• Blowdry wafer with N_2 prior to placing in machine

				• Check deposition rate first (~5 min)
	21	Nanospec	Measure SiO_2 thickness (Silicon dioxide on silicon) Goal: 7500Å	Measure subtract field oxide thickness to calculate deposited thickness
	22	PECVD nitride	STS PECVD: 7500Å Recipe: HFSINST Time: ~50min	
	23	Nanospec	Measure Si_3N_4 thickness (silicon nitride on silicon dioxide) Goal: 7500Å	For previous oxide thickness, type in average from step #21
IV. Open electrodes/soldering pads				
Lithography II	24	Dehydration bake	T=150°C Time ≥ 5 min	Drive off moisture
	25	HDMS coat	Improve PR adhesion Time ≥ 5 min	
	26	Photoresist spin coat	PR: AZ5214-EIR Thickness: ~1.6µm 2500 RPM Ramp = 1000 Time = 30sec	• Clean wafer chuck with acetone • Make sure PR covers at least 2/3 of the wafer surface prior to spin
	27	Soft bake	T=100°C, time = 1 min. (critical) Place at the center of hotplate	Make sure wafer is flat on hotplate
	28	Exposure	Karl Suss alignment: Soft contact, expose for 18 sec (when power = 8 mW/cm^2)	If power varies, use this formula to correct exposure time: t (sec) = 18*(8/actual power in mW/cm^2)
	29	Development	Remove exposed PR DIW:AZ400K = 5:1 ~19 sec.	Swishing back and forth
	30	Microscope	Inspection	Make sure wafer is fully developed.
	31	Hard bake	T = 150°C, 5min. Place at center of hotplate	• Do not post bake before inspection • Let cool before storing
Nitride/Oxide Etch	32	Si wafer carrier	Apply moist cooling grease on 500µm Si wafer carrier Bake more than 3min @ 75°C on hotplate	• Use q-tips to apply grease in circles over entire surface of carrier wafer • Make sure wafer backside is clean of grease

				• Stick wafer onto carrier wafer tightly by placing onto wafer and rotating until flats are aligned
	33	Nitride and oxide etch	AOE (recipe: OXIDAPIC) Etch time: ~4 min. (this etch time may be longer or shorter depending on the status of the AOE)	• Remove 1.5μm of nitride and oxide insulation layer • Do not run the etching more than 2 min for each time
	34	Inspection	Voltmeter or Nanospec	• Voltmeter: check if resistance between test metal is zero • Nanospec: check if thickness of oxide ≤field oxide thickness (oxide thickness<10,000A)
Cleaning Steps	35	PR strip	Matrix stripper "3 min strip" recipe	Make sure to keep wafer stuck to carrier wafer until after this step
	36	Release carrier	Slide wafer off carefully	Clean wafer backside and carrier wafer with acetone
V. Define probe outline				
Lithography III	37	Dehydration bake	T=150°C Time ≥ 5 min	Drive off moisture
	38	Photoresist spin coat	PR: AZ4620 Thickness: ~7μm 3000RPM, Ramp: 1000, Time: 30sec	• Clean chuck with acetone • Make sure PR covers at least 2/3 of wafer surface
	39	Soft bake (prebake)	T=100°C, 1'30". (critical) Place at center of hotplate	Make sure wafer is flat on hotplate
	40	Exposure	Karl Suss alignment: Soft contact, exposure time: 18 sec (power: 8mW/cm^2)	If power varies, use this formula to correct exposure time: t (sec) = 18*(8/actual power in mW/cm^2)
	41	Development	Remove exposed PR DIW:AZ400K = 4:1 4-10 mins.	
	42	Microscope	Inspection	Make sure wafer is fully developed
		Hard bake	120°C for 5 mins	
Si Wafer Etch-Through	43	Si wafer carrier	Apply moist cooling grease on 500μm thick Si carrier wafer	• Use q-tips to apply grease in circles over

			Bake 3 min. @ 75°C	entire surface of carrier wafer • Make sure wafer backside is clean of grease • Stick wafer onto carrier wafer tightly by placing onto wafer and rotating until flats are aligned
	44	Nitride/oxide etch	AOE (recipe: OXIDAPIC) Etch time: ~7-8 min. (this etch time may be longer or shorter depending on the status of the AOE)	• Remove all nitride and oxide from exposed areas • Do not run the etching more than 2 min for each time
	45	Si etch through	FDRIE (deep reactive ion etch): Recipe FN-DY ~20 min. total etch time (this etch time may be longer or shorter depending on the status of the FDRIE)	• Do not run DRIE for more than 5 minutes at a time (could overheat the wafer) • O_2 plasma clean for 30 min BEFORE use
	46	Inspection	Microscope	Do not release wafer from carrier until etch through of silicon is confirmed. Should be able to see cooling grease through the outlines for silicon etch through
Stripping PR	47	Release carrier	Slide wafer off carefully	Clean carrier with acetone
	48	PR strip	PR stripper sink (ALEG 355) T=75°C, at least 30 min.	Rinse with DI water for 2 min. after Blow dry with N2

Appendix B: Preparation of Glutamate and Choline Sensors

B.1 Materials

- *m*-Phenylenediamine (Sigma)

- Nafion (5 wt. % in lower aliphatic alcohols and water, contains 15-20% water) (Sigma)
- Bovine serum albumin lyophilized powder (Sigma)
- Glutaraldehyde solution, 25% in water (Sigma)
- L-Glutamate oxidase (EC 1.4.3.11) (US Biological)
- Bis(sulfosuccinimidyl)suberate (Thermo Fisher Scientific)
- Choline oxidase from *Anthrobacter globiformis* (Sigma)
- Sodium phosphate buffer (PBS) was composed of 50 mM sodium phosphate (dibasic) and 100 mM sodium chloride (pH 7.4). Deionized water was generated using a Millipore Milli-Q Water System and was used for preparation of all solutions.

B.2 Procedure

B.2.1 Probe Assembly

1. Detach each probe off of wafer (press on corner w/ fine forceps) and check for broken leads, chipped site and poor insulation layer under microscope.
2. Cut plastic square coverslips into strips and secure microprobe on it with epoxy. Leave approximately 5 min for drying.
3. Cut 4 insulated Pt wires per probe and strip one end ~1 cm, another end ~2 mm.
4. Solder (@ 510 °C) wires on soldering pads of the microprobe. Apply soldering flux during soldering to remove impurity on soldering pad surface for better soldering results.
5. Sonicate the soldered microprobe in isopropyl alcohol for approximately 2 minutes. Rinse with DI water and blow dry with gas. Repeat this step with another cleaner isopropyl alcohol again.
6. Insulate the soldered part with epoxy on the back/front side of microprobe. Repeat this step until no wire and solder is exposed.
7. Label probe with tape

B.2.2. Acid clean

A clean scan in 0.1 M H_2SO_4 (diluted with DI water; Cyclic voltammetry: -0.2 V to 1.5 V, 50 mV/s, 5 cycles) was done to remove any surface impurities.

B.2.3 Bare sensor test

1. Make 10 mM H_2O_2 (diluted with DI) dilution solution
2. A bare sensor test in 10 mL PBS (0.7 V vs Ag/AgCl) was done to check sensor response to 20 μM H_2O_2 (inject 20 μL of 10 mM H_2O_2). Good sensors should give an increase in current of ~2 nA.

B.2.4 PPD deposition and Nafion coating

1. Prepare 5 mM PPD in 1X PBS (5.4 mg PPD powder + 10 mL 1X PBS) in 15 mL falcon tube. Vortex and sonicate for complete mixing.
2. Electrodeposit PPD: Apply 0.85 V vs Ag/AgCl until charge, Q (nA*h) reaches 0.21
3. Dip-coat in 2% Nafion and bake the sensor at 115 °C for 20 minutes.

B.2.5 Enzyme Immobilization

1. One 2 μL aliquot of GluOx (0.25 U/μL; 3 mg/ml diluted with DI) was mixed with 1-4 μL BSA solution (10 mg/mL diluted with DI) depends on the status of GlutOx; Or one 4 μL aliquot of ChOx (0.5 U/μL; 20 mg/ml diluted with DI) was mixed with 2 μL BSA solution (60 mg/mL diluted with DI). Enzyme solution was manually spreading on the surface of the sensor by using a microsyringe and the process was monitored under a microscope.
2. 174 mM BS3 (1mg BS3 in 10ul PBS; make it right before use) was placed into a microsyringe and manually coated once on top the previous enzyme layer.
3. Sensor stored at 4 °C in dessicant at least overnight.

Appendix C: Measurement of Response Time

Response time is defined here as the time for the current signal to reach 90% of its steady-state value in response to a step change in analyte from zero to 40-60 μM. A reliable measurement of the intrinsic response time should be conducted under conditions where external mass transfer is essentially eliminated. Figure. 1 shows our first generation of flow cell set-up specially designed for response time measurement for the microprobe. A flow rate is maintained using a pump, and the switch between the load and injection position is controlled by using an automated Rheodyne valve. During the load mode, the central loop is bypassed and filled with analyte. Switching to the injection mode brings the loop into the flow path. Once the analyte is injected, it passes through the custom flow cell, where the diameter of an inner reservoir is designed to be 30 mm, reaching the sensing sites of microprobe. However, one of the most important concerns using this set-up is that the intrinsic response time is obscured by dispersion of the analyte in the flow system. Diffusion and dispersion of analyte in PBS traveling the transport tube and the flow cell (~ more than 5 cm) before analyte reaching the electrode surface greatly affect the observed response time. This problem was confirmed when the dye solution was used as analyte and the traveling path was monitored. Response time of our Glut or Ch microsensors evaluated from using this set-up is in few seconds range (~0.8 s at best).

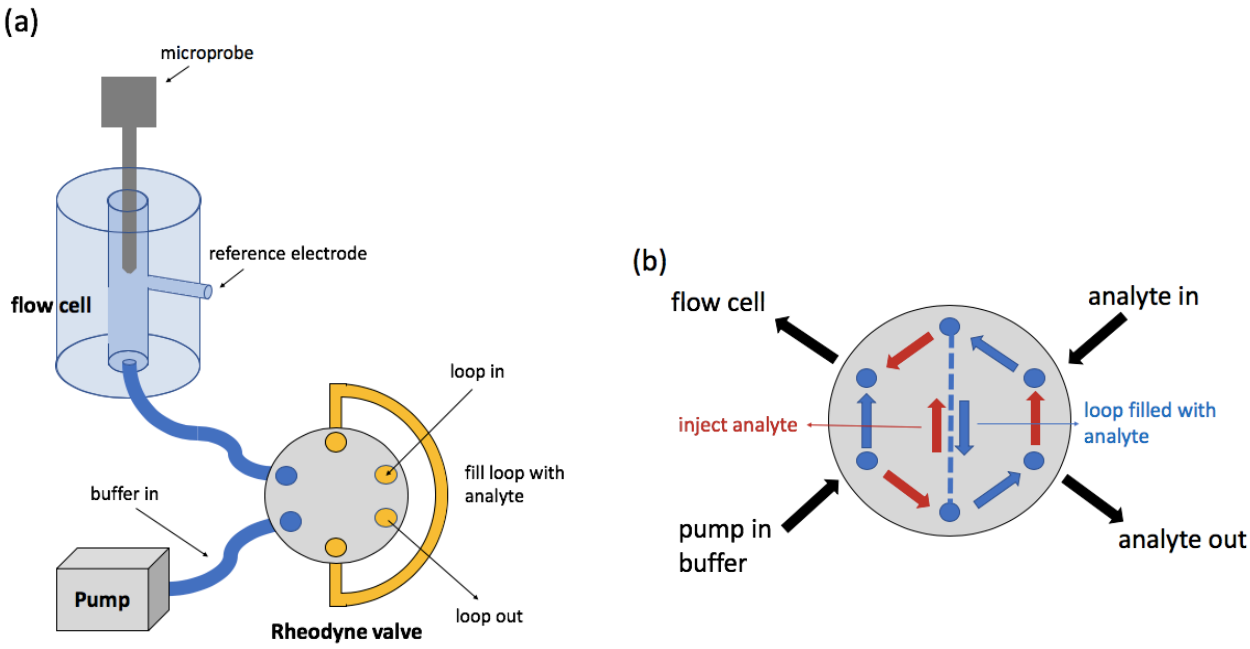

Figure C.1. (a) First generation of flow cell set-up. The flow injection system for the measurement of response time for a microprobe consists of a pump, a Rheodyne valve and a flow cell. (b) Schematic working mechanism of an automated six-port Rheodyne valve switching between analyte loading mode (shown in blue arrows) and analyte injecting mode (shown in red arrows).

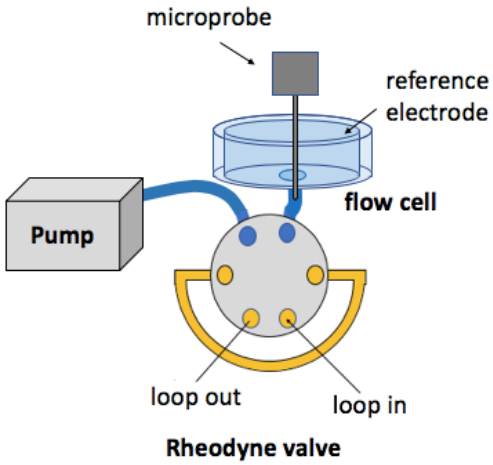

Figure C.2. The second generation of flow cell set-up with shorter and straighter traveling path from Rheodyne valve to the electrode surface.

Figure. 2 shows the second generation of flow cell where the travel distance from Rheodyne valve and electrode surface was greatly shortened (~ less than 2.5 cm). This set-up allows the easy measurement of response time of our Glut sensors less than 1 s (with avg ~0.5 s). The dispersion issue can be studied by testing the bare Pt response to H_2O_2 which is supposed to appear as a near step change as expected given very rapid electrooxidation kinetics. In this set-up, bare Pt response to 20 μM H_2O_2 was ~0.1 s, which push us to keep modifying the set-up to eliminate the dispersion issue. Besides the flow cell design, the flow rate controlled by pump also plays an important role in the response time observed (Fig. 3.c). As the result, flow rate should be optimized individually for different set-up.

The latest set-up for test the response time consists of two peristaltic pump-driven streams of solution (PBS buffer and analyte) flowing from separate pipette tips were positioned close to the microprobe tip (Fig. 3.a and b). Rapid step changes in analyte concentration at the microsensors were achieved by alternating between PBS buffer and analyte streams by turning pumps on and off. Response time of Pt electrode response to H_2O_2 was as fast as 0.08 s using this new set-up. However, parallel flow was not preferable due to the difficulty of keeping sensors exposed to solutions. In addition, the orientation, position and distance all need to be carefully modified and considered during the test in order to get the best results. Both peristaltic and syringe pumps are working in our case, even though peristaltic causes fluid flow to be pulsated rather than smooth and continuous. Since our electroenzymatic sensors respond fast enough, response time of sensor can still be clearly evaluated before the disturbance caused by the peristaltic pump. For example, in Figure. 4.a the current signal already reaches maximum of its steady-state value in response to a step change in analyte, which is at the point of ~365 s, before the pump pulsation occurred.

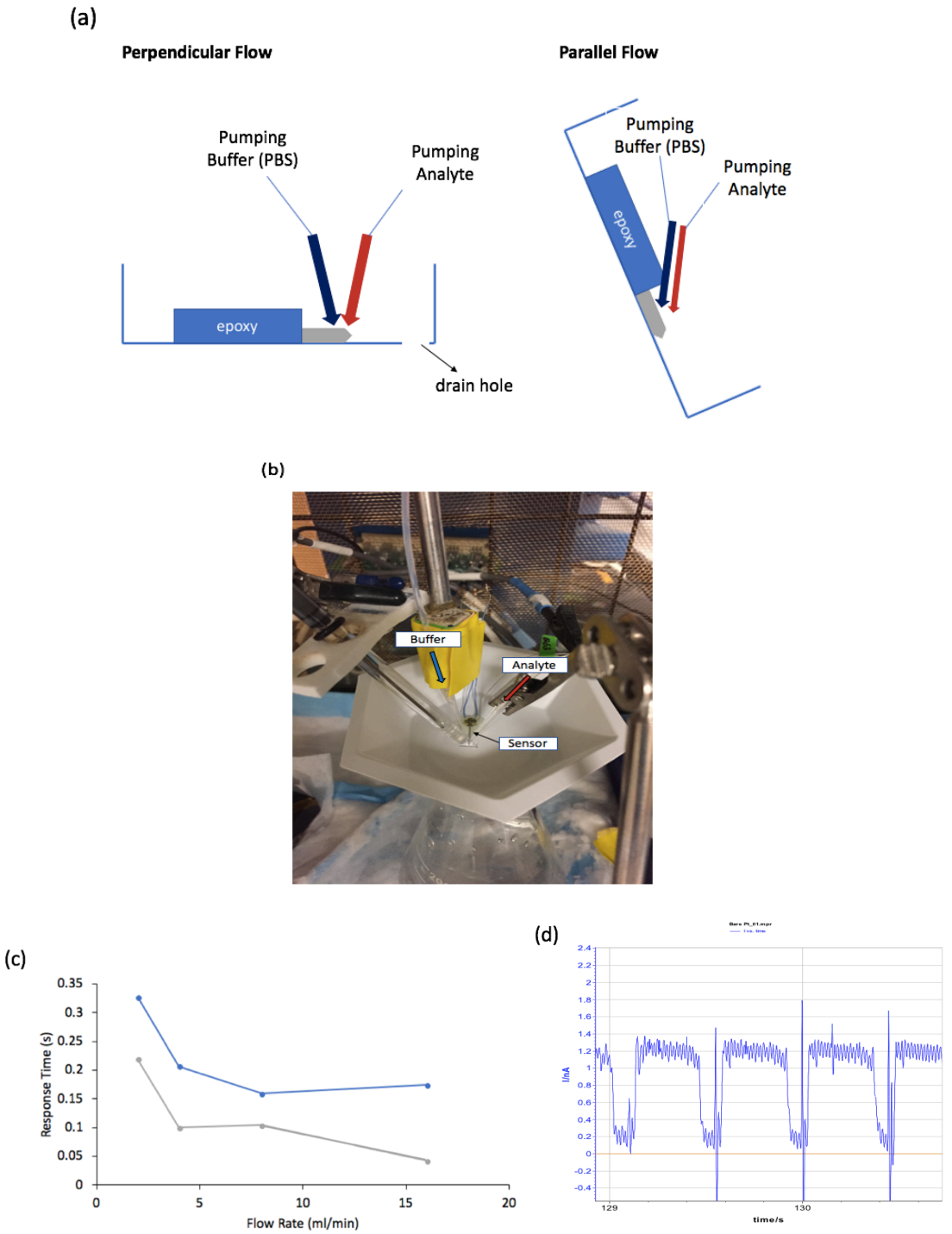

Figure C.3. (a)(b) Testing set-up for microsensor response time. Rapid switching of solution flow onto the microprobe was controlled by alternating between pumped streams of PBS buffer and analyte solution. (c) Representative Glut sensor response time versus flow rate with response to H_2O_2 shown in grey trace and to Glut shown in blue trace. (d) Representative experimental result of current versus time.

Lastly, flow cell might not be preferable for testing sensors such as Ch electroenzymatic sensors. Two different steady states with smaller current value (smaller than the sensitivity calculated from stirring beaker) in the first steady state corresponding to pump-on flowing mode, following by a slow increase in current after switching pump off to stop the flow, always happen when using the flow cell to test Ch sensors (Fig.4.b). It is hypothesized that, unlike Glut sensor that GlutOx directly catalyzes Glut to the final product in one step, ChOx catalyzes the oxidation of Ch to an intermediate, glycine-betaine, which reacts further to give the last products. Certain amount of the intermediate generated might be continuously flowed away from the electrode surface when the pump is on so that less concentrated glycine-betaine is available to react further and generate expected signals. As the result, step change in current in the first steady state cannot completely represent the response time of Ch sensors and it is suggested to use stirring beaker to evaluated response time for Ch sensors.

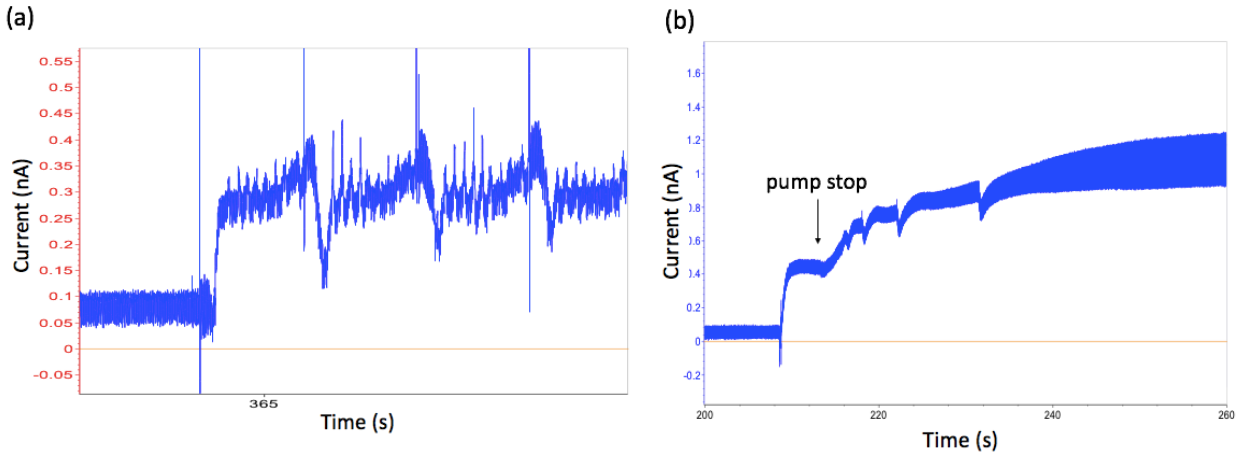

Figure C.4. Representative current versus time result for (a) Glut and (b) Ch sensors using peristaltic pump to introduce analyte to the flow cell.

Appendix D: Microprobe Fabrication for In_2O_3-based FETs array

Formation of In_2O_3 semiconductor layer

1. Aqueous solutions of 0.1 M indium(III) nitrate hydrate (99.999%) were spin-coated onto the 4" Si substrates at 3000 rpm for 30 s
2. Prebake at 100 °C for 5 min
3. Bake at 350 °C for 3 h.

Metal electrode deposition

4. Photoresist (PR), AZ® 5214-E, is spin-coated on the wafer at 2500 rpm (with 300 rpm/sec ramp) for 30 sec.
5. Soft bake at 100 °C for 1 min.
6. After alignment UV is exposed for 15 sec.
7. PR is developed in AZ 400K developer. (AZ 400K : DI water = 1 : 6)
8. Rinse wafer with DI and blow dry with a nitrogen gun
9. Use CHA electron-beam evaporator to grow 10 nm Ti and 30 nm Au films at 10^{-8} Torr with an evaporation rate of 0.1 nm/s.
10. Sonicate wafer in acetone to lift off unwanted metals.
11. Check broken leads and chipped sites under microscope

Si etch through to define outline of the probe

12. Photoresist (PR), AZ® 4620, is spin-coated on the wafer at 3000 rpm with ramp of 1000 rpm/s for 30 s
13. Soft bake at 100 °C for 1 min 30 second.
14. After alignment UV is exposed for 18 sec.
15. PR is developed in AZ 400K developer. (AZ 400K : DI water = 1 : 3)
16. Hard bake at 120 °C for 5 min.

17. Applying cooling grease on a 500 μm carrier wafer and stick thin wafer with the carrier wafer. Bake at 80 °C for more than 3 mins
18. Use AOE to etch the top In_2O_3 and SiO_2 layer (recipe: OXIDAPIC for ~10s).
19. Use Nanospec to check oxide thickness (should show less than 100Å).
20. Clean FDRIE chamber by running a O_2 clean for 30 min before uses
21. Use FDRIE to etch through Si wafer (recipe: FN-DY for 5 min at most each time; total etching time ~ 22 min); Consult with nanolab member to check the best recipe each time
22. FDRIE etching until grease or carrier wafer can be seen from the front side
23. Slide wafer off from carrier wafer
24. Remove PR using ALEG heated at 75 °C at least 30 min. Rinse wafer with acetone, DI and blow dry with N_2 gun

Parylene Deposition

25. Use SCS Parylene C coating system to deposit parylene C (~1 μm thick)

Pattern Parylene

26. Stick blue tape on the back side of the wafer
27. Photoresist (PR), AZ® 5214-E, is spin-coated on the wafer to define the source and drain electrodes at 2000 rpm (with 1000 rpm/sec ramp) for 30 sec
28. Carefully remove the blue tape
29. Soft bake at 100 °C for 1 min
30. After alignment UV is exposed for 18 sec
31. Use Technics oxygen plasma (Process pressure ~300 torr; RF power ~300 watt; etching time no more than 30 s for better thickness control) to etch In_2O_3 layer until blue-colored In_2O_3 shown on the tip
32. Leave wafer in acetone for more than 30 min to remove PR

Appendix E: Troubleshooting and Common Issues

E.1 Microprobe fabrication

The most challenging part of microprobe fabrication is the final etch through of Si wafer to define the probe outline. At this step, thermal grease should be applied equally in proper amount to make sure even etching rate on the whole 4-inch wafer. To prevent wafer stick on the wafer holder in FDRIE, thick 4620 PR covered on the edge of wafer should be completely cleaned out by using a blade to scratch the PR layer followed by using acetone to wipe out any residue. Check the logbook and consult with nanolab staff regarding the best performing recipe before using it. Each Si etching should not be more than 5 min to reduce the chance of PR burn and undercut of Si. In addition, etching rate should be evaluated frequently to ensure wafer is etched in the minimum amount of time that it need.

It is also particularly challenging to create a patterned insulation layer on In_2O_3 covered wafer. Conventional SiO_2 deposition following by AOE etching is not working for our case since the recipe for etching SiO_2 usually also etches the metal oxide, especially when the In_2O_3 layer on our probe is only few nm thick. To keep the In_2O_3 layer on the wafer, we used parylene C as insulation layer and used the anisotropic oxide etcher (Technics) that has a recipe with lower frequency reactive ion to better control etching of parylene C. Due to the relatively lower melting temperature of parylene C and higher processing temperature for Si etching in FDRIE, Si etching step (defining probe outline) should be done before the deposition of parylene C.

In addition, to stripping the photoresist off after parylene etching was done, acetone should be used instead of ALEG. We tried using photoresist AZ 4620 and strip it with ALEG at the beginning, however, parylene layer was also stripped off along the AZ 4620 in the ALEG. This could be due to the reaction of AZ 4620 and parylene upon heating so that the aggressive photoresist stripper, ALEG, can remove parylene. Here, we suggest to use photoresist AZ 400k

as protecting layer during etching, using Technics etcher, which process wafer in lower temperature and finally strip the photoresist by immersing wafer in acetone for longer period of time to ensure the integrity of patterned insultation layer.